# Broadband Microwave Spectroscopy on Correlated Electrons

Von der Fakultät Mathematik und Physik der Universität Stuttgart zur Erlangung der Würde eines Doktors der Naturwissenschaften (Dr. rer. nat.) genehmigte Abhandlung

Vorgelegt von

## Marc Scheffler

aus Hildesheim

| | |
|---|---|
| Hauptberichter: | Prof. Dr. M. Dressel |
| Mitberichter: | Prof. Dr. K. von Klitzing |
| Tag der mündlichen Prüfung: | 17. September 2004 |

1. Physikalisches Institut der Universität Stuttgart

2004

# Contents

# Kurzfassung

Bei der Erforschung elektronischer Eigenschaften von Festkörpern gehört die optische Spektroskopie zu den am vielseitigsten einsetzbaren experimentellen Methoden, da die verwendete Strahlung in ihrer Frequenz und damit ihrer Energie über viele Größenordnungen den zu untersuchenden Prozessen angepasst werden kann [1]. Während etwa die charakteristischen Energieskalen von normalen Metallen, Halbleitern und Isolatoren durch deren Bandstruktur gegeben sind und in der Größenordnung von eV liegen, sind für kollektive Effekte, die durch die Wechselwirkung der Elektronen untereinander entstehen, die charakteristischen Energieskalen viel kleiner, typischerweise im Bereich von meV, also im Ferninfraroten. Bei diesen Energien können optische Experimente noch mit Aufbauten durchgeführt werden, die der geometrischen Optik entsprechen. Sobald die Wellenlänge der verwendeten Strahlung aber die Abmessungen der Probe oder anderer Elemente des Spektrometers (z.B. Linsen, Blenden, Strahlteiler) erreicht oder gar übertrifft, kann die Welle nicht mehr im Freifeld verlaufen, sondern muss geleitet werden, etwa mit einem Hohlleiter oder Koaxialkabel. Typischerweise ist dies bei Wellenlängen oberhalb von 1 cm (also unterhalb von Frequenzen von 30 GHz bzw. unterhalb von Energien von ca. 0.1 meV) der Fall.

So niedrige Energien sind bei der Untersuchung von Materialien von Bedeutung, die ausgesprochen starke Korrelationen zwischen den Elektronen aufweisen. Eine solche Materialklasse bilden die sogenannten Schwere-Fermionen-Verbindungen, zu denen das in dieser Arbeit untersuchte System $UPd_2Al_3$ gehört. In Schwere-Fermionen-Verbindungen wird bei tiefen Temperaturen ein metallischer Zustand beobachtet, der durch die Annahme einer sehr großen effektiven Masse

der Ladungsträger (typischerweise in der Größenordnung hundert freie Elektronenmassen) beschrieben werden kann. Eine Erhöhung der effektiven Masse geht einher mit einer entsprechenden Verlangsamung der für den Ladungstransport charakteristischen Zeitskala [2], nämlich der Relaxationszeit $\tau$. Während die durch die Relaxationszeit definierte Frequenz, die Streurate $\Gamma = 1/\tau$, für normale Metalle im Ferninfraroten liegt, wird sie für Schwere-Fermionen-Verbindungen typischerweise im Grenzbereich von Submillimeter- und Mikrowellenstrahlung angenommen, also bei niedrigeren Frequenzen als mit konventionellen Spektrometern zugänglich ist, weshalb es bisher kaum Messungen an Schwere-Fermionen-Verbindungen im Frequenzbereich der Streurate gibt. Für $UPd_2Al_3$ haben vor kurzem durchgeführte Untersuchungen mit einem Submillimeterspektrometer die Streurate nicht direkt nachweisen können, d.h. sie wurde folglich bei noch niedrigeren Frequenzen, im Bereich von einigen GHz vermutet [3,4]. Diesen Sachverhalt experimentell aufzuklären war Ziel dieses Projektes.

Da der hier interessierende Frequenzbereich von einigen GHz mit den bisher verfügbaren experimentellen Methoden nicht zu untersuchen war, wurde zunächst ein Spektrometer aufgebaut, das den durch diese Fragestellung vorgegebenen Anforderungen gerecht wird, also der breitbandigen Bestimmung der frequenzabhängigen Leitfähigkeit im Mikrowellenbereich. Dabei muss das Spektrometer Tieftemperaturmessungen ermöglichen, da die Charakteristika der schweren Fermionen nur dann beobachtbar sind. Derzeit sind mit dem inzwischen routinemäßig betriebenen Spektrometer Messungen von 1.65 K bis 300 K möglich (in einem $^4$He-Badkryostat), der standardmäßig zugängliche Frequenzbereich beträgt 45 MHz bis 20 GHz.

Wie in Abb. 1 dargestellt, wurde für das Spektrometer die Corbino-Geometrie gewählt. Hierbei wird das Mikrowellensignal von der Quelle eines Netzwerkanalysators durch ein Koaxialkabel zur Probe geleitet, die dieses Koaxialkabel abschließt. Das Signal wird von der Probe reflektiert, läuft in derselben Leitung wieder zurück zum Netzwerkanalysator und wird dort detektiert. Aus hinlaufender und reflektierter Welle bestimmt der Netzwerkanalysator den Reflexions-
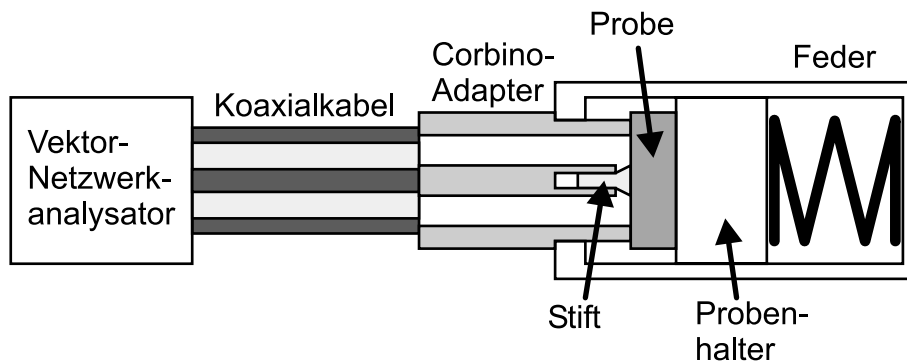
**Abb. 1:** Schematische Darstellung des Mikrowellenspektrometers in Corbino-Geometrie (nicht maßstabsgetreu).

faktor als komplexe Größe ('vektoriell'). Aus dem Reflexionsfaktor lässt sich die Impedanz der Probe bestimmen und hieraus bei bekannter Probengeometrie die komplexe Leitfähigkeit.

Die Schwierigkeit bei einem solchen Aufbau besteht darin, dass der vom Netzwerkanalysator bestimmte Reflexionsfaktor nicht nur von der Probe abhängt, sondern auch - und in viel größerem Maße - von unerwünschten Effekten wie der Dämpfung im Koaxialkabel oder Reflexionen an Steckern des Kabels. Um diese Effekte bei der Datenauswertung berücksichtigen zu können, muss eine umfangreiche Kalibrierung vorgenommen werden, im allgemeinen mit drei verschiedenen Standards mit jeweils bekanntem Reflexionsfaktor. Hierfür werden ein Kurzschluss, ein möglichst perfektes offenes Ende sowie ein Lastwiderstand verwendet, die in unserem Fall mit einer massiven Aluminiumprobe, einem Teflonzylinder sowie einem NiCr-Dünnfilm realisert werden (jeweils mit nahezu temperatur- und frequenzunabhängigen Mikrowelleneigenschaften). Da die Präzision des gesamten Spektrometers durch die Kalibrierung bestimmt wird, muss diese äußerst sorgfältig durchgeführt werden, was für den Ablauf einen recht großen Aufwand bedeutet, der für verlässliche Messungen aber unvermeidbar ist.

Ein entscheidender Punkt hierbei ist die begrenzte Reproduzierbarkeit der Verbindungen mittels Mikrowellenstecker: Durch das Lösen und Wiederverbinden von Steckern werden die Eigenschaften der Koaxialleitung in gewissem Maße verändert. Um diesen Effekt beim Austausch von Probe und Kalibrierstandards

zu vermeiden, darf zwischen solchen Messungen keine Steckerverbindung gelöst werden. Dies führt dazu, dass bei unserem Aufbau nicht wie üblich zum Probenwechsel der Einsatz aus dem Kryostat entfernt wird, sondern der Kryostat vom Einsatz, was mit erheblich größerem Aufwand verbunden ist.

Ein ebenfalls äußerst wichtiger Punkt ist die Temperaturabhängigkeit der Transmissionseigenschaften der Mikrowellenleitung. So wird die Dämpfung des Koaxialkabels durch die ohmschen Verluste in Innen- und Aussenleiter bestimmt und ist dadurch stark temperaturabhängig. Deshalb müssen die Kalibrier- und Probenmessungen bei derselben Temperaturverteilung des Koaxialkabels, sprich im gesamten Kryostaten, durchgeführt werden. Da die (Kalibrier-)Proben nur bei Raumtemperatur ausgetauscht werden können, bedeutet dies, dass die Kühlung bzw. das Heizen bei Kalibrier- und Probenmessungen in ihren Details (Pegel von flüssigem Helium und Stickstoff, Kontaktgasdruck, Heizleistung, zeitlicher Ablauf einer temperaturabhängigen Messung) genau reproduziert werden müssen.

Umfangreiche Tests bezüglich der Kalibrierung haben gezeigt, dass mit dieser Vorgehensweise das Spektrometer eine Empfindlichkeit von 0.001 im Reflexionsfaktor erreichen kann. Damit übertrifft unser Spektrometer das einzige andere, in der Literatur vergleichbar charakterisierte Spektrometer [5] sowohl in der Auflösung als auch im abgedeckten Frequenzbereich deutlich.

Mit dem so charakterisierten Spektrometer wurden $UPd_2Al_3$-Dünnfilme untersucht, die an der Universität Mainz hergestellt wurden. Das Auflösungsvermögen des Spektrometers erlaubt lediglich die Untersuchung von Dünnfilmproben von Schwer-Fermionen-Materialien, da Volumenproben einen Reflexionsfaktor besitzen, der experimentell nicht von dem eines perfekten Kurzschlusses zu unterscheiden ist. Da $UPd_2Al_3$ unterhalb von 2 K supraleitend wird, kann dieser supraleitende Zustand zur Kalibrierung des normalleitenden Zustandes bei etwas höheren Temperaturen verwendet werden, was die Empfindlichkeit dieser Messungen merklich erhöht.

Die Frequenz- sowie Temperaturabhängigkeit des Realteils der Leitfähigkeit im gesamten mit dem Corbino-Spektrometer zugänglichen Bereich ist in Abb. 2
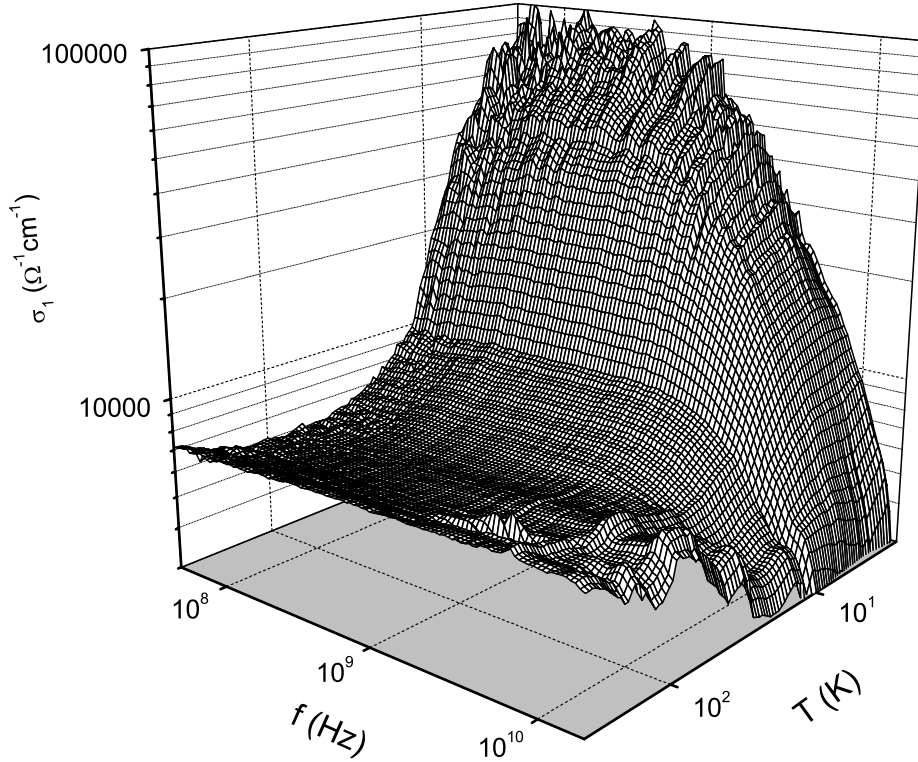
**Abb. 2:** Dreidimensionale Darstellung der Frequenz- und Temperaturabhängigkeit der Leitfähigkeit $\sigma_1$ von $UPd_2Al_3$.

dargestellt. Die wichtigsten Ergebnisse sind hier einerseits, dass die charakteristische Temperaturabhängigkeit bei niedrigen Frequenzen genau der der bekannten Gleichstromleitfähigkeit entspricht, dann die frequenzunabhängige Leitfähigkeit bei hohen Temperaturen (wie sie für ein normales Metall für diesen Frequenzbereich erwartet wird) und schließlich die starke Frequenzabhängigkeit bei tiefen Temperaturen mit einem ausgeprägten Abfall zu hohen Frequenzen hin. Dieser Abfall ist genau der gesuchte Effekt, der diese Untersuchung an $UPd_2Al_3$ motiviert hat.

Dieser für Metalle charakteristische Abfall der Leitfähigkeit wurde bereits von Drude in seiner Theorie für die elektrische Leitung in Metallen vorhergesagt. Nach dem Drude-Modell folgt die Frequenzabhängigkeit der komplexen Leitfähigkeit $\sigma(\omega)$ folgender Formel:

$$\sigma(\omega) = \sigma_1(\omega) + i\sigma_2(\omega) = \sigma_0 \frac{1}{1 - i\omega\tau} = \sigma_0 \left( \frac{1}{1 + \omega^2\tau^2} + i\frac{\omega\tau}{1 + \omega^2\tau^2} \right) \quad . \quad (1)$$
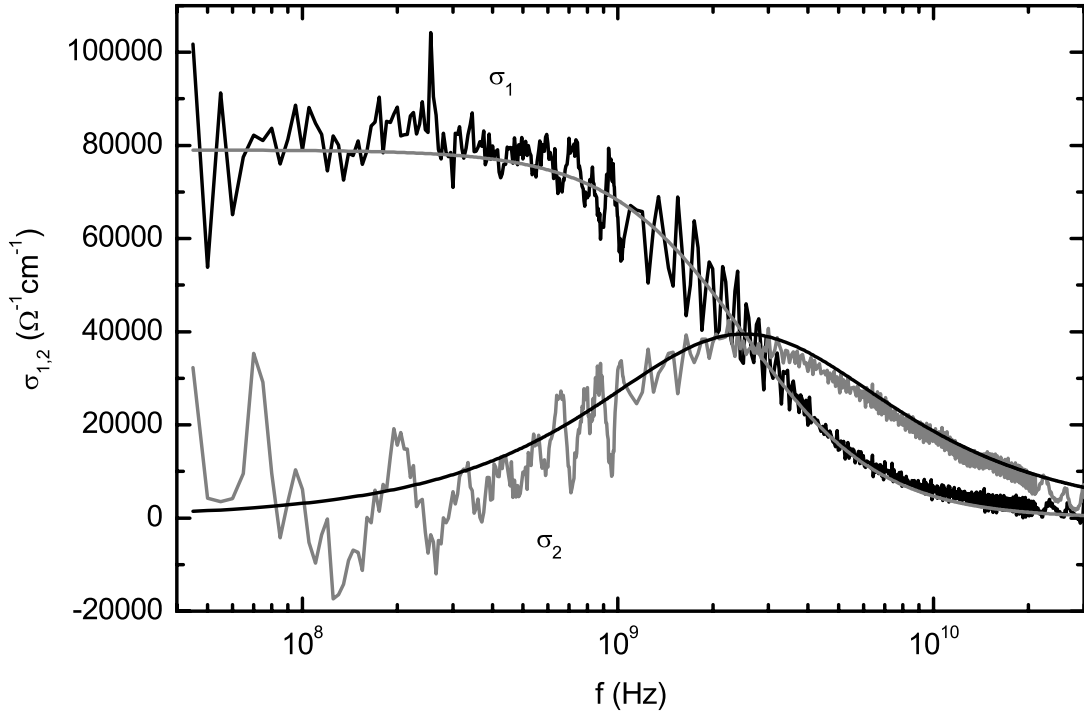
**Abb. 3:** Gemessene Leitfähigkeit von $UPd_2Al_3$ bei 3.3 K zusammen mit einem gemeinsamen Drude-Fit von Real- und Imaginärteil.

Hierbei gilt für die Gleichstromleitfähigkeit $\sigma_0$, den Grenzfall der frequenzabhängigen Leitfähigkeit $\sigma(\omega)$ für niedrige Frequenzen:

$$\sigma_0 = \frac{ne^2\tau}{m} \quad , \tag{2}$$

d.h. die Gleichstromleitfähigkeit wird von der Dichte $n$ der Ladungsträger und deren effektiver Masse $m$ bestimmt, sowie von der Relaxationszeit $\tau$, die auch die charakteristische Frequenz $\Gamma = 1/\tau$ in Gleichung (1) vorgibt, bei der sich der Abfall in $\sigma_1(\omega)$ und ein Maximum in $\sigma_2(\omega)$ zeigen.

Die experimentell bestimmte Leitfähigkeit von $UPd_2Al_3$ bei tiefen Temperaturen, also im Schwere-Fermionen-Zustand, folgt der Vorhersage des Drude-Modells sehr getreu, wie Abb. 3 zu entnehmen ist. Dort sind Real- und Imaginärteil der Leitfähigkeit mit einem gemeinsamen Fit gemäß Gleichung (1) dargestellt. Offenkundig beschreibt der Fit den gemessenen Frequenzverlauf sehr gut über den sehr großen, experimentell erschlossenen Frequenzbereich, der mehr als zwei Größenordnungen abdeckt. Bei diesen Messungen handelt es sich nicht

nur um die bisher erste, vollständige Beobachtung eines Drude-Verlaufs in einem Schwere-Fermionen-Materials (frühere Messungen waren auf einzelne Frequenzen beschränkt), sondern ist auch unter den optischen Untersuchungen anderer Metalle ohne Vergleich. Es ist hiermit das erste Mal gelungen, den Drude-Verlauf der Leitfähigkeit eines Metalls direkt zu messen, im Real- und im Imaginärteil.

Da der gesamte Drude-Verlauf in $UPd_2Al_3$ studiert werden konnte, ist eine direkte Zuordnung der Streurate $\Gamma$ bzw. der Relaxationszeit $\tau$ zweifelsfrei möglich. Werden Spektren bei verschiedenen Temperaturen ausgewertet, so zeigt sich eine Proportionalität der Relaxationszeit $\tau$ und der Gleichstromleitfähigkeit $\sigma_0$. Gemäß Gleichung (2) bedeutet dies ein temperaturunabhängiges Verhältnis $n/m$, d.h. beide können bei tiefen Temperaturen als konstant angenommen werden. Eine quantitative Auswertung von $n/m$ unter Berücksichtigung der aus unabhängigen Messungen bekannten effektiven Masse führt zu einer Ladungsträgerdichte, die viel niedriger ist als bisher angenommen (weniger als ein Elektron pro Uran-Atom). Hierbei ist aber zu berücksichtigen, dass es bisher keine unabhängige Messung der Ladungsträgerdichte in $UPd_2Al_3$ gibt.

Die geringe Dichte der Ladungsträger, die sich auf die Leitfähigkeit auswirkt, kann auch im Zusammenhang mit einer anderen Beobachtung aus den Mikrowellenmessungen betrachtet werden. Im Rahmen des sogenannten erweiterten Drude-Modells lässt sich die komplexe Leitfähigkeit in Bezug auf eine Frequenzabhängigkeit der Streurate sowie der effektiven Masse auswerten. Wie vom geradezu beispielhaften Drude-Verlauf der gemessenen Leitfähigkeit zu erwarten ist, ist die so erhaltene Streurate als Funktion der Frequenz fast über den gesamten zugänglichen Frequenzbereich konstant, lediglich bei den höchsten Frequenzen (oberhalb von 5 GHz) zeigt sich ein Anstieg der Streurate. Dieser Anstieg ist aber ziemlich ausgeprägt und lässt sich nicht mit der allgemein erwarteten frequenzabhängigen Streurate gemäß der Theorie der Fermi-Flüssigkeiten vereinbaren, dort ist der Anstieg nämlich deutlich schwächer.

Eine mögliche Erklärung dieses starken Anstieges wäre hingegen das Vorhandensein mehrerer Ladungsträgersysteme, die durch verschiedene Streuraten ge-

15

kennzeichnet sind und somit unabhängig voneinander zur Gesamtleitfähigkeit von $UPd_2Al_3$ beitragen (im Gegensatz zum einfachen Drude-Modell, das eine einzige mittlere Streurate für sämtliche am Ladungstransport beteiligten Ladungsträger annimmt). Für eine solche Kombination unabhängiger Leitungssysteme können stark frequenzabhängige effektive (d.h. im Experiment beobachtbare) Streuraten auftreten. Die mögliche Existenz getrennter Leitungssysteme wird durch de Haas-van Alphen-Messungen bestätigt. Dort wurden für verschiedene Bereiche der aus mehreren, sich stark unterscheidenden Teilflächen bestehenden Fermi-Fläche sehr unterschiedliche effektive Massen gefunden. Somit wäre nur ein kleiner Teil der freien Ladungsträger als schwere Fermionen präsent, die als solche aber die Leitfähigkeit des gesamten Systems dominieren.

Somit wurde durch die Bestimmung der frequenzabhängigen Mikrowellen-leitfähigkeit von $UPd_2Al_3$ einerseits das Drude-Modell bzgl. seiner Vorhersage des Frequenzverlaufes mit einer so nicht erwarteten Genauigkeit bestätigt, anderseits hat die quantitative Analyse überraschende Ergebnisse bzgl. der Details des Ladungstransports in $UPd_2Al_3$ ergeben. Dies zeigt die Leistungsfähigkeit unseres Spektrometes bzw. der Mikrowellenspektroskopie im allgemeinen, was die Aufklärung elektronischer Prozesse bei extrem niedrigen Energien betrifft.

# Chapter 1

# Introduction

In the field of condensed matter physics, the study of the electronic properties of various compounds has remained a major endeavor. This comprises not only materials known from every-day life like insulators and metals but also more unusual ones that require special conditions, like low temperatures, to reveal their exciting properties, e.g. superconductivity as a particularly popular example. An appropriate tool to access these electronic properties is optical spectroscopy: here the interaction of electromagnetic radiation with the electrons in the solid can be probed in a frequency range spanning many orders of magnitude corresponding to an extremely wide energy range. For many materials the frequency range of interest is within or close to optical frequencies (corresponding to energies of order eV), e.g. to study single-particle phenomena as reflected by the band structure of normal materials like insulators, semiconductors, or metals. On the other hand, the characteristic energies that are due to many-body effects are much smaller (resulting in phenomena that occur only at low temperatures), typically of the order of meV. Thus for more exotic electronic states (to just mention a few keywords: strongly correlated electron systems, heavy fermions, Kondo materials, low-dimensional systems, superconductors, spin and charge density waves) the suitable probe is electromagnetic radiation of comparably low energy, and therefore far-infrared spectroscopy plays an important role in solid state physics. In very special cases the characteristic energy scales might be at even lower fre-

quencies in the submillimeter and microwave frequency ranges. But while the far-infrared and even the submillimeter frequency ranges can be explored with setups that resemble optical spectrometers in the way that the radiation is guided through free space by the use of lenses, mirrors, beamsplitters, and other components that are used in geometrical optics, in the microwave region different techniques have to be employed (in particular the wave has to be guided by coaxial cables or other waveguides) because here the wavelength of the radiation is of the order or even larger than typical dimensions of the samples to be studied, of typical sample holders, and many other objects in a typical laboratory environment, and the interaction of the radiation with all these elements can hardly be distinguished from the intrinsic response of the sample that one wants to study.

Apart from guiding a microwave, its interaction with the sample has to be in a well-defined manner, the most common way being the use of resonators. Unfortunately resonators are by definition restricted to individual frequencies, and therefore it is hard to obtain the electrodynamic parameters as a complete spectrum for the microwave region. There have been attempts to obtain frequency-dependent data in the microwave range by different techniques but none of them has become widely used: the effort to obtain reliable data is rather large and many designs are appropriate for particular samples only. From a technical point of view the current project therefore had the following rather general goal: development of a versatile cryogenic broadband microwave spectrometer. This spectrometer was intended as an extension of the frequency range that was already covered by broadband spectrometers at the 1. Physikalisches Institut (from the near-infrared to the submillimeter range), but working with guided waves at as high frequencies as possible to match the lowest frequencies available in free-space setups.

The scientific need for such a spectrometer became obvious in recent submillimeter measurements on the heavy-fermion compound $UPd_2Al_3$. Like all heavy-fermion materials, $UPd_2Al_3$ can be considered to be a metal, but the characteristic energy scales have decreased several orders of magnitude. Therefore

the so-called Drude roll-off, a strong decrease of the conductivity that occurs in the far infrared for normal metals, was expected at lower frequencies, in the sub-millimeter range. But the submillimeter measurements showed that the Drude roll-off has to be at even lower frequencies, in the microwave regime. A thorough study of a Drude response (which is the most direct access to the dynamics of the heavy quasiparticles that constitute the heavy-fermion state) requires more than just a single frequency available with a resonator, and therefore a broadband spectrometer was obviously in demand. The current spectrometer thus served as the tool for the exploration of the Drude behavior of heavy-fermion $UPd_2Al_3$, but from the beginning the spectrometer was designed as versatile as possible to allow measurements on other materials (e.g. less conductive samples like Kondo insulators or highly doped silicon as a model system of electron glasses with peculiar hopping conduction) as well as to permit future upgrades in different ways (e.g. different probe geometries that allow for the study of anisotropic materials or the incorporation of a magnetic field). But as previous experience with broadband microwave setups showed: such experiments have to be performed with extreme care, and therefore the current spectrometer was first characterized in detail before the 'real' experiments were started. This characterization now serves as a benchmark for the current study on $UPd_2Al_3$ but also for future projects with this particular spectrometer as well as with possible upgrades, but it should also help when different microwave spectrometers are to be considered or compared.

Thus the current project will hopefully serve as the foundation for a series of broadband microwave spectroscopy studies. Therefore the present dissertation will describe not only the spectrometer itself in great detail but also contains an extensive comparison to other microwave experiments. There is an evident need to document the spectrometer thoroughly and to compare it to others because to this date there is no review article or comparable literature that covers the field of broadband microwave spectroscopy on conducting solids, and furthermore those few other comparable spectrometers that can be found in the literature are described only in a rather general manner and even the corresponding PhD theses

do not serve as exhaustive guides to these spectrometers. This is particularly unfortunate as in microwave physics any single detail can spoil the performance of a spectrometer if not applied with maximum care. Therefore four chapters of this dissertation are devoted to technical aspects of the current spectrometer. They contain an overview of the state of the art in microwave spectroscopy, the details of the design of our particular instrument, the calibration procedure as the crucial point when broadband measurements are performed, and test measurements that help to characterize the performance of the spectrometer.

The physical question addressed with the spectrometer, the Drude behavior of the heavy-fermion compound $UPd_2Al_3$, will be dealt with in the subsequent two chapters: first the high-frequency and optical properties of normal metals as well as heavy-fermion materials in general and of $UPd_2Al_3$ in particular will be reviewed. Here the focus will be on the low-energy response of the heavy fermions as this is the core of what characterizes these peculiar materials: the name already points at the 'heaviness' of the charge carriers, an increased 'inertia' compared to that of free electrons and expressed by an enhanced effective mass. But the effective mass is only a way to quantify the effect that the charge carriers react much more slowly to an applied external field. Arguably this 'slow reaction' can be observed by low-frequency spectroscopy more directly than by any other experimental technique and this is what will be presented in the chapter on the experimental results and their analysis.

After the conclusions several appendices supply additional information concerning details of particular procedures that were employed in the current project. Most of them have either been developed in the course of this project or they are only incompletely documented in literature and thus these appendices can hopefully serve as references for future projects as well as the rest of this dissertation.

# Chapter 2

# Microwave Spectroscopy

While the term 'spectroscopy' is nowadays used for many different experimental schemes where measurements as a function of energy are performed [6], the current project employs a more traditional spectroscopic idea: studying the interaction of solid material with electromagnetic radiation as a function of frequency of the radiation. The non-traditional part of this scheme is the frequency range from 45 MHz to 20 GHz in opposition to standard spectroscopy originating at visible light frequencies and its extension to adjacent frequencies still using optical techniques.

Strictly speaking the spectrometer described in this thesis works at frequencies at the transition from radio frequencies ('rf', 300 kHz to 300 MHz) to microwave frequencies (300 MHz to 300 GHz), but for simplicity this frequency range will be referred to simply as 'microwaves' in the following.

## 2.1 Microwave Experiments in Condensed Matter Physics

Studying low-temperature condensed matter systems with microwaves is a well-established technique and has revealed several important results. Among the most famous came from experiments on high-temperature superconductors, in particular those studying the nature of the superconducting order parameter by

measurements of the penetration depth [7]. For such experiments cavity or other resonant setups are most common, but these do not allow frequency-dependent measurements. The present project on the other hand is devoted particularly to the study of the frequency dependence of the conductivity of non-superconducting solid state systems. The framework for this study are the high-frequency experiments currently available, and therefore the following section describes briefly the common cavity resonators and covers those techniques documented in literature that allow for frequency-dependent microwave measurements at cryogenic temperatures. Here the focus will be on the frequency range from 1 GHz to 10 GHz, and this thesis will concentrate on this range although the spectrometer will finally cover a considerably larger frequency range. The frequency range discussed in the present study is in the gap between conventional optical or quasioptical spectrometers for infrared and submillimeter radiation using free-space wave propagation and the radio frequency experiments that can be performed using modified standard dc experiments. Therefore first these two techniques and in particular their limitations in frequency will be discussed.

## 2.2 Radio Frequency Experiments

In studies of condensed matter systems in the audio and radio frequency ranges [8], the wavelength of electromagnetic radiation is of the order of many meters and more, and therefore any experiment with standard laboratory dimensions can be treated similarly to the dc case. Thus sample geometries are the standard four-point probe for conducting samples and capacitors for insulating materials. Then the impedance of probe including sample can be obtained as a function of frequency either by direct, phase-sensitive measurement of current and voltage using lock-in amplifiers or in a bridge configuration where the probe impedance is balanced by a variable compensation impedance. Instruments for such measurements are commercially available, but they are limited to higher frequency (around 100 MHz [1]) due to their neglect of the wave character of the electro-

magnetic signal. At higher frequencies the finite dimensions of the experimental setup come into play and in particular the cables transmitting the radio frequency signal will influence and finally dominate the measured response. Thus higher frequencies, in the GHz range, require an approach known from microwave engineering where the characteristics of the transmission line are the core of the experimental setup and analysis.

## 2.3 Far-Infrared and Quasioptical Experiments

If we now approach our frequency range of interest, the lower GHz region, from the other side, from higher frequencies, then we find that far-infrared spectroscopy is a well-known technique not only in condensed matter physics, and convenient Fourier transform spectrometers are commercially available as well as the appropriate optical cryostats. These spectrometers can typically reach frequencies down to about 300 GHz (10 cm$^{-1}$), limited by the intensity of their radiation sources and the sensitivity of the detectors, respectively.

For lower frequencies, so-called quasioptical setups can be employed [9]: here typical optical devices like lenses and beamsplitters are still employed (albeit their realization can differ considerably from those for visible light), but due to the large wavelength (of the order mm) diffraction by all elements within the optical path and by the sample will influence the beam. This also gives the low-frequency limit of such quasioptical spectrometers.

Nowadays there are three well-established techniques for quasioptical spectroscopy differing in the way how the signal is produced and how it is detected:

**Coherent source submillimeter wave spectroscopy:** Here backward wave oscillators (BWOs) [9] create coherent electromagnetic radiation in the frequency range from 30 GHz to 1200 GHz by sending an electron beam through a spatially modulated field. BWOs are monochromatic and can be tuned in frequency by about a factor of two, i.e. to cover the complete frequency range available, several BWOs have to be employed. The signal is detected either by a Golay

cell (an optical-acoustical detector) or by more sensitive helium-cooled semiconductor bolometers. These detectors only yield the amplitude of the signal, but phase-sensitive transmission measurements can be performed using interferometric optical setups.

**Millimeter-wave vector network analysis:** Extending conventional microwave network analysis to higher frequencies, this approach [10,11] employs standard semiconductor devices to create electromagnetic radiation from 8 to 350 GHz via frequency multiplication of base frequencies from 8 to 18 GHz. Using semiconductor elements as detectors as well gives the opportunity of direct phase-sensitive measurements. Main disadvantage of this technique involving non-linear processes in signal generation is the low output power.

**Terahertz time-domain spectroscopy:** Unlike the two previous, frequency-domain setups, the third works in time domain [12]. Here a femtosecond-laser pulse triggers a photoconductive switch to emit a burst of electromagnetic radiation (of the order of 1 ps long) containing mainly frequencies from many GHz to a few THz. This pulse can interact with the sample and then be probed by a similar photoconductive switch that is triggered by the same but delayed laser pulse. By stepping the delay, the time-dependent field strength of the THz pulse can be monitored with a time resolution much shorter than the period of the THz radiation and can then be transformed to a frequency-dependent response function. Because the time structure of the THz pulse contains intensity as well as phase information, complex material properties can be obtained directly.

The 1. Physikalisches Institut, Universität Stuttgart has expertise as well as apparatus for Fourier-transform infrared and coherent source submillimeter wave spectroscopies spanning the frequency range from the near infrared down to around 30 GHz. The microwave spectrometer developed in the current project serves as an extension of this spectral range, enabling frequency-dependent measurements at even lower frequencies.

## 2.4 Cavity Resonators

Cavity resonators are by far the most common microwave technique to study solids. They are not only used to study general high-frequency properties like the conductivity [13], but they are also very common in the study of resonant mechanisms of solids, e.g. electron spin resonance (ESR), ferromagnetic resonance (FMR), antiferromagnetic resonance (AFMR), and similar magnetic resonance effects. To study these effects, the intrinsic resonance frequency of the sample is tuned to the resonance frequency of the cavity by applying an external magnetic field. Since the present study does not address such resonances, also this section is confined to cavities used in the study of the bare conductivity without additional resonant effects.

A typical cavity resonator consists of a well-defined volume limited by conducting walls made of good electrical conductors like copper or even superconductors [14]. By choice of an appropriate shape (typically cylindrical or box shaped), the cavity has well-defined resonance frequencies and in general only one of those is used for the measurements. To examine this resonance, a microwave signal is sent into the cavity and the response of the cavity is studied by measuring the reflected or - more commonly used - the transmitted signal. By sweeping the frequency of the applied microwave, the resonance frequency and the linewidth are obtained. Both are affected if a sample is introduced into the cavity,[1] and by measuring these two quantities, the complex surface impedance $Z_s$ (yielding all other electrodynamic quantities like the complex conductivity) of the sample can be determined, provided the size and shape of the sample are well known.

The great advantage of cavity resonators is their enormous sensitivity, due to the fact that small changes of a resonant structure - such as introducing the sample - strongly affect the resonance. Furthermore, frequency shifts can be measured easily with a high accuracy. But the use of a resonant frequency

---

[1]If large, flat samples are available, one complete wall of the cavity can be replaced by the sample as well.

has an equivalent disadvantage as only this particular frequency can be studied, frequency-dependent studies are not possible with just one cavity. Another disadvantage is the limited frequency range where cavity resonators can be operated. Since the dimensions of the resonator are of the order of the wavelength that is used, practicable frequencies are from 10 GHz to 300 GHz.

## 2.5  Other Single-Mode Resonators

In addition to cavities, other resonant techniques have been employed in particular for the study of high-$T_c$ superconductors. Of those only the following should be mentioned:

Parallel plate resonators [15,16] can be used if large, flat samples are available. Here two such samples are arranged parallel to each other, forming a resonant structure with resonance frequencies typically around 10 GHz. Since the whole resonator is formed by the sample material, this design is restricted to low-loss samples like superconductors.

A different approach is the split-ring resonator [17, 18], where a highly conducting cylindrical ring with a slit splitting the ring is employed within a conducting cavity. The sample is brought into the vicinity of the resonant split ring, thus perturbing resonance frequency and linewidth. Resonance frequencies are in the range 200 MHz to 5 GHz, right in the otherwise hardly studied frequency range around 1 GHz that is too low in frequency to be addressed with standard resonant cavities.

## 2.6  Microwave Spectroscopy Using Cavities

Since resonant cavities are the most common microwave technique to study solid state samples, they were also employed for attempts to obtain frequency-dependent data, a rather arduous path since in general different cavities have to be employed for each single frequency point. One way to overcome this problem is to excite a cavity not only in one mode, but in a series of modes with different

frequencies. This strategy in addition to using several cavities was employed successfully by the group of Stephen Hill [19] to obtain a set of resonances separated by a few GHz each, but only for rather high frequencies, starting around 40 GHz.

To obtain frequency dependences at lower frequencies, other resonators have to be used. Hosseini *et al.* [20] have used split-ring resonators in combination with cavities to obtain five frequency points from 1 GHz to 75 GHz. But also in this case, three frequencies from 1 GHz to 13 GHz are definitely not enough to cover our core frequency range of interest from 1 GHz to 10 GHz in a satisfying manner, and a different approach is necessary.

## 2.7   Multiresonant Techniques

All resonators mentioned so far are usually designed to work at a single frequency only. Whereas cavities rely on three-dimensional field configurations, resonators derived from the one-dimensional geometry of a microwave transmission line are also possible, and these can easily be used at higher orders, leading to a series of resonant frequencies that can be used for measurements. The two designs of this type that were used for solid state studies are the helical and the microstrip (and the similar stripline) resonators.

### 2.7.1   Stripline and Microstrip Resonators

Microstrip resonators played an important role in the first microwave measurements of high-temperature superconductor thin films [21–23]. But also low-temperature superconductors were studied extensively using microstrip resonators. However, for the temperature dependence only a single resonance frequency is studied, while we are interested in the frequency dependence which can also be studied with microstrip resonators.

A microstrip line consists of a planar conducting line held parallel to a conducting ground plane at a small distance. (Striplines are of the same design but with an additional conducting plane on the other side of the conducting line and

generally can be be treated very similarly.) Microstrip lines are well-established in microwave circuitry as they are easy to implement on circuit boards [24]. If a microstrip line is given a particular length (e.g. by choosing a closed ring [25] or by gaps in the line, so-called capacitive coupling), it can act as a resonator if the length is a particular multiple of the wavelength of the microwave radiation. If the dimensions of the line are chosen appropriately, more than a dozen equidistant resonant frequencies can be employed [26, 27] at frequencies between 600 MHz and 20 GHz. However, microstrip transmission lines have rather high losses hampering the use as a resonator where low losses and high quality factors are desired. That is why up to now studies with microstrip resonators were focused on superconducting materials. However, as a side effect of those studies the surface resistance of gold was also measured with a modified niobium stripline resonator [28], albeit for rather few frequencies.

## 2.7.2 Helical Resonators

Helical resonators consist of a solenoid mounted on the axis of a cylinder ('coaxial transmission line with helical inner conductor'), both made of a conductor (copper) or a superconductor (niobium or lead). One end of the helix is shorted to the outer conductor whereas the other end is left open, leading to a simplified model of a quarter-wavelength resonator. The properties of the resonator are studied by measuring the transmission of a high-frequency signal that is introduced and extracted from the resonator via two coupling holes or antenna probes.

In the traditional setup [29, 30], insulating materials are studied by introducing the sample into the gap between helix and outer conductor, either filling it completely or leaving a gap between sample and conductor, leading to a reduced sensitivity but avoiding contact effects [30, 31].

Typically the dimensions of the resonator are chosen to obtain a fundamental resonance around 100 MHz, and about a dozen higher modes can be examined up to around 2 GHz. The quality factors can be very high, like $3 \times 10^7$ at helium temperatures [29], but this cannot be expected to convert easily to extremely good

sensitivity of the interesting material properties of the sample since the quality factor is not only affected by the sample itself but also by stray capacitances around the sample, and these can be hard to model.

Such helical resonators were used for the first measurements [31–33] addressing the frequency dependence of the hopping conductivity of doped silicon (so-called electron glasses), a topic that has been recently studied with other techniques at higher frequencies as well [34–37].

In a more recent approach [38, 39] the sample was introduced into the volume inside the helix, without electrical contact. Moving the sample along the cylindrical axis of the resonator from a field node to an antinode involves a change of the resonance frequency and quality factor, and these can be used to obtain the dielectric function and the surface resistance $R_s$.

Another recent approach [40] is to introduce the sample as a cylinder spanning the whole length of the resonator inside the helix. Here measurements on low-loss powder samples were demonstrated at room temperature and above, but probably this technique cannot be easily adjusted to standard solid state experiments with small samples and cryogenic temperatures.

# 2.8 Broadband Microwave Spectrometers

The resonators based on one-dimensional transmission lines allow for measurements at about a dozen distinct frequencies in the frequency range of hundreds of MHz to a few GHz. However, we are interested in true broadband spectroscopy covering the frequency range of interest continuously. Therefore our approach has to be completely different.

## 2.8.1 General Requirements for a Broadband Spectrometer

The instrument we are interested in shall reveal the complex material properties of conducting samples at microwave frequencies. Any spectrometer capable of

this task and furthermore offering data as a function of frequency is composed of the following elements:

- source of radiation

- path for radiation from source to sample

- interaction of radiation and sample

- path for radiation from sample to detector

- detector for radiation

- frequency-discriminating element

In the present project these elements now have to be realized for microwave frequencies. As a combination of source and detector for microwave radiation which already has an inherent frequency-discriminating element, network analyzers are available commercially for frequencies of a few Hertz up to many Gigahertz.[2] A network analyzer is a combination of several elements: the radiation is created by a tunable source, typically a semiconductor device like a voltage-tuned oscillator. The radiation is sent to the sample (in general called device under testing) by a test set which can put the radiation through one of two ports. The signal coming back to the network analyzer enters the test set either through the same port (reflection) or the other (transmission). In the test set the microwaves on the transmission line are separated by directional couplers, depending on their direction of travel, and they are then converted to lower frequencies (intermediate frequency, IF) and finally sensed by detectors. These detected signals can be compared phase sensitively and therefore reveal the complex reflection or transmission coefficient. As the microwave source creates monochromatic radiation that is tuned to obtain a spectrum, the source already acts as frequency-discriminating element.[3]

---

[2]Agilent offers a network analyzer system operating up to 110 GHz, but for frequencies above 65 GHz only few microwave components like connectors are available. At yet higher frequencies network analyzers are available using waveguides, matching those mentioned in Section 2.3.

[3]The microwave source used for the current study, HP83650B Option 008, offers a frequency resolution of 1 Hz [41].

Commercial network analyzers have ports for either coaxial cables or waveguides. Since we are interested in a broadband setup that covers at least one decade in frequency, waveguides are not applicable (they cover only a factor of two in frequency). The most common way to send an electromagnetic wave to a sample at higher (e.g. optical) frequency is free transmission through air or vacuum, but this cannot be applied in our case because of the long wavelength (1 GHz corresponds to 30 cm) that is not practicable for laboratory use. Thus coaxial transmission lines are the only way how we can send the microwave signal from the network analyzer to the sample and back.[4] However, coaxial cables have a few disadvantages that will be dealt with when our setup is described in detail, namely the strong damping and problems with cryogenic cooling.

## 2.8.2   Corbino Geometry

A very direct way to construct a broadband cryogenic microwave spectrometer using a network analyzer is to let the sample terminate the coaxial transmission line coming from the network analyzer. Thus the microwave signal is reflected by the sample and returns to the network analyzer through the same coaxial line. This design, called Corbino Geometry, is the technique we have employed and the details will be described in Section 3. Although the principle of this setup is very simple, performing meaningful measurements at low temperatures proved to be a serious task. Only two groups have published data concerning absolute conductivity measurements in the GHz-range at low temperatures.[5] The

---

[4]Other techniques like stripline, microstrip, coplanar and similar transmission lines are also broadband but they have even higher losses than coaxial cables and are harder to employ for cases like ours where the microwave line has to be of considerable length and has to be fed into a cryostat.

[5]In contrast to measurements on conducting, solid samples there are several groups working with Corbino-like setups on insulating materials, in particular liquids, glass formers, polymers etc. where sample mounting is much easier compared to conducting samples [8]. There are also several studies with Corbino-probes in the GHz range where an external parameter, the magnetic field, is swept and the dependence on this parameter is studied, but no absolute values of conductivity are obtained [42, 43].

group of Steven M. Anlage at the University of Maryland [44] has studied high-$T_c$ superconductor thin-films [45, 46] as well as ferromagnetic resonance (FMR) and antiresonance (FMAR) [47–49] on single crystals of manganites exhibiting the colossal magnetoresistance effect (CMR). The group of Mark Lee at the University of Virginia [5] has studied the conductivity of the electron glass Si:B [34].

### 2.8.3 Other Broadband Geometries

The Corbino geometry is not the only conceivable broadband interaction geometry of microwave radiation and sample. In principle any element that guides a microwave signal or interacts with it can be used if part of the element is replaced by the sample. However, as will be shown in the section on the current spectrometer, the requirements concerning reproducibility when samples are exchanged are very strict and are even harder to accomplish compared to the Corbino setup if the sample is introduced into a more complicated probe. Also typical solid state samples cannot be given arbitrary shape, and therefore elements like parts of a coaxial cable cannot be easily structured from solid samples (in contrast to liquid (or gaseous) dielectric samples that can be introduced into a hollow coaxial cable as dielectric).

However, in a stripline or microstrip transmission line a flat solid sample (or in particular a thin film on a flat substrate) can be used either as transmission line itself or as ground plate. Compared to the Corbino setup, such a design would offer the possibility to measure transmission instead of reflection coefficients and the transmission coefficient could be tuned to an appropriate value by adjusting the length of the strip. Furthermore microwave transmission measurements require a less demanding calibration procedure (one calibration measurement instead of three, see Section 4) and the calibration might be performed by the sample itself (using different lengths of the transmission line), possibly reducing effects due to contacts.

The general possibility of broadband measurements using a stripline design was already proven by Goglio *et al.* [50]. Here ferromagnetic nanowires were

incorporated into the dielectric of a microstrip transmission line and studied at room temperature. These nanowires are extremely lossy, resulting in very strong absorption that can be seen easily in transmission spectra even without particular care concerning calibration. Therefore this single experiment shows that such a design can work, but the adaption for a versatile solid state spectrometer for less lossy samples and cryogenic temperatures still remains a demanding task.

On the other hand there exist several studies on the microwave conductivity of two-dimensional electron systems that employ a modified coplanar transmission line as probe, and these experiments were performed at very low temperatures, in dilution refrigerators [51–56]. But here the magnetic field was tuned as an external parameter and only effects that depend on the magnetic field were studied whereas we are interested in the absolute values of the conductivity at zero magnetic field.

## 2.8.4   Bolometric Approach

As mentioned in Section 2.3, bolometers are commonly used as detectors for infrared radiation that is reflected from or passed through the sample. On the other hand the idea of a bolometer can also be employed to measure the absorption by a sample more directly since any sample that absorbs electromagnetic radiation heats up, thus acting like a bolometer itself. If the amount of absorbed heat can be measured with a temperature sensor and the intensity of the incident radiation is known, the absorptivity of the sample can be obtained. The idea of the bolometric approach for microwave measurements is as follows: the sample is exposed to electromagnetic radiation (inside of a waveguide) with a modulated intensity (typically with a modulation frequency of a few Hertz). The radiation heats the sample but due to the modulated radiation the temperature of the sample also changes with the modulation frequency. This periodic temperature change of the sample is measured by a temperature sensor that is thermally coupled to the sample. This experimental design is very general and allows for rather simple measurements if the dependence on an external quantity like a magnetic field

is studied [57]. Absolute measurements, however, are more complicated because usually it is hard to know the absolute power of the radiation at the location of the sample *a priori*. Therefore simultaneously the temperature change of a calibration sample at an equivalent field position is determined. A more severe disadvantage is that a bolometer only determines the magnitude of the absorption but is phase-insensitive. Therefore only one quantity of the complex surface impedance can be obtained by this technique (see e.g. [58], albeit for a fixed frequency of 30 GHz only).

Only recently this technique was used to study the microwave properties of high-$T_c$ superconductors as a function of frequency: in one case backward-wave oscillators were used as radiation sources in the frequency range 20 GHz to 150 GHz to study the Josephson plasma resonance [59] (which does not require absolute values since it is a strong resonant feature) whereas the other recent, most ambitious experiment [60] of this type up to now covered the frequency range 600 MHz to 21 GHz as a means to study the quasiparticle scattering [61].

The bolometric approach is a very elegant way to overcome the most crucial problem of any other cryogenic broadband microwave spectrometer: measuring the unavoidable calibration sample. Here this measurement is performed simultaneously, thus avoiding any changes with time or due to adjustments of the microwave setup when the samples are exchanged. However, there are several restrictions of this design, the most severe being the insensitivity to the phase of the response of the sample with respect to the radiation. Other problems arise due to the fact that sample and calibration sample have to be matched appropriately and that the sensitivity of standard temperature sensors strongly depends on temperature.[6] These two limitations of a bolometric spectrometer might be acceptable for particular studies like those mentioned on superconducting mate-

---

[6]Since all experiments mentioned in this section are devoted to superconductors, the cryogenic environment necessary for such sensors is no disadvantage, but the broadband 0.6 to 21 GHz-experiment [60] could only be performed in the very limited temperature range from 1.3 to 10 K and also the only other quantitative experiment [58] is limited to 30 K with the noise increasing considerably above 10 K.

rials, but they are restrictive when the right approach for a generic instrument that allows studies of very different samples (in particular having strongly differing losses) in wide temperature and frequency ranges is sought after.

## 2.9   Comparison of Different Techniques

Except for the cavity resonators, all of the techniques described in this chapter have only been used for rather few scientific studies. This might have several reasons connected with the problems when actually performing such experiments, and these are usually hard to estimate. To compare the different techniques that have been used to study solid state materials at low temperatures using microwaves, Table 2.1 serves as a compilation of the main features of the techniques.

The variety of different techniques described above shows that there has been interest in frequency-dependent measurements also in the microwave frequency range for many years, but the difficulties connected with each single technique have prevented any of the approaches to become widely used in solid state spectroscopy of conducting media. Therefore no 'standard' solution is available and each setup documented in literature has only been used for a very limited number of sample types. Among those the Corbino geometry is the most intuitive as it conserves the coaxial geometry implemented in all commercial network analyzers for this frequency range. Furthermore this technique seems to be rather generic in terms of the different types of samples [7] and the required sample size of a few mm$^2$ is moderate. These characteristics of the Corbino setup have only been matched or surpassed recently by the bolometric approach which has the advantages of extremely high sensitivity, real-time calibration, and even better versatility of the samples that can be studied. However, there are serious draw-

---

[7]The exception being low-dimensional systems. While ideal two-dimensional systems can also be studied with Corbino setups (e.g. there are studies on the magnetoconductance of quantum Hall systems [42, 43]) it will be hard to obtain absolute values for three-dimensional crystals of quasi-two-dimensional systems. If one-dimensional systems are to be measured with a Corbino setup, the data analysis will be even more complicated.

backs of the bolometric technique namely the difficulty to retain over a larger temperature range the high sensitivity nowadays available only at very low temperatures and, more fundamental, the limitation of measuring only the amplitude of the absorbed radiation and thus the impossibility to obtain the complex electrodynamic properties of the sample generally without additional assumptions.

Because the current project aimed not only to measure the electrodynamic properties of a particular heavy-fermion system but furthermore to exploit the capabilities of a generic cryogenic microwave spectrometer that can be used as a solid foundation for future extensions in temperature range, probe geometry, or features like applied magnetic fields, we have chosen the Corbino geometry for the current spectrometer.

| method | frequency range | studied materials | comments |
| --- | --- | --- | --- |
| cavity resonator [13, 14] | 10 - 300 GHz | numerous | single frequency |
| parallel plate resonator [15, 16] | approx. 10 GHz | high-$T_c$ [64] | single frequency, thin films |
| split ring resonator [17, 18] | 200 MHz - 5 GHz | high-$T_c$ [65–68] | single frequency |
| stripline/microstrip resonator [23] | 600 MHz - 20 GHz | high-$T_c$ [21, 22, 25–27, 38–40] | multiresonant |
| helical resonator [29, 30] | 100 MHz - 2 GHz | electron glasses [31–33], insulators [29] | multiresonant |
| Corbino [5, 44, 49, 62, 63] | 10 MHz - 20 GHz | high-$T_c$ [45, 46], manganites [47–49], Coulomb glass [34], dielectrics | broadband |
| bolometric [60] | 100 MHz - 20 GHz | high-$T_c$ [57–59, 61] | broadband, $\sigma_1$ only |

**Table 2.1:** Comparison of techniques previously used to study the microwave properties of solids at low temperatures.

# Chapter 3

# Microwave Spectrometer in Corbino Geometry

As motivated in the previous section, the Corbino geometry was chosen for the design of the current microwave spectrometer. It was already pointed out that the calibration is the crucial part of any broadband microwave spectrometer and Chapter 4 deals with this issue in detail whereas in the present chapter the Corbino geometry and its use for microwave spectroscopy are described in general as well as the details of the setup established at the 1. Physikalisches Institut.

## 3.1   Corbino Geometry and Microwave Spectroscopy

In his original studies [69] Corbino used the geometry that is nowadays named after him to study the dc magnetoresistance of metallic samples. The main idea of this design is that the sample under study is a flat, circular disc with the electric current flowing radially through the sample, i.e. one of the two current supplies is connected to the center of the disc and the other to its circumference. This can be seen schematically in Figure 3.1. If a magnetic field is applied perpendicular to the sample disc, the magnetic field is also perpendicular to the currents flowing in the disc, but due to the circular geometry no Hall voltage builds up at the edges of the sample (in contrast to the common Hall bar geometry).
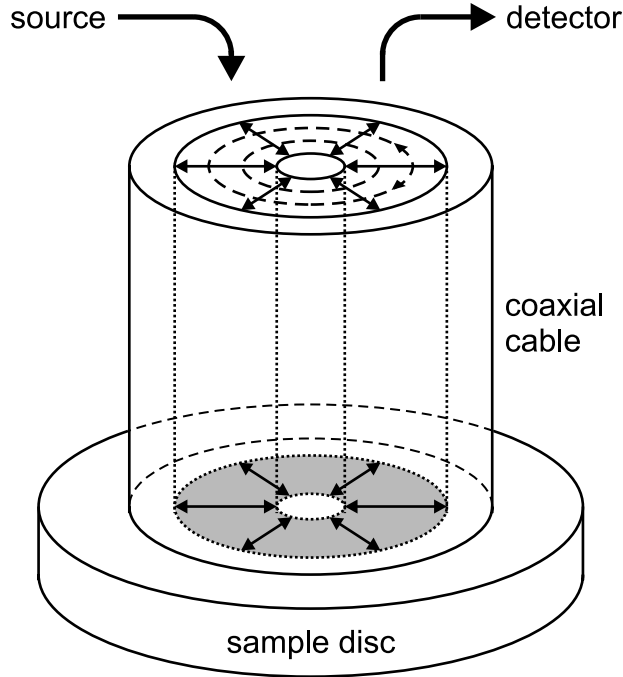
**Figure 3.1:** Scheme of the Corbino geometry. At the top of the coaxial cable the high-frequency electric (full arrows) as well as the magnetic (dashed) fields are indicated. The currents flowing through the Corbino disc (shaded) are shown with full arrows.

This geometry has a similar effect when type II superconductors are studied in a magnetic field. In the Abrikosov phase, i.e. with magnetic flux penetrating the sample as vortices, electric current causes the vortices to move perpendicularly to the current. In Corbino geometry the current flows radially, and the vortices move in circles around the symmetry axis of the disc. Thus no vortices leave or enter the sample, in contrast to samples in a bar geometry. This effect was one of the reasons why the group of Steven M. Anlage at the University of Maryland started to study the high-frequency properties of high-$T_c$ superconductors in Corbino geometry [45, 46, 70], leading to a pioneering, truly broadband microwave experiment on a conducting condensed matter system where absolute values for the material properties were obtained. Another already mentioned crucial argument for the use of the Corbino geometry for microwave spectroscopy is that it is the easiest way to make use of commercial network analyzers for microwave spectroscopy. These network analyzers are connected to devices under test via coaxial
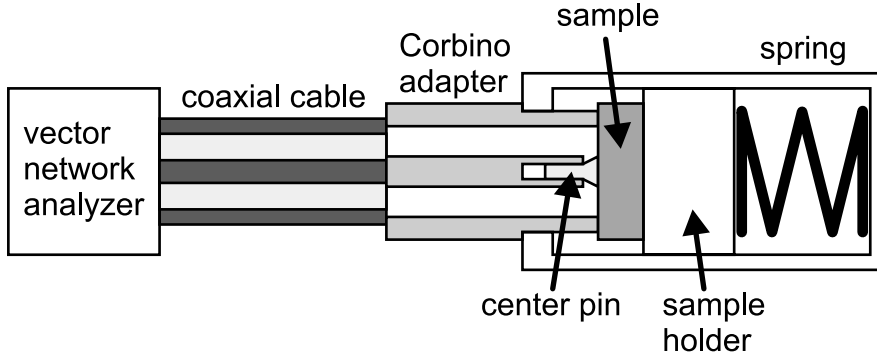
**Figure 3.2:** Schematic plot of Corbino microwave spectrometer (not to scale).

cables and connectors, and the Corbino geometry simply keeps this geometry to obtain a well-defined interaction of microwaves and sample.

For Corbino's original studies the magnetic field applied perpendicular to the sample disc was essential. Our current setup is not equipped with an external magnetic field, but nevertheless the term 'Corbino' will be used for it (like by other groups [5,44]) although the term 'open-ended coax' was also introduced for such a setup [62].

## 3.1.1 Principle of Microwave Corbino Spectrometer

While in dc or low-frequency experiments the properties of the Corbino disc sample can be obtained by measuring the relevant current and voltage directly, this procedure does not work at microwave frequencies. Here network analysis techniques are applied. The principal microwave setup necessary for a broadband Corbino spectrometer is sketched in Figure 3.2: a microwave signal is created by the source of a network analyzer and fed into a coaxial transmission line. The signal is then reflected by the sample that terminates the otherwise open-ended coaxial cable at the Corbino probe. The reflected signal travels back through the same coaxial cable and is detected by the network analyzer. The output variable of the network analyzer is the complex reflection coefficient $S_{11}$ [1], the phase-

---

[1]In the field of network analysis $S_{11}$ is the conventional notation for the reflection coefficient measured at port 1 of a device under testing, i.e. the signal enters the device at this port and exits it at the same port, in contrast to e.g. the transmission coefficient $S_{12}$.

sensitive ratio of the voltages of the reflected and outgoing waves as determined at the location of the 'reference plane' which has to be established by a calibration. The obtained reflection coefficient is determined by the impedance $Z_L$ of the load to be studied (which includes everything behind the reference plane, in particular the sample itself and the contact resistance between the probe and the sample) via the following relation (that is derived in Appendix A.1):

$$S_{11} = \frac{Z_L - Z_0}{Z_L + Z_0} \quad , \tag{3.1}$$

where $Z_0$ is the wave impedance of the coaxial cable, in our case the conventional standard of 50 $\Omega$. Since the contact resistance cannot be distinguished from the intrinsic response of the sample, it is desired to keep the contact resistance as low as possible, e.g. by depositing additional contact pads of a good conductor onto the sample.

It might be pointed out already now that the microwave measurements rely on network analysis procedures and as such are limited to reasonably high frequencies whereas the simultaneous dc measurement described in Section 3.2.3 is completely independent of the high-frequency measurements.

Extremely important for reliable performance of the spectrometer is good contact between the sample and the Corbino probe (bad mechanical contact causes large contact resistance). In our case this is maintained by two springs, one for the outer conductor and one for the inner. The sample holder, a cylinder usually made of copper, with the sample attached to it is pressed against the Corbino probe by a strong spring. This ensures that the sample and the outer conductor of the Corbino probe have tight contact. The inner conductor is connected to the sample by a small pin with a conical end. This pin bridges the gap between the plane of the outer conductor contact and the end of the inner conductor (which is slightly recessed in the case of our Corbino probes which are fabricated from commercial microwave adapters). Additionally, the conical end of the pin in combination with the design of the inner conductor of the probe (with small resilient fingers at the end) results in a small force that presses the pin against the sample. Thus both, inner and outer conductors are connected to the sample

by springlike constructions ensuring good contact even when the probe is cooled to cryogenic temperatures with the possibility of different thermal contraction of different parts of the probe.

## 3.2   Design of Cryogenic Microwave Corbino Spectrometer

The general design of a Corbino spectrometer is rather simple whereas the actual construction of a cryogenic microwave Corbino setup requires careful design as well as implementation. The most important issues to consider in the design stage are the frequency range to be covered, the available temperature range, and the sensitivity of the spectrometer. Unfortunately the last point, the sensitivity, is almost impossible to calculate before the instrument is completed because it depends crucially on the reproducibility of the spectrometer (when sample and known calibration standards are exchanged), and this can be degraded by almost any part of the spectrometer when not applied with maximum care.

Limits to the frequency range can be considered more easily. The core frequency range of this project is from 1 GHz to 10 GHz, but the frequency range should extend to frequencies as high as possible to join or even overlap with the frequency range covered by the submillimeter spectrometers that are available at the 1. Physikalisches Institut. There the nominal frequency range is from 30 GHz to 1.2 THz, but measurements below 100 GHz are very hard and cannot be performed for all samples.[2] The frequency range covered by the Corbino spectrometer depends first of all on the network analyzer that is used. Commer-

---

[2]For the quasioptical spectrometer the sample size should be at least of the order of the wavelength of the radiation, i.e. for 30 GHz the sample size should be 1 cm, which is hard to maintain for many materials of current scientific interest. One path to overcome this problem is to work with a near-field setup, like is also pursued by the 1. Physikalisches Institut [71, 72]. In fact the Corbino spectrometer can also be regarded as a near-field device since the high-frequency wave approaches the sample in a mode that is not supported by unstructured media (i.e. no inner and outer conductors) and therefore decreases exponentially in the sample, and the sample can be much smaller than the wavelength.

cial network analyzers with coaxial cables (e.g. Agilent/Hewlett Packard 8510 and PNA series and Anritsu 37000 series) can work up to 50 GHz or 65 GHz, frequency ranges in accord with the norms of 2.4 mm or 1.85 mm (alternatively called V-) connectors.[3] However, experiments with the Corbino spectrometer in the group of Steven M. Anlage at the University of Maryland [46] showed that reproducibility is hard to obtain at frequencies above 20 GHz, and unfortunately also in the current project this limit could only be lifted for very special measurements. Thus the Hewlett Packard 85107B vector network analyzer that is employed in the current setup and works in the frequency range from 45 MHz to 50 GHz offers the frequency range that we need including some space for possible future improvements as well as for those special measurements where the 20 GHz limit could be overcome.

The temperature range to be covered by the spectrometer depends on the important scientific questions to be addressed. Starting with heavy-fermion systems, the interesting features typically occur at temperatures below 10 K. Measurements with the submillimeter spectrometer can be performed to temperatures slightly below 2 K, and for this temperature broadband microwave measurements were highly desired. Therefore the Corbino spectrometer was designed to work at 2 K, meaning using standard cryogenic techniques for liquid $^4$He as a cryoliquid. For many scientific problems measurements at lower temperatures, using $^3$He as a cryoliquid or even a dilution refrigerator, are desirable,[4] but our strategy was first to establish a spectrometer for the $^4$He range and then use the experience gained with this spectrometer for possible further experiments at even lower temperatures.

Experience of the Maryland group shows that excellent microwave characteristics can be obtained by incorporating a Corbino probe into a continuous-flow

---

[3]Network analyzers for higher frequencies are also commercially available but usually employ rectangular waveguides.

[4]There are interesting high-frequency effects in the so-called quantum regime where the energy $\hbar\omega$ of the radiation is larger than the thermal energy $k_B T$ which means temperatures below 300 mK for frequencies of 10 GHz.
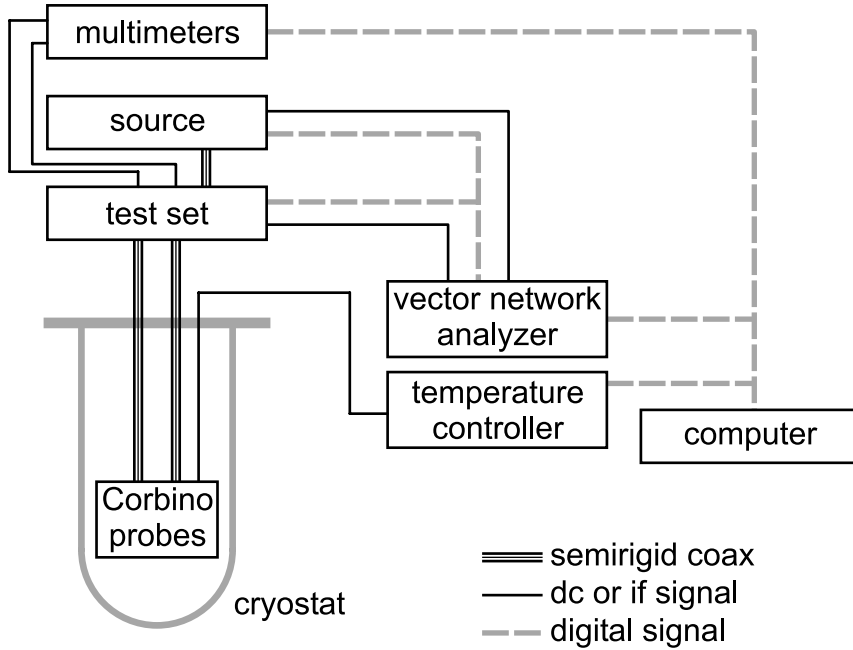
**Figure 3.3:** Scheme of the different instruments that form the spectrometer. The wiring includes semirigid coaxial cables for the microwaves, flexible coaxial cables as well as twisted copper wires for intermediate frequency (if) and dc signals, and GPIB/HPIB cables for digital signals.

cryostat, but then temperatures below 20 K are hard to reach [73] because of the large heat transfer through the coaxial cable. Since we definitely need temperatures below 4.2 K, we decided to work with a $^4$He bath cryostat as the easiest way to reach these temperatures with large cooling power.

### 3.2.1 Microwave Setup

The whole spectrometer was optimized with respect to its performance at microwave frequencies with minor priority for all other characteristics of the instrument. Thus most effort was put into the details of the microwave setup which consists of the network analyzer, the cables connecting the network analyzer to the probe, and the probe itself. A scheme of the different instruments that are used to constitute the Corbino spectrometer is shown in Figure 3.3. We use a Hewlett Packard HP 85107B vector network analyzer set working up to 50 GHz. This network analyzer consists of an HP 83650B microwave source, an HP 8517B

test set, and the HP 8510C network analyzer itself. The network analyzer is equipped with 2.4 mm connectors (compatible with 1.85 mm connectors) which thus define the standard for the whole spectrometer. Unfortunately the 2.4 mm and 1.85 mm standards are not widely in use (because frequencies higher than 20 GHz are not yet used for many commercial applications), and therefore only few companies offer connectors of this type and the appropriate cables. Fortunately some of these microwave parts proved to be compatible with cryogenic environments, and we were able to build the spectrometer of commercially available microwave equipment, which is more convenient to adjust or replace than completely home-built equipment [74].

As coaxial cables have high losses at high frequencies (in our case 2.7 dB/m for 20 GHz at room temperature for copper coaxial cable [75]), the length of the microwave line should be kept as short as possible, in our case the total length is about 1.2 m, i.e. for 20 GHz the total loss due to the cables is about 6.5 dB (for reflection measurements), thus almost 80% of the signal are dissipated by the cable. (We use semirigid cables because they have lower losses than flexible ones, and, more important, they give more reproducible results because they do not bend during normal use.)

For the major part of the experiments described in this thesis (i.e. those for temperatures from 1.65 K to 300 K), the coaxial cables used [76] are made of copper for outer and inner conductors (the outer conductor additionally tin-plated for better solderability, the inner conductor additionally silver-plated) and of low-density teflon (which has lower losses than other conventional dielectrics) for the dielectric. The tests at lower temperatures were performed using a coaxial cable [77] with stainless steel outer conductor, silvered copper covered steel inner conductor, and standard teflon dielectric.

The losses in the coaxial cable strongly depend on temperature, in particular when employed at cryogenic temperatures like in our case. The resistive losses in the coaxial cables reduce considerably when the cable is cooled to low temperatures due to the reduced resistivity (an effect partially compensated by the

decreasing skin depth). As a result the measured reflection coefficient will indicate lower losses which are not due to the sample but due to the coaxial cable. This effect has to be taken into account by the temperature-dependent calibration procedure that involves calibration measurements with standard samples at the same cryogenic temperatures. Obviously this procedure can only work out if the temperature distribution of the coaxial cable is reproduced in sample and calibration measurements. This was achieved by carefully reproducing the parameters of the cooling process, i.e. levels of cryoliquids, contact gas pressure, and timetable of a set of measurements at different temperatures.

The connections of network analyzer, coaxial cables, and probe were established using commercial microwave connectors by M/A-COM [78] and Anritsu (so-called V-connectors) [79]. Both types worked reliably in the course of our measurements, but only M/A-COM connectors were used at cryogenic temperatures as their extended cylindrical shape make them easier to incorporate tightly into the probe head than the V-connector with its smaller, hexagonal body.

The Corbino probes were manufactured from commercial microwave male-female adapters. As the work by the Maryland group showed [44], Corbino probes made from commercial connectors have several advantages compared to completely homemade probes: they can easily be soldered to coaxial cables, they can be expected to have excellent microwave propagation properties, they are readily obtainable, and most important: a Corbino probe made of a commercial connector can be calibrated with commercial standards at room temperature. The last point is less crucial for eventual measurements if a full calibration with three (cryogenic) standards is performed. But in many cases a different calibration is used that employs only one low-temperature calibration but also the room-temperature one. Furthermore, a commercially calibrated probe is convenient during the process of adjusting probe and sample because the spectra acquired by the network analyzer can be interpreted directly.

In contrast to the Maryland setup, no commercial connectors were used for the Corbino probe but commercial adapters. The motivation for this was twofold:

experience gained at Maryland showed that the center conductor of the Corbino probe is pushed rather hard during the course of the measurements, with the most critical being the insertion of the small center pin, which is performed whenever the probe itself or the network analyzer calibration is changed. These forces can cause the center conductor to bend or even break, which means that the connector has to be replaced completely or even the whole coaxial cable if its length is restricted (replacing a connector means shortening the cable by approximately 1 cm). If a microwave adapter is used for the Corbino probe instead of a connector, it can be replaced completely very easily without changing the rest of the transmission line.[5] The second reason was that by using adapters it is easier to test different adapters by different suppliers without changing the coaxial cable that connects the network analyzer and the probe. Thus it is easier to compare different adapters than connectors as the quality of a microwave coaxial cable can be degraded if a connector is not soldered to it carefully.

Several commercial male-female adapters of 2.4 mm or 1.85 mm norm were machined into Corbino probes by removing most of the threading of the female connector on a lathe. These Corbino probes were then tested at room temperature and fortunately the Rosenberger Adapter [80] as the most reliable of these also proved to work at liquid helium temperatures with reproducible microwave properties.[6]

## 3.2.2 Reproducibility of Microwave Connections

A general problem of microwave experiments using coaxial cables is that extreme care has to be taken with respect to all connections of the transmission lines. The transmission and reflection characteristics of commercial connectors can al-

---

[5]In the present study the problem of a breaking Corbino center conductor never occurred. This might be due to the particular adapter in use but also due to the fact that the center pin was taken out and reinserted only very rarely, due to the standardized measurement procedure.

[6]Probes made of adapters by Spectrum [81] and M/A-COM [82] did not work reliably enough at room temperature and adapters by Hewlett-Packard [83] with otherwise superb microwave characteristics could not be converted to Corbino probes due to their special construction of the center conductor.

ter dramatically if not connected carefully. Therefore torque wrenches are used to have reliable performance. However, even this procedure will not give perfect results. The problem with disconnecting microwave transmission lines is illustrated in Figure 3.4. There two impedance spectra of a stainless steel sample
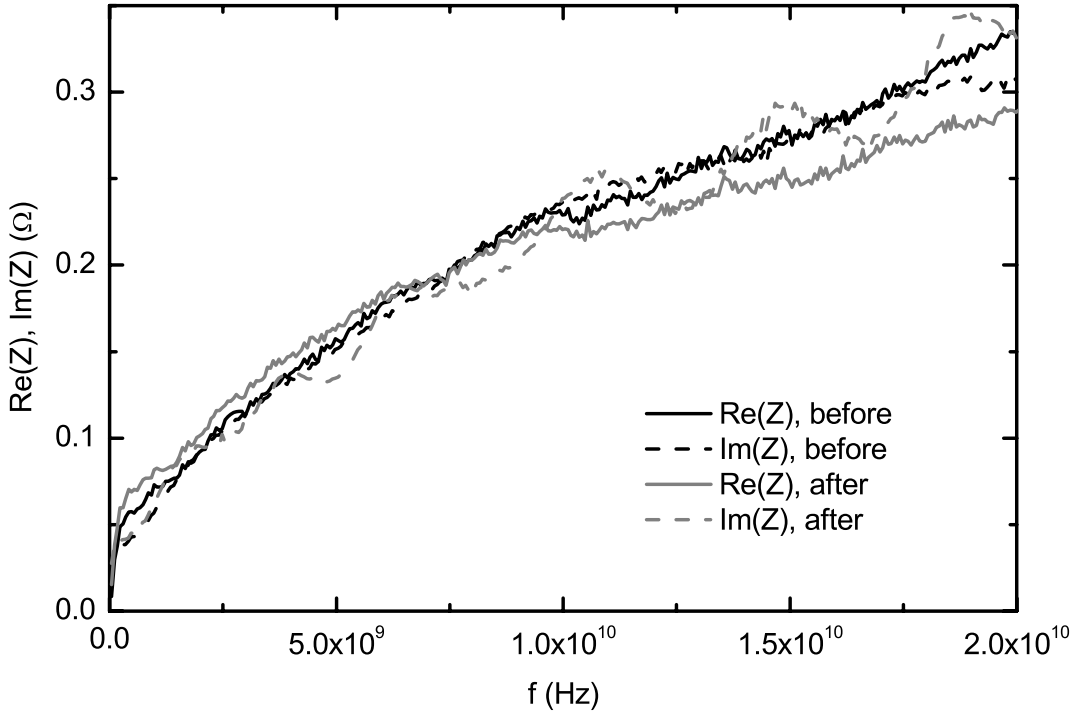


**Figure 3.4:** Real and imaginary parts of the impedance of a bulk stainless steel sample measured at room temperature. The first measurement was performed without disconnecting the probe adapter, for the second measurement the adapter was disconnected and reconnected. The general square-root frequency dependence is expected for the surface impedance of a metal.

measured at room temperature are shown. The procedure was as follows: the Corbino adapter acting as a probe was attached directly to the test set to remove any further influence of other cables and connectors, i.e. no measurement with the Corbino adapter can be performed more reliable than this one. First a bulk copper sample was measured as a calibration standard. Then the copper sample was replaced by the stainless steel sample and the first spectrum in Figure 3.4 was obtained. Then the adapter (with the stainless steel sample attached to it) was disconnected from and reconnected to the test set and the second calibra-

tion spectrum was measured. Both measurements reveal an overall square-root frequency dependence for the real and imaginary parts of the impedance, as is expected for a bulk sample where the surface impedance is probed (i.e. the sample is much thicker than the skin depth), but the second measurement shows a strong oscillation in the imaginary part of the impedance, and this effect has to be attributed an artefact of the removal of the probe adapter. Among the tests of this sort the reproducibility shown in Figure 3.4 was not surpassed and thus it has to be concluded that any removal of microwave connections reduces the overall quality of the measurements and it is desirable for a broadband microwave setup to exchange samples without disconnecting any microwave connections.

This restriction causes severe limitations concerning the whole spectrometer setup as soon as the probe is located in a cryostat. Usually the probe insert of a $^4$He cryostat is taken out of the cryostat to exchange samples, and for this the insert is disconnected from the signal cables etc. that are used during the experiment.[7] Instead we require all microwave connections to stay attached. That means that either the microwave setup as a whole (including network analyzer) has to be moved out of the cryostat or the cryostat has to be moved away from the microwave setup. We chose the second approach and this proved to work out nicely.[8]

### 3.2.3 Simultaneous dc Measurement

As mentioned before in Section 3.1.1, the Corbino spectrometer effectively measures the impedance of the sample in combination with the contact impedance of sample and probe. Without additional information the latter cannot be extracted

---

[7]In this case the changes for the microwave equivalent will be stronger than those shown above because the disconnecting of such a microwave cable from the network analyzer usually involves some bending of the cable.

[8]Another possibility is to choose a cryogenic setup that allows to exchange the sample without disassembling cryogenics and microwave setup. This approach is realized by the Maryland spectrometer where the probe is cooled by the coldfinger of a continuous-flow cryostat and the coaxial cable can be extremely short. But as mentioned in Section 3.2, we could not follow that route since we need temperatures below 4.2 K.

from the microwave data, thus the procedure relies on the assumption that the contact impedance can be neglected with respect to the sample impedance. One indication that this assumption holds can be obtained by a simultaneous measurement of the combined two-point dc resistance of microwave line, probe, and sample. This two-point resistance can be measured in a way that is independent of and simultaneous with the microwave measurements thanks to an additional access to the microwave line: the test set includes a separator for dc and microwave signals sent into and coming back from the microwave transmission line. Although commercially intended to apply dc voltages to microwave devices under testing, this additional access can also be used to measure the dc resistance of the sample. To achieve this, a multimeter [84] measures the two-point dc resistance of the microwave transmission line including the sample shorting the line and the contact resistance.

This two-point resistance measurement can yield very useful additional information during the measurement procedure. When the sample is attached to the probe at room temperature, the contact resistance can be estimated if additional information about the sample is available (e.g. the estimated dc resistance of the sample) or similar samples have been measured already. This *ad hoc* check concerning the contact resistance can help to avoid time-consuming low-temperature measurements with strong contact contributions as well as indicate microwave spectra spoiled by poor contact (this often results in capacitive effects with $1/\omega$ frequency dependence and large dc resistance), and in particular calibration measurements with a short require excellent contact which can be estimated from the dc resistance value.

Furthermore the temperature dependence of the dc resistance also yields valuable information. Any jumps in the dc resistance are indications of changes in the contact and the resulting spectra have to be checked carefully or might require a remeasurement. But more important is the observation of the characteristic temperature dependence of the dc resistance of the sample. Here comparison of the dc resistance with literature data or independently obtained four-point resis-

tivity data can give indications on the sample quality. In the current study the two-point resistivity obtained in the course of the microwave experiments usually agreed well with independent four-point measurements on the same samples, and therefore the absolute resistivity was often obtained from the dc measurements with the microwave setup without additional four-point measurements.

If not only relative dc resistance values are sought after but also absolute dc resistivity values, the contribution of the coaxial cable and the test set has to be subtracted from the measured resistance dc values first.[9] This can be done easily by using the measured values of the calibration short. Typically this contribution can be considered temperature-independent (with a value of about 1.5 $\Omega$).

The simultaneous dc measurement also proved extremely useful for two other particular problems of the current setup: the temperature correction described in Section 3.3.5 and the problem of poor contacts described in Appendix B.2.

## 3.2.4   Dual Setup

The network analyzer is connected to the probe via the test set. Since this is commercially designed to measure a full response of microwave devices, it has two ports that enable measurements of the transmission coefficients in both directions as well as reflection coefficients from both directions without disconnecting the device. Since our probe does not allow for transmission measurements at the current state, we can use the two ports of the test set to measure two equivalent probes independently during one cooldown, i.e. effectively the total speed of the measurement can basically be doubled. (The two spectra are measured by the same network analyzer, i.e. the bare time of all the measurements performed at a particular temperature doubles as well, but the time of actual measurements is small compared to the other time periods of cooling the cryostat, reaching higher temperatures, stabilizing the temperature etc.) A principal disadvantage of using

---

[9]This particular procedure will not be necessary to obtain absolute values from the high-frequency data because there true network analysis is performed where the influence of the coaxial cable is accounted for by the general error model as described in Chapter 4.

two probes simultaneously is that two coaxial cables are fed down the cryostat which might actually double the transferred heat, an effect that has to be taken into account when the current setup is to be extended to lower temperatures.

### 3.2.5 Cryogenics

As described in Section 3.2, a base temperature below 2 K was required for the spectrometer, and due to the large heat transfer through the coaxial cables a $^4$He bath cryostat was the natural choice to reach these temperatures. This cryostat was purpose-built for this spectrometer with the overall length of the cryostat being the most important characteristic, which was chosen rather short for a bath cryostat for two main reasons: the first one is that the total microwave losses in the coaxial cable increase with cable length, and therefore the influence of the cable to the measured signal is stronger the longer the cable is. Thus reproducibility and finally resolution generally improve when the coaxial cable is shorter. The other, minor reason is convenience of use of the cryostat. For a standard cryogenic setup the height of the (fixed) cryostat plus the height of the insert should be less than the height of the laboratory because otherwise the insertion of the insert will be complicated. As mentioned in Section 3.2.2, in our case the cryostat is moved with respect to the insert. In this case it is convenient if some more space is left atop of the then fixed insert for those cases when the insert is removed from its fixture (which was done frequently in the first part of the project when different microwave parts had to be tested) or for the helium transfer tubing which in that case can also be removed easily. This motivation led us to a cryostat with an inner height of approximately 75 cm. The cryostat itself is a typical $^4$He glass cryostat with four walls separating an outer isolation vacuum (that was pumped after the cryostat was finished and then sealed permanently), a liquid nitrogen tank, an inner isolation vacuum (that is pumped typically after a week of low-temperature measurements to remove possible helium that has leaked in), and the liquid helium volume (the fully shielded height of the helium volume is approximately 55 cm).

To move the cryostat from the insert, the cryostat is attached to a massive aluminium plate which is connected to a pneumatic system allowing a controlled and smooth vertical movement of the cryostat. When removed from the insert, the cryostat can be moved sideways on solid rails to allow for convenient access to the insert and the probe.

Since temperatures below the boiling temperature of $^4$He at ambient pressure of 4.2 K were necessary, the pressure of the helium bath can be reduced using powerful pumps namely a rotary prepump and an additional Roots pump. However, most of the measurements described in this thesis were performed using the prepump only reaching a typical base temperature of 1.63 K.

To allow controlled measurements through the complete temperature range from the $^4$He base temperature up to room temperature, the probe was not inserted into the liquid helium directly but the probe is located inside of a stainless steel cylinder which is immersed in the liquid helium bath. The probe insert is then cooled via exchange gas (typically a few mbar of $^4$He).

## 3.3 Performance of Low-Temperature Setup

The most important part of the spectrometer of course are the microwave elements. However, as mentioned in Section 3.2.1, reproducible microwave measurements require reproducible low-temperature conditions of all parts of the spectrometer. Therefore first the cryogenic performance of the setup is discussed before focussing on the microwave properties in the later sections.

### 3.3.1 Temperature Range

The temperature that was necessarily be achieved by the spectrometer was 2 K. As already mentioned, we chose a $^4$He bath cryostat design for the cryogenics but the severe requirements for the microwave setup lead to a rather short glass cryostat which might result in a slightly higher base temperature as well as a shorter time period available for measurements at low temperatures. The latter

point is of less importance in our case since the experiments themselves are fast (acquisition time of one spectrum is of the order of one minute) and the limiting factor for the overall speed of the measurements is the time necessary to warm up the cryostat before samples can be exchanged at room temperature. Concerning the first point, apparently the reduction is not particularly pronounced as the lowest temperature reached with this cryostat up to now was 1.16 K (in the typical range for $^4$He cryostats) during test measurements with a stainless steel coaxial cable (described in Section 5.6.2), using the rotary as well as the roots pump for cooling of the liquid helium and a contact gas pressure only slightly below the vapor pressure of the bath. Because these test measurements with standard stainless steel coaxial cables showed problems with reproducibility, we went back to low-loss copper coaxial cable with much higher heat conductivity resulting in higher base temperatures. With this setup typical base temperatures are around 1.63 K and measurements are performed from 1.65 K up to 300 K. Here the probe rod is not optimized for low temperatures but for microwave reproducibility, and these temperatures are reached with the rotary pump only.[10]

## 3.3.2 Temperature Measurement and Control

For any cryogenic experiment, measuring the relevant temperatures is important. In our case this is particularly the case because at the current state the spectrometer was designed for optimal microwave characteristics and thermal considerations were given less priority. Thus the following problems concerning the temperature measurement occur:

**Temperature gradients in the cryostat:** Due to large heat transfer into the cryostat via the copper coaxial cables a large cooling power is required. This gives a low base temperature, but already at slightly higher temperatures significant

---

[10]Tests with the roots pump showed that due to the use of copper coaxial cables in the current setup temperatures below 1.6 K are unstable because the required contact gas pressure is so high that the contact gas may condense, an effect to be avoided since a reproducible temperature distribution is crucial for the calibration procedure.

temperature differences at different points of the probe head are measured. This effect is partially due to the fact that we do not decrease the contact gas pressure when the temperature is increased (this is to ensure reproducibility between the sample and reference measurements).

**Distance between sample and temperature sensor:** It was already pointed out that any broadband microwave measurement requires an extremely high reproducibility. Therefore replacing sample and reference samples should leave most of the setup untouched, and our setup is a realization of this concept. As a result it is impossible to have the temperature sensor (we use Cernox sensors [85]) positioned right at the sample in our current setup: the Corbino probe itself, the modified microwave adapter, has no space for a sensor. The same is true for the front side of the sample holder. Actually the whole sample holder is inconvenient for the temperature sensor since it is replaced every time the sample is exchanged and furthermore the sample holder moves and rotates while the sample approaches the probe (i.e. wiring has to be more elaborate). As can be seen in Figure 3.5, the location closest to the sample that is suitable for a temperature sensor is between the two Corbino adapters, about 1.5 cm away from the sample. This sensor will be denoted 'A' in the following.

**Heater:** To control the temperature of the sample at constant contact gas pressure, a homemade resistive heater (a coil of nichrome wire [86]) is used. This heater is located a few centimeters above the sample stage (see Figure 3.5) to obtain a homogenous temperature below the heater, but due to the large cooling power this is not the case. A second temperature sensor (sensor 'B') is located right at the heater. This setup also allows for the common Two-Sensor-Approach [87] (one sensor close to the sample to measure the temperature, one sensor close to the heater for good temperature control), but temperature control using the sensor close to the sample is already extremely good (with the advantage that the real sample temperature is much closer to the setpoint compared to using the second sensor). Therefore the sensor close to the heater is used for determination of temperature gradients only.
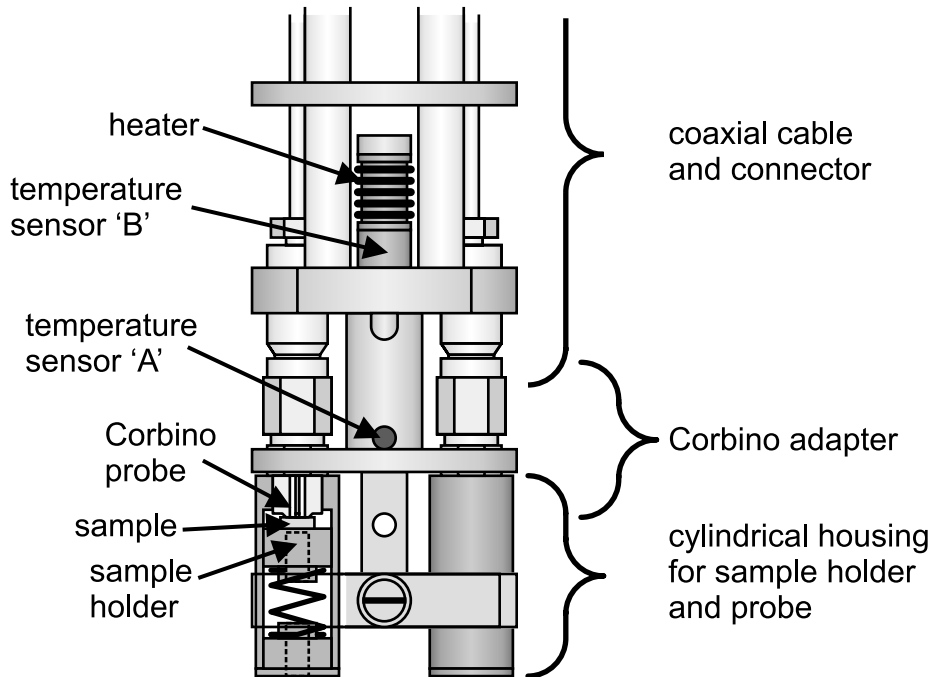
**Figure 3.5:** Design of the probe head incorporating two Corbino adapters and sample holders as well as heater and temperature sensors.

The large temperature gradients in our system show that the sample temperature cannot be expected to be the temperature measured by the closest temperature sensor. However, since the cryogenic parameters (level of helium and nitrogen and the contact gas pressure) are reproduced for all measurements, so are the temperature gradients. This allows for a recalibration of the measured temperatures to real sample temperatures as described in Section 3.3.5.

The temperature is controlled by a LakeShore 340 Temperature Controller that monitors the temperature of the two sensors and applies the appropriate current to the heater in the probe head. As will be shown in the next section, the temperature control proved to be extremely reliable, giving typical temperature variations of only a few millikelvin while the data of a microwave spectrum is taken.

It should be mentioned at this point that the possibility to measure the temperature while the microwave measurements are performed enables a direct check whether the microwave radiation heats the sample.

### 3.3.3 Temperature Stability and Reproducibility

Temperature stability during the measurement of each microwave spectrum and in particular reproducibility of the different temperatures during a complete temperature-dependent measurement from 1.65 K up to room temperature are very important for the current spectrometer. The main reason is that the calibration procedure requires sample and up to three calibration runs to be performed at the same state of the spectrometer, particularly in the same state concerning the microwave characteristics, and these (like the damping in the coaxial cable) depend crucially on the local temperature in all regions of the cryostat. Thus a reliable microwave calibration requires high reproducibility of the temperature conditions in the whole cryostat throughout the measurements.

Temperature stability during each measurement is of additional importance if samples with strongly temperature-dependent properties are studied. Thus the temperature has to be stable to avoid possible temperature-dependent effects during the acquisition of a spectrum. The temperature stability achieved with the Corbino spectrometer can be estimated from Figure 3.6. There the standard deviation of the temperature during the acquisition of a spectrum (761 frequencies corresponding to 761 temperature measurements), averaged over 99 standardized low-temperature measurements, is plotted versus temperature. Striking features in this temperature dependence are the extremely low very first data point (basically at the base temperature with minimal heating only), large standard deviation at 5.5 K when the helium bath is not pumped on any more, a minimum between 20 K and 30 K where the temperature control was optimized, a maximum around 100 K when the helium level is low or the helium has evaporated already completely, and rather low changes at the highest temperatures when the heater is almost at its maximum power but nevertheless the temperature changes only very slowly. Considering the complete temperature range covered by the spectrometer, the overall stability is rather good. During a measurement the temperature change is typically around a tenth of a percent or even less.
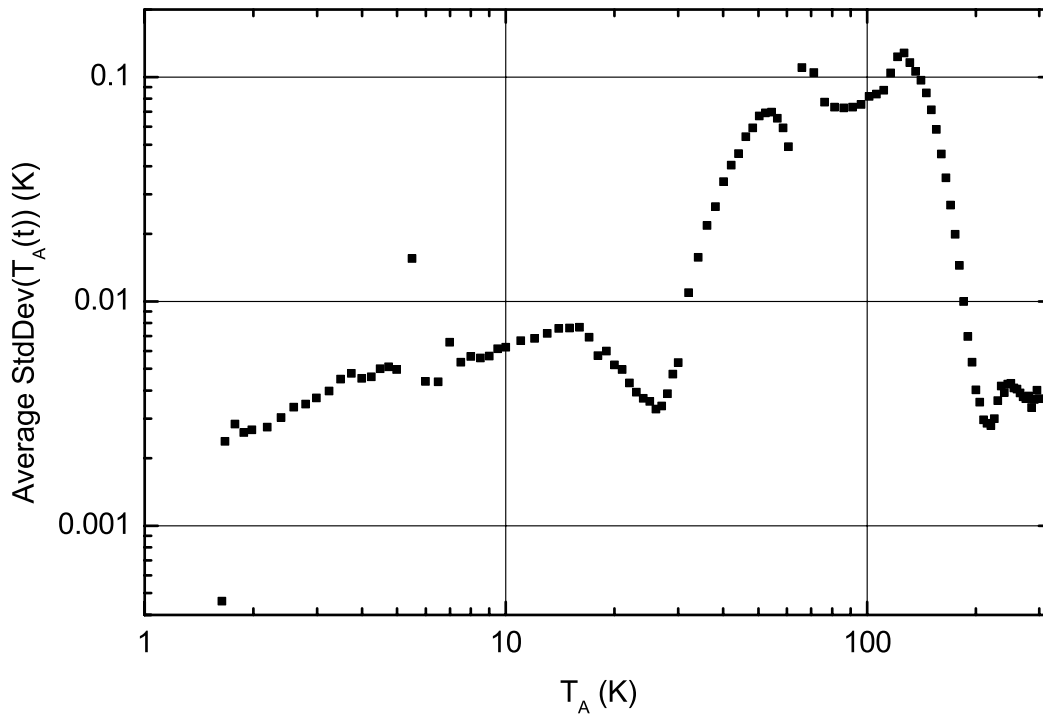
**Figure 3.6:** Temperature stability: average (99 standardized measurements) of the standard deviation of the temperature during the acquisition time of a spectrum.
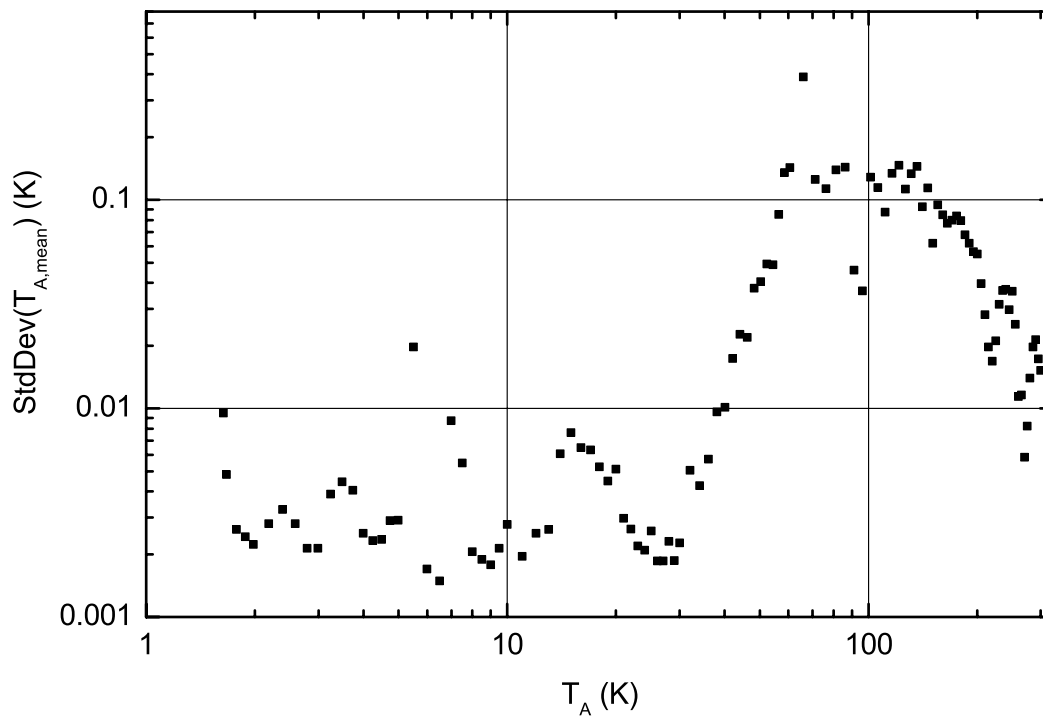


**Figure 3.7:** Reproducibility: standard deviation of (average) temperature determined from 99 standardized measurements.

While temperature stability is important for each single measurement, reproducibility is of particular importance when it comes to the crucial calibration procedure. The temperature reproducibility through the set of 99 standardized measurements is shown in Figure 3.7. The average temperatures of each single measurement were analyzed statistically and the standard deviation of these temperatures at a fixed setpoint temperature is shown in the graph. Here the overall temperature dependence is very similar to that shown in the temperature-dependent stability, and particular features occur at the same temperatures for the same reasons as discussed there. Also the absolute values are similar: typically the temperature is reproduced among different cooldowns to less than a tenth of a percent.

The rather good reproducibility is not only due to the general cryogenic setup and the temperature control in particular but also due to the strict reproduction of the other factors: the levels of liquid helium and nitrogen are controlled to about 1 cm and the contact gas pressure to approximately 5%.

### 3.3.4 Temperature Gradients

Up to now only the temperature that is measured by the temperature sensor between the Corbino adapters (sensor 'A') was studied. Since another temperature sensor (sensor 'B') is located at a slightly different position, right at the heater, it is possible to study the temperature gradients within the cryostat insert. The temperature difference measured by the two sensors (again an average of the 99 standardized measurements) is shown in Figure 3.8. Obviously, the temperature differences are substantial, in particular at low temperatures. Here the temperature difference is of the same order as the absolute temperature, indicating that the temperature gradients present in the Corbino insert are rather large during the standardized measurements. This directly calls for close consideration of the actual sample temperature, as will be given in the next section, and results in a temperature correction procedure with a temperature correction curve that is valid for all of the standardized measurements. Such a general correction is only
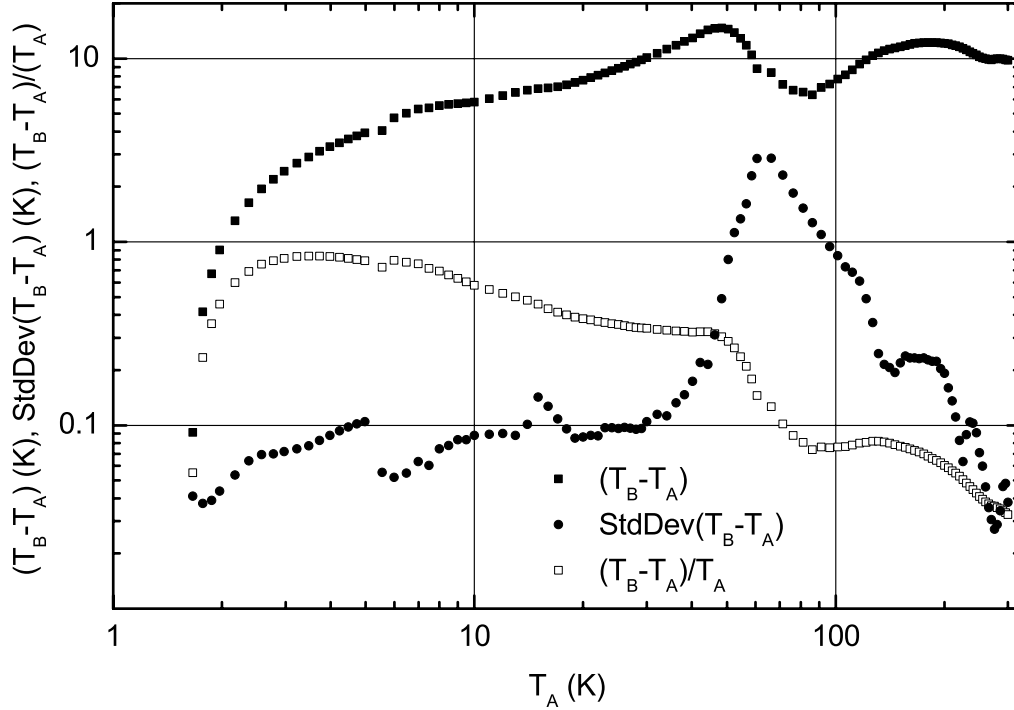
**Figure 3.8:** Average temperature difference (absolute and relative) between temperature sensors A and B and the standard deviation (of 99 standardized measurements).

appropriate because the temperature gradients are reproduced as can be seen in Figure 3.8: for most of the interesting temperatures below 40 K the standard deviation of the temperature difference is almost two orders of magnitude smaller than the difference itself. This again demonstrates the reproducibility of the conditions inside the cryostat during the standardized measurements and justifies the general temperature correction.

### 3.3.5 Temperature Correction

As just mentioned, the temperature gradients in the current setup are considerable and therefore the measured temperature cannot be expected to be the temperature of the sample. However, since the setup is run always with the same settings (levels of cryoliquids, contact gas pressure, heater output, controller settings, timetable), the temperature gradients can be expected to reproduce throughout the different measurements, and the temperature of the sample can be obtained if

a conversion curve from measured to real temperature is at hand. Such a conversion curve was deduced from the measured dc resistance of several samples. The dc resistance of the sample is obviously connected to the real sample temperature which in turn then can be deduced if the temperature dependence of the sample dc resistance is known. Since the dc resistance measured with the Corbino setup is a two-point resistance, the conversion curve from dc resistance to temperature has to be obtained with the same setup. This can be done while the setup is cooled down since then the temperature gradients in the probe are much weaker because the heater is off. Thus the temperature dependence of the dc resistance measured while cooling the setup can act as a conversion curve when the probe is heated. However, this only works out if the sample has a strong and monotonic temperature dependence. For many samples this holds only for limited temperature ranges (e.g. semiconductors are well suited for low temperatures but poor for higher temperatures). To obtain a reliable, generally applicable conversion from measured temperature to real sample temperature, data taken with seven different samples are combined. These data, presented in Figure 3.9, show that the real temperature is always lower than the measured one and that the data of the different samples generally coincide nicely[11] except for certain temperature ranges. Further details on deviations among the different samples can be seen in Figure 3.10. Here the average difference of measured and real temperatures, indicating the temperature gradient in the probe, is plotted together with the standard deviation of the data used for the correction curve. Characteristic features occur above 5 K when the pump working on the liquid helium is turned off and above 40 K when the helium level is very low. The deviation of the real temperature between different measurements is rather large at this latter stage because small deviations in the helium level cause large differences in the applied heater power resulting in larger differences of the temperature gradient in the sample. Thus in general the real sample temperature is hard to obtain in this temperature range but for samples with particularly interesting effects in this

---

[11]Additional confirmation comes from superconducting transitions.
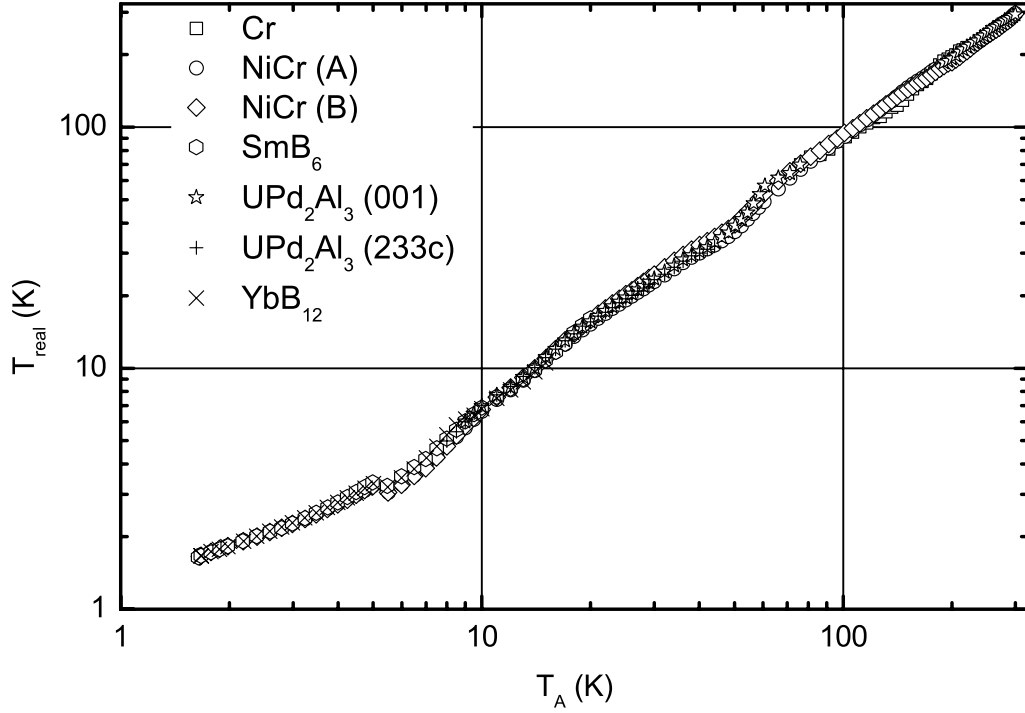
**Figure 3.9:** Real sample temperatures (from dc resistance) versus measured temperatures for those samples used for temperature correction.
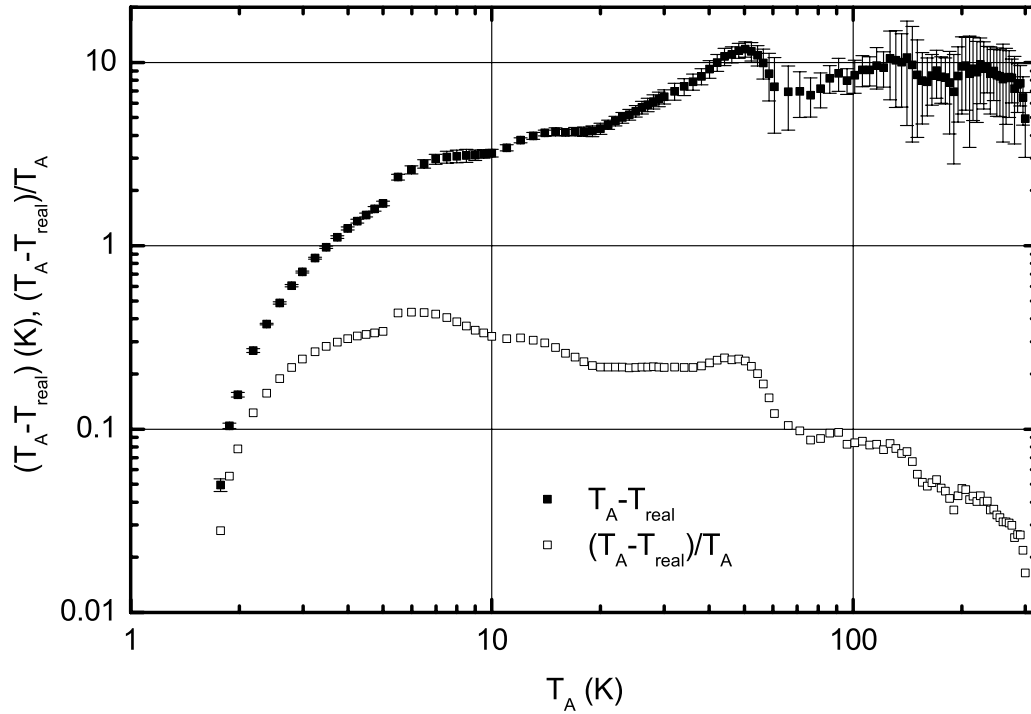


**Figure 3.10:** Average difference (absolute and relative) of measured and real temperatures. Error bars indicate the standard deviation among the data sets used for the temperature correction.

temperature range a completely different cryogenic setup would be much more reasonable anyway.[12] For the lower temperatures the real sample temperature is much more reproducible and therefore the inability to measure the real sample temperature directly can be compensated completely by the temperature correction scheme that uses the average of the data shown in Figure 3.9 as a correction curve.

---

[12]Like the continuous-flow cryostat used by the Maryland group.

# Chapter 4

# Calibration of Corbino Setup

The most crucial point when performing broadband microwave measurements is a careful calibration [88]. Any broadband microwave setup has to be calibrated, and this calibration has to be considered much more thoroughly than e.g. that of a comparable, conventional optical experiment. The main reasons for this are that the microwave equivalent of beam splitters, so-called directional couplers, are far from a perfect performance and that the wave is guided along transmission lines with considerable damping and non-perfect connectors.

## 4.1   General Error Model

Since calibration of microwave setups is a general problem of severe importance in particular for measurements with network analyzers, this topic has been dealt with in detail in the literature of microwave engineering [88] and the current study only requires an adaption of these result to the special case of cryogenic spectroscopy. Any microwave reflection measurement with any number of error sources can be described mathematically by the following general model with three error terms which is shown as a signal flow graph in Figure 4.1: the microwave signal produced by a source is reflected by the sample (or more general the device under test) with actual reflection coefficient $S_{11,a}$, and the ratio of the reflected signal measured by the detector and the signal emitted by the source is the measured reflection coefficient $S_{11,m}$. The two quantities $S_{11,a}$ and $S_{11,m}$ differ
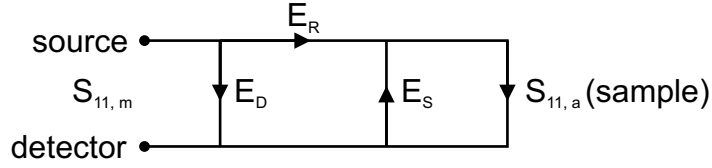
**Figure 4.1:** General error model for a microwave reflection measurement.

due to errors introduced by the signal path. Generally there are three different error sources possible: $E_D$, $E_S$, and $E_R$. Here the directivity $E_D$ describes that part of the emitted signal that is transmitted directly to the detector without interaction with the sample. The source match $E_S$ accounts for the part of the signal that already interacted with the sample but that is reflected again on the way to the detector, thus adding to the incoming signal from the source. The reflection tracking $E_R$ finally describes attenuation and phase shift in the transmission lines. In general the error coefficients are complex quantities and depend on frequency and in our case also on the temperature of the coaxial cable that is located inside of the cryostat whereas for an ideal reflection experiment the error coefficients $E_S$ and $E_D$ vanish and $E_R$ equals one.

For this general error model the measured reflection coefficient is given by the following formula:

$$S_{11,m} = E_D + \frac{E_R S_{11,a}}{1 - E_S S_{11,a}} \quad . \tag{4.1}$$

This equation is equivalent to the following that yields the actual reflection coefficient out of the measured one as soon as the error coefficients are known:

$$S_{11,a} = \frac{S_{11,m} - E_D}{E_R + E_S(S_{11,m} - E_D)} \quad . \tag{4.2}$$

In the general calibration procedure the three error coefficients $E_S$, $E_D$, and $E_R$ are determined by measuring the reflection coefficients of three standards with known actual reflection coefficients. Typically a short, an open, and a matched load, with reflection coefficients $S_{11,a}^{short} = -1$, $S_{11,a}^{open} = +1$, and $S_{11,a}^{load} = 0$, respectively, are chosen. With this choice the range of possible actual reflection coefficients (i.e. $|S_{11,a}| \leq 1$) is covered and additionally these reflection coefficients of the above standards ideally are frequency-independent.

## 4.2 Calibration at Room Temperature

Since our Corbino probe is manufactured from a commercial microwave adapter, it can be calibrated with the appropriate commercial calibration standards [89] at room temperature. The standards that are used are a perfect short ($Z = 0$), a perfect open ($Z = \infty$), and a perfectly matched load ($Z = 50\ \Omega$ corresponding to the characteristic impedance of the coaxial cable). While short and open can be realized to high perfection rather easily, this is much harder for the matched load, in particular for high frequencies. Therefore two different approaches are used as a matched load: for lower frequencies (up to 4 GHz) a broadband load is used directly whereas for higher frequencies a sliding load is employed. Here the load terminates an airline and the reflection coefficient is measured for different lengths of this airline. From this set of measurements a more precise determination of the desired 'actual' reflection coefficient of the load is possible.

The result of such a commercial calibration of the Corbino spectrometer is shown in Figure 4.2. There the frequency dependences of the magnitudes of the three error coefficients $E_D$, $E_S$, and $E_R$ are shown.[1] This plot also gives an impression of the importance of the different error coefficients: throughout the complete frequency range $E_R$ is larger than $E_D$ and $E_S$, but the latter two are not much smaller than 1. Therefore they cannot be neglected, and the full calibration procedure with three error coefficients has to be taken into account.

Using such a commercial calibration allows to measure the impedance of microwave components to high precision. But to measure material properties with our Corbino setup requires additional calibration steps even at room temperature. The reason is that the commercial procedure allows for calibrated measurements to be performed in the 'reference plane' which is the plane defined by the outer conductor of the microwave connector, and this is exactly the plane where the microwave radiation hits our sample. However, the commercial calibration is

---

[1] The real and imaginary parts of the error coefficients are not shown because they 'oscillate' extremely rapidly as a function of frequency.
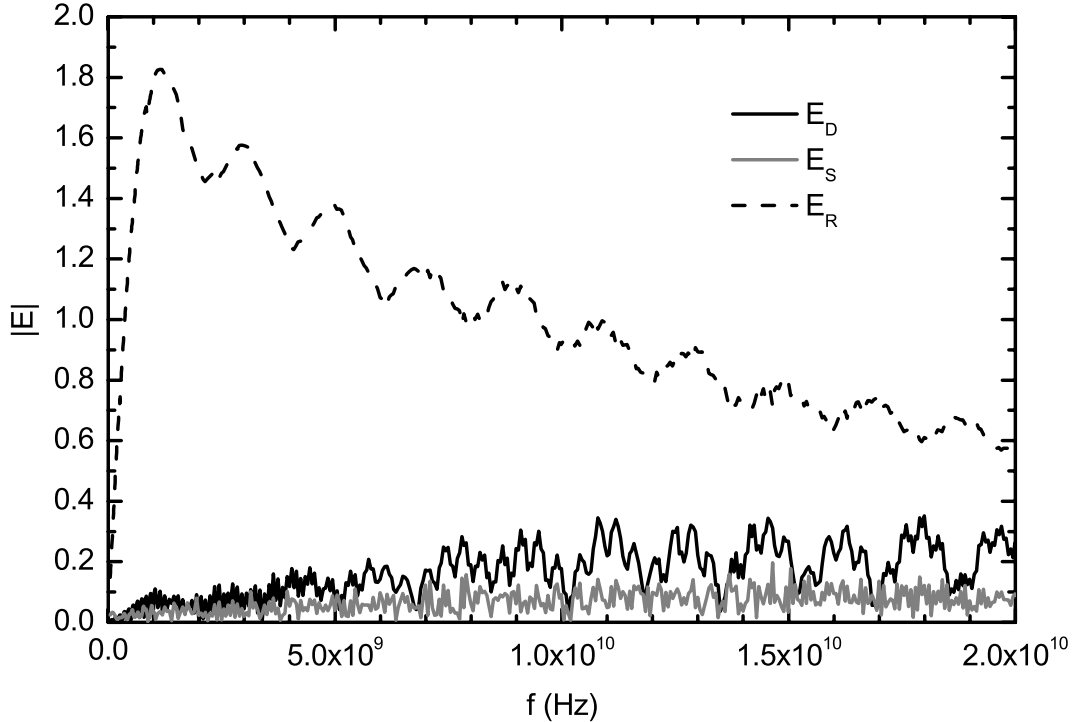
**Figure 4.2:** Frequency dependences of the magnitudes of the three error co-
efficients $E_D$, $E_S$, and $E_R$ as obtained for the Corbino probe with
a commercial calibration set at room temperature.

designed for measurements of devices that are connected with the appropriate
microwave connectors. Instead we introduce the small center pin for contact be-
tween sample and center conductor of the probe. This center pin is not accounted
for by the commercial calibration, but its effect has to be taken into account by
additional calibration steps.

As will be described below, we often perform low-temperature calibration
measurements using three calibration samples which give us a complete set of
the three error coefficients determined at low temperature. Thus in principle we
do not need a commercial room temperature calibration for our measurements.
However, all our measurements are performed using a commercial room temper-
ature calibration and the obtained data is later converted to the low-temperature
calibration. Using the room temperature calibration has the advantage that the
microwave spectra can be studied at once (whereas the uncalibrated spectra basi-
cally show the errors of the network analyzer and hardly depend on the sample).

This is very helpful when new samples are mounted and the contact resistance is to be minimized or when temperature-dependent effects are studied.

# 4.3 Calibration at Cryogenic Temperatures

The low-temperature calibration of the Corbino spectrometer is the crucial point of the whole measurement procedure and had to be addressed carefully. The general error model with the three error coefficients mathematically describes the properties of the microwave setup including the network analyzer, the Corbino probe, and the coaxial cable that links the two. But these properties depend on temperature, in particular the damping of the coaxial cable will change dramatically due to reduced conduction losses when it is cooled to cryogenic temperatures. Additionally, there can be phase shifts due to changes of the dielectric constant, and also reflections, losses, and phase shifts at microwave connectors can depend on temperature.

Obviously, a calibration has to be performed at the temperature of the sample measurement. Principally the above room-temperature calibration procedure can be used at low temperatures, but the commercial standards are designed for room-temperature use only, and furthermore the problem of including the center pin to the calibration cannot be solved by the commercial standards. Thus independent calibration standards have to be used at low temperatures.

## 4.3.1 Documented Procedures

Different groups working with similar microwave Corbino setups have published differing calibration procedures but none of them was later used by other groups, i.e. there is no widely accepted standard in the (very small) community. Therefore in the course of the current project the different procedures were tested and compared to establish procedures that can be employed for further generic measurements with the current Corbino spectrometer. Before these results are described an overview of the documented procedures is given.

## 4.3.2 Low-Temperature Calibration with one Additional Standard (as by Maryland Group)

Measurements performed by the Anlage group (University of Maryland) [44, 70] employ only one low-temperature calibration measurement and accordingly only one of the three error coefficients is considered temperature dependent whereas for the two others the room temperature values obtained with commercial standards are used. Motivation for this procedure is as follows: the Maryland Corbino probe is a modified commercial microwave connector (similar to our probe), and therefore the reference plane of the commercial calibration is the sample plane. The only effects that have to be accounted for by the additional calibration are the center pin and the temperature-dependent effects of the transmission line. Considering the three error coefficients, $E_S$ and $E_D$ are mainly due to imperfections of the network analyzer (in particular the directional couplers involved) and therefore do not depend on the temperature in the cryostat whereas $E_R$ depends crucially on the temperature in the cryostat (e.g. damping) and therefore has to be temperature dependent. Furthermore the magnitude of $E_R$ as measured at room temperature is much larger than that of $E_S$ and $E_D$, and therefore possible temperature dependences of $E_S$ and $E_D$ will be dominated by that of $E_R$. The single low-temperature calibration measurement to obtain $E_R$ is performed with bulk copper as a perfect short.

## 4.3.3 Low-Temperature Calibration with three Additional Standards (as by Leiden Group)

The Brom group (Leiden University), interested in studying the dielectric properties of polymers and liquids, describes how they use three low-temperature standards [62] to perform a full low-temperature calibration: open (no sample), short (indium), and quartz. The calibration procedure assumes the actual reflection coefficients of the standards to be ideal, i.e. the values of the open and short have actual reflection coefficients $S_{11,a}^{open} = 1$ and $S_{11,a}^{short} = -1$, respectively, and for quartz a frequency-independent dielectric constant of 3.81 is assumed.

### 4.3.4 Low-Temperature Calibration with three Additional Standards (as by Virginia Group)

The Lee group (University of Virginia), aiming at measurements on insulating Si:B, also employs three standards [5, 63]: open (fused silica), short (bulk aluminium), and NiCr thin films. Here the actual values of the reflection spectra that enter the low-temperature calibration analysis are not the ideal values, but those measured at room temperature. The idea behind this scheme is that the calibration samples themselves are not perfect but can be assumed to be temperature independent. Since the room-temperature measurements can be performed to rather high precision (using commercial standards), they give high-quality spectra of the calibration samples including their imperfections.

## 4.4 Calibration at Cryogenic Temperatures: Procedure and Standards

In the present study up to three types of calibration standards were employed at low temperatures: short, open, and load. Whereas the short could be easily realized by pieces of bulk copper or aluminium, the open and load standards had to be chosen carefully. Finally small cylinders of teflon were used for the open and thin NiCr films on glass substrate were chosen for the load.

### 4.4.1 Low-Temperature Standard: Short

For the short a bulk piece of metal was used, either copper or aluminium, both materials with very high electrical conductivity. Our measurements could not resolve any systematic differences of these two materials but finally aluminium was preferred for low-temperature work. Furthermore no differences between polished and unpolished samples were found,[2] nor between samples with additional gold

---

[2]This is expected as long as the surface roughness does not affect the contact resistance and as long as it is much less than the wavelength. The second restriction will always hold for our experiment because of the considerably low frequencies.

contacts and such without (which is also expected for any mechanical contact of good metals). This on the one hand shows the limitations of the present setup, on the other hand it shows the validity of the calibration scheme as far as the short is concerned.

While it is little effort to produce a short standard from a sheet of aluminium, particular care has to be taken when it is actually used as a short and assembled on the sample holder and pressed against the Corbino probe. While for the load and in particular for the open standards the impedance is rather high and additional contributions due to contact resistance can usually be neglected, this is not the case for the short standard. I.e. an increased contact resistance of the short standard will directly affect the measured reflection coefficient and subsequently the complete error correction procedure. This will be the more important the lower the resistance of the samples to be studied is. Some of the measurements presented later deal with a sample resistance of less than 100 mΩ, i.e. contact resistance contributions of the order of a few mΩ (at the sample as well as short calibration measurements) will influence the data analysis considerably. Thus it has to be checked at room temperature whether the reflection coefficient of the short standard is affected by poor contact.

An additional way to perform the short calibration measurement arises if the sample to be studied at low temperatures becomes superconducting at even lower temperatures. In these cases the superconducting sample can act as a short calibration for measurements of the normal state of the same sample at slightly higher temperatures. Such a procedure assumes that the superconducting sample has an actual reflection coefficient $S_{11,a} = -1$. This is the case if the conductivity of the superconducting sample is much higher than that in the normal state for all frequencies of interest. While a superconductor by definition has zero resistance at zero frequency, for higher frequencies the conductivity decreases, at $T = 0$ it actually vanishes for frequencies below the energy gap. In many cases the detailed frequency dependence of the microwave conductivity of superconductors is unknown, and as a result it is not known *a priori* whether a superconducting

sample can act as a short standard for the complete frequency range of interest. Furthermore the temperature of the superconducting sample has to be chosen properly: if the temperature is too low, the microwave conductivity might be too low because the frequencies are below the gap energy, but if the temperature is too high, the sample might not be completely in the superconducting state.

In practice the procedure was as follows: only if the results of a calibration with aluminium or copper as a short and those of a calibration with the superconducting sample as a short coincide, then the superconducting calibration is considered to be valid. In this case the advantage of the superconducting calibration is that no mechanical replacement is required for the short measurement. Thus imperfections of the calibration procedure are considerably reduced, in particular concerning the phase measurement that determines the imaginary part of the measured sample impedance.

## 4.4.2   Low-Temperature Standard: Open

The easiest way to realize an open standard is to measure the probe without any sample attached. But this has the disadvantage that without a sample the center pin slightly protrudes from the probe, and the resulting effects on the microwave characteristics of the probe are hard to determine.[3] To keep the center pin at its desired position during the calibration measurement of the open standard, a piece of a solid insulator can be used as a standard. Starting with the proposal of Stutzman *et al.* [5], we have used pieces of fused silica. They have the major disadvantage that they can act as dielectric resonators. For reasonable sizes of the silica pieces their lowest resonant mode lies within our frequency range of interest, and at frequencies around the resonance of the open the calibration is completely spoiled. Best results were obtained with silica cylinders of 3 mm diameter and 2 mm height with only the lowest resonance frequency of approximately 17 GHz in our frequency range of interest of up to 20 GHz.

---

[3]Martens *et al.* [62] use air as an open standard, but their probe has a fixed center conductor, and therefore they do not have the problem of a protruding center pin.
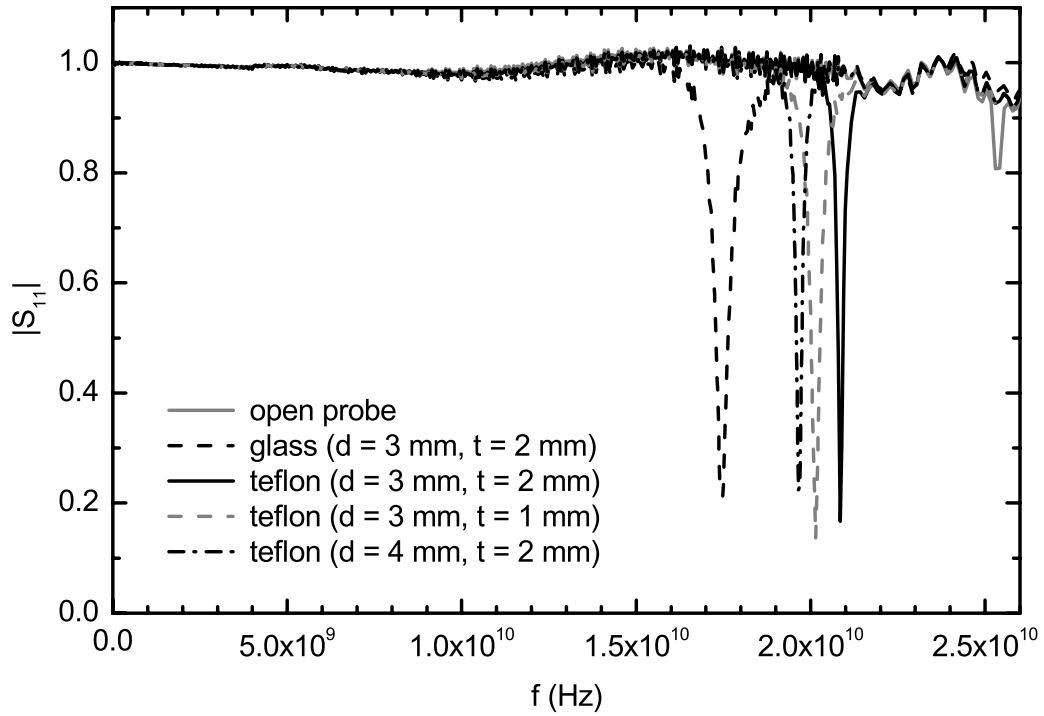
**Figure 4.3:** Amplitude of measured reflection coefficients (room temperature) of different open standards (d: diameter, t: thickness).
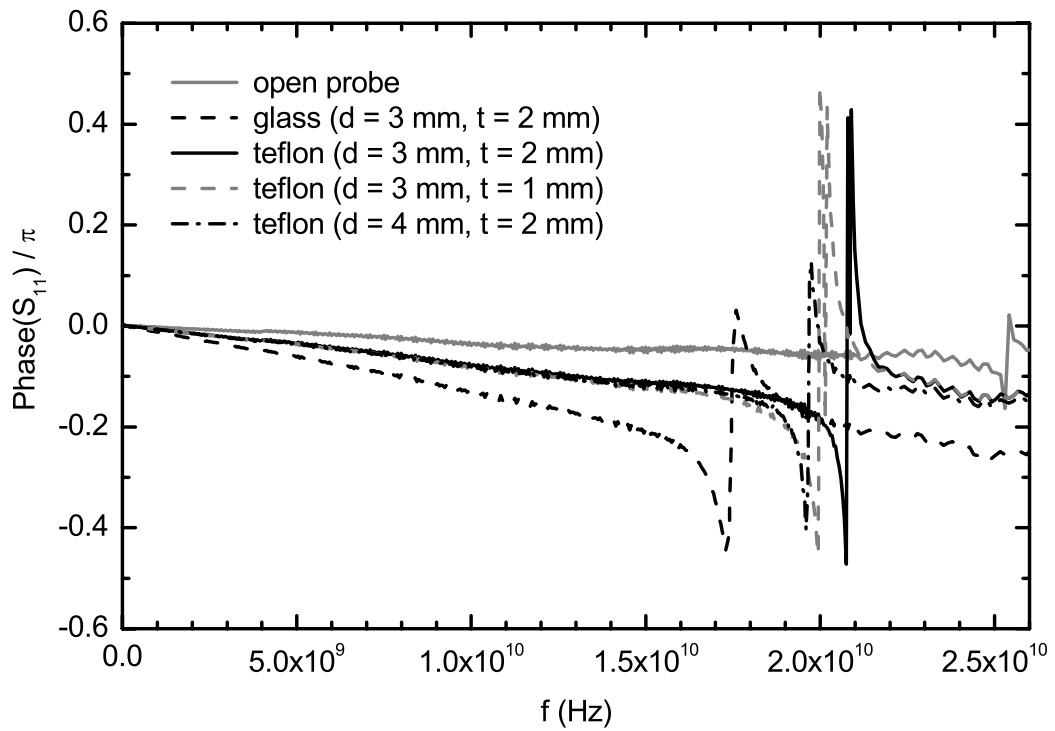


**Figure 4.4:** Phase of measured reflection coefficients (room temperature) of different open standards (d: diameter, t: thickness).

Since the resonance frequency of a dielectric resonator also depends on the dielectric constant of the resonator, an additional shift to higher resonance frequencies was possible by using teflon cylinders. Although the dielectric constant of teflon is almost a factor of two smaller than that of silica, the resonance frequency only shifts to approximately 21 GHz for a sample of the same dimensions. However, this frequency is slightly higher than our frequency range of interest and thus such a teflon sample was successfully used as an open. How the lowest resonance frequency of possible open standards depends on the material as well as the dimensions is shown in Figure 4.3. There the amplitude of the reflection coefficient at room temperature (using the commercial calibration) is shown. The amplitude is basically 1 for all frequencies except for close to the resonance.

The lower dielectric constant of teflon compared to fused silica has an additional advantage. The dielectric constant of the material used as an open determines the imaginary part of its reflection coefficient. For a perfect open (dielectric constant 1) with reflection coefficient $S_{11,a} = 1$, the imaginary part of $S_{11,a}$ is zero, but this is not the case for materials with higher dielectric constants, and the difference to the perfect open increases with the dielectric constant. This can be seen in Figure 4.4 where the phase of the reflection coefficient is plotted for different open standards. Therefore the teflon open standard is closer to the perfect standard than the silica one, and for measurements of conducting samples it is treated as a perfect open.[4]

The other way to avoid this problem is going back to the empty probe as an open (without any sample) as mentioned in the beginning of this section. This procedure was also tested and gave reflection coefficients at room temperature even closer to $1 + 0$ i than the teflon samples and the lowest resonance excited in the open copper cylinder is much higher (around 25 GHz), but for most of the measurements the teflon open was used because of its better defined geometry in particular at low temperatures: without sample the small center pin is not fixed

---

[4]If insulating samples are studied where the dielectric constant is of interest (and in the range of the dielectric constant of teflon), a correction has to be taken into account [62].

and might move when the probe is cooled to low temperatures or even fall out of the probe. Therefore the more reliable procedure with the teflon open was preferred. But tests without sample showed that this procedure also works and might be more appropriate if insulating samples are studied.

## 4.4.3 Low-Temperature Standard: Load

For the known load as third calibration standard we use NiCr thin films as proposed by Stutzman *et al.* [5]. If a metallic film is deposited on an insulating substrate with a film thickness much less than the skin depth for the frequencies of interest, then the sheet resistance of the film is just proportional to the resistivity of the metal and the inverse thickness of the film, in contrast to bulk samples where the sheet resistance is governed by the frequency-dependence of the skin depth. Since the conductivity of a normal metal at microwave frequencies can be considered frequency independent and real (the Hagen-Rubens limit), a metallic thin film can thus be employed as a broadband load with a frequency-independent, real impedance. The impedance can then be tuned by choice of the material as well as the film thickness. The reason why NiCr is used as the metal of choice for these thin films is its temperature dependence of the electrical resistance: NiCr, an alloy of 80% Ni and 20% Cr, is a well-established [90], commercially available material with almost temperature-independent electrical conductivity. Thus a NiCr film will keep its impedance down to cryogenic temperatures whereas the impedance of a normal metal will easily change by more than 80% when cooled to helium temperature. The NiCr films for this study were grown on sapphire or glass substrates by standard thermal evaporation [91] of commercial NiCr pellets [92]. The temperature dependence of the dc resistance of some of the films as measured with the Corbino spectrometer in two-contact geometry are shown in Figure 4.5. The change in dc resistance throughout our temperature range of interest is typically between 2 % and 4 % for the films used as microwave calibration standards.
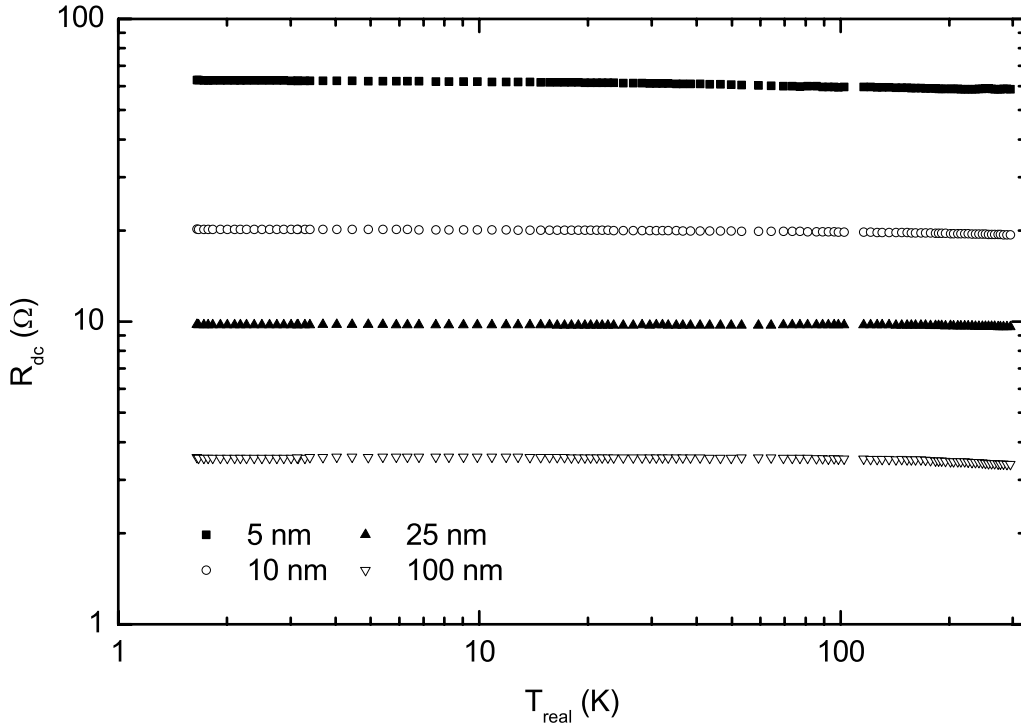
**Figure 4.5:** Temperature dependence of dc resistance of several NiCr films (with different nominal thicknesses) measured in Corbino geometry simultaneously with microwave spectra. Due to the two-point type measurement, the data includes the resistance of the coaxial transmission line as a slightly temperature-dependent offset of approximately 1.5 $\Omega$.

The thinnest NiCr films with reproducible sheet resistance have thicknesses around 10 nm (corresponding to an impedance of approximately 20 $\Omega$), a technological limit known from literature [93]. Thinner films probably do not cover the substrate completely, and thus their sheet resistance is extremely sensitive to the (mean) film thickness.

For a general calibration procedure the desired matched load should have an impedance of 50 $\Omega$ whereas the NiCr thin films we have used as load standards usually had impedances between 10 $\Omega$ and 20 $\Omega$. Besides being easier to produce than a 50 $\Omega$ NiCr thin film, these thicker NiCr films have an additional advantage: for a frequency-independent impedance the films have to be thinner than the skin depth.[5] This means that a considerable fraction of the microwave signal will

---

[5]At 10 GHz the skin depth of NiCr is approximately 5 $\mu$m.

penetrate the film and enter the substrate, and the reflected wave can pass the film again and contribute to the measured microwave signal. For most frequencies this will not affect the validity of the calibration scheme presented here, the exception being frequencies around a resonant mode of the (dielectric) substrate. Similar to the procedure used for the open standard, the influence of the substrate resonance was decreased by moving the lowest resonance to frequencies as high as possible by reducing the size of the substrate and using glass as a substrate instead of sapphire. But obviously the influence of any substrate resonances will also reduce if the film thickness is larger and thus a smaller fraction of the signal can penetrate it.

However, using thin films with an impedance other than 50 $\Omega$ causes a disadvantage concerning the data analysis: if the impedance of the load standard equals 50 $\Omega$, the extraction of the error coefficients is very easy because in this case the actual reflection coefficient of the load vanishes and its measured reflection coefficient directly gives the directivity $E_D$. With $E_D$ known, a much easier, linear system of equations has to be solved for only two variables $E_R$ and $E_S$. However, if the impedance of the load differs from 50 $\Omega$, the more complicated analysis has to be performed. One particular problem in this case is that the actual impedance (or the actual reflection coefficient respectively) of the load has to be known for the analysis. An independent way would be to determine the sheet resistance of the NiCr film as a function of temperature in a four-point measurement and then calculate impedance and reflection coefficient. But this would be rather arduous: the films differ from sample to sample and furthermore each film can reliably be measured at low temperatures only once in the Corbino spectrometer because the film is often heavily scratched afterwards. I.e. each microwave load calibration would require an additional four-point measurement. To avoid this workload, we have chosen a different step which again takes use of the simultaneous dc resistance measurement performed with the Corbino setup. An offset for the resistance of the coaxial line (around 1.5 $\Omega$) is subtracted from the measured dc resistance of the load film, and the obtained value is taken as

the true impedance of the film. The disadvantage of this technique is that the offset is poorly defined: it can change up to 0.1 $\Omega$ for different measurements and this difference will not be determined by our procedure. To at least minimize this error, the offset is taken as the measured dc resistance of the short standard that enters the calibration procedure. Thus at least the general temperature dependence of the offset is taken account of and furthermore long-term changes in the offset are also partially removed because the short measurement that enters the calibration was typically performed only a few days before or after the load measurement. One final advantage of this procedure is that it is clearly defined and can easily be included into the automated data-analysis software.

## 4.5 Calibration at Cryogenic Temperatures: Experiments

As described in the previous section, different procedures for cryogenic calibrations of Corbino spectrometers exist but were never compared in terms of measurements performed with the same spectrometer. Thus in the course of this project extensive tests with different methods were carried out. The problem with the evaluation of the calibration procedure is that it has to be based on actual test measurements (theoretical considerations can easily be spoiled by imperfections that cannot be avoided in actual measurements) which require that appropriate test samples are available. As such NiCr films were used (basically the same as described in Section 4.4.3), following the proposal by Stutzman *et al.* [5]. These tests will also establish the overall performance of the spectrometer and will be dealt with in detail in Section 5.3.1. Thus at this stage we assume that meaningful test measurements can be performed and this section only describes the results concerning the calibration procedure.

First of all it should be noted that the three different calibration standards work reliably at low temperatures and their low-temperature performance is basically the same as the room-temperature one.

## 4.5.1 Results of Low-Temperature Calibrations

Using three calibration standards (assuming their ideal reflection coefficients as the actual ones) at low temperatures as the most general procedure sets the guiding line for the validity of all calibration procedures. Main result of the low-temperature measurements is that a low-temperature calibration is unavoidable and that $E_R$ is strongly temperature dependent. The error coefficients $E_R$, $E_S$, and $E_D$ as determined from three calibration measurements using the formulae presented in Appendix A.3 are plotted as a function of temperature for the exemplary frequency of 10 GHz in Figures 4.6 and 4.7 (black lines) as determined from a low-temperature calibration using a bulk aluminium sample as short, a teflon cylinder as open, and a NiCr thin film as load.

As already seen in the room temperature calibration of Figure 4.2, the magnitude of $E_R$ is much larger than that of $E_D$ and $E_S$. It is also evident that $E_R$ depends on temperature. For the example shown it is more apparent in the imaginary part of $E_R$, but this is no general characteristic and can be completely the opposite for other frequencies.

The temperature dependence of $E_R$ reflects some of the characteristic events of the measurement procedure that were already mentioned in Section 3.3: at 5 K a sharp kink in $\text{Im}(E_R)$ matches the turning-off of the helium pump and a second kink at 14 K corresponds to the opening of the helium recovery line as soon as atmospheric pressure is reached inside of the cryostat. The strong temperature dependence of $E_R$ can easily be explained in terms of the changing electrical resistivity of the copper coaxial cable that governs most of the damping of the microwave signal. Turning off the helium pump not only changes the state of the helium bath but also induces a dramatic increase of the contact gas pressure leading to enhanced cooling of the insert including the coaxial cable. The strong change in $E_R$ above 40 K reflects the warming of the complete insert. (At lower temperatures the resistivity of a normal metal is basically temperature independent and the effects seen in $E_R$ at those lower temperatures are governed by that part of the coaxial cable that is at higher temperature.)
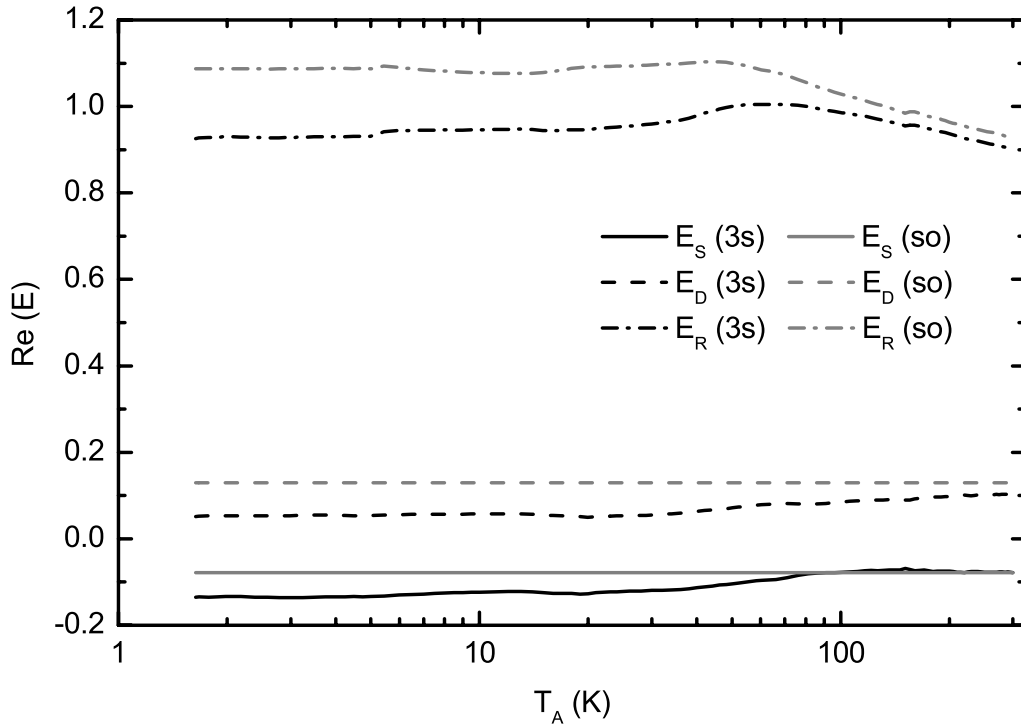
**Figure 4.6:** Temperature dependences of real part of error coefficients for 10 GHz, three-standards (3s) and short-only (so) calibrations.
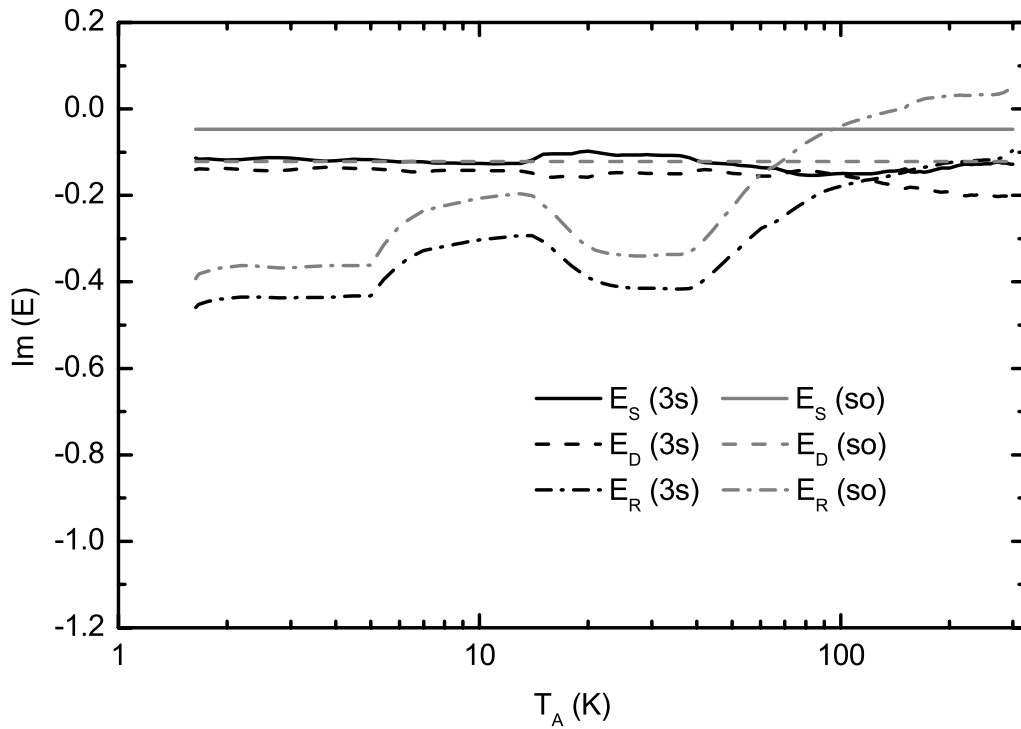


**Figure 4.7:** Temperature dependences of imaginary part of error coefficients for 10 GHz, three-standards (3s) and short-only (so) calibrations.

The strong temperature dependence of $E_R$ in particular temperature ranges confirms the need of good temperature control and in particular reproducibility that was already demanded in more general terms in Section 3.3.3. Since the overall precision of the microwave spectrometer crucially depends on the calibration procedure, any differences of the temperatures of the sample and calibration measurements directly affect the performance of the spectrometer. On the other hand for those temperature ranges where $E_R$ is basically constant, like below 5 K in the standardized procedure, the requirements are much weaker. This justifies the use of a superconducting sample as a short: as long as both the calibration measurement in the superconducting state and the probe measurement in the normal state are performed within a temperature range of constant $E_R$, the calibration procedure is valid and the temperature difference between the two measurements will not affect the quality of the calibration. Obviously, the valid temperature range for such a calibration can be extended by continued pumping on the helium bath above 5 K. This departure from the standardized measurement procedure is adequate if a short-only calibration using the superconducting state is performed.

Compared to $E_R$, the two other error coefficients $E_S$ and $E_D$ change very little with temperature, and since it is very hard to determine the uncertainty of the error coefficients in particular at higher temperatures (where the temperature distribution is not as strictly reproduced as at low temperatures), these temperature changes should not be considered significant. Thus $E_S$ and $E_D$ can be rated temperature independent.

$E_S$ and $E_D$ being temperature independent was a necessary assumption for the calibration procedure with just one calibration measurement ('short-only'). Now that this assumption is fulfilled, the short-only calibration can be compared with the three-standards calibration and thus the error coefficients from the short-only calibration (obtained via the formalism documented in Appendix A.4) are also shown in Figures 4.6 and 4.7 (gray lines). Here $E_S$ and $E_D$ are the room-temperature values and thus by definition temperature independent. It can be

seen that the temperature-dependent values of $E_S$ and $E_D$ (of the three-standard calibration) are close to the room-temperature ones, corroborating again the assumption of these error coefficients to be basically constant with temperature. The temperature dependence of $E_R$ as obtained by the short-only procedure resembles that of the three-standard one, all the strong features at low temperatures are reproduced.

Thus the temperature dependence of the error coefficients obtained by the three-standard and by the short-only calibration suggest that both are valid procedures to obtain the actual reflection coefficients from the measured ones.

## 4.5.2   Validity Range of Short-Only Calibration

Although the above measurements suggest that $E_S$ and $E_D$ do not depend on temperature, one cannot rule out completely that they are to a small extent. In the latter case the short-only procedure subsumes the temperature dependences of all three standards into the temperature dependence of $E_R$ alone. Then one might naively expect that this procedure fails if it is applied to reflection coefficients that differ strongly from the one of the calibration measurement, i.e. the short. To check for this, the consistency of the two procedures was tested with experimentally determined error coefficients (from the same data set as those presented in Figures 4.6 and 4.7). For a range of (real) impedances the reflection coefficients according to the three-standards calibration was calculated and from these reflection coefficients the impedance was recalculated using the short-only procedure. Exemplary data for different frequencies and temperatures is shown in Figure 4.8. Obviously the two procedures are consistent for small impedances, where the ratio becomes constant. However, already in this case the ratio can differ from unity, indicating an incorrect experimental determination of the error coefficients. The sources of these errors are hard to pinpoint: they can stem from the short measurement that enters both calibrations, as well as from the open or load measurements that enter the three-standard calibration, but also from the room temperature calibration that enters the short-only calibration. The result-
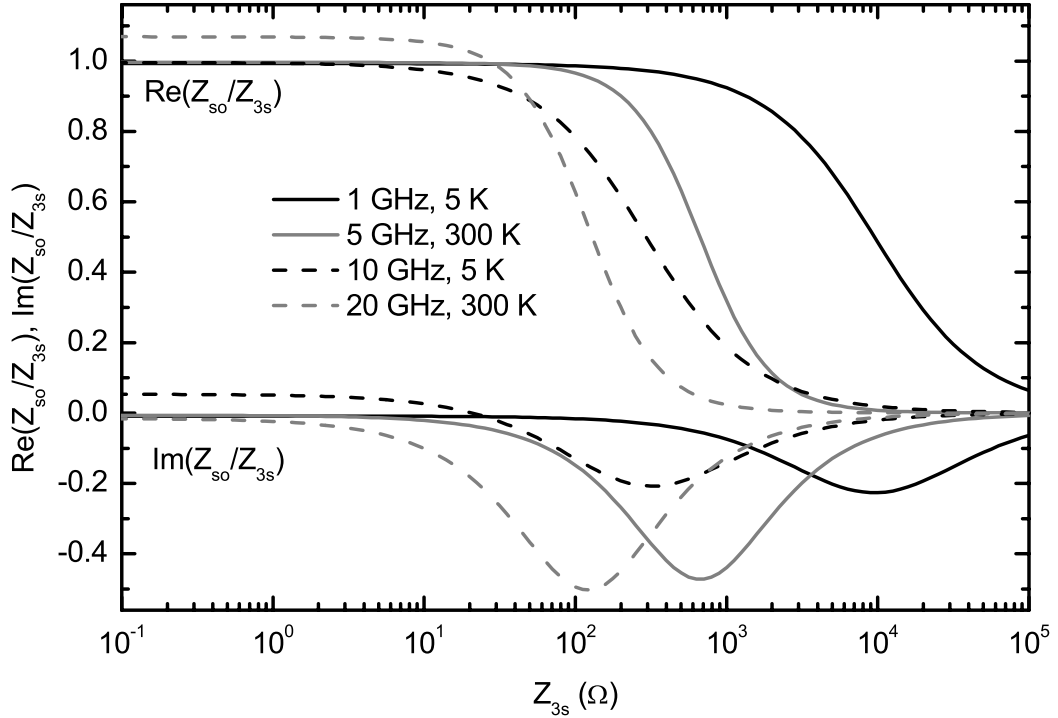
**Figure 4.8:** Consistency of short-only (so) and three-standards (3s) calibrations: ratio of the impedances when obtained by the two procedures (based on experimentally determined error coefficients).

ing error in impedance is of order 10%, giving a first estimate for the final error of the spectrometer when the calibration procedure is included.

For larger impedances the impedance ratio from the two calibrations deviates strongly from unity. Taking again 10% deviation of the magnitude of the impedance as the cutoff, impedances above 30 $\Omega$ should not be analyzed using the short-only procedure, at least for frequencies of 10 GHz or above. However, we are interested in the complex response, i.e. real and imaginary parts of the impedance, and thus the validity of the short-only calibration is considerably confined as can be seen from the imaginary part of the ratio plotted in Figure 4.8. Now the impedance to be studied should not extend 10 $\Omega$ (with the requirement that real and imaginary parts differ less than 10% of the magnitude from their 'real' values). But this estimate was only based on experimental data gathered with the current spectrometer and is governed by the errors that contribute during the calibration procedure. For a different, less reproducible spectrometer this

range might be reduced even further and the validity of the short-only calibration procedure has to be verified before it is applied.

Thus the short-only calibration is valid as long as highly conductive samples are studied, and in this case that procedure is more convenient because it only requires one additional low-temperature calibration measurement. For different studies focussing on lossy or insulating samples a modified procedure where $E_R$ at low temperatures is determined by measuring an appropriate low-temperature standard like a load or an open might apply, but this was not investigated in the current project.

### 4.5.3    Procedure of Virginia Group

As described in Section 4.3.4, the group of Mark Lee at the University of Virginia also measured three calibration standards but the actual reflection coefficients of these standards were not assumed to be ideal ones, but instead spectra measured at room temperature were used. This procedure was also tried for some of our data to compare this procedure with the other ones. A typical spectrum is plotted in Figure 4.9: there the low-temperature impedance spectrum of a $UPd_2Al_3$ thin film is shown as obtained from a normal three-standards calibration assuming the actual reflection coefficients of the standards to be ideal as well as from the Virginia-type calibration where the room-temperature spectra of the standards are used as the actual ones at low temperatures. While the spectrum with the normal calibration shows the behavior expected for a metal at low frequencies, i.e. the impedance is real and constant (the upturn in Re(Z) and the downturn of Im(Z) above a few GHz are peculiar behavior of this material and will be dealt with in detail in Chapters 6 and 7), the spectrum with the Virginia-type calibration shows additional features like a maximum in Re(Z) around 1 GHz, a strong downturn in Im(Z) above 1 GHz, and steps in Re(Z) and Im(Z) at 4 GHz. All these features stem directly from the room-temperature spectrum of the aluminium short which is also shown in Figure 4.9: Im(Z) of short and sample basically coincide, and the features in Re(Z) are the same. While the overall
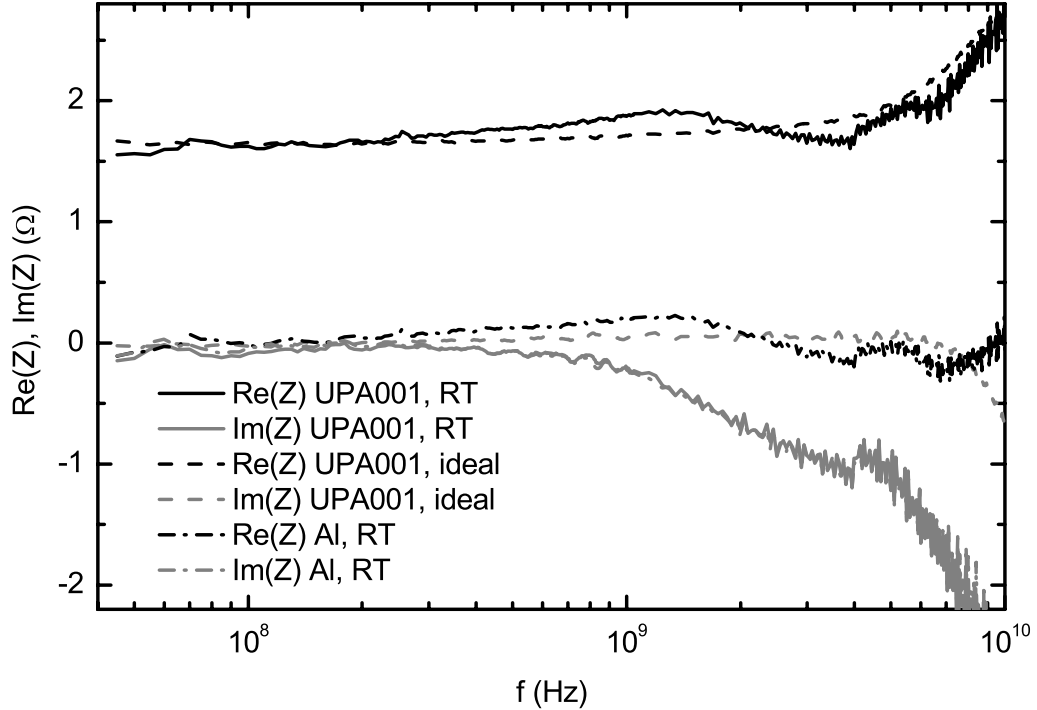
**Figure 4.9:** Impedance Z of a $UPd_2Al_3$ sample at 1.7 K calibrated assuming ideal spectra or measured room temperature (RT) ones. For comparison the room temperature spectrum of the aluminium short is shown.

deviations of the short spectrum from $Z = 0$ are due to the difference of the commercial calibration reference plane to the actual measurement (in particular the center pin instead of a normal center conductor of a microwave connector), the step at 4 GHz can directly be attributed to an imperfection of the room temperature calibration where the spectra of the load standards, broadband load and sliding load, are matched.

All these imperfections of the room-temperature measurements are transferred directly to the low-temperature spectra if the Virginia-type calibration procedure is performed whereas they are removed by the normal three-standard calibration assuming ideal spectra of the standards. Thus for our measurements the standard procedure is clearly superior to the Virginia one. This situation might change if an independent measurement of the room-temperature spectra of the standards is available that does not show the errors that occur in a Corbino measurement

as presented here. But right now there seems to be no such room-temperature spectrometer available and furthermore the other error sources present in our spectrometer are much larger than the imperfections of the calibration standards.

## 4.6 Comparison of Calibration Procedures

In the previous sections different calibration procedures were described and the results gained with our spectrometer were documented. It was found that the general three-standards calibration where ideal, frequency-independent actual spectra for the standards open, short, and load are assumed, gives an excellent general calibration procedure that should be the starting point for any data analysis. This procedure is in particular much better suited for our setup than the procedure where the actual spectra for the standards are obtained by room-temperature measurements (like was applied by the Virginia group). If the sample impedance to be studied is small over the complete frequency range of interest, then the three-standards calibration can be replaced by a short-only calibration. The latter one has the advantage that only one low-temperature calibration measurement has to be performed instead of three. Thus the time necessary for the calibration procedure is reduced considerably, and furthermore the number of possible error sources can be reduced provided that a commercial room-temperature calibration was performed extremely carefully and thus is of better quality than the low-temperature calibration measurements (which are harder to perform). In many cases this last point might not hold *a priori* because a commercial calibration requires partial disassembling of the probe and therefore was not performed regularly at least in the later period of the current project. However, for low-impedance samples the short-only calibration usually coincided with the three-standards calibration and thus the short-only calibration was often favored because of its convenience.

# Chapter 5

# Tests, Performance, and Data Analysis

The previous chapters described the basic properties of the Corbino spectrometer established at the 1. Physikalisches Institut and the calibration procedures that allow the extraction of the actual reflection coefficient of an unknown sample from the reflection coefficient measured by the network analyzer. In the following sections, more details related to actual measurements and the performance of the spectrometer will be discussed and in particular its resolution will be addressed.

## 5.1 Performing Low-Temperature Microwave Experiments

As could already be seen in Figure 3.3, the complete spectrometer is controlled by a computer that assembles the data gathered by the network analyzer, the multimeters, and the temperature controller and furthermore governs the different processes involved in the measurement, using purpose-written LabView software. This automated procedure is not only convenient for the operator of the spectrometer but is very important for the reproducibility of the low-temperature state of the spectrometer. A schedule of the different steps that constitute a low-temperature measurement is given in Appendix B.3. The standardized low-temperature cycle that was obeyed for most of the measurements presented in

this theses takes somewhat less than 24 hours and thus one low-temperature measurement can be performed per day.

## 5.2   Power Dependence

At the current stage the Corbino spectrometer is designed and used to measure the linear response of the sample under study, i.e. we are not interested in power-dependent (non-linear) effects. However, one always has to make sure that an obtained frequency-dependent response really is an effect of frequency and not an effect of a difference in the probe power at different frequencies. One way to do this is keeping the power constant over the complete frequency range of interest. At room temperature this can easily be done for our spectrometer since a commercial 'power flatness' procedure for the network analyzer exists that is based on a power measurement with an external power sensor (in contrast to the detectors that are part of the network analyzer) which can be attached directly to our probe (since it is a modified commercial microwave adapter). However, this procedure only works at room temperature: when the setup is cooled down, the damping of the coaxial cables is reduced considerably and this reduction strongly depends on frequency. Thus a constant power at the sample over the complete temperature range would require a different, frequency-dependent output power of the microwave source for each particular temperature. To avoid this large effort, a different approach was chosen. That is confirming the linearity of the response by dramatically changing the output power of the source and checking that the reflection coefficient does not change, i.e. basically performing a power-dependent measurement. Since this is only a check for consistency and not the main interest of our studies, this was not incorporated into the main measuring procedure. Instead a set of spectra differing up to a factor 1000 in output power was recorded only at one temperature, 4.2 K, previous to the standardized measurement procedure. Additionally, it is possible to perform two complete measurements with a different output power and compare them. For all of these procedures one has to keep in mind that also the commercial calibration of the

network analyzer can be power dependent and therefore might not be valid if the applied power does not match that of the calibration measurements. However, no power dependence was found for any of the measurements that will be presented in the following sections.

## 5.3   Tests: Thin Films

To demonstrate the functionality of our Corbino spectrometer and of the calibration procedure in particular, several test measurements were performed. The main problem with these test measurements is to obtain well-known samples that can be measured - the main motivation for the project was that there are almost no broadband measurements at all, and as a consequence there are few examples as references.

### 5.3.1   NiCr Films

Stutzman *et al.* [5] have used thin NiCr films to show the capability of their spectrometer at low temperatures, Figure 5.1 reproduces their main results: the real part of the impedance is basically constant for much of the frequency range (up to 12 GHz) and the imaginary part is proportional to the frequency. This was taken as evidence for the performance of the cryogenic spectrometer (because it resembles data taken at room temperature) whereas the additional, resonant features were attributed 'spurious remnants of the transmission line that were incompletely removed by the calibration procedure' [5]. Possible explanations for those high-frequency structures might also be substrate modes, and the strong linear frequency dependence of the imaginary part of the impedance might stem from the high dielectric constant of the substrate (sapphire).

To compare the performance of our spectrometer, similar measurements were performed. The NiCr films we used were grown in the same manner as those that we use as load calibration standards and that were described in Section 4.4.3. As a direct comparison to the data by Stutzman *et al.* serves a film of nominal thickness
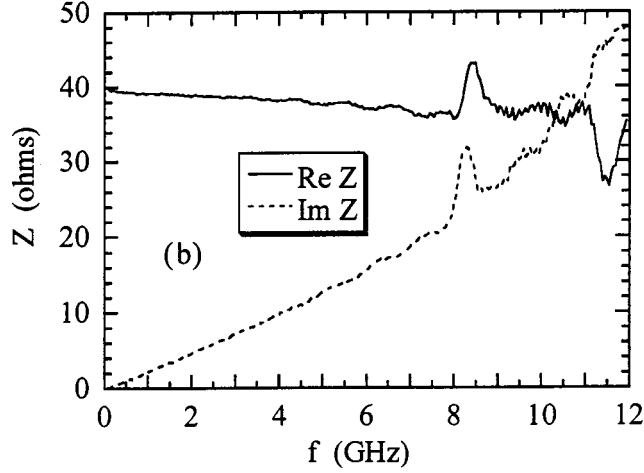
**Figure 5.1:** Frequency dependence of a NiCr film at 4.2 K as published by Stutzman *et al.* [5]

10 nm, corresponding to $\approx 28\ \Omega$ in our spectrometer, but due to differences in probe geometry corresponding to $40\ \Omega$ for Stutzman *et al.*[1] As can be seen in Figure 5.2, the obtained real part of the impedance of the 10 nm film is basically constant throughout the complete frequency range up to 20 GHz (the maximum change is 10%). Within the frequency range documented by Stutzman *et al.* (up to 12 GHz), our spectrum changes by 6% whereas they state a value of 9% 'not counting the resonant structures near 8.5 and 11 GHz'. Any such resonances are absent in our spectra up to 20 GHz due to the choice of the glass substrate instead of sapphire and the teflon open standard instead of fused silica. An additional advantage of our measurements might be due to the use of a thicker film for the load standard (approximately twice as thick) with consequently reduced substrate effects. Concerning the imaginary part of the impedance, our measurement shows a spectrum much closer to zero, as expected for a metal. This again might be attributed to the change in film substrate and the different film thicknesses.

For comparison the low-temperature impedance of a thicker NiCr film is also shown in Figure 5.2. Here the imaginary part of the impedance is even closer to

---

[1]The Virginia spectrometer employs SMA connectors. Although these connectors also have a characteristic impedance of 50 $\Omega$, the ratio of the diameters of outer and inner conductors is different due the use of a dielectric.
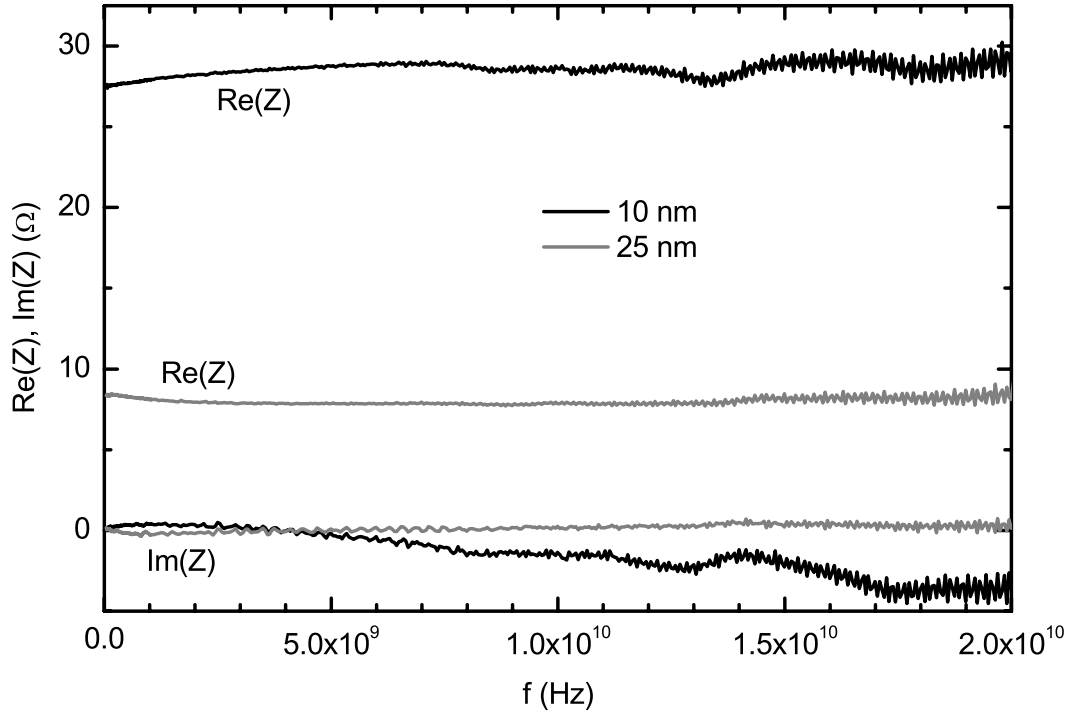
**Figure 5.2:** Real and imaginary parts of impedance of two NiCr thin films of nominal thicknesses 10 nm and 25 nm measured at 1.7 K.

the expected value of zero, probably due to the reduction of substrate influence by increased film thickness.

Comparing our data with that by Stutzman *et al.* shows that our spectrometer has reached and even surpassed their accuracy (about 50% better in the frequency range covered by their instrument) in a much larger frequency range (20 GHz instead of 12 GHz) and at lower temperatures (1.7 K instead of 4.2 K).

## 5.3.2 Aluminium Films

In addition to the tests with NiCr films we have studied aluminium films as an example of a standard metal. We have chosen aluminium for two reasons: firstly thin films can be grown easily and these films cover the substrate homogeneously already for thicknesses of about 8 nm [94] when grown at room temperature. This is important since we need very thin films to have the thickness smaller than the skin depth and the sheet resistivity high enough to be measured by our spectrometer. The second reason to choose aluminium is its superconductivity. Bulk alu-

93

minium has a transition temperature of 1.19 K [95] which cannot be reached with our current setup, but aluminium thin films show an enhanced transition temperature of up to 4.5 K for 5 nm thick films grown at low temperatures [96]. Our films of 8 nm or 10 nm thickness, grown at room temperature on sapphire, show a transition temperature of about 2 K, easily detectable by our spectrometer. The
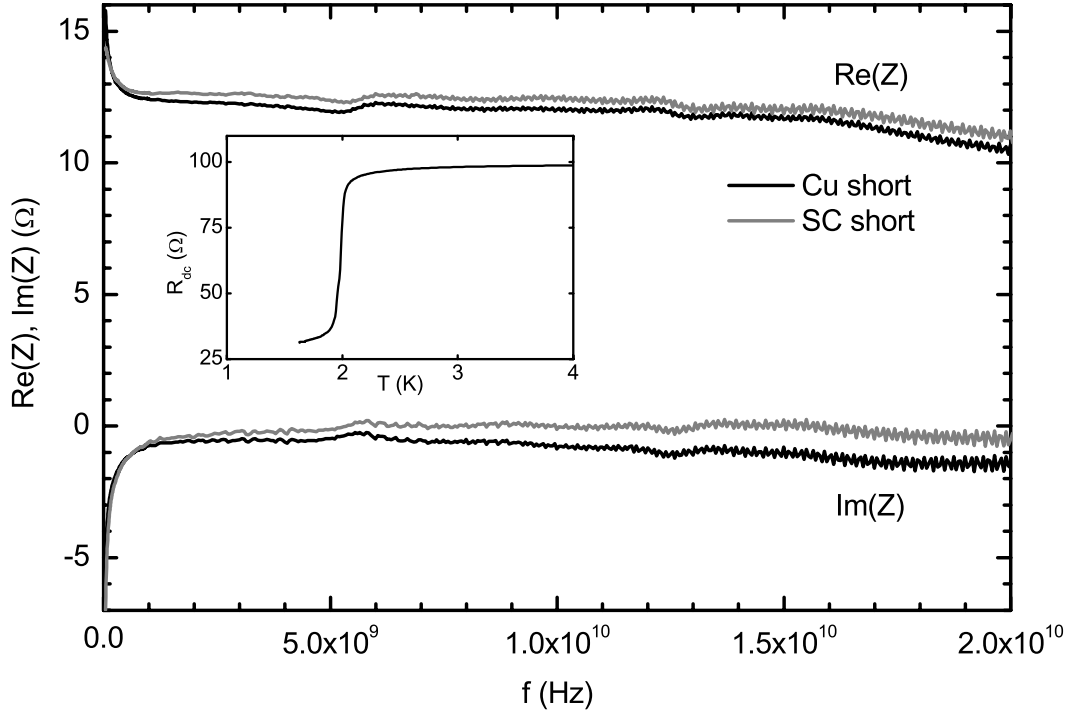


**Figure 5.3:** Real and imaginary parts of low-temperature impedance of a 8 nm thick aluminium film at 3 K calibrated either with bulk copper ('Cu') or the superconducting sample ('SC', at 1.7 K) as short. The inset shows the two-point dc resistance indicating the superconducting transition at 2.0 K.

temperature dependence of the two-point dc resistance of such a film, measured with the Corbino setup, is shown in the inset of Figure 5.3, clearly indicating the drop in resistance when the sample becomes superconducting. The absolute resistance values obtained from the dc measurements, in both the normal and superconducting states, indicate a strong additional resistive contribution compared to the microwave results. This is probably due to parallel capacitive and Ohmic components of the contact resistance, the capacitive contribution can also be seen in the low-frequency limit of the impedance spectra.

94

The main plot of Figure 5.3 shows that the impedance at 3 K is basically real and frequency independent above 1 GHz (i.e. above the capacitive contribution) as is expected for a metallic film thinner than the skin depth. The impedance data was obtained from the measured reflection coefficients using a calibration with three low-temperature standards: teflon as an open, a nichrome film as load (both at 3 K), and either bulk copper at 3 K or the aluminium film itself in the superconducting state at 1.7 K as short. The spectra stemming from the two different calibrations cannot be distinguished within the typical error of 10%. Thus this measurement shows the validity of using a superconducting sample as a short calibration for measurements on the same sample at slightly higher temperatures in the normal state.

In fact the imaginary part of the impedance obtained with the superconducting short is considerably closer to the expected value of zero which might indicate that the superconducting calibration is more accurate in terms of phase differences that govern the imaginary part of the obtained impedance.

## 5.4 Data Analysis: Obtaining the Conductivity

The test measurements showed that the Corbino spectrometer covers a broad frequency range down to 1.65 K. But the calibration procedure described in Chapter 4 only governs how to obtain the true reflection coefficient of the sample from the reflection coefficient measured by the network analyzer. When an unknown sample is measured, it still remains the task to obtain the material parameters of interest, e.g. the complex conductivity, from the true reflection coefficient.

As was already shown in Equation (3.1.1) and derived in Appendix A.1, the reflection coefficient and the (load) impedance $Z_L$ of the sample are related:

$$S_{11} = \frac{Z_L - Z_0}{Z_L + Z_0} \quad \Leftrightarrow \quad Z_L = Z_0 \frac{1 + S_{11}}{1 - S_{11}} \quad , \tag{5.1}$$

where $Z_0 = 50\ \Omega$ is the characteristic impedance of the coaxial cable.

Many measurements presented in this thesis (including those on the heavy-fermion compound $UPd_2Al_3$) were performed on thin films. Data analysis of the

reflection coefficient of thin films is particularly simple because they can typically be treated as samples with a skin depth much larger than the film thickness. In this case the electric and magnetic fields can be assumed uniform in the direction perpendicular to the sample surface, and the same can be assumed for the current densities within the sample. If substrate contributions can be neglected (typical substrates are low-loss dielectrics that usually do not affect the real part of the impedance but might influence the imaginary part), then the sample can be treated as an impedance that only depends on the desired conductivity $\sigma$, the thickness $d$ of the film, and the ratio $a_2/a_1$ of the outer and inner diameters of the Corbino disc:

$$Z = \frac{\ln(a_2/a_1)}{2\pi d\,\sigma} \qquad (5.2)$$

Thus the conductivity can be obtained easily from the corrected reflection coefficient, and this procedure was applied for all the measurements on thin films. However, the assumption that the film thickness is much thinner than the skin depth has to be checked for self-consistency on the finally obtained data.

Such analysis assumes that the reflection coefficient is governed by the sample under study and possible effects of the contacts can be neglected. Unfortunately this assumption did not hold for measurements on one particular $UPd_2Al_3$ sample on which most of the data presented in Chapter 7 was obtained. However, the contribution of the contacts can be modelled as documented in Appendix B.2.

If the sample is much thicker than the skin depth, as is usually the case for metallic bulk samples (e.g. the room temperature test measurement presented in Figure 3.4), then the reflection coefficient is governed by the surface impedance [1] and has to be analyzed appropriately, but no such data is presented in this thesis.

The actual analysis to obtain conductivity spectra out of data measured with the Corbino spectrometer is performed with another purpose-written LabView program that matches the one that controls the measurements. The different spectra of sample and calibration measurements are combined using the different calibration schemes (with the formulae documented in Appendix A), and the conductivity is obtained either within the thin film or bulk sample assumption.
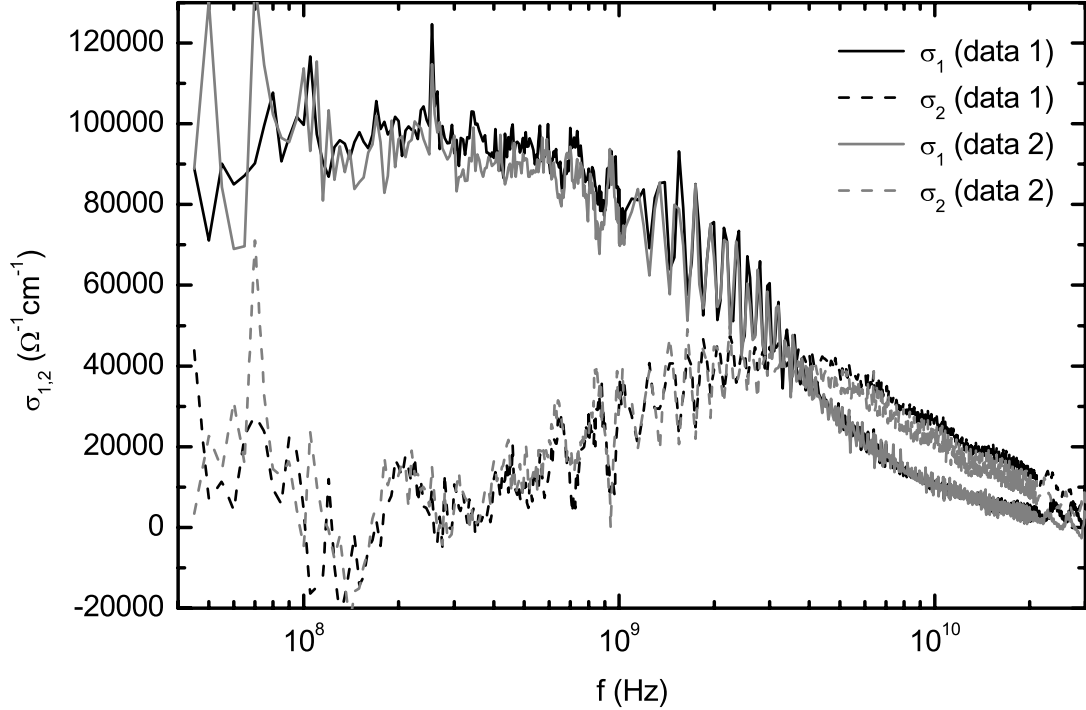
**Figure 5.4:** Two conductivity spectra taken on the same $UPd_2Al_3$ sample UPA233c at 2.3 K. The two data sets were taken three months apart and each calibrated with the superconducting spectrum at 1.7 K using the short-only calibration procedure.

## 5.5 Performance of Corbino Spectrometer

To finish the chapter on the details of the current Corbino spectrometer, its performance should be quantified. The temperature range was already discussed in Section 3.3.1: currently the spectrometer is routinely operated from 1.65 K to 300 K, and the frequency range covered is 45 MHz to 20 GHz. For special measurements where the superconducting state of the sample itself can be used to calibrate the normal state of the sample, frequencies up to 30 GHz or even higher might be meaningful, but have to be considered very carefully. Such measurements are presented in Figure 5.4. Here two different measurements taken three months apart on the same $UPd_2Al_3$ sample are shown. The coincidence thus shows the enormous reproducibility of the microwave spectra in particular for this case, when the calibration of these data taken at 2.3 K was performed using the short-only procedure with the superconducting sample at 1.7 K as short

(that was measured 33 and 36 minutes earlier, respectively). The strong oscillations between 1 GHz and 4 GHz are probably due to changes in standing wave patterns between the two temperatures of 1.7 K and 2.3 K or due to errors in the room-temperature calibration. But even this 'artefact' is reproduced completely, documenting the high reproducibility of the environmental details concerning the coaxial transmission line during different measurements.

However, the overall 'noise' of these measurements seems to be rather large but this is a result of the extremely low impedance of this sample which directly affects the sensitivity.

## 5.5.1 Sensitivity

The final sensitivity of a microwave Corbino spectrometer can hardly be estimated before actual test measurements are performed, and thus the following comments are drawn from the experience gained by the numerous measurements performed with the spectrometer, focussing on highly conductive samples.

In the fortunate case when the superconducting sample acts as the calibration standard, the reflection coefficient resulting from the calibration scheme reaches an error of as low as 0.0005 (in the real as well as the imaginary part), and 0.001 should be considered a value that can be achieved for standard measurements. For a highly conductive sample with an impedance of 0.1 $\Omega$ (like the UPA233c sample of Figure 5.4), the error in reflection coefficient leads to an error of 0.025 $\Omega$ in the sample impedance (applying standard error propagation theory and assuming that the measured reflection coefficient is solely determined by the sample). This value is small compared to the resistance scale of 50 $\Omega$ as the characteristic impedance of the coaxial cable, but of course the relative error is 25%. Such an error might sound large but has to be compared to other techniques: for absolute conductivity values obtained with optical spectrometers in the far-infrared or submillimeter frequency ranges, errors of 20% are not uncommon, and even for the measurements in the GHz range with resonant cavities, highly regarded for their extraordinary sensitivity, the finally obtained absolute conductivity values

have error bars of typically 10% to 20% because of the problems to account for the sample shape. Therefore our spectrometer can compete with the well-established techniques, and for samples with a higher impedance the relative error can even drop considerably. The error in the impedance as obtained from the reflection
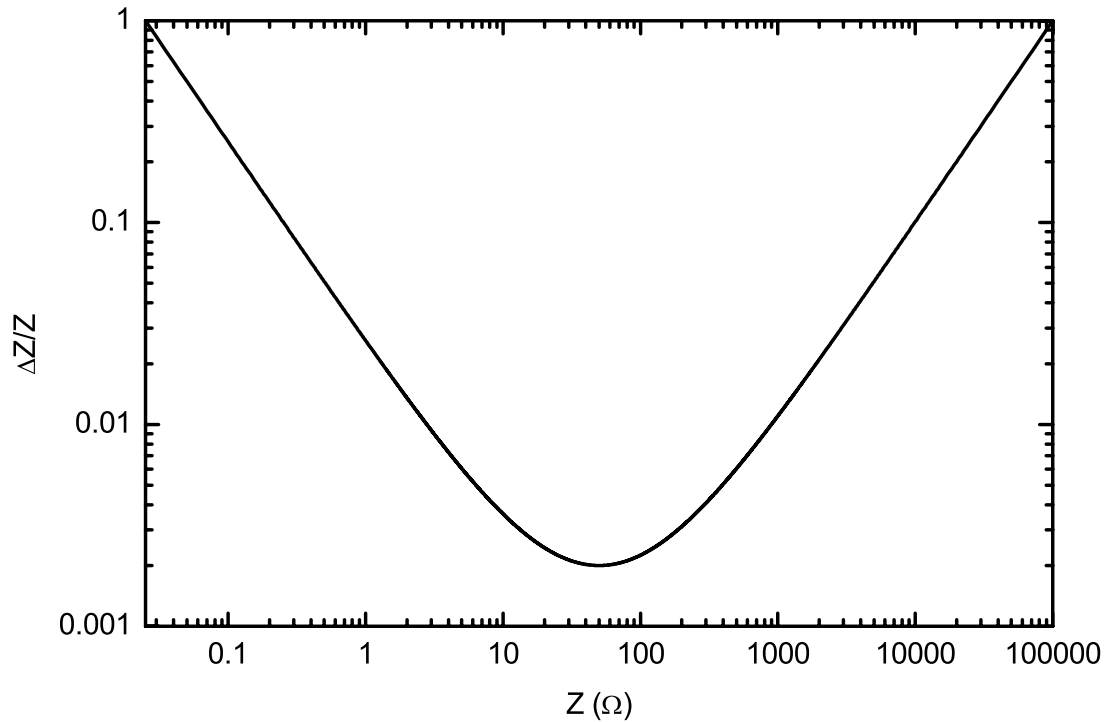


**Figure 5.5:** Calculated relative error of obtained sample impedance (and correspondingly of conductivity), assuming an error in the measured reflection coefficient of 0.001 as the only error source and a real sample impedance.

coefficient is shown in Figure 5.5 as a function of sample impedance. There one finds a characteristic symmetry (on this logarithmic plot) with respect to an impedance of 50 $\Omega$ corresponding to the characteristic impedance of the coaxial transmission line. Also one can see how the relative error decreases dramatically as the sample impedance approaches the matching value of the transmission line. Therefore any measurement with a Corbino spectrometer should be performed with a sample impedance as close to 50 $\Omega$ as possible, but unfortunately this is usually impossible for bulk metallic samples. Therefore metallic thin films with their possibility to tune the impedance by choice of the film thickness are

the perfect samples for this Corbino spectrometer as soon as the impedance can be tuned to the order of 1 $\Omega$. For even larger sample impedances, like for less conducting or even insulating materials, a wide range of measurable impedances can be found up to sample impedances of several k$\Omega$.

But the figure also shows clearly that a sample impedance of 0.1 $\Omega$, as is the case for measurements like in Figure 5.4 and in Chapter 7, is at the edge of what can be reasonably measured with this spectrometer.

## 5.5.2 Overall Error Estimation

The sensitivity presented in the previous section only discussed how the sensitivity of the spectrometer depends on the impedance that is measured by the spectrometer. However, we are finally interested in the conductivity of the sample and this involves additional uncertainties, in particular those due to the crucial calibration procedure, which were not explicitly included. But these uncertainties are hard to calculate because they are not dominated by a single cause but depend on the interplay of the complete spectrometer during the measurements (e.g. on how well all settings of the cryogenics are reproduced). Systematic errors can arise if the calibration standards measured for the low-temperature calibration are not ideal, in particular if the contact resistance of the short is too high or if the load samples are not perfect and have some frequency dependence of the impedance. These errors are not only hard to quantify in general, they are already hard to pinpoint in a particular measurement and can usually only be attributed if not only the sample of interest is measured, but additional test measurements with known samples (e.g. NiCr films) are performed using the same calibration data.

Thus the only practical way to estimate an overall uncertainty of the Corbino spectrometer is to judge from experimentally obtained data. In Section 4.5.2 it was shown that the three-standards and short-only might differ up to 10% in the finally determined impedance (and thus in the conductivity). This already sets a limitation for the uncertainty of the absolute values that can be obtained.

However, usually we are interested in the frequency dependence of the conductivity and there we can judge from the test measurements, in particular those on NiCr presented in Section 5.3.1. Here the measured impedance as a function of frequency (considering our complete frequency range up to 20 GHz) changed by 10%, again indicating an error of this size. But this error is not independent of that found in Section 4.5.2: there the 10% estimate was obtained from the difference of the impedances obtained by the two procedures, but the data in Figure 4.8 also shows that this difference changes as a function of frequency by the same margin. Thus the error found there will directly enter the final impedance spectra and that is what was found. The fact that here the experimentally determined error is not larger shows that there are no strong additional error sources.

Thus an overall estimation of the experimental error of the low-temperature spectra obtained with the Corbino spectrometer is 10% unless the impedance of the sample is in a range where the relative sensitivity of the spectrometer is reduced below that value as described in Section 5.5.1.

## 5.6 Future Improvements of Corbino Spectrometer

The Corbino spectrometer as presented in this thesis covers a frequency range from 45 MHz to 20 GHz and temperatures from 1.65 K up to room temperatures, and for these temperatures and frequencies the current instrument is without parallel among the only few other comparable instruments documented in literature. However, while our spectrometer now enables us to perform high-quality broadband microwave measurements at cryogenic temperatures, additional steps are possible to enable an even larger variety of measurements.

### 5.6.1 Frequency Range

The frequency range of our instrument is limited to lower frequencies by our microwave source and to higher frequencies by imperfections of the microwave

setup (in particular cables and connectors) leading to reduced reproducibility with a breakdown of the calibration procedure. Right now there seems to be no way to handle these imperfections, and thus the frequency range will not be extended to higher frequencies in the near future. However, if other microwave cables and connectors become available, this might change. For example the Corbino adapter itself was tested successfully up to 25 GHz at room temperature. Extending the frequency range to lower frequencies could be done by using a network analyzer for lower frequencies, and such network analyzers are commercially available. However, for measurements in the low MHz range and below, other experimental techniques are established (see Section 2.2), and with them it is possible to avoid the problems of contact resistances that cannot be ruled out in a Corbino setup. Thus the frequency range of our instrument will probably remain the same for near future Corbino setups.

## 5.6.2 Temperature Range

Our spectrometer was routinely operated from 1.65 K to 300 K. Many interesting solid state phenomena occur at low temperatures (which was the initial reason to build a cryogenic microwave spectrometer), and therefore measurements at even lower temperatures are desirable. It is expected that the current spectrometer can be modified with reasonable effort to work at temperatures down to 1.2 K or even slightly lower. Basis for this expectation is that the current setup was not optimized for lowest temperatures, and therefore several improvements are possible. The most stringent restriction considering lower temperatures is due to the coaxial cables that are used. For the measurements presented in this thesis, solid copper coaxial cables were used to minimize microwave losses. Test measurements with stainless steel coaxial cables led to temperatures lower than 1.2 K, and reproducible microwave measurements at these temperatures should be possible with reasonable effort.

However, even lower temperatures are necessary if effects exhibiting the quantum nature of electronic systems are to be studied. There one is often interested

in optical experiments with photon energies $\hbar\omega$ much larger than the thermal energy $k_B T$. As a temperature of 1 K corresponds to a frequency of 30 GHz, our current setup never reaches this quantum limit, considerably lower temperatures are needed.

Temperatures below 1 K cannot be reached with a $^4$He cryostat as is used for the current spectrometer. $^3$He cryostats have base temperatures around 0.3 K, even lower temperatures (below 100 mK) can be reached with $^3$He/$^4$He dilution refrigerators. There have already been several cases where microwave coaxial cables were fed into dilution refrigerators [34, 42, 43], but there the restrictions concerning the nature of the coaxial cable are extremely high. Thus for our approach with the aim to accurately measure absolute conductivity (and not relative ones e.g. as a function of magnetic field), the next step will naturally be a $^3$He cryostat.

In the design stage for such a project, one has to consider carefully whether one wants to continue with the 'keeping all microwave connections untouched'-approach that worked so successfully within the current $^4$He cryostat. If one does, then the easiest way is to replace the insert of the current setup by a so-called vacuum-loading $^3$He refrigerator, and as a result the procedure in terms of the microwave calibration etc. would not change considerably. However, such an insert would be rather short for a $^3$He cryostat, and thus the base temperature might be enhanced. A longer insert cannot be incorporated into the present setup, and therefore not disconnecting the insert would require an even more spacious apparatus than the present one.

The other option is to actually disconnect the microwave transmission line when samples are replaced. This means that the reliable calibration procedure presented in this thesis cannot be applied any more. But this problem might be circumvented by help of the present spectrometer. As can be seen in Figures 4.6 and 4.7, the error coefficients are basically temperature independent at low temperature (there up to 5 K, when the pumping on the helium path was stopped). If a sample was already studied in the current spectrometer, then

the low-temperature data could be used to effectively calibrate a $^3$He cryostat at the same temperature (using a one-standard-only procedure like mentioned in Appendix A.4 as the generalization of the short-only procedure), and if the microwave properties of the $^3$He setup do not change below that temperature, then the sample can be studied at lower temperature (provided the impedance of the sample does not change as much with temperature as might let the one-standard-only calibration fail).

### 5.6.3  Magnetic Field

There are several scientific questions where cryogenic microwave measurements in a magnetic field are desirable, in particular experiments studying magnetic resonance phenomena (like the ferromagnetic resonance and antiresonance studies on CMR manganites in the Maryland group performed with a Corbino spectrometer at much higher temperatures [47–49]). In the current Corbino spectrometer no magnetic field can be applied, but the design of the spectrometer was such as to allow a future addition: the glass cryostat has a diameter much larger than that of the stainless steel cylinder, and here a solenoid can be located. Since it will be in the liquid helium bath, it will be at low temperatures, allowing large currents in a conventional metallic coil or even a superconducting coil.

### 5.6.4  Other Probe Geometries

Our spectrometer uses the Corbino geometry. However, broadband microwave experiments could be performed in other geometries (see Chapter 2), e.g. using microstrips. Such measurements will suffer the same problems concerning reproducibility as the Corbino setup and will require the same efforts such as not disconnecting the microwave line. Therefore the general setup of such a spectrometer will be the same as the one of the Corbino spectrometer, only the probe itself will be different. However, the design of the current spectrometer was made with the possibility of a switch to another probe geometry in mind and such a switch will be possible with replacing the probe head as the only necessary hard-

ware modification. (Keep in mind that a microstrip measurement will preferably be performed in transmission, meaning two coaxial lines are necessary, but these are implemented already now.)

# Chapter 6

# Optical Properties of Normal Metals and Heavy Fermions

Heavy-fermion systems have been a focus of solid-state research for more than two decades, but this class of materials still puzzles physicists in many regards. One of these open questions concerns their optical properties at comparably low frequencies (in the GHz range) [97]. To address this particular problem was the main aim from the beginning of the current project.

The description of the optical properties of heavy-fermion materials is generally based upon the Drude model that is starting point for any analysis of the optical properties of a (normal) metal. Therefore the Drude model will be described first in its general form and then its application to heavy-fermion compounds will be described.

## 6.1   Drude Model of Normal Metals

The Drude model of metals was introduced by Paul Drude in 1900 [103] and has become the established theory to describe general electrodynamic properties of metals [104] and in particular their optical conductivity [1]. This is somewhat surprising since the Drude model is based on classical physics whereas the description of solid state physics in general and the behavior of electrons in solids in particular requires quantum mechanics which were introduced only a few decades

after the Drude model. However, main results of the Drude model hold even when basic quantum mechanical effects are considered.

## 6.1.1 Basic Properties of the Drude Model

In his model of the properties of charge carriers in metals, Paul Drude applied ideas of the previously established theory of gases to the conduction mechanisms in solids. He assumed that the electric conduction in solids is performed by charged carriers, nowadays considered to be the conduction electrons. These electrons move freely in a positively charged background (that results in charge neutrality when combined with the electrons) except for scattering events with the background that take place on average after a relaxation time $\tau$ for each electron. After such a collision, the electron is assumed to move in a random direction with a speed related to the local temperature, i.e. how an electron moves before a collision does not affect its movement after the collision.

## 6.1.2 Direct Current Conductivity

Starting from these very general assumptions, the dc conductivity of a metal can be calculated: if an electric field E is applied, then this field will accelerate each electron between subsequent scattering events. At a given moment each electron contributing to the overall current is on average accelerated for a time period $\tau$, resulting in a velocity $\mathbf{v} = -e\mathbf{E}\tau/m$ where $e$ is the charge of the electron and $m$ its effective mass. Thus the current density caused by the applied electric field is $\mathbf{j} = -ne\mathbf{v} = ne^2\mathbf{E}\tau/m$ where $n$ is the concentration of charge carriers. Assuming a linear relationship of field and current density according to Ohm's law

$$\mathbf{j} = \sigma\mathbf{E} \quad , \tag{6.1}$$

one obtains the following result for the dc conductivity $\sigma_0$:

$$\sigma_0 = \frac{ne^2\tau}{m} \quad . \tag{6.2}$$

## 6.1.3 Frequency-Dependent Conductivity

The Drude model can also be employed to obtain the frequency-dependent conductivity. First we introduce an equation of motion that actually is behind the previously described dc conductivity as well, as the term 'relaxation time' already suggests. Let us assume that in the absence of any external field the momentum $p$ of an electron relaxes according to

$$\frac{d\mathbf{p}}{dt} = -\frac{\mathbf{p}}{\tau} \quad . \tag{6.3}$$

I.e. the momentum will relax exponentially, and the time constant is the relaxation time $\tau$. Now an external electrical field $\mathbf{E}$ is introduced that modifies the equation of motion:

$$\frac{d\mathbf{p}}{dt} = -\frac{\mathbf{p}}{\tau} - e\mathbf{E} \quad . \tag{6.4}$$

To describe the motion at finite frequencies, we assume a time dependent external electric field $\mathbf{E}(t)$:

$$\mathbf{E}(t) = \mathbf{E}(\omega)e^{-i\omega t} \quad . \tag{6.5}$$

Later we focus on the frequency-dependent response, and therefore the amplitude $E(\omega)$ of the oscillating electric field is already denoted as a possibly frequency-dependent quantity at this point. Since we are interested in the linear response of the electrons only, we seek for a solution of the form

$$\mathbf{p}(t) = \mathbf{p}(\omega)e^{-i\omega t} \quad . \tag{6.6}$$

Using these forms for $\mathbf{p}$ and $\mathbf{E}$, we obtain from Equation (6.4):

$$-i\omega\mathbf{p}(\omega)e^{-i\omega t} = -\frac{1}{\tau}\mathbf{p}(\omega)e^{-i\omega t} - e\mathbf{E}(\omega)e^{-i\omega t} \tag{6.7}$$

$$\Leftrightarrow \left(\frac{1}{\tau} - i\omega\right)\mathbf{p}(\omega) = -e\mathbf{E}(\omega) \quad . \tag{6.8}$$

Applying $\mathbf{v} = \mathbf{p}/m$, $\mathbf{j} = -ne\mathbf{v}$, and the frequency-dependent version of Equation (6.1):

$$\mathbf{j}(\omega) = \sigma(\omega)\mathbf{E}(\omega) \quad , \tag{6.9}$$

109

one obtains the frequency-dependent conductivity:

$$-ne\mathbf{v}(\omega) = -ne\mathbf{p}(\omega)/m = ne^2\mathbf{E}(\omega)/\left(\frac{1}{\tau} - i\omega\right) = \sigma(\omega)\mathbf{E}(\omega) \qquad (6.10)$$

$$\Rightarrow \sigma(\omega) = \frac{ne^2\tau}{m}\frac{1}{1 - i\omega\tau} = \sigma_0\frac{1}{1 - i\omega\tau} \quad . \qquad (6.11)$$

Defining a new parameter, the so-called plasma frequency

$$\omega_p = \sqrt{\frac{4\pi ne^2}{m}} \qquad (6.12)$$

the conductivity of Equation (6.11) can be written as:

$$\sigma(\omega) = \frac{\omega_p^2}{4\pi}\frac{\tau}{1 - i\omega\tau} = \frac{\omega_p^2}{4\pi}\frac{1}{\frac{1}{\tau} - i\omega} \quad . \qquad (6.13)$$

Like any frequency-dependent material parameter, the conductivity $\sigma(\omega)$ is a complex quantity $\sigma(\omega) = \sigma_1(\omega) + i\sigma_2(\omega)$. Its real and imaginary parts $\sigma_1(\omega)$ and $\sigma_2(\omega)$ are:

$$\sigma_1(\omega) = \sigma_0\frac{1}{1 + \omega^2\tau^2} \quad \text{and} \quad \sigma_2(\omega) = \sigma_0\frac{\omega\tau}{1 + \omega^2\tau^2} \quad . \qquad (6.14)$$

The frequency dependences of the real and imaginary parts of the conductivity are shown in Figure 6.1 for a good metal like gold. The characteristic features are: well below the scattering rate $\Gamma = 1/\tau$ ,[1] the real part $\sigma_1$ of the conductivity is basically frequency independent and equal to the dc conductivity. At the scattering rate the real part $\sigma_1$ drops considerably and approaches zero for higher frequencies. The imaginary part $\sigma_2$ on the other hand is small for the complete frequency range except for the frequencies around the scattering rate where $\sigma_2$ has a peak. The limiting behavior for frequencies much smaller or larger than the scattering rate can be seen from the formulae as well as from the log-log plot in the lower panel of Figure 6.1: for small frequencies $\sigma_1$ is constant whereas $\sigma_2$ rises linearly, above the scattering rate $\sigma_1$ decreases quadratically and $\sigma_2$ linearly with increasing frequency.

---

[1]Keep in mind that the scattering rate is given in terms of $\omega = 2\pi f$, whereas all plots show spectra as a function of the experimentally employed frequency $f$.
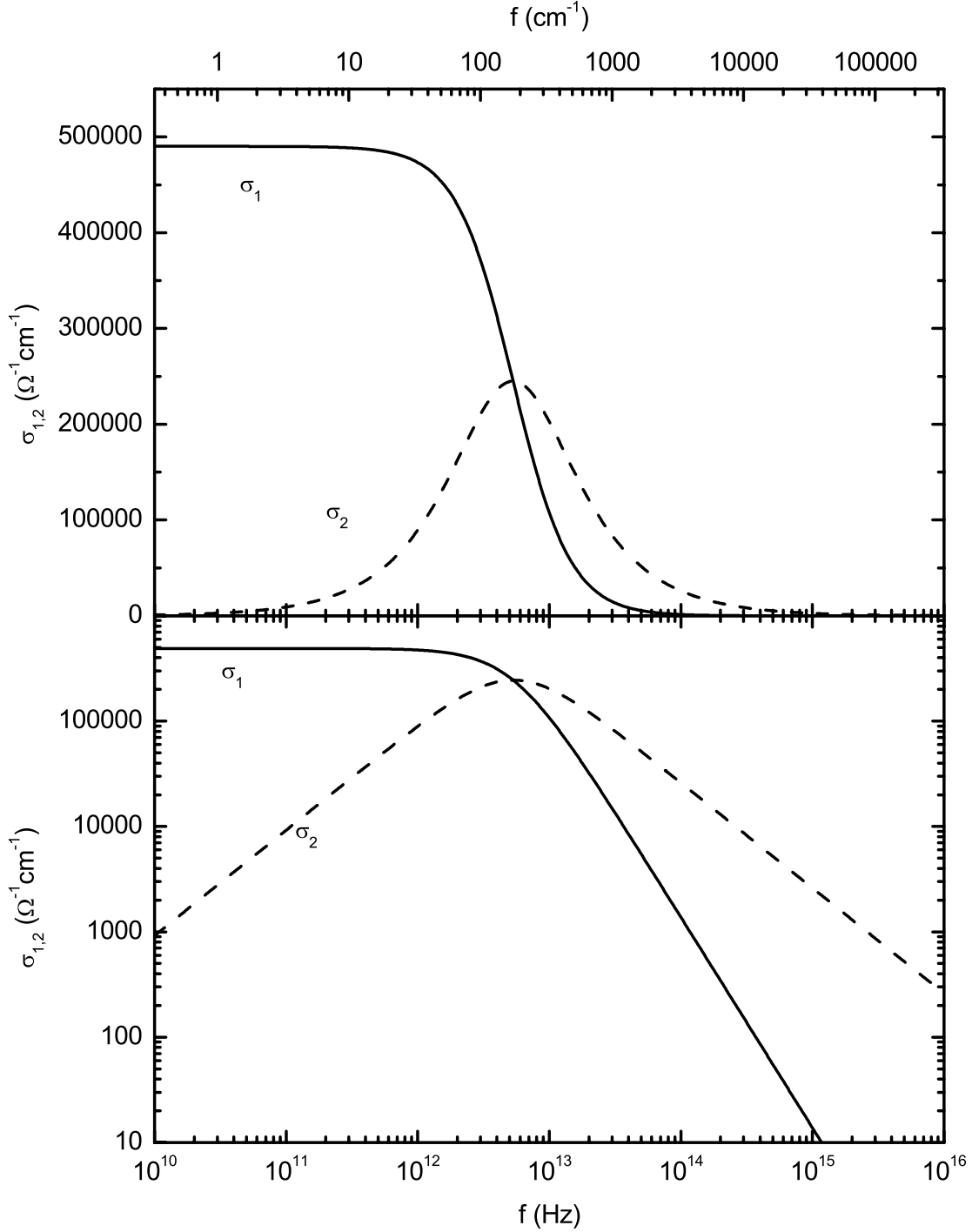
**Figure 6.1:** Frequency dependence of the complex conductivity for a Drude metal with parameters $\sigma_0 = 1/\rho_0 = (2.04 \cdot 10^{-6}\,\Omega\text{cm})^{-1}$ and $\tau = 3.0 \cdot 10^{-14}\,\text{s}$ like gold at 273 K [104]. The characteristic decrease in $\sigma_1$ and the maximum in $\sigma_2$ occur at the frequency corresponding to the scattering rate.

## 6.1.4   Measuring the Drude Response

Studies of the high-frequency response of metals are usually performed by measuring the frequency-dependent reflectivity with infrared spectrometers because transmission measurements on bulk metals cannot be performed as their transmittivity cannot be resolved. The reflectivity spectrum of a metal calculated according to the Drude model is shown in Figure 6.2 and from this plot it can already be seen, why for a standard metal the Drude behavior cannot be observed directly with conventional techniques: the reflectivity at low frequencies is very
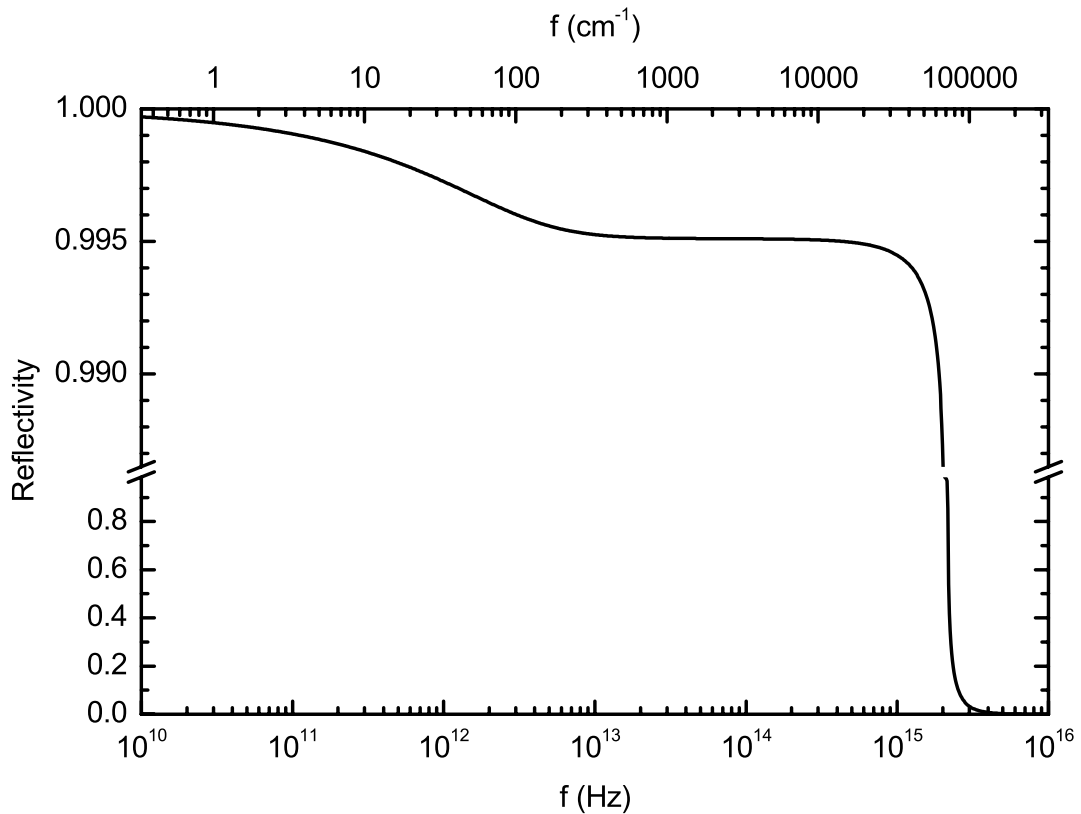


**Figure 6.2:** Frequency dependence of the reflectivity of a Drude metal (same parameters as in Figure 6.1). The sharp drop occurs at the plasma frequency whereas at the scattering rate only a weak feature shows up.

high, more than 99%, which is basically impossible to distinguish from a perfect reflection coefficient of 100% by conventional infrared spectrometers with a typical accuracy of 1%. The strong decrease in the reflectivity at higher frequency

at the so-called plasma frequency on the other hand is a typical feature that is observed by optical spectroscopy on metals, but this feature does not directly reflect the scattering rate $\Gamma = 1/\tau$ that is the core frequency scale of the Drude model. At the scattering rate there is only a weak structure in the reflectivity of order 0.1%, impossible to resolve with conventional spectrometers.

Measuring the reflectivity of a normal metal at frequencies corresponding to the scattering rate is further hampered by approaching the low-frequency limit of conventional far-infrared spectrometers, where it is has to be kept in mind that in conventional spectroscopy measuring the reflectivity (as a real quantity without phase information), one has to employ a Kramers-Kronig transform to obtain a complex quantity like the conductivity. Such a Kramers-Kronig transform includes extrapolations, and in particular when the interesting features are at the limit of the measured frequency range it cannot be ruled out that these extrapolations - that typically assume that the sample *is* a Drude metal - influence the obtained conductivity. Therefore conventional infrared spectroscopy measuring the reflection of bulk samples cannot be employed to satisfactorily measure a Drude response of a metal.

One path to overcome at least some of the problems is by using thin films instead of bulk samples. In principle if a metallic film is thin enough, then the transmitted radiation can be measured and it is possible to obtain the complex conductivity of the sample directly from such measurements without the need of a Kramers-Kronig transformation. But such a measurement cannot be performed on a normal metal because its conductivity is so high that the film thickness (of the order of the skin depth) has to be very thin, of the order of 10 nm. But then the mean free path of the electrons is of the order or even larger than the film thickness and thus surface effects will dominate the transmission and not the bulk conductivity that one wants to study. Thus the Drude response of a normal metal cannot be measured directly by optical spectroscopy.

The concept that is behind the idea of using thin films is first of all to actually decrease the number of charge carriers that contribute to the measured signal.

Another way to achieve this is by dramatically reducing the density of the effective charge carriers. Starting point for such a procedure is just the opposite: a semiconductor is doped until the increased charge carrier density causes metallic characteristics. While such a system might not be a metal in the common sense (e.g. the absolute conductivity is still rather low compared to normal metals and the resistivity increases with decreasing temperature), the frequency dependence of such a system can be metal-like. Transmission measurements on such highly-doped semiconductor samples were performed using terahertz time-domain transmission spectroscopy like described in Section 2.3. Since this technique is phase sensitive, the complex conductivity could be determined directly and Drude-like spectra were obtained [105,106]. But the dynamic range of this technique hardly exceeds an order of magnitude, whereas the Drude behavior is characterized by a broad frequency response and measurements on a larger frequency range would be desired. Furthermore the data analysis is not completely free of the assumption that the sample actually behaves like a Drude metal [105].

Coming back to normal metals, we have seen that it is hard to observe their Drude response directly. Thus to actually measure a metallic Drude response requires that the system to be studied has the scattering rate in a frequency range other than for conventional metals. One way to overcome the problem of too high reflectivity or too small skin depth would be to choose a system with a much higher scattering rate corresponding to a much lower conductivity. However, starting with the relaxation time of gold at room temperature of $3.0 \times 10^{-14}$ s [104], the characteristic decrease in the real part of the conductivity occurs at a frequency of 180 cm$^{-1}$ (compare Figure 6.1), and to measure the response completely requires to go to frequencies approximately one order higher in frequency, i.e. 1800 cm$^{-1}$, corresponding to 220 meV. If one now looks for a metal with much higher scattering rate, one immediately reaches the energy range of a few eV where interband transitions become important, and therefore in that frequency range it is impossible to measure the Drude response, which only describes intraband transitions, directly without interband effects.

114

Thus going to higher frequencies does not help in the quest for a direct experimental observation of a Drude response. The only other possibility is to go to much lower frequencies. If the frequencies of interest come within the limits of microwaves, the problem of obtaining the complex conductivity directly can be solved by measuring a complex quantity like the reflection coefficient directly. Thus one has to look for ways to increase the relaxation time of the charge carriers dramatically compared to normal metals in order to reach corresponding frequencies in the microwave range. One path could be by cooling the metal, thus freezing out phonon scattering, plus increasing the sample quality, thus reducing impurity scattering. But such an increase of the relaxation time directly increases the conductivity as well and thus the reflectivity of bulk samples is still too high to be measured and thin films still have to be thinner than the (now anomalous) skin depth, but the mean free path of the carriers is of course much longer than before. Thus this strategy does not work out directly. But it can be combined with the idea of using thin samples to avoid too high reflectivity when transformed to a different level by actually using a two-dimensional system of charge carriers. Studying two-dimensional electron systems has been a focus of semiconductor physics for decades and phase-insensitive measurements of the Drude-behavior of such systems have already been performed in the 1970s [107, 108] in the far-infrared spectral range. More recently a similar experiment [109] was possible at much lower frequencies (due to improved techniques to prepare high-mobility two-dimensional electron gas samples), in the GHz range. There the complex impedance of a two-dimensional electron system was measured directly using network analysis procedures similar to those of our spectrometer and extremely long relaxation times of up to a few hundred ps were found, corresponding to scattering rates in the GHz frequency range. This particular experiment leaves a dynamic range of only a factor 5 to study the response of the two-dimensional electron system directly, as for lower and higher frequencies the contacts necessary to probe the sample dominate the observed response.

While in high-mobility two-dimensional electron gases scattering rates in the GHz range can be reached (and measured) by increasing the mobility of the charge carriers, for three-dimensional bulk systems this does not work as a path to directly measure a Drude response for the reasons stated above. However, a solution to this dilemma is to lower the scattering rate without increasing the mobility (and the corresponding conductivity). This can be achieved if the effective mass of the charge carriers can be increased considerably above the free-electron mass. High effective masses are the naming characteristic of heavy-fermion materials and thus these compounds are a natural choice for direct measurements of a Drude response. As the following sections will show, such measurements are possible and were performed in the current project using the broadband Corbino spectrometer, although only at the limit of its resolution.

Finishing this section on why it is so hard to directly measure a Drude response, one property of Fermi liquids (the focus of Section 6.4.1) that results in another difficulty should be anticipated. Fermi liquid theory, the generally accepted theory to describe the electrical conductivity of normal metals at low temperatures, predicts that the scattering rate increases quadratically with temperature as well as with frequency while impurities contribute a constant scattering rate. The classical Drude metal on the other hand assumes a frequency-independent scattering rate. Observing a pure Drude response in a Fermi liquid therefore requires that the frequency-dependent contribution has to be much less than the impurity or thermal contributions while the latter two have to be small as well because we want to reach low scattering rates in the first place as motivated above. But this means in particular that the probing frequency has to be smaller than what corresponds to the temperature. Heavy-fermion conductivity is a low-energy and thus low-temperature effect, this state is reached below a characteristic 'coherence' temperature $T_{coh}$ that for typical compounds is of order 10 K. This temperatures roughly correspond to the frequency 10 cm$^{-1}$, and therefore it is obvious that a classical Drude response in a heavy-fermion compound can only be observed at extremely low frequencies, in the microwave range.

## 6.2   Heavy-Fermion Systems

The previous section explained why heavy-fermion materials [97] might be worth a try if one wants to directly measure a complex Drude response of a metal. However, the heavy-fermion material $UPd_2Al_3$ was chosen for the current project because heavy fermions constitute very interesting systems in their own right, in particular they belong to the prime examples of strongly correlated electron systems which go far beyond the description of electrons in metals as a (non-interacting) Fermi gas. The field of heavy-fermion materials further offers or is closely related to several other major topics of current solid state physics including so-called Kondo insulators (or Kondo semiconductors) [110], non-Fermi liquid behavior [110–112], quantum criticality [113], and unconventional superconductivity. These topics can experimentally be addressed by optical spectroscopy at low energies, and therefore the broadband spectrometer presented in this thesis might also be used to study these topics in upcoming projects. From the rich field of heavy-fermion physics, the following section will only describe those parts that are important in terms of optical spectroscopy and the microwave properties of these materials.

### 6.2.1   General Properties of Heavy-Fermion Systems

While the term 'heavy fermion'[2] only generally refers to charge carriers with a high effective mass, its common use in solid state physics is restricted to a particular class of materials: namely intermetallic compounds that include rare-earth or actinide elements with partially filled f-shells (like Ce or U) and behave as metals at low temperatures in a way principally similar to normal metals but renormalized due to a large effective mass. (Famous examples are $CeAl_3$, $CeCu_2Si_2$, $CeCu_6$, $UBe_{13}$, $UPt_3$, and $UPd_2Al_3$.) The physical quantity that is generally taken as the hallmark to reflect this effective mass is the electronic contribution to the low-temperature specific heat. At low temperatures, the

---

[2]Some authors use the term 'heavy electron' instead.

specific heat $C$ due to the conduction electrons in a solid is linear in temperature:

$$C(T) = \gamma \, T \quad . \tag{6.15}$$

The Sommerfeld coefficient $\gamma$ of the linear specific heat is proportional to the density of states at the Fermi level which in turn is proportional to the effective mass. Thus a large specific heat linear in $T$ at low temperatures can be attributed to a large effective mass. For heavy-fermion compounds this effective mass is typically of the order 100 to 1000 times the free electron mass. Also the magnetic susceptibility depends on the effective mass: like the Sommerfeld coefficient of specific heat, the Pauli susceptibility of the conduction band electrons is proportional to the density of states at the Fermi level or the effective mass, respectively. Thus from both quantities, specific heat and susceptibility, the effective mass of heavy fermions can be extracted. However, both quantities are affected by other temperature-dependent contributions than the high effective mass of the electrons, and as a result reliable measurements on heavy-fermion compounds have to be performed at rather low temperatures, typically much below 1 K.

An explanation for the large effective mass is to be found in the interaction of the localized f-electrons, introduced to the materials by the rare earth or actinide, with the conduction band electrons. At high temperatures these f-electrons can be treated as single magnetic ions in the metallic host material in the way of the Kondo model describing magnetic impurities in non-magnetic metals, in particular the increase of resistivity at low temperatures known as the Kondo effect. In this picture the high-temperature electrical resistivity of heavy-fermion materials, which does not decrease strongly with decreasing temperature like for normal metals but is almost temperature independent and might even increase with decreasing temperature in a way reminiscent of the Kondo effect in normal metals, is termed to be due to incoherent Kondo scattering.

But in contrast to dilute Kondo impurities in normal metals, the magnetic ions in heavy-fermion materials are rather concentrated and furthermore part of the crystal lattice and therefore often called 'Kondo lattices'. As a result of

this concentrated and periodic arrangement, at low temperatures the f-ions interact strongly with the conduction electrons and with themselves. Thus below a characteristic coherence temperature $T_{coh}$ the system changes continuously into a coherent state that is characterized by the hybridization of the originally localized (in space as well as energy) f-electrons with the (extended) conduction band electrons. This results in a strongly enhanced density of states in a small energy width. Model calculations show that in this region of enhanced density of states a narrow gap opens. Now it depends on whether the Fermi energy lies within this so-called hybridization gap or in one of the maxima of density of states adjacent to it, to determine the material to be a Kondo insulator or a heavy-fermion metal, respectively. Thus heavy fermion systems have a strongly enhanced density of states at the Fermi level and the related strongly enhanced effective mass. The energy scale of the enhanced density of states and the hybridization gap is 10 meV, once again emphasizing the low-energy nature of the heavy-fermion state that can only be probed at low energies.

The interpretation of entering a coherent state below $T_{coh}$ also explains the observed temperature dependence of the resistance - a strong decrease at low temperature - in the way that the incoherent Kondo scattering vanishes. The temperature of the maximum in the temperature-dependent resistance is thus often taken as a measure for $T_{coh}$.

## 6.2.2   Optical Properties of Heavy-Fermion Systems

Heavy-fermion materials have been investigated intensively using optical spectroscopy (for overviews see e.g. [110, 114, 115]), an excellent tool to study the excitation spectrum of these materials because, with tuning the frequency of the radiation, the characteristic energies of these materials can be probed. An experimental difficulty that has to be kept in mind is that optical spectroscopy cannot be performed at very low temperatures as easily as thermodynamical measurements like specific heat. Thus optical measurements on heavy-fermion materials are typically performed down to the $^4$He temperature range.

119

A very schematic plot of how a typical optical response (represented by the real part $\sigma_1$ of the conductivity) of a heavy-fermion material looks is shown in Figure 6.3. At high temperatures (above $T_{coh}$) the material can be considered
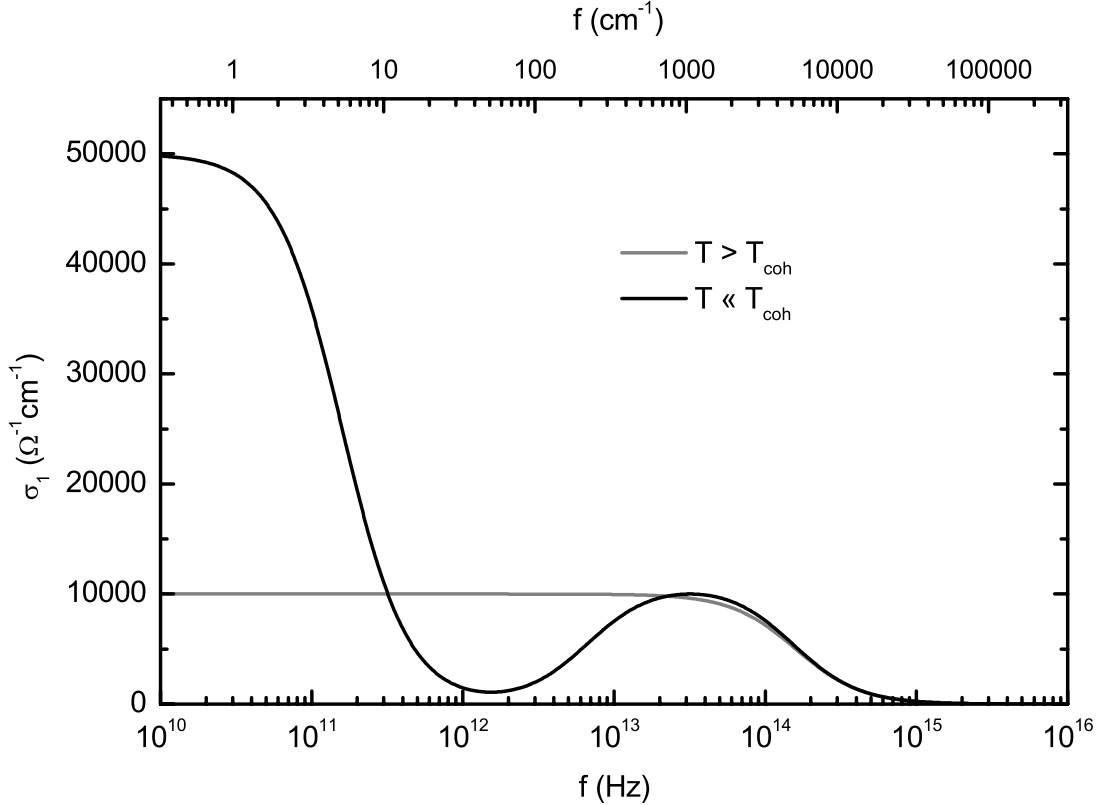


**Figure 6.3:** Schematic plot of the frequency-dependent conductivity of a heavy-fermion material. Above the coherence temperature $T_{coh}$ the material can be considered a Drude metal. Below $T_{coh}$ the hybridization gap opens (giving the minimum in $\sigma_1$ around 1 THz) and an extremely narrow Drude roll-off emerges.

to be a poor metal, i.e. the optical response is Drude-like with a rather high scattering rate and correspondingly a small low-frequency and dc conductivity. The heavy-fermion features show up when the material enters the coherent state below $T_{coh}$. Then the response at high energies remains basically unchanged compared to high temperatures, but at lower frequencies there are two features that are generally regarded as the canonical signs of heavy-fermion behavior in optical spectra: first there exists a gaplike feature in the optical conductivity (i.e. a minimum in $\sigma_1$). This gap (which in fact is a pseudogap only as $\sigma_1$ does not

vanish completely) is considered to directly reflect the hybridization gap in the density of states mentioned above.

At frequencies above the gap the optical conductivity of a heavy-fermion system resembles that of the normal state at high temperatures: here the energy of the radiation is too large to probe the correlated electrons and only single-electron excitations are possible like in the normal metal. Therefore the correlated electronic state and in particular its dynamics can only be studied at lower energies corresponding to lower frequencies of electromagnetic radiation at submillimeter and microwave frequencies.

The few experimental studies on this low-frequency response of heavy fermions have revealed a Drude-like behavior as shown in Figure 6.3 with a conductivity roll-off at extremely low frequencies compared to normal metals. This can be explained in the framework of Fermi-liquid theory as a renormalization of the scattering rate equivalent to the strongly enhanced effective mass. This explanation is solidified theoretically by Millis and Lee [2] in their calculation to describe the frequency-dependent conductivity for the Anderson lattice, an accepted concept to model heavy-fermion behavior [110]. In the low-temperature, low-frequency limit where impurities dominate the scattering rate and conductivity (thus labelled $\tau_i$ and $\sigma_i$, respectively), they find

$$\sigma_i(\omega) = \frac{ne^2}{m} \frac{\tau_i}{1 + (m^*/m)^2 \omega^2 \tau_i^2} = \frac{ne^2}{m^*} \frac{\tau_i^*}{1 + \omega^2 (\tau_i^*)^2} \quad , \qquad (6.16)$$

where the conductivity is expressed in terms of an enhanced mass $m^*$ and a renormalized scattering rate $\tau^*$:

$$\tau_i^* = (m^*/m)\tau_i \quad . \qquad (6.17)$$

Thus, according to Equation (6.16), the low-frequency, low-temperature frequency-dependent conductivity corresponds to the Drude formula, Equation (6.14), except for the renormalized scattering rate and effective mass. The dc conductivity as the low-frequency limit of Equation (6.16) is not affected by the renormalization. However, such an unaffected dc conductivity is not seen in experiments because the transition from the non-interacting system to the interacting, renor-

malized system cannot be tuned by an independent external parameter. Experimentally the transition is performed by reducing the temperature below $T_{coh}$. Reducing the temperature for a normal metal decreases phonon scattering, thus increases the relaxation time and the dc conductivity, and therefore an increased dc conductivity is also found for heavy fermions when going from the incoherent state at high temperatures to the coherent state at low temperatures as is schematically indicated in Figure 6.3. Millis and Lee predict extremely low renormalized scattering rates [2]: 'If the impurity scattering is weak, as in a good metal, the frequency $\omega^* = 1/\tau_i^*$ at which $\sigma(\omega)$ has fallen to half of its dc value may be of order $10^9$ Hz [..], a remarkably small value.'

## 6.2.3 Measuring the Drude Response in Heavy Fermions

While the hybridization gap of heavy-fermion compounds typically can be found at frequencies of order 10 cm$^{-1}$ to 100 cm$^{-1}$ (300 GHz to 3 THz) in the far infrared, the dynamics of the correlated, heavy electrons that are reflected in the Drude-like low-frequency behavior have to be probed at lower frequencies in the submillimeter and microwave frequency ranges. As described in Chapter 2, these frequency ranges are particularly hard to access experimentally, and therefore only very few experimental studies on the dynamics of the heavy-fermion state have been performed so far at these very low frequencies. Quasioptical submillimeter studies suffer the problem mentioned in Section 6.1.4 that the reflectivity of bulk samples is so high in this frequency range that the changes in conductivity to be studied cannot be resolved. (An example of this can be found in [116]. This problem has only been overcome for UPd$_2$Al$_3$ [3,4] where thin films are available.)

In particular microwave cavity measurements have given evidence that the heavy electrons actually exhibit strongly renormalized Drude behavior at low frequencies as indicated in Figure 6.3: the relaxation time is strongly enhanced, corresponding to the enhancement of the effective mass of the electrons that can also be found in the thermodynamical measurements. The material where the use of microwave cavities has most convincingly resulted in the observation
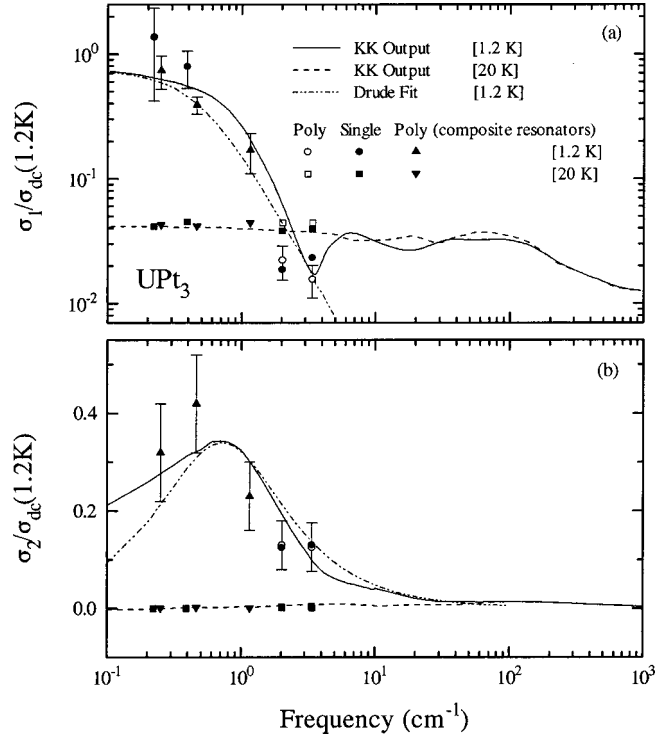
**Figure 6.4:** Low-temperature Drude behavior of UPt$_3$ taken from [120].
Symbols were obtained by cavity measurements on single- and
polycrystalline samples, lines denoted 'KK output' by Kramers-
Kronig transform of inter- and extrapolated absorptivity data.

of the Drude response is UPt$_3$, and the results after more than a decade of
experimental work [116–120] with different experimental setups and on different
samples can be found in Figure 6.4. Here the characteristic Drude behavior, a
decrease in $\sigma_1$ and a maximum in $\sigma_2$, were found at frequencies of approximately
1 cm$^{-1}$. Since resonant cavities were employed, $\sigma_1$ and $\sigma_2$ could be obtained
directly, but the error bars reveal the experimental difficulties. The lines denoted
as 'KK Output' were obtained via Kramers-Kronig transformation of inter- and
extrapolated absorptivity data and as such not measured directly.

The only other cases where direct measurements of the Drude-response of
heavy-fermions are documented in the literature were performed on CePd$_3$, CeAl$_3$,
and U$_2$Zn$_{17}$. The corresponding low-temperature conductivity spectra are shown
in Figures 6.5 and 6.6. In all these spectra data obtained via Kramers-Kronig
transform of far-infrared absorptivity data is combined with direct results of cav-
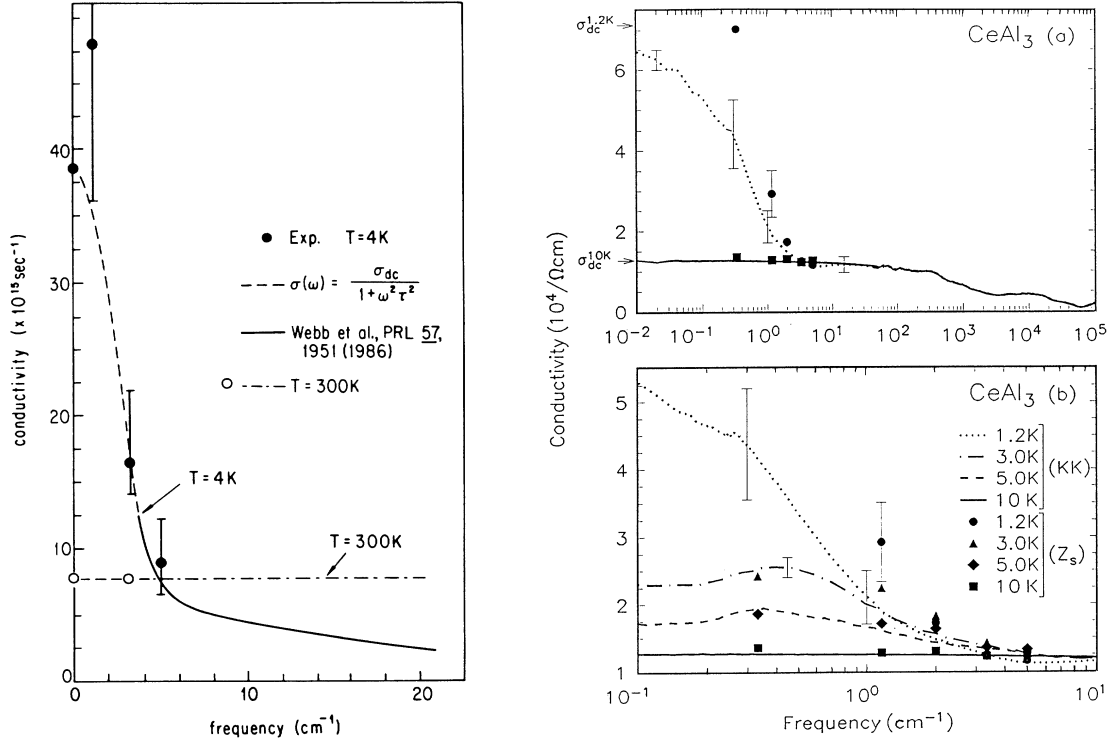
**Figure 6.5:** Left: low-temperature Drude behavior of CePd$_3$ taken from [121]. The full line gives data by Webb *et al.* that was obtained via a Kramers-Kronig transform [122].
Right: low-temperature Drude behavior of CeAl$_3$ taken from [123]. 'KK' again means Kramers-Kronig transform whereas the data denoted 'Z$_\mathrm{s}$' was obtained by cavity measurements.

ity experiments. It is evident that the actual Drude roll-off in $\sigma_1$ falls within the range covered by the cavities and only rather few frequencies were accessed with them. While all these data are consistent with a Drude-like response (in particular in view of the theoretical predictions by Millis and Lee [2]), the scarcity and uncertainty of the available data have not shown unambiguously (maybe with the exception of UPt$_3$) that the low-frequency response of any heavy-fermion compound actually behaves Drude-like.

Finally it should be pointed out that even recent optical spectroscopy measurements [124–126] on heavy-fermion materials in the far-infrared frequency range with low-frequency limits between to 20 cm$^{-1}$ or 40 cm$^{-1}$ were interpreted as evidence for a renormalized Drude behavior although the measurements
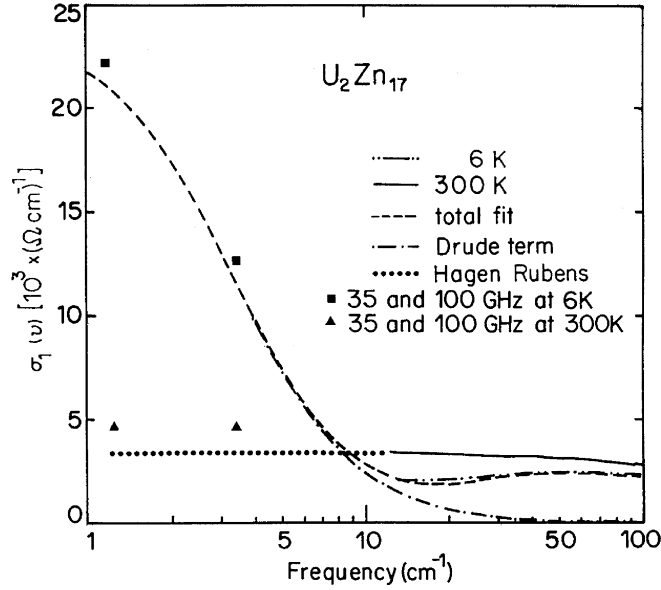
**Figure 6.6:** Low-temperature Drude behavior of $U_2Zn_{17}$ taken from [114]. The data at 6 K shows a narrow Drude roll-off but temperature dependent measurements of the dc conductivity [114] suggest that this will be even more pronounced at lower temperatures.

hardly passed the minimum of the hybridization gap towards lower frequencies. This practice has to be considered carefully as the data analysis usually involves Kramers-Kronig transforms including low-frequency extrapolations that assume Drude behavior and the detailed submillimeter studies on $UPd_2Al_3$ [3, 4] that will be described in more detail in Section 6.5.1 showed that such a procedure can miss the real low-frequency characteristics completely, a conclusion that is backed by the results of the current thesis.

## 6.3 Beyond the Original Drude Model

The original Drude formalism described in Section 6.1 leads to the frequency dependence of the conductivity given by Equation (6.11):

$$\sigma(\omega) = \frac{ne^2\tau}{m} \frac{1}{1 - i\omega\tau} \tag{6.18}$$

Although not specified particularly in the beginning, the effective mass $m$ was assumed to be the bare electron mass in case of a free electron model and the band

125

mass in case of a normal metal. The parameter that actually sets the scales for the frequency dependence is the relaxation time $\tau$ corresponding to a scattering rate $\Gamma = 1/\tau$. In the original Drude model both $m$ and $\tau$ are assumed to be real and frequency independent. As we have just seen, the low-frequency response of heavy fermions has a Drude-like behavior but with an extremely low scattering rate compared to those known from normal metals. To account for such changes, the original Drude model was modified.

## 6.3.1 Renormalized Drude Model

Without changing its functional form, the Drude conductivity of Equation (6.18) can be employed for heavy-fermion compounds by a subtle change: let the relaxation time and effective mass explicitly be the renormalized quantities $\tau^*$ and $m^*$, a procedure sometimes called 'renormalized Drude model' [1]:

$$\sigma(\omega) = \frac{ne^2\tau^*}{m^*}\frac{1}{1 - i\omega\tau^*} \qquad (6.19)$$

When it comes to the interpretation of an experimentally determined spectrum and scattering rate and effective mass are extracted, then the original and the renormalized Drude model of course give the same results, but in the second case these quantities are explicitly understood as the result of some renormalization effect inherent to the studied system. Thus the only motivation to employ the renormalized Drude formalism is to deliberately contrast such a spectrum to another, unrenormalized spectrum, e.g. to compare a low-temperature heavy-fermion spectrum with a high-temperature one, as by such a procedure the theoretical results of Millis and Lee as stated in Equations (6.16) and (6.16) can be mimicked. But obviously it is hard to experimentally define a sharp distinction between 'normal' and renormalized states.

## 6.3.2 Extended Drude Model

The original as well as the renormalized Drude models assume frequency-independent relaxation time and effective mass. However, these frequency independences

do not enter the frequency dependence of the conductivity of Equation (6.18) explicitly. Therefore this formula, regarded as the description of the conductivity at a single frequency, can still be valid even if the relaxation time and the effective mass are themselves functions of frequency. For example a quadratic frequency dependence of the scattering rate is predicted by Fermi-liquid theory.

Using frequency-dependent scattering rate and mass within the Drude formalism leads to the so-called 'extended Drude model'. Introduced to the field of optical spectroscopy by Allen and Mikkelsen [127], the extended Drude model supplies a rather general description of high-frequency properties of conduction electrons [1] and has in particular become a widely accepted method to analyze low-frequency optical data obtained on heavy-fermion systems [110] after it was first used in this context by Sievers and coworkers [118, 122], but it was also applied to other classes of materials like high-$T_c$ superconductors [128, 129], CMR manganites [130], and low-dimensional organic conductors [131].

Phenomenologically the Drude formalism as presented in Section 6.1 can be generalized by simply introducing a frequency-dependent scattering rate as well as a frequency-dependent effective mass (which are real quantities, in contrast to the complex scattering rate that will be dealt with later) to Equation (6.10):

$$\sigma(\omega) = \frac{ne^2\tau^*(\omega)}{m^*(\omega)} \frac{1}{1 - i\omega\tau^*(\omega)} \tag{6.20}$$

Since the objective is to model the conductivity of systems that cannot be described by the normal Drude model, we have explicitly used the starred quantities $\tau^*$ and $m^*$. As for the renormalized Drude model, the inherent assumption is that there exists a 'normal' system (with $\tau$ and $m$) that can be related to the renormalized one. Thus Equation (6.20) can be considered the generalized, complex version of Equation (6.16) by Millis and Lee (where only $\sigma_1$ was treated).

Equation (6.20) can be used to match any experimental data by proper choice of $\tau^*(\omega)$ and $m^*(\omega)$ and as such for any single frequency values for the relaxation rate and the effective mass can be obtained if real and imaginary parts are measured (assuming that the carrier density $n$ is known).

However, from Equation (6.20) no information concerning the actual form of the frequency dependences of $\tau^*(\omega)$ and $m^*(\omega)$ can be inferred. But the conductivity is a physical response function and has to be compatible with a Kramers-Kronig transform [1] (i.e. real and imaginary parts of the function are related in an integral form [1] which is equivalent to being a causal function [132]), and Allen and Mikkelsen have shown [127] that this results in restrictions of the possible forms of $\tau^*(\omega)$ and $m^*(\omega)$. The bare Drude function is Kramers-Kronig transformable. Obviously a physically meaningful extended version requires that this will also hold for the conductivity of Equation (6.20) including the combined frequency dependences of $\tau^*(\omega)$ and $m^*(\omega)$. Thus there are not only restrictions concerning particular choices of $\tau^*(\omega)$ and $m^*(\omega)$, but furthermore the two are connected: the choice of one of them fixes the other. To show this interrelation of $\tau^*(\omega)$ and $m^*(\omega)$ more explicitly, the two can be combined to a complex scattering rate $\hat{\Gamma}$ by using a frequency-dependent mass enhancement factor $\lambda(\omega)$ defined as $(1+\lambda(\omega)) = m^*/m$ where $m$ is the unrenormalized mass (in contrast to the equations shown up to now, the complex variables $\hat{\sigma}$ and $\hat{\Gamma}$ are now denoted explicitly as such to avoid confusion with the real variables $\tau^*$ and $m^*$):

$$\hat{\sigma}(\omega) = \frac{ne^2}{m^*(\omega)} \frac{\tau^*(\omega)}{1 - i\omega\tau^*(\omega)} = \frac{ne^2}{m^*(\omega)} \frac{1}{\frac{1}{\tau^*(\omega)} - i\omega}$$

$$= \frac{ne^2}{m(1 + \lambda(\omega))} \frac{1}{\frac{1}{\tau^*(\omega)} - i\omega}$$

$$= \frac{ne^2}{m} \frac{1}{\frac{(1+\lambda(\omega))}{\tau^*(\omega)} - i(1 + \lambda(\omega))\omega}$$

$$= \frac{ne^2}{m} \frac{1}{\frac{(1+\lambda(\omega))}{\tau^*(\omega)} - i\lambda(\omega)\omega - i\omega}$$

$$= \frac{ne^2}{m} \frac{1}{\hat{\Gamma}(\omega) - i\omega} \quad . \tag{6.21}$$

Here the complex scattering rate is defined as:

$$\hat{\Gamma} = \Gamma_1 + i\Gamma_2 = \frac{(1 + \lambda(\omega))}{\tau^*(\omega)} - i\lambda(\omega)\omega \quad . \tag{6.22}$$

Thus the conductivity $\hat{\sigma}(\omega)$ will obey Kramers-Kronig relations if (and only if) the complex scattering rate $\hat{\Gamma}(\omega)$ does.

The meaning of a complex scattering rate is hard to grasp within the bare Drude picture where the scattering rate describes the mean frequency of scattering events. However, a complex scattering rate is important for more general transport theory based on the Boltzmann equation [127, 129] from which the Drude result can also be derived [1, 127]. Here the complex scattering rate plays the role of a frequency-dependent memory function [129, 133]. Its meaning is more obvious in time space instead of frequency space. There the general relaxation of a system can be described as follows [127]: assuming linear response, the change $\frac{\partial f}{\partial t}$ of the distribution function $f$ of the system towards its equilibrium $f^0$ is determined by the memory function $G$ as follows:

$$-\frac{\partial f(t)}{\partial t} = \int_{-\infty}^{t} G(t - t')(f(t') - f^0)dt' \quad . \tag{6.23}$$

Here the upper limit $t$ of the integration instead of the more general integration from $-\infty$ to $+\infty$ is chosen because the memory function $G(t - t')$ is assumed to vanish for $t < t'$. This means that the system only responds to its prior states, i.e. it is causal. This assumption directly leads to the Kramers-Kronig compatibility of the frequency-dependent memory function [132] which is given by:

$$\hat{\Gamma}(\omega) = \int_{-\infty}^{\infty} G(t)e^{i\omega t}dt \quad . \tag{6.24}$$

Thus the notion of the frequency-dependent relaxation time and effective mass can be combined in a complex scattering rate, which in turn is a memory function, which directly ensures that the resulting frequency-dependent conductivity, Equation (6.20), obeys the generally required property of a physical response function of being Kramers-Kronig transformable.

The classical Drude result with a frequency-independent scattering rate is recovered within this framework if the response of the system is assumed to be local in time, i.e. does not depend on history. In this case the memory function is a delta function $G(t) = 1/\tau \ \delta(t)$, and the scattering rate of Equation (6.24) resumes its well-known form $\Gamma = 1/\tau$.

## 6.3.3   Analysis of Experimental Data

The typical application of the extended Drude model is to extract scattering rate and effective mass from measured conductivity spectra. This allows not only to assign a scattering rate quantitatively to systems at all that do not follow a simple Drude response (or for cases where the Drude roll-off is outside of the experimentally accessible frequency range) but also to study the frequency dependences of scattering rate and effective mass. The common way [1] to obtain these two quantities from complex conductivity data is as follows: starting from Equation (6.21) one has:

$$
\hat{\sigma}(\omega) = \frac{ne^2}{m^*(\omega)} \frac{1}{\frac{1}{\tau^*(\omega)} - i\omega} = \frac{ne^2}{m} \frac{1}{\frac{m^*(\omega)}{m} \frac{1}{\tau^*(\omega)} - i\frac{m^*(\omega)}{m}\omega}
$$

$$
= \frac{\omega_p^2}{4\pi} \frac{1}{\tau(\omega) - i\frac{m^*(\omega)}{m}\omega} \quad , \tag{6.25}
$$

where $m^*/m = \tau^*/\tau$ [2] and the definition of the plasma frequency $\omega_p^2 = 4\pi ne^2/m$ were used. Thus the frequency-dependent scattering rate and effective mass can be obtained as follows:

$$
\frac{1}{\tau(\omega)} = \frac{\omega_p^2}{4\pi} \operatorname{Re}\left(\frac{1}{\sigma(\omega)}\right) = \frac{\omega_p^2}{4\pi} \frac{\sigma_1(\omega)}{|\sigma(\omega)|^2} = \frac{\omega_p^2}{4\pi} \rho_1(\omega) \quad , \tag{6.26}
$$

$$
\frac{m^*}{m} = -\frac{\omega_p^2}{4\pi\omega} \operatorname{Im}\left(\frac{1}{\sigma(\omega)}\right) = \frac{\omega_p^2}{4\pi\omega} \frac{\sigma_2(\omega)}{|\sigma(\omega)|^2} = -\frac{\omega_p^2}{4\pi\omega} \rho_2(\omega) \quad . \tag{6.27}
$$

A few comments should be made concerning these formulae: firstly one has to keep track of whether one deals with the 'normal' or the renormalized quantities, in particular the scattering rate. While the effective mass $m^*/m$ obviously is the renormalized one, this is not the case for the scattering rate $1/\tau$: this is the scattering rate of the unrenormalized charge carriers. I.e. the scattering rate obtained from Equation (6.26) is not the scattering rate $1/\tau^*$ corresponding to a Drude roll-off that might be seen in the conductivity spectrum, but the latter one is given by $1/\tau^* = m/m^* \, 1/\tau$. Secondly the plasma frequency should be discussed. Using the definition $\omega_p^2 = 4\pi ne^2/m$, the plasma frequency can be calculated from the charge carrier density and mass (the effective mass of the

normal state). If these two parameters are known, then the plasma frequency can be calculated, but often this is not the case *a priori*. For standard optical spectroscopy this problem is solved by analysis of the normal state since the unrenormalized plasma frequency can either be determined directly from the drop in the reflectivity (compare Section 6.1.4) or from the well-known sum rule [1]:

$$\frac{\omega_p^2}{8} = \int_0^\infty \sigma_1(\omega) d\omega \quad , \tag{6.28}$$

where again the integration is performed on the conductivity in the normal state. This procedure assumes that the charge carrier density does not change upon the transition from the 'normal' to the renormalized state. But this assumption of a temperature-independent charge carrier density can be violated if carriers localize with decreasing temperature, and therefore simply applying the normal state plasma frequency to the renormalized state can lead to incorrect results.

## 6.4 Fermi Liquid Theory

If the frequency dependence of the scattering rate can be obtained by optical experiments, then it should be compared with the prevailing theoretical predictions. As already mentioned, the starting point for a theoretical description of heavy-fermion materials is Fermi liquid theory as pioneered by Landau [134]. Fermi liquid theory [135, 136] describes systems of interacting fermions (i.e. Fermi liquids) assuming a one-to-one correspondence to the non-interacting system (i.e. a Fermi gas). By continuously tuning the interaction from the non-interacting system to the interacting system, the general nature of the excitations of the system (the so-called quasiparticles) is preserved (inherently limiting the validity of Fermi liquid theory to low temperatures) with the characteristic numerical parameters rescaled compared to the non-interacting system. Fermi liquid theory is the generally accepted description of the electron-electron interaction in metals, and the ground state of a 'normal' metal is assumed to be a Fermi liquid. For such a system the prediction for the low-temperature dc resistance is the well-known '$T^2$ law' ($\rho(T) \propto T^2$) which is a direct consequence of a quadratic

temperature dependence of the scattering rate. Since for any experimentally observable (non-superconducting) system there is always a residual resistivity $\rho_{res}$ due to lattice imperfections and impurities, the resistivity of a Fermi liquid to be found in experiments is

$$\rho(t) = \rho_{res} + aT^2 \qquad (6.29)$$

with a temperature-independent prefactor $a$. This quadratic temperature dependence can only be found at very low temperatures because at higher temperatures other contributions like phonons dominate over the electron-electron scattering.

Some heavy-fermion materials are considered prime examples of materials exhibiting Fermi-liquid behavior (e.g. the prefactor $a$ in heavy fermions is strongly enhanced compared to normal metals and thus it is much easier to study Fermi-liquid behavior experimentally [98, 137]) whereas others exhibit strong deviations from Fermi-liquid behavior and were studied intensively within the thus emerging subject of 'non-Fermi liquid behavior' [110–112]. While for typical non-Fermi liquid materials the deviations from the Fermi-liquid predictions, e.g. the $T^2$ law of resistivity, are obvious, the opposite question of 'search for a real Fermi liquid' is very subtle and has attracted much less attention in recent years. The subtlety of this problem comes with ambiguity of different theoretical predictions, e.g. under particular circumstances a $T^2$ law of resistivity can have causes others than electron-electron interactions and thus in cases of doubt the observation of such behavior cannot be taken as absolute evidence for a Fermi liquid.

## 6.4.1 Frequency-Dependent Scattering Rate

The heavy-fermion system of the current study, $UPd_2Al_3$, is considered to be a prime example of heavy-fermion compounds that behave like a Fermi liquid at low temperature. Since our broadband microwave measurements reveal the frequency dependence of the conductivity and, following the procedure described in Section 6.3.2, the frequency-dependent scattering rate is accessible, we can compare this to the predictions of Fermi liquid theory. A general equivalency of energy in mind, it is natural and became generally accepted [1, 104] to expect a

quadratic frequency dependence as the counterpart of the quadratic temperature dependence of the scattering rate:[3]

$$1/\tau = A(k_B T)^2 + B(\hbar\omega)^2 \quad . \tag{6.30}$$

The theoretical predictions for the relative importance of the two contributions, i.e. the ratio A/B, are either $\pi^2$ [135, 136, 138–141] or $(2\pi)^2$ [142–144]. These two different values are explained by Degiorgi [110] as being 'for quasiparticle (seen in photoemission experiment) or transport (seen in optical experiment) scattering rate, respectively.' It should be pointed out that the quadratic temperature and frequency dependences of the bare Fermi liquid theory is conserved in more complicated models that were conceived to describe the peculiarities of heavy-fermion compounds, e.g. the aforementioned work by Millis and Lee concerning the Anderson lattice [2].

Experimental studies concerning a Fermi-liquid-like frequency dependence of the electronic scattering rate in metals are scarce, in particular when it comes to heavy-fermion compounds which include some materials that are considered to be prime examples of Fermi-liquid behavior. Here the experimental difficulties are hard to overcome, again it is the required combination of low temperatures and spectroscopy at rather low frequencies. While this combination is generally required to study Fermi-liquid behavior since this theory describes only low-energy excitations of the electronic systems, it is particularly true for heavy-fermion materials since their characteristic behavior is by definition limited to low temperatures and energies.

Those few low-frequency studies on heavy-fermion compounds that address the question of whether the frequency-dependent scattering rate complies with Fermi-liquid theory [4, 110, 117–120, 122, 123] have at most only found qualitative agreement with Equation (6.30), whereas for the ratio A/B no agreement with Fermi-liquid theory was found. The only two publications that state actual

---

[3]Different prefactors $a$ and $A$ are chosen, depending on whether the resistivity or the scattering rate is considered, but they only differ by a constant factor.
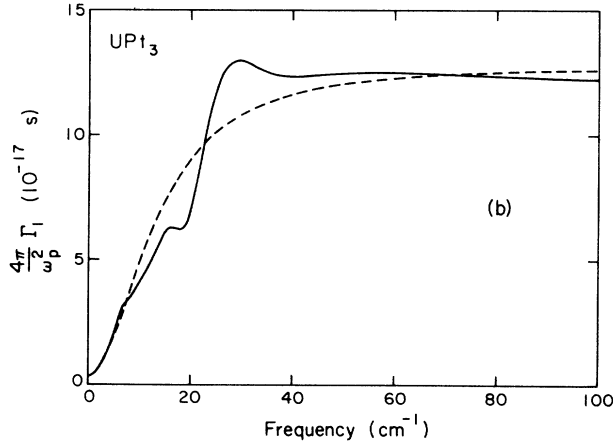
**Figure 6.7:** Frequency-dependent scattering rate of $UPt_3$ at 1.2 K taken from [118]. The dashed line is a fit with a quadratic frequency dependence in the low-frequency limit.

numbers are both on $UPt_3$. Figure 6.7 shows the frequency-dependent scattering rate as determined by Sulewski *et al.* from far-infrared spectroscopy data [118]. Concerning the equivalence of frequency and temperature according to Fermi-liquid theory, Sulewski *et al.* report that 'from the data an upper limit of $p = 1$ may be determined' [118], corresponding to an upper limit of $A/B$ of $\pi^2$ in our notation. But for this question the data are not well suited as can already be seen in Figure 6.7: data and quadratic fit coincide for the lowest frequencies only, arguably below 5 cm$^{-1}$. But this frequency range is at the low-frequency limit of what was actually measured (down to 2 cm$^{-1}$), and, since this was an absorption experiment, the data analysis relies on a Kramers-Kronig transform with the well-known problems concerning extrapolations. To add insult to injury, later studies on $UPt_3$ at lower frequencies showed that in this material at low temperatures a pseudogap develops around 3 cm$^{-1}$ [116], i.e. right at the edge of the data used by Sulewski *et al.* Thus their data entering the quadratic fit spans a frequency range including the pseudogap and cannot reflect the behavior of a Fermi-liquid state, thus also their estimate of the ratio $A/B$ has no solid ground anymore.

Recently another estimate on $A/B$ was published by Tran *et al.* [120], and the corresponding frequency dependence of the scattering rate is reproduced in part (a) of Figure 6.8. As was already discussed in Section 6.2.3, this study
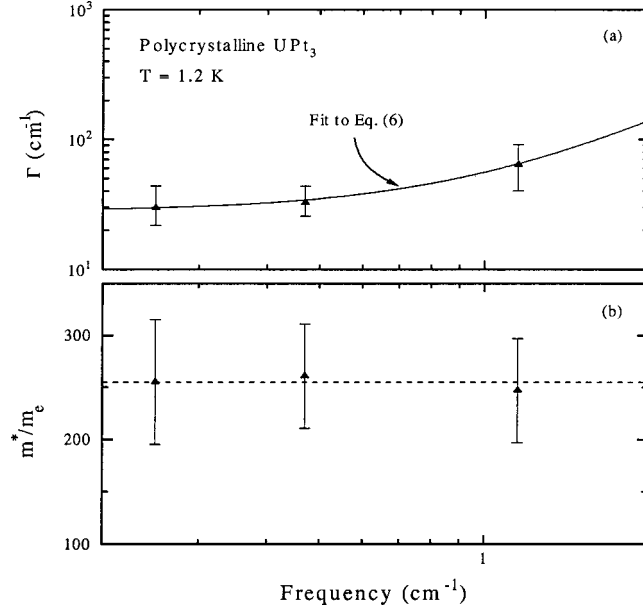
**Figure 6.8:** Frequency-dependent scattering rate (a) and effective mass (b) of UPt$_3$ at 1.2 K taken from [120].

employed cavity resonators, i.e. combines measurements of distinct, fixed frequencies. The maximum frequency is 1.2 cm$^{-1}$, i.e. below the pseudogap (and well within the Drude response, compare Section 6.2.3), and thus the obtained frequency dependence should reflect the heavy Fermi liquid. Tran *et al.* state values of 0.31 and 0.37 for the ratio $A/B$ determined from temperature- and frequency-dependent data, respectively. However, as is evident from Figure 6.8, only three frequencies were used to determine a quadratic behavior, thereby raising serious doubts concerning the significance of the conclusions drawn from this data, even more so when the error bars are considered.

Thus the field of frequency-dependent scattering rates in general and in particular in terms of studying the equivalence of temperature and frequency as predicted by Fermi liquid and related theories is still rather open from an experimental point of view.

# 6.5 Heavy-Fermion System UPd$_2$Al$_3$

Now that the heavy-fermion systems have been introduced in general and their optical properties in particular, we should focus on the compound that was examined in the present study, UPd$_2$Al$_3$. As soon as it was synthesized and characterized by Geibel *et al.* [145] in 1991, this material has been the subject of numerous experimental and theoretical studies. This interest is triggered by the rich low-temperature properties of this material: within the heavy-fermion state,[4] UPd$_2$Al$_3$ becomes an antiferromagnet below $T_N = 14$ K and a superconductor below $T_c = 2$ K [145]. In particular the superconducting state, with its rather high critical temperature for a heavy-fermion compound, has been studied intensively and with fascinating results: the combination of tunneling experiments [146] and neutron scattering [147] gave convincing evidence that the superconducting pairing of the electrons is of magnetic origin, in striking contrast to conventional superconductors where superconductivity is due to phononic interactions. While non-phononic origins of superconductivity have been discussed for numerous 'unconventional' superconductors, UPd$_2$Al$_3$ still seems to be the only example where a magnetic pairing could be demonstrated experimentally [148].

In the current study, however, we concentrate on the heavy-fermion properties of UPd$_2$Al$_3$ above $T_c$, but its superconducting state below $T_c$ plays an important role for the calibration procedure.

## 6.5.1 Optical Properties of UPd$_2$Al$_3$

Among the numerous heavy-fermion compounds that have been studied by optical means, only UPt$_3$ [116–120] and UPd$_2$Al$_3$ [3,4] have also been examined in detail at lower frequencies than the conventional far infrared, making UPd$_2$Al$_3$ a very suitable candidate for the broadband microwave studies. While earlier, standard far-infrared experiments on UPd$_2$Al$_3$ were interpreted in the conventional picture

---

[4]Thermodynamical measurements yield a moderately high effective mass of 66 [145] or 49 [150], respectively.

of heavy-fermions (a hybridization gap and a narrow Drude response) [114, 115], only the more recent studies in the submillimeter and microwave frequency ranges [3, 4] showed that this picture was incomplete.
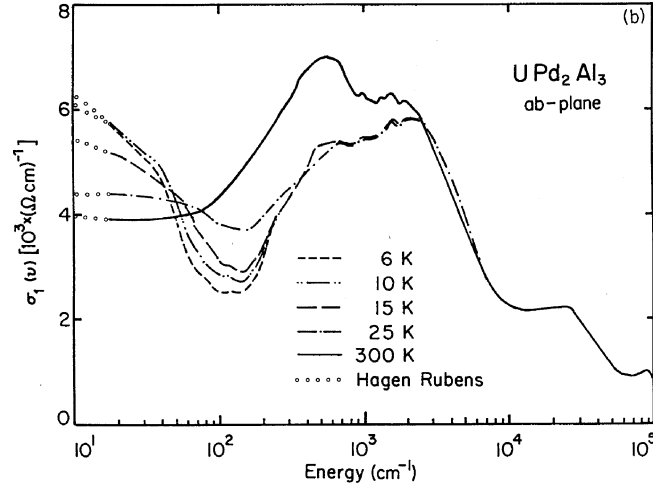


**Figure 6.9:** Optical conductivity of UPd$_2$Al$_3$ taken from [114]. Far-infrared reflectivity data down to 20 cm$^{-1}$ was Kramers-Kronig transformed to obtain the optical conductivity.

Figure 6.9 shows conventional far-infrared conductivity spectra obtained by Kramers-Kronig transforming reflectivity data [114]. As a low-frequency extrapolation the Hagen-Rubens limit (i.e. the low-frequency behavior of the Drude model) was assumed. This procedure was based on the observation that the measured dc conductivity and the microwave conductivity at 100 GHz (3 cm$^{-1}$) had similar temperature dependences, suggesting frequency-independent, Drude-like behavior in this frequency range. From the spectra a renormalized scattering rate $\Gamma^* = 60$ cm$^{-1}$ at 6 K (the lowest temperature studied) was deduced [114].

When the group of Prof. Adrian in Mainz succeeded in growing high-quality UPd$_2$Al$_3$ thin films (that were also the basis for the tunnelling experiments [146]), for the first time transmission measurements in the submillimeter range could be performed (thus solving the restrictions of reflection measurements on bulk samples mentioned in Section 6.1.4). The most conclusive conductivity spectra were obtained on a large thin film sample (approximately 1×1 cm$^2$ in size) with a coherent source submillimeter wave spectrometer (as described in Section 2.3)
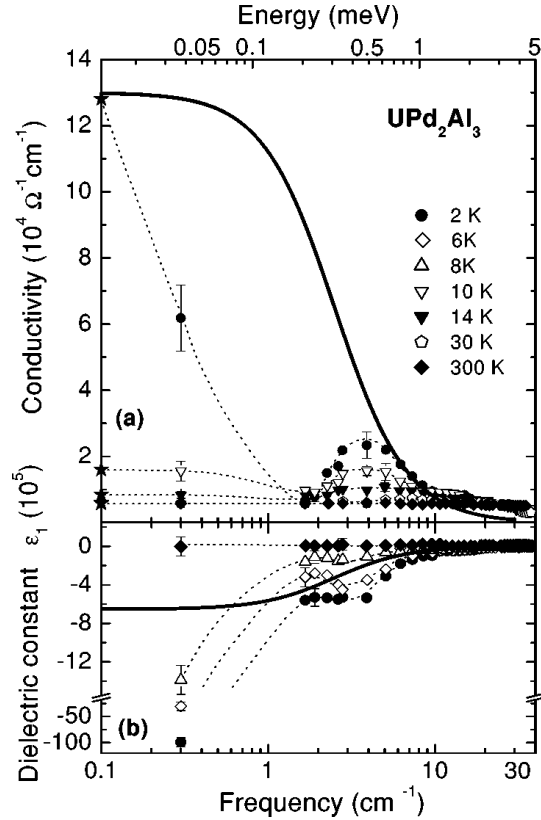
**Figure 6.10:** Optical conductivity of $UPd_2Al_3$ at submillimeter and microwave frequencies taken from [4]. The full line shows how a simple renormalized Drude interpretation with a scattering rate $\Gamma^* = 16$ cm$^{-1}$ misses the low-temperature behavior completely.

at temperatures down to 2 K (just above the critical temperature of 1.8 K for that particular sample) in our group in Stuttgart and are shown in Figure 6.10. The spectra at the lowest temperatures show that there is an increase of $\sigma_1$ below 40 cm$^{-1}$ similar to that seen in the previous far-infrared study [114] and that was assigned as the Drude roll-off at that point. But the more recent experimental data show that $\sigma_1$ has a maximum around 5 cm$^{-1}$ and decreases for lower frequencies up to the lowest frequency accessible with that spectrometer of around 1 cm$^{-1}$. I.e. a Drude-like increase of $\sigma_1$ towards the dc conductivity was not found in the submillimeter spectra. The maximum in $\sigma_1$ around 5 cm$^{-1}$ and the connected minimum around 1 cm$^{-1}$ (so-called pseudogap) become more pronounced with decreasing temperature below $T_N$ and they are interpreted to
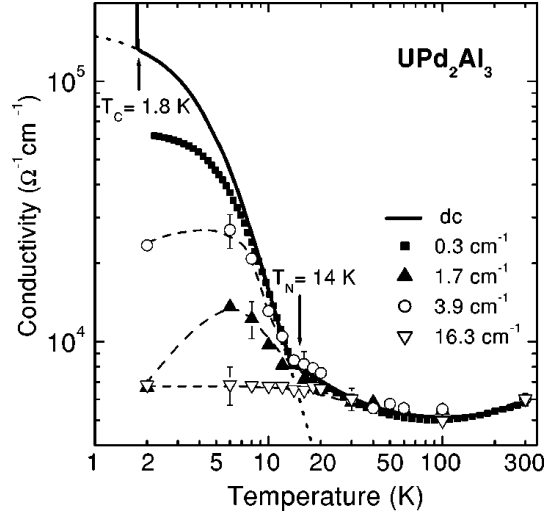
**Figure 6.11:** Temperature dependence of the dc and optical conductivity of UPd$_2$Al$_3$ at fixed submillimeter and microwave frequencies taken from [4].

stem from magnetic correlations [3,4]. The existence of an actual minimum in $\sigma_1$ around 1 cm$^{-1}$ was inferred from additional microwave cavity measurements. In particular measurements at 10 GHz revealed the complex conductivity directly and the results are also shown in Figure 6.10. As can be seen there from the frequency dependence or in particular from the temperature dependence of the conductivity as shown in Figure 6.11, the conductivity at 10 GHz coincides with the dc conductivity at high temperatures, deviates from it below 10 K, and has approximately half of the dc value at the lowest temperatures around 2 K. This suggests that at the lowest temperatures the characteristic Drude roll-off occurs around 10 GHz, but of course a complete Drude behavior cannot be deduced from data at a single frequency and furthermore the interpretation is hampered by the fact that the 10 GHz data were taken on a different sample than the dc and submillimeter data. Since the sample quality of UPd$_2$Al$_3$ thin films is disclosed in particular in the low-temperature conductivity (which strongly depends on impurities) it cannot be ruled out that different sample quality will result in misleading frequency dependences as soon as data obtained with different techniques are combined. Thus the need for a broadband measurement in the microwave range to settle the uncertainties of the Drude behavior in UPd$_2$Al$_3$ is evident.

An earlier study [151] on $UPd_2Al_3$ thin films already included non-resonant radio and microwave frequency measurements but their results were not conclusive and even the authors point out that 'However, due to the contact type of measurements these results reveal large uncertainties and further measurements are necessary before final conclusions can be drawn.'

The current project obtained such 'further measurements' disagreeing with the former data, but since our Corbino spectrometer is much better characterized and suited for this type of measurements, the disagreement is assumed to be due to technical problems with the former experiments. We can disregard these experiments and do not discuss them any further.

# Chapter 7

# Microwave Measurements on UPd$_2$Al$_3$

In the previous chapter it was shown that the Drude response of heavy-fermion compounds in general has not been studied in depth and that the most detailed optical study on a heavy-fermion material down to the submillimeter and microwave frequency ranges (on UPd$_2$Al$_3$ [3,4]) has left the demand of an in-depth study of the microwave properties of this material. The current project delivers this in-depth study and the results of these measurements will be described in the following sections.

## 7.1   UPd$_2$Al$_3$ Samples

As described in Section 5.5, the Corbino setup is limited in sensitivity and therefore samples with very low impedance (with reflection coefficient close to -1) are hard to measure. Heavy-fermion systems in general and UPd$_2$Al$_3$ as one example show metallic conductivity in the normal state above $T_c$ (single crystals of UPd$_2$Al$_3$ reach conductivities of up to $5 \cdot 10^5$ ($\Omega$cm)$^{-1}$ [152]). Thus the reflection coefficient of a bulk sample would be indistinguishable from the calibration measurement of a perfect short and therefore unresolvable.[1] Following Section 6.1.4,

---

[1]Estimating from the dc conductivity, one obtains Re(S$_{11}$) $\approx$ -0.99980 and $|\text{Im(S}_{11})| \approx 0.00036$.

141

this problem can be overcome by using thin film samples with thicknesses smaller than the skin depth. In the light of the present situation where experimental work on heavy fermions focusses almost completely on single crystals, we were extremely fortunate to obtain such thin film samples for our experiments.

The UPd$_2$Al$_3$ thin film samples for the present study were grown by molecular beam epitaxy (MBE) by Martin Jourdan and coworkers in the group of Prof. Adrian at the Johannes Gutenberg-Universität in Mainz in a setup that was designed to grow samples for tunnelling spectroscopy [146, 153, 154]. The films are deposited on LaAlO$_3$(111) substrates by simultaneous evaporation of the three constituents U, Al, and Pd with individually controlled evaporation rates [153–155]. The quality of the epitaxial thin films grown with this procedure was shown by studies of the crystallographic as well as the electrical properties. Two important measures for the quality are the transition temperature $T_c$ to the superconducting state of up to 2.0 K and the resistance ratio (room temperature resistance divided by the residual resistance of the (normal) cryogenic conductivity, see Section 7.1.1) of up to 39 for the best thin film samples.

Unfortunately only few UPd$_2$Al$_3$ thin film samples are suitable for Corbino measurements. High-quality films require thicknesses of at least 60 nm [154] (typical high-quality samples are thicker than 100 nm), whereas the Corbino measurements desire films of thicknesses less than 40 nm. Thus a tradeoff between sample quality and sensitivity of the spectrometer cannot be avoided. Finally most of the data was obtained on a 150 nm thick sample (sample number UPA233c) that belongs to the group of samples that were the best UPd$_2$Al$_3$ thin films ever grown. Results obtained on other samples will be discussed in Section 7.5. Unfortunately the particular UPA233c sample is a little smaller than the standard dimensions for our probe, and furthermore this sample already showed small cracks before we started our measurements (an additional problem with that sample are the contacts, see Appendix B.2). However, this sample proved to show much more significant features at low temperatures than all the other samples that were measured. Sample quality is also an important issue when different measurements

are compared as is the case here for the comparison with data obtained at higher frequencies and presented in Section 7.3.3.

## 7.1.1   Resistivity

The temperature-dependent dc resistivity of the UPd$_2$Al$_3$ thin films matches the general behavior of poly- and single-crystalline samples known from literature [145, 149, 152, 156]. Figure 7.1 shows the dc resistivity of the highest-quality UPd$_2$Al$_3$ thin film sample UPA233c in comparison with the highest-quality single crystal sample documented in literature [152]. Its temperature dependence is typ-
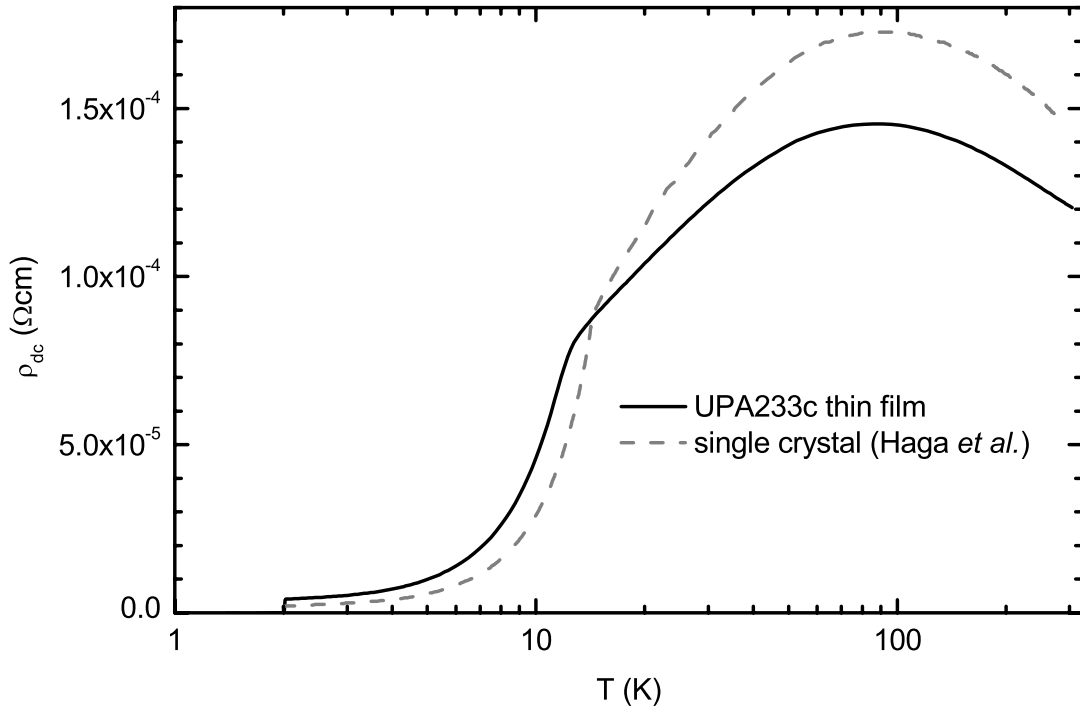


**Figure 7.1:** Temperature-dependent dc resistivity of UPd$_2$Al$_3$ thin film sample UPA233c compared to single-crystal data extracted from a figure of Haga *et al.* [152].

ical of heavy-fermion compounds: at high temperatures the resistivity increases with decreasing temperature reminiscent of the Kondo effect. Around 80 K the resistivity has a maximum (giving a measure of the coherence temperature) and decreases for lower temperatures. Below 14 K the system enters the antiferromagnetic state and the resistivity decreases drastically due to the reduction of

spin-flip scattering. For temperatures below 4 K the resistivity follows a $T^2$-behavior [149] that is taken as an indication of Fermi-liquid behavior, and finally the system reaches the superconducting state at 2 K. This general behavior is found for the thin-film as well as the single-crystal data, and also their absolute resistivities roughly correspond.
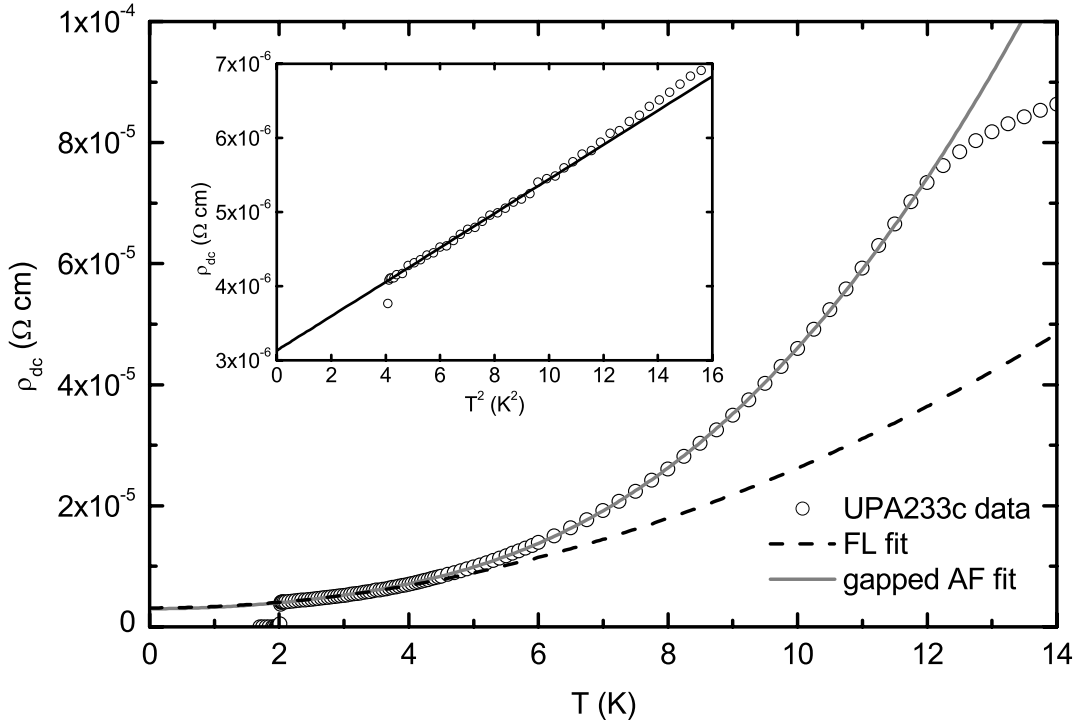


**Figure 7.2:** Low-temperature dc resistivity of UPd$_2$Al$_3$ thin film sample UPA233c with Fermi liquid and gapped antiferromagnet model fits. The inset shows the quadratic temperature dependence as predicted by Fermi liquid theory.

The sample quality is often expressed using residual resistivity ratios. Comparing the resistivity at 300 K either to that at 2 K right above the superconducting transition or to that at 0 K by use of an extrapolation (see below), for the particular UPA233c sample one obtains $R_{300K/2K} = 30$ or $R_{300K/0K} = 40$, respectively. These values are extremely high for thin film samples [154, 155, 157, 158], whereas the highest-quality single crystal has $R_{300K/0K} = 104$ [152].

For the later discussion concerning Fermi liquid behavior in Section 7.4.1, the low-temperature resistivity is of particular interest. For a Fermi liquid the

| parameter | UPA233c data | | literature | | |
|---|---|---|---|---|---|
| | Fermi liquid | gapped AF | [150] | [159] | [155] |
| $\rho_0$ ($\Omega$cm) | $3.1 \cdot 10^{-6}$ | $3.0 \cdot 10^{-6}$ | $1 \cdot 10^{-6}$ | $6.2 \cdot 10^{-6}$ | $2.63 \cdot 10^{-5}$ |
| $a$ ($\Omega$cm/K$^2$) | $2.3 \cdot 10^{-7}$ | $2.5 \cdot 10^{-7}$ | $2.3 \cdot 10^{-7}$ | $2.4 \cdot 10^{-7}$ | $5.11 \cdot 10^{-7}$ |
| $b$ ($\Omega$cm/K) | - | $1.0 \cdot 10^{-5}$ | $2.4 \cdot 10^{-5}$ * | $3.0 \cdot 10^{-5}$ | $7.01 \cdot 10^{-6}$ |
| $E_g$ (K) | - | 23 | 40 | 39 | 21.3 |

**Table 7.1:** Comparison of fit parameters obtained from dc resistivity of the UPA233c sample (using Fermi liquid and gapped antiferromagnet fits) and from literature.
*The value for $b$ given in [150] is obviously a misprint ('24 m$\Omega$cm/K') and was changed to the arguably correct value.

resistivity is expected to be quadratic in temperature. The inset of Figure 7.2 shows that for the UPA233c sample such a quadratic behavior is obeyed up to approximately 3.2 K, corresponding to previously published upper limits of 4 K (single crystal [149]) and 3-3.5 K (thin films [155, 158]). The resulting Fermi liquid fit ($\rho(T) = \rho_0 + aT^2$) is shown on the main plot together with the data and another fit model that additionally includes an energy gap of an antiferromagnet ($\rho(T) = \rho_0 + aT^2 + bT(1 + 2T/E_g)e^{-E_g/T}$) as was previously used to describe the resistivity of UPd$_2$Al$_3$ below $T_N$ [4, 150, 155, 159] (although other descriptions are also possible [160]). A compilation of the results of the fits and the values from literature can be found in Table 7.1. There is a general agreement of the data taken on the UPA233c thin film sample and literature data, in particular the prefactor $a$ of the Fermi liquid contribution that will be important in Section 7.4.1 matches the bulk results [150, 159]. (The discrepancy to the thin film result [155] is attributed to the considerably higher quality of the present sample as evident from the residual resistance and the corresponding resistivity ratio.)

## 7.2   Microwave Measurements

Broadband microwave measurements on UPd$_2$Al$_3$ were performed with the Corbino spectrometer using the procedures documented in detail in previous chap-

ters. The particular highest-quality sample UPA233c with its combination of high conductivity and rather large thickness (150 nm), leading to a very high reflection coefficient, could only be measured close to the resolution limit of our spectrometer, exemplary spectra are shown in Figure 7.3. Here the measured
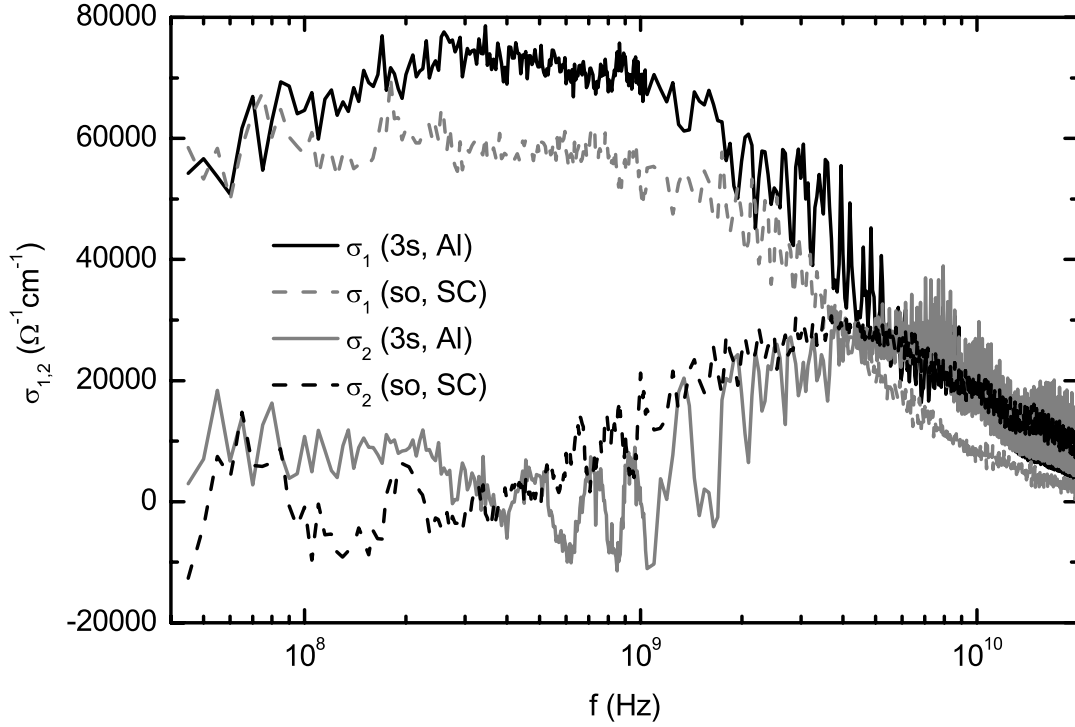


**Figure 7.3:** Spectra of the UPA233c sample at 3 K: comparison of short-only calibration (so, SC) using the superconducting sample as short and three-standards calibration (3s, Al) using bulk aluminium as short, teflon as open, and a NiCr thin film as load.

reflection coefficient of the UPA233c sample at 3 K was analyzed using the short-only procedure with the superconducting sample at 1.7 K as short as well as with the three-standards procedure with aluminium, teflon, and a NiCr thin film as short, open, and load, respectively. The main features, the roll-off in the real part and a maximum in the imaginary part of the conductivity around 4 GHz, can be found in both data sets. This verifies that our findings definitely stem from the sample and are not due to the calibration procedure. However, when it comes to a quantitative analysis, some differences can been seen. Because of better reproducibility (recall Figure 5.4) in particular concerning the imaginary

part of the conductivity, the superconducting sample was generally preferred as a short, and since the low-temperature impedance of this sample is rather low, the quantitative analysis was performed with the short-only calibration procedure.

Unfortunately the low impedance of the UPA233c sample causes problems due to the imperfect nature of the contacts as already mentioned in Section 5.4. These effects were modelled as described in Appendix B.2 to obtain the intrinsic properties of the sample. However, as will be shown, the main results do not depend on this correction but also hold for the uncorrected data.
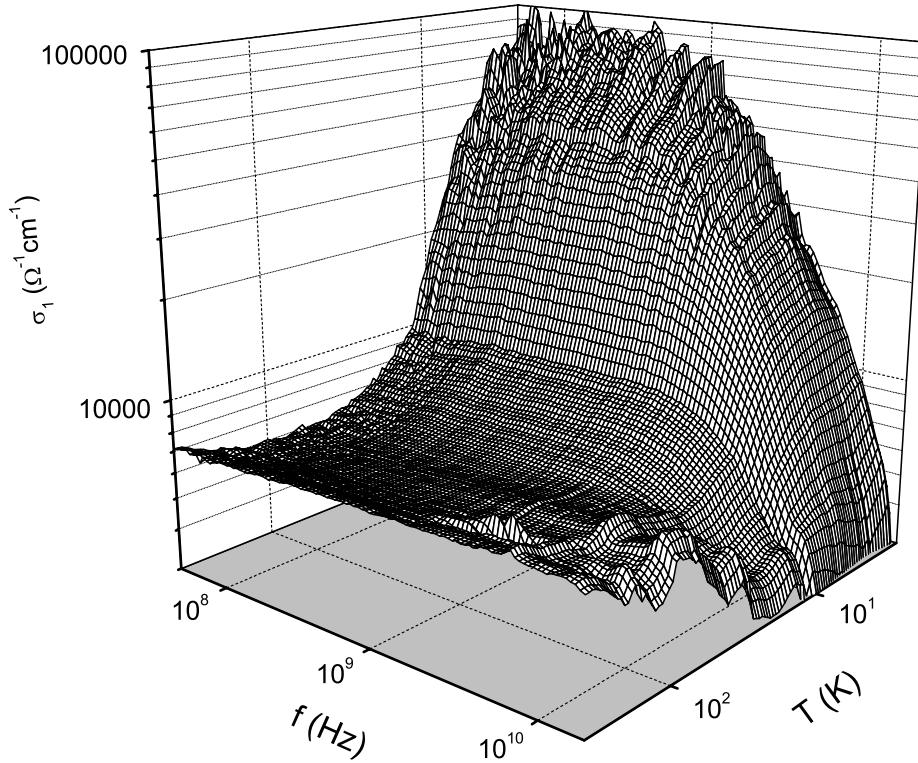


**Figure 7.4:** Three-dimensional visualization of $\sigma_1$ of UPd$_2$Al$_3$ at frequencies from 45 MHz to 20 GHz and temperatures from 2 K to 300 K.

To give an impression of the wealth of the obtained data on the UPA233c sample as well as some major findings, a surface plot of the temperature- and frequency-dependent conductivity is shown in Figure 7.4 (without correction of the contact impedance). Here the real part of the conductivity is plotted on a logarithmic scale versus frequency and temperature, each on logarithmic scales as well. For the lowest frequencies the temperature dependence of the conduc-

147

tivity basically reflects the dc conductivity as already discussed in Section 7.1.1, including (starting from room temperature) the high-temperature Kondo-like decrease of the conductivity, a minimum at the onset of coherence, a kink at the Néel temperature, and finally the strong increase of the conductivity up to the superconducting transition (which was excluded from the plot). Furthermore the low-frequency conductivity does not change for about a decade in frequency, thus suggesting that the conductivity will be frequency independent from the lowest frequencies of the Corbino experiment (45 MHz) down to dc as well (which is confirmed by the simultaneous measurement of the two-point dc resistance).

For the highest temperatures of up to 300 K, the conductivity is almost constant over the complete studied frequency range as expected for a normal metal (i.e. for temperatures above the heavy-fermion state). For the lowest temperatures (but still above the superconducting transition) on the other hand, the conductivity shows a strong frequency dependence: above approximately 1 GHz the conductivity decreases strongly with increasing frequency. This decrease is the Drude-type roll-off that was missing in previous studies of UPd$_2$Al$_3$ [3,4] and therefore was the main feature to be studied in the current project.

## 7.3   UPd$_2$Al$_3$ as a Drude Metal

As was already evident in the figures of the previous section, a Drude-like behavior can clearly be observed for low temperatures, i.e. at low temperatures UPd$_2$Al$_3$ behaves like a Drude metal with an extremely low scattering rate in the GHz range as was expected from its heavy-fermion characteristics and in particular in the light of the previous measurements at higher frequencies [3,4] that were discussed in Section 6.5.1. A typical low-temperature conductivity spectrum is shown in Figure 7.5. There data up to 30 GHz is shown[2] together

---

[2]As mentioned in Section 5.5, a superconducting sample as short might allow measurements up to 30 GHz instead of the standard upper limit of 20 GHz. Slightly above 20 GHz there is an apparent change in the measured curves due to the reduced number of data points at higher frequencies.
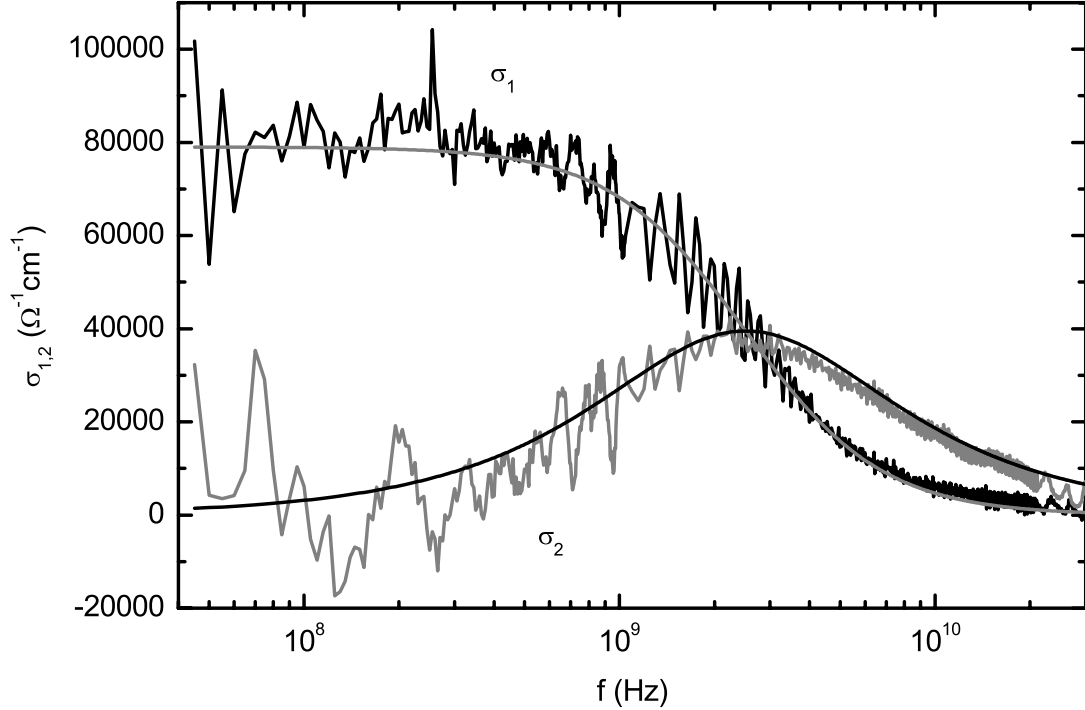
**Figure 7.5:** Conductivity spectrum of the UPA233c sample at 3.3 K together with a combined Drude fit of the real and imaginary parts (without considering the contacts).

with a combined fit of the real and imaginary parts of the conductivity according to the Drude model, and obviously the data are described extremely well by the simple Drude model, and in particular real and imaginary parts show corresponding behavior. Thus these measurements are not only the first detailed microwave measurements on UPd$_2$Al$_3$, but they are also unparalleled in a much larger framework. As was discussed in Section 6.2.3, microwave measurements on heavy-fermion compounds in general are scarce, and those that lead to conclusions concerning the frequency dependence of the microwave conductivity had to be assembled from many different experimental setups and even different samples. Thus the present measurements are much more significant, in particular keeping in mind that the final spectra are directly calculated from the measured complex reflection spectrum, the calibration spectrum of the same cooldown at lower temperatures in the superconducting state, and the room-temperature calibration, i.e. no further assumptions were made nor were any parameters adjusted.

But even in a yet more general framework there is hardly any comparable measurement in the following sense: here a Drude response was observed directly for real and imaginary parts of the conductivity over a frequency range that spans almost three orders of magnitude with the scattering rate almost in the center of this frequency window. As was illustrated in Section 6.1.4, such measurements cannot be performed for normal metals, and the present measurements is arguably superior to any of the few comparable measurements on metallike systems.
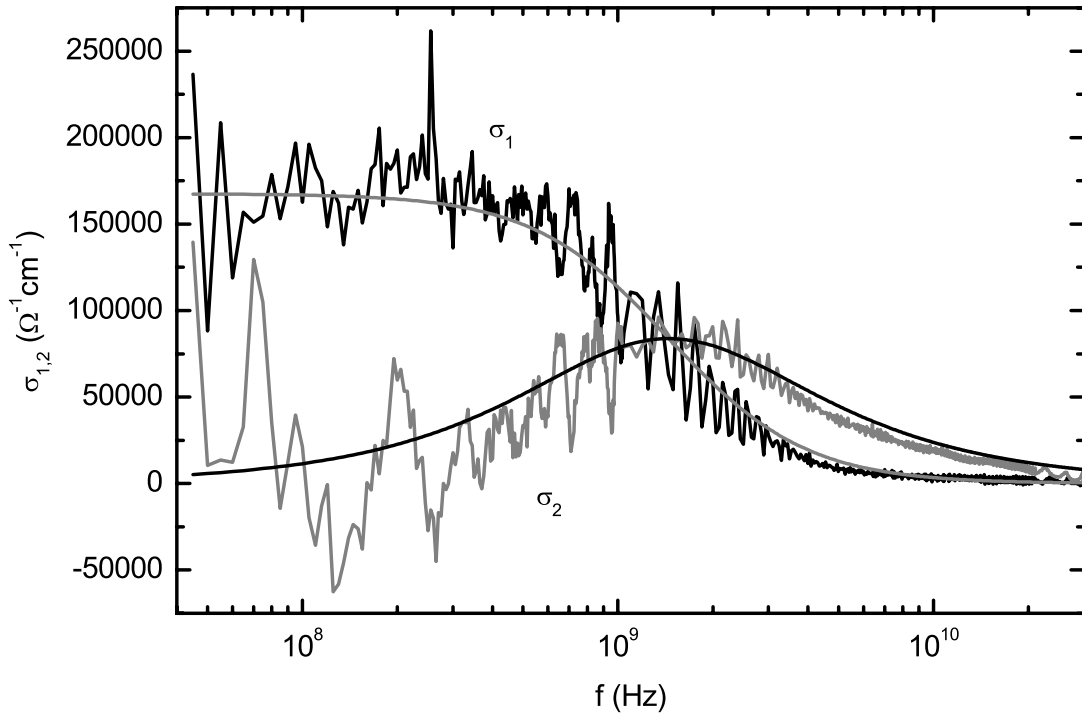
**Figure 7.6:** Conductivity spectrum of the UPA233c sample at 3.3 K where the influence of the contacts has been modelled, together with a combined Drude fit of both parts of the conductivity.

The data in Figure 7.5 were obtained without considering the contact problem discussed in Appendix B.2. However, when the influence of the contacts is included according to the model described there, then the overall statement that the conductivity spectra closely follow the Drude model still holds as can be seen in Figure 7.6 where the data corresponding to that of Figure 7.5 is shown now with the contact influence being modelled. This might be somewhat surprising since modelling the contacts does not simply scale the conductivity by a constant
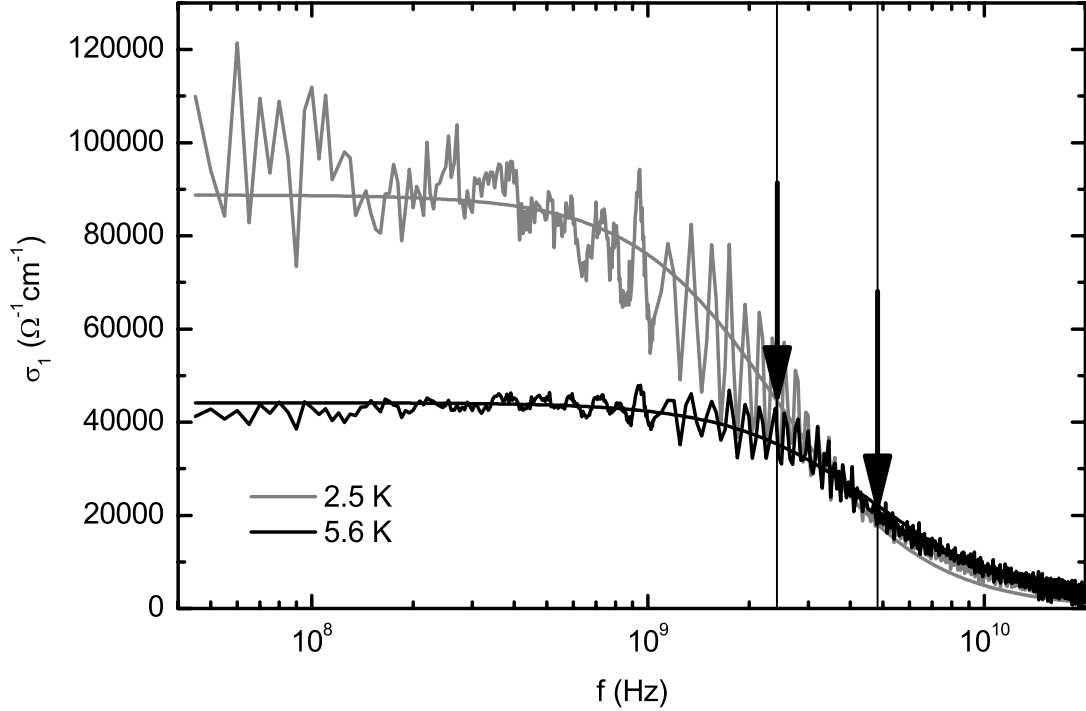
**Figure 7.7:** Conductivity spectra of the UPA233c sample at two temperatures without considering the influence of the contacts, together with Drude fits. The arrows indicate the scattering rates.

factor but actually also changes the shape of the conductivity spectra as is evident from the change in the scattering rate that can easily be found by comparing the frequency of the maximum in $\sigma_2$ in Figures 7.5 and 7.6.

## 7.3.1 Temperature Dependence

As could already be found in Figure 7.4, the microwave conductivity of UPd$_2$Al$_3$ strongly depends on temperature. We are particularly interested in the behavior at low temperatures where we can observe the Drude roll-off in the conductivity and concentrate on this temperature range. Typical spectra of the real part of the conductivity for two different temperatures are shown in Figure 7.7 together with the Drude fits following Equation 6.11:

$$\sigma_1(\omega) = \sigma_0 \frac{1}{1 + \omega^2 \tau^2} \tag{7.1}$$

Here it can be found that with increasing temperature the low-frequency con-
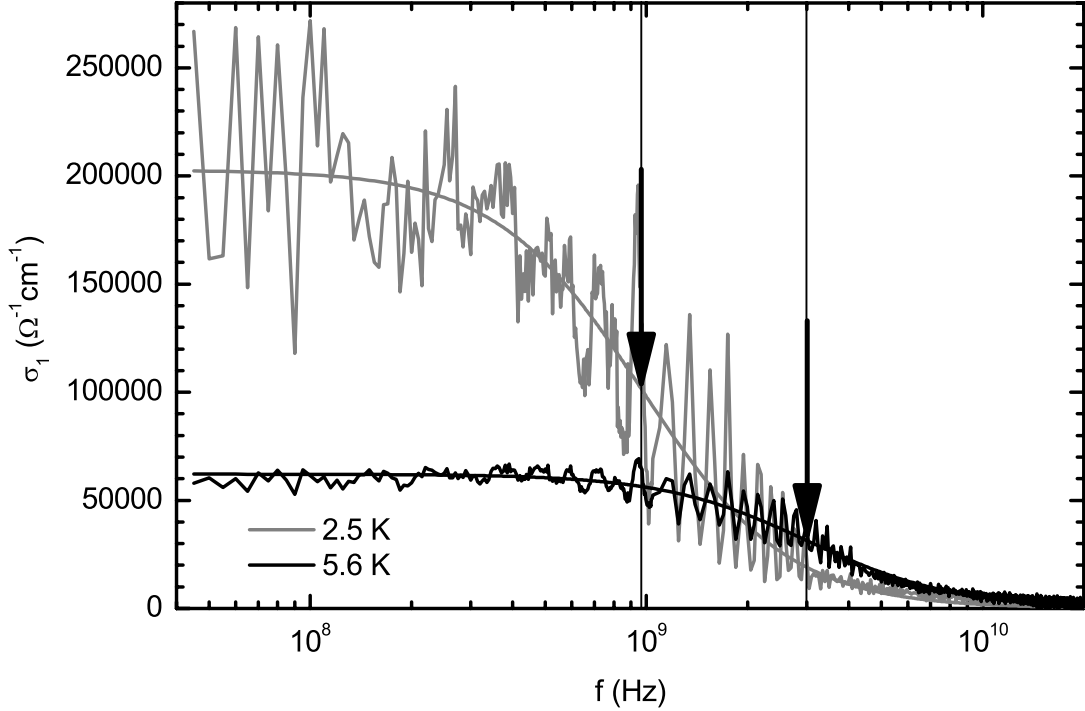
**Figure 7.8:** Conductivity spectra of the UPA233c sample at two temperatures where the influence of the contacts has been modelled, together with Drude fits. The arrows indicate the scattering rates.

ductivity of the spectra as well as the corresponding parameter $\sigma_0$ of the Drude model decrease strongly as was already evident from Figure 7.4 and corresponding to the simultaneous measurement of the dc resistance. What is less obvious from Figure 7.4 is the temperature dependence of the scattering rate, i.e. the frequency where the Drude roll-off occurs. This frequency is indicated in Figure 7.7 for the two exemplary temperatures, and it is found that the scattering rate also strongly depends on temperature, in approximately the inverse way: while for the higher of the two exemplary temperatures the dc conductivity is roughly half of that at the lower temperatures, the scattering rate approximately doubles.

The data shown in Figure 7.7 did not take into account the influence of the imperfect contacts. However, as was already evident from the comparison of Figures 7.5 and 7.6, a general Drude behavior of the conductivity spectra is conserved if the contacts are modelled according to Appendix B.2. The effect of considering the contacts on the temperature dependence can be found in Figure 7.8 where

the data sets of Figure 7.7 have been corrected with respect to the influence of the contacts: now obviously the low-frequency conductivity and $\sigma_0$ depend on temperature like the dc conductivity of the sample as determined from the four-point measurement since this is how the only free parameter of the model for the influence of the contacts was determined. But the temperature dependence of the scattering rate also behaves much the same way as before: while $\sigma_0$ decreases roughly by a factor of three from $T = 2.5$ K to $T = 5.6$ K, the scattering rate increases by approximately the same factor.

Considering UPd$_2$Al$_3$ as a Drude metal means that the electrodynamics of the system can be completely described by just two parameters, the dc conductivity $\sigma_0$ and the relaxation time $\tau$ (or correspondingly the dc resistivity $\rho_0 = 1/\sigma_0$ and the scattering rate $\Gamma = 1/\tau$). As was already suggested from Figures 7.7 and 7.8, the temperature dependences of $\rho_0$ and $\Gamma$ correspond. This finding is documented in Figure 7.9 where $\Gamma$ and $\rho_0$ (as determined from Drude fits to the conductivity spectra) are plotted as a function of temperature. It can clearly be found that at low temperatures the scattering rate $\Gamma$ and the dc resistivity $\rho_0$ obtained from Drude fits are proportional to one another.[3] Additionally, it can be seen that for the data corrected with respect to the contacts (main plot of Figure 7.9) the dc resistivity $\rho_0$ obtained from the spectra corresponds to the independent four-point results $\rho_{dc}$ over a rather large temperature range. Similar to what is described in Appendix B.2 for the two-point dc measurements, this is a general confirmation of the contact correction procedure where the only free parameter was adjusted with respect to the four-point resistivity at one particular temperature (typically 2.3 K) and then kept constant for all other temperatures.

The proportionality of resistivity and scattering rate evident from Figure 7.9 suggests that the temperature dependence of the resistivity is completely governed by that of the scattering rate. Since we have $\rho_0 = 1/\sigma_0 = \frac{m}{ne^2\tau} = \frac{m}{ne^2}\Gamma$,

---

[3]The upturn of $\Gamma(T)$ at the lowest temperatures is arguably an artefact of the calibration using the superconducting sample as short, it is not found for an aluminium short. Nevertheless the superconducting calibration was preferred because of the superior determination of the imaginary part of the conductivity.
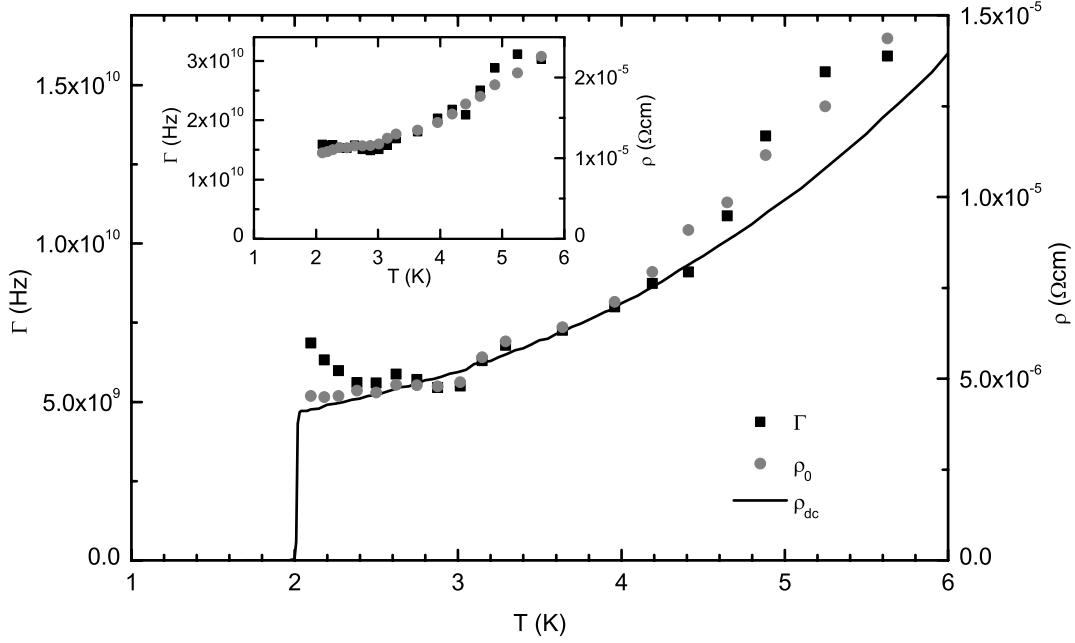
**Figure 7.9:** Temperature dependence of scattering rate $\Gamma = 1/\tau$ and resistivity $\rho_0 = 1/\sigma_0$, obtained from Drude fits of the UPA233c sample. The main plot was obtained from data corrected for contacts, inset data was not corrected for contacts. Additionally, the dc resistivity from four-point measurements is shown.

this means that $n/m$, the ratio of charge carrier density and effective mass, is temperature independent. This in turn can be explained most naturally by these two quantities themselves being constant in the temperature range under consideration.

Analyzing several measurements on the UPA233c sample and taking an average over the low-temperature region (below 6 K) where resistivity and scattering rate clearly correspond, a value $\sigma_0/\tau = \Gamma/\rho_0 = (1.3 \pm 0.4) \cdot 10^{15}$ ($\Omega$cm s)$^{-1}$ was obtained.[4]

---

[4]Within experimental uncertainty no difference was found between data corrected for imperfect contacts and such without this correction.

## 7.3.2 Quantitative Analysis and Discussion

The two parameters that are obtained from the Drude analysis, $\sigma_0$ and $\tau$ (or the reciprocal quantities $\rho_0$ and $\Gamma$), can first of all be compared to other experimental studies. As can be seen directly in Figure 7.9, the dc resistivity $\rho_0 = 1/\sigma_0$ obtained from the microwave spectra matches $\rho_{dc} = 1/\sigma_{dc}$ as obtained from independent dc measurements. This equivalency is necessary to establish the observed microwave conductivity to be the Drude response of the system: if $\sigma_0$ and $\sigma_{dc}$ differed, then additional features at lower frequencies would be necessary to explain the data, and then the observed roll-off in the GHz range could not be the Drude response. But obviously this is not the case for our measurements as is also evident from the frequency independence of $\sigma_1$ over at least an order of magnitude in frequency at the low-frequency end of the spectra.

For the relaxation time $\tau$ of the heavy fermions the present measurements based on microwave spectroscopy are arguably the most direct measurements since the scattering rate $\Gamma = 1/\tau$ is such a prominent feature in the Drude-like conductivity spectra. Other experiments that can reveal relaxation times are de Haas-van Alphen measurements [161], and the superconducting as well as 'normal' heavy-fermion states of UPd$_2$Al$_3$ have been studied intensively with this technique [152, 162–165], the results of these experiments concerning the band structure and effective masses will be discussed later. The relaxation times observed in de Haas-van Alphen experiments are usually expressed in terms of the Dingle temperature $T_D = \hbar/(2\pi k_B \tau)$ [161, 166, 167]. For different de Haas-van Alphen orbits in UPd$_2$Al$_3$ Dingle temperatures between 0.10 K and 0.28 K corresponding to relaxation times from $4.3 \cdot 10^{-12}$ s to $1.2 \cdot 10^{-11}$ s (or scattering rates $\Gamma$ from $8.2 \cdot 10^{10}$ Hz to $2.3 \cdot 10^{11}$ Hz) were found. These relaxation times are much shorter than found from the microwave spectra although the de Haas-van Alphen experiments were performed at even lower temperatures (the high magnetic field suppresses the superconductivity) and on single crystals with even higher quality than our UPA233c thin film sample as evident from the residual resistivity ratios [152,164] (the single crystal that is included in Figure 7.1 was one

of those used for these studies). But as was already pointed out by Dingle [168], the relaxation time obtained from de Haas-van Alphen experiments can differ from the relaxation time effective in transport measurements, with the latter one exceeding the former one, and this effect is generally found in experiments [161]: scattering rates determined from de Haas-van Alphen experiments are a factor 10 to 100 larger than those deduced from transport experiments, and right this behavior is also found for the current study on UPd$_2$Al$_3$.

In the previous section it was found from the observed relaxation time $\tau$, the dc conductivity $\sigma_0$, and the relation

$$\sigma_0 = \frac{ne^2\tau}{m} \tag{7.2}$$

that the ratio $n/m$ of charge carrier density and effective mass at low temperatures is constant. Thus from knowledge of either charge carrier density or effective mass the other quantity can be obtained. Let us employ an estimate for the charge carrier density from literature: the unit cell of UPd$_2$Al$_3$ has a volume of $\Omega = 1.029 \cdot 10^{-22}$ cm$^3$ [150] and each unit cell contains one uranium atom. It was found experimentally [160, 169] that the valence electrons constitute two distinct systems, one of itinerant nature that is responsible for the heavy-fermion behavior and the superconductivity and one localized system responsible for the magnetic properties. Theory for this so-called 'dual model' has established that each uranium atom contributes two electrons to the localized system and one to the itinerant system [170, 171]. Thus the charge carrier density for the electric conductivity in the heavy fermion state can be estimated to be approximately $10^{22}$ cm$^{-3}$. From this estimate and using the experimental result for $\sigma_0/\tau$ from the microwave experiments, one obtains an effective mass of 2200 for the heavy charge carriers, much larger than the values of 66 [145] or 49 [150] obtained from specific heat measurements. For this considerable difference five causes are possible and they will be briefly discussed in the following, namely: Equation (7.2) does not hold, the determination of the relaxation time or the dc conductivity from the microwave spectra is flawed, the literature value of the effective mass is too low, or the literature value for the charge carrier density is too high:

**Validity of Equation (7.2):** In Section 6.1.2 this equation was obtained on classical grounds, whereas the electronic conduction in metals is clearly governed by quantum mechanics. However, applying Fermi statistics, exactly the same equation is obtained for the model of free electrons [1, 104, 166, 172] where the Fermi surface is spherical. In fact the Fermi surface of UPd$_2$Al$_3$ is not spherical, but has a much more complex shape as will be discussed in Section 7.4.3. Thus the Fermi surface will be larger compared to the ideal spherical case, leading to an enhanced conductivity whereas we observe the opposite effect, the conductivity is much smaller than expected from Equation (7.2).

**Microwave result of dc conductivity:** The low-frequency limit of the conductivity spectra does not only comply with independent dc measurements on the same samples but also with thin-film and single-crystal data from literature. Thus this data is beyond doubt.

**Relaxation time from microwave spectra:** The roll-off in the frequency-dependent conductivity at low temperatures is a huge effect and is seen for different calibrations as well as different samples (see Section 7.5). Thus this feature is established on solid experimental grounds. One could argue that this reduction in $\sigma_1$ does not reflect the Drude response but is due to some different, unknown origin. But then it would be surprising that the conductivity spectra follow the Drude form so closely. Furthermore the temperature dependence of the obtained scattering rate scales with that of the dc resistivity (Figure 7.9), another strong indication that the observed relaxation time also determines the dc resistivity. Thus there seems to be no other plausible explanation for the conductivity roll-off than the Drude response with the appropriate scattering rate.

**Effective mass:** In the literature there exist several estimates for the effective mass of the heavy quasiparticles in UPd$_2$Al$_3$. The generally accepted determination of the mass of heavy fermions is from specific heat data. Here, in contrast to the procedure employed by Dalichaouch *et al.* [150], that used by Geibel *et al.* [145, 173, 174] also considers parameters of the superconducting state and is independent of an estimation of the charge carrier density and as

such more authoritative. The resulting effective mass of 66 [145] (Dalichaouch *et al.*: 49 [150], where three electrons per uranium atom were assumed) corresponds to the largest cyclotron effective mass of 65 found in UPd$_2$Al$_3$ [152, 164] using de Haas-van Alphen oscillations, another technique that directly reveals the effective mass without assumptions on the charge carrier density. This coincidence of two rather different techniques provides strong confidence in their results. However, the analysis of specific heat data assumes a spherical Fermi surface, which is not the case for UPd$_2$Al$_3$.

**Charge carrier density:** There is no direct experimental determination of the itinerant charge carrier density in UPd$_2$Al$_3$. As mentioned above, the dual model assumes one itinerant electron per uranium atom resulting in a charge carrier density of approximately $10^{22}$ cm$^{-3}$. If this number is used for the effective mass calculation by Dalichaouch *et al.* mentioned above (instead of three electrons per uranium atom) then one obtains an effective mass of 71, in reasonable agreement with the the independent determinations of the effective mass stated above. This supports the estimation of the itinerant charge carrier density.

Thus none of the possible causes for the severe quantitative disagreement is an obvious candidate. The quantity with least experimental support seems to be the charge carrier density and in Section 7.4.3 another experimental indication will be given that in the microwave experiments only a fraction of the itinerant electrons in the system cause the main response, but that this can account for a factor of more than thirty seems to be a pretty large stretch.

One more intricate possible cause for the mismatch is that for the specific heat data as well as in the derivation of Equation (7.2) a spherical Fermi surface is assumed whereas the Fermi surface of the real material has a much more complex shape. But since the microwave data closely follows the form of the Drude model and the effective mass determined from specific coincides with the de Haas-van Alphen results, one is tempted for both cases to accept that this assumption does not affect the applicability of the conclusions drawn from it. Thus the problem remains unsolved at this point.

## 7.3.3   Comparison with Submillimeter Results

Before moving to an analysis of the microwave data in the framework of the extended Drude model, another comment on the obtained microwave data should be made, that is the comparison with the data that was obtained with a submillimeter spectrometer at higher frequencies and that was discussed in Section 6.5.1, i.e. the combination of data obtained in adjacent frequency ranges.
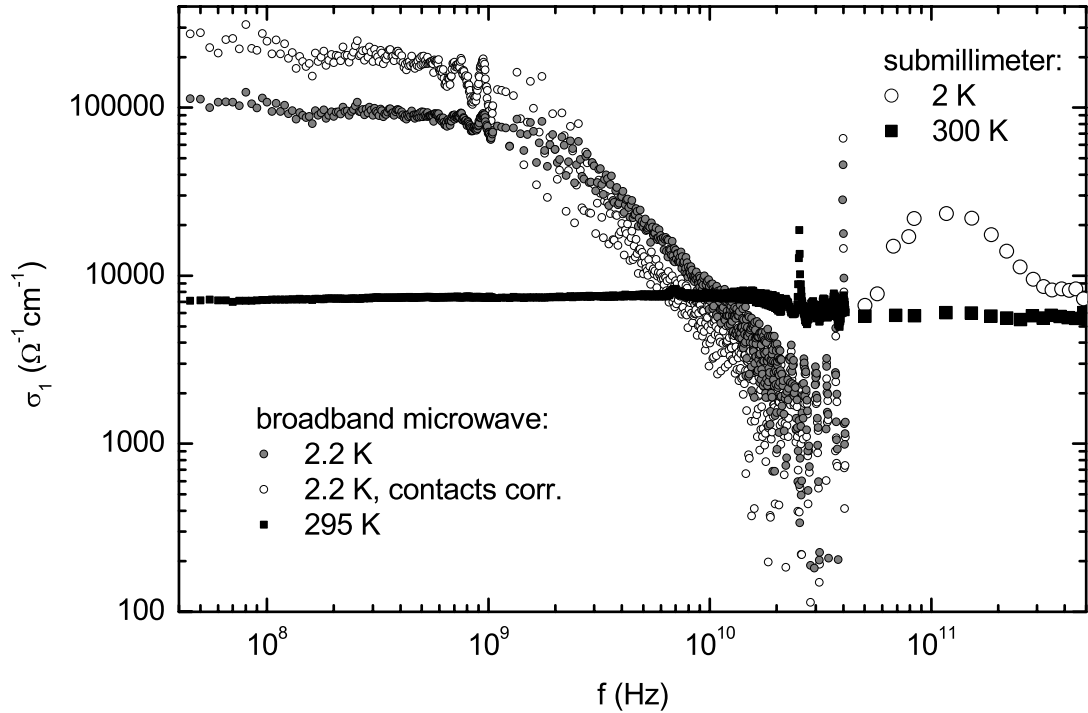


**Figure 7.10:** Combined plot of conductivity spectra of UPd$_2$Al$_3$ obtained by broadband microwave (with and without correction of imperfect contact) and submillimeter spectroscopies at two different temperatures. Microwave and submillimeter data were obtained on different samples. Reliable frequency range of the microwave spectrometer is up to 20 GHz. Submillimeter data taken from [4].

Figure 7.10 shows spectra obtained by the two techniques for two temperatures, one around room temperature and one right above the superconducting transition around 2 K. For the low-temperature microwave measurements the data are shown with and without consideration of the contribution of the contacts. For the microwave data one has to keep in mind that the microwave Cor-

bino spectrometer works reliably up to 20 GHz, but in this figure data exceeding 40 GHz is also plotted, although the problems in this frequency range are evident from the large scattering of the data at low temperature and the resonant feature at high temperature. One drawback of this comparison is that the microwave and submillimeter data could not be obtained on the same sample due to geometrical instrumental limitations. Both samples are high-quality thin films grown by the Mainz group [155, 157], but the sample used for the microwave spectra is slightly superior compared to the one for the submillimeter measurements in terms of a larger residual resistivity ratio as well as a higher $T_c$ .

Unfortunately there is no overlap of the frequency ranges of the two spectrometers. However, at room temperature the conductivity spectra in both frequency ranges are basically constant and even the absolute conductivity values only differ by 25%, for optical spectroscopy spanning such a large frequency range and data obtained on different samples a very small value. At low temperature the situation is more complicated. As discussed in Section 6.5.1, the submillimeter experiments found a suppressed conductivity around 1 cm$^{-1}$, and the microwave spectra show the Drude roll-off to highest observed frequencies. Thus the combination of the two techniques clearly hints at a minimum in $\sigma_1$ , but unfortunately this minimum has to be somewhere in the frequency range that is accessible by neither of the two techniques. Although the frequency range reliably covered by the Corbino spectrometer is only up to 20 GHz, data at higher frequencies seem to be meaningful at least up to 30 GHz (due to the calibration with the superconducting state) whereas at yet higher frequencies the data is strongly affected by experimental errors evident in several data points with negative $\sigma_1$. The submillimeter data on the other hand has 1.7 cm$^{-1}$, corresponding to 50 GHz, as the lowest accessible frequency for this particular sample, already an extremely low value for quasioptical experiments. Thus the data of the two different techniques are consistent also at low temperatures, but the interesting feature of the minimum in $\sigma_1$ around 1 cm$^{-1}$ (corresponding to 30 GHz) cannot be observed directly since it is right in the frequency gap between the two spectroscopic techniques.

# 7.4   UPd$_2$Al$_3$ Beyond the Drude Model

The fact that the microwave spectra of UPd$_2$Al$_3$ can be fit with the Drude model inherently characterizes UPd$_2$Al$_3$ as a Fermi liquid. The Fermi liquid description [135], as based on Landau's theory [134], is the generally accepted way to describe the electronic properties of 'normal' metals. The quadratic temperature dependence of the dc resistivity at low temperatures that was discussed in Section 7.1.1 is usually taken as the hallmark of Fermi liquid behavior, this temperature dependence of the resistivity is caused by a quadratic temperature dependence of the scattering rate. Starting from a general equivalence of temperature and energy, one expects the scattering rate not only to depend on temperature, but also on frequency and this frequency dependence can be probed by spectroscopic means like the present study.

## 7.4.1   Frequency-Dependent Scattering Rate

As shown in Section 6.3.3, the frequency-dependent scattering rate can be deduced from the conductivity spectra. In particular the scattering rate is proportional to the real part of the frequency-dependent resistivity, Equation (6.26). Unfortunately the proportionality factor, the plasma frequency, is difficult to obtain in our special case. In general it can either be calculated from the effective mass and charge carrier density in the normal state (from independent studies) or it can be obtained from optical spectra in the normal state. But both approaches are problematic for our material: as discussed in the previous section, the charge carrier density of the heavy-fermion state is not established, and if the plasma frequency of the normal state is used, then one does not know whether all charge carriers of the normal state actually enter the heavy fermion state, an effect that is not included in the analysis presented in Section 6.3.3. But to study just the frequency dependence of the scattering rate, this problem can be avoided by simply using the frequency-dependent resistivity instead of the scattering rate, thus neglecting the prefactor. This is particularly fortunate since this allows direct

comparison with the temperature-dependent dc resistivity, which is also related to the scattering rate (via the Drude formula) but incorporates the same problems concerning the charge carrier density and the effective mass. Thus only the resistivity will be discussed in this section, but the conclusions directly hold for the scattering rate.

## 7.4.2 Fermi Liquid Theory

Since we are concerned with the question whether the frequency-dependence of the resistivity (or the scattering rate, respectively) can be explained by Fermi liquid theory, we focus on that temperature range which exhibits a $T^2$ behavior in the dc resistivity, i.e. from 2.0 K up to 3.2 K. Figure 7.11 shows a typical resistivity spectrum of the UPA233c sample at 2.5 K where the effects of the contacts have been taken into account to allow for a quantitative comparison with the dc resistivity data. For frequencies below 5 GHz the real part $\rho_1$ of resistivity is basically constant but increases considerably at higher frequencies. Unfortunately the scattering of the data at high frequencies is rather large, but nevertheless the increase is evident. Figure 7.11 also shows the prediction of Fermi liquid theory according to:

$$\rho = \rho_0 + a \left( T^2 + B/A \left( \frac{h}{k_B} f \right)^2 \right) \quad , \tag{7.3}$$

where $\rho_0 = 2.0 \cdot 10^{-6}$ Ωcm and $a = 2.4 \cdot 10^{-7}$ Ωcm/K² were used according to the dc resistivity data, and $B/A$ was set to $(2\pi)^{-2}$ as described in Section 6.4.1. Obviously this prediction does not describe the data sufficiently, the predicted increase in resistivity from $4.500 \cdot 10^{-6}$ Ωcm to $4.506 \cdot 10^{-6}$ Ωcm is orders of magnitude smaller than the experimentally observed one. Thus the data was fit to Equation (7.3) with $B/A$ as the only free parameter and the result gives a satisfactory description of the data as is also shown in Figure 7.11. Obviously the resulting $B/A$ is much larger than theoretical predictions, from measurements at different temperatures and from several cooldowns a value $B/A = 100 \pm 40$ was deduced. This is more than three orders of magnitude larger than the prediction
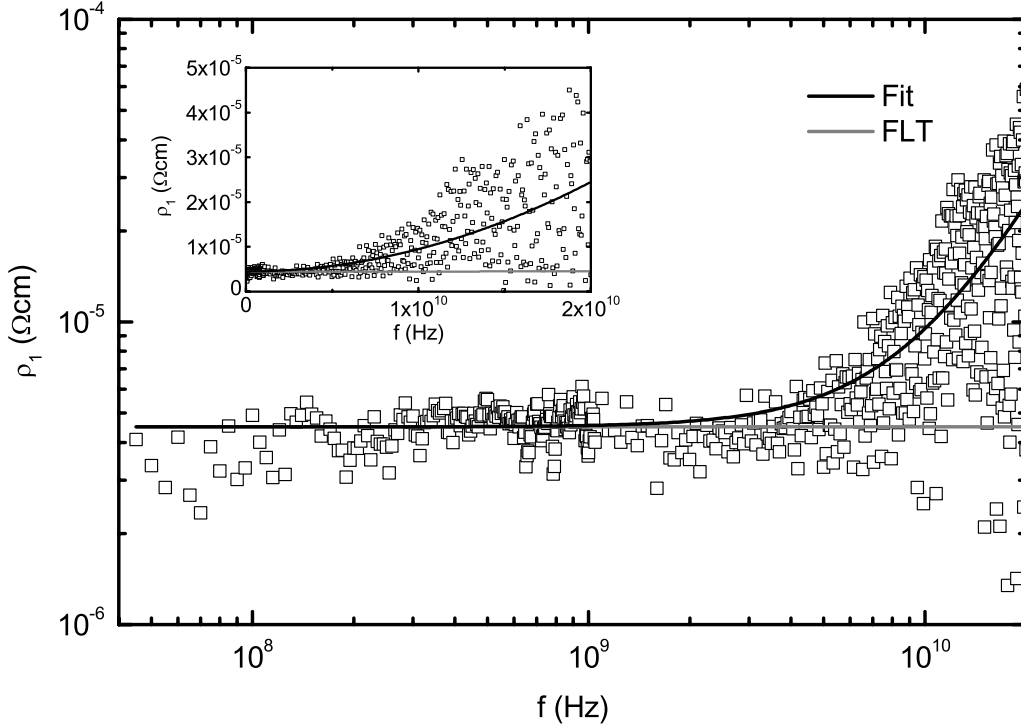
**Figure 7.11:** Real part $\rho_1$ of resistivity of the UPA233c sample at 2.5 K with a Fit and the Fermi liquid theory (FLT) prediction. The main plot is on logarithmic scales, the inset shows the same data on linear scales.

of Fermi liquid theory. This huge difference raises some doubts whether electron-electron scattering really is the dominant scattering mechanism in this compound as was generally assumed or at least whether the frequency dependence predicted by Fermi liquid theory is masked by another, much stronger frequency dependence of different origin. Unfortunately the quality of the experimental data is far from perfect, and therefore it is hard to determine the ratio $B/A$ accurately, but the shortcomings of the basic Fermi-liquid prediction are clearly seen. While the recent results of 0.31 and 0.37 for the ratio $A/B$ by Tran *et al.* [120] were already much smaller than the theoretical prediction of $(2\pi)^2 \approx 40$, our estimate of 0.01 is yet much smaller. I.e. the two experiments differ considerably, but both show that a simple Fermi-liquid description is inadequate to describe the experimental observations.

Strictly speaking Equation (6.30) and thus also Equation (7.3) only hold in the low-energy limit, i.e. these equations give the leading frequency and temperature

dependences for energies much smaller than the relevant energy scale (in basic Fermi liquid theory the Fermi energy, in our case the Kondo scale of the heavy fermions). But they only hold if either temperature or energy is dominant with respect to the other whereas in the case that the two are of the same order of magnitude the scattering rate has a slightly different form as calculated by Morel and Nozières [135, 139]:

$$1/\tau \propto \frac{(\pi k_B T)^2 + (\hbar\omega)^2}{1 + \exp(-\hbar\omega/k_B T)} \quad . \tag{7.4}$$

Here the denominator $1 + \exp(\hbar\omega/k_B T)$ gives rise to an additional frequency-dependent contribution. But the effect is only of order one (for the above example at 2.5 K the denominator of Equation 7.4 changes from 2 for $f = 0$ Hz to 1.68 for $f = 20$ GHz). Including this function into the fit, i.e.

$$\rho = \rho_0 + \frac{2a}{1 + \exp(-\hbar\omega/k_B T)} \left( T^2 + B/A \left( \frac{h}{k_B} f \right)^2 \right) \quad , \tag{7.5}$$

where $B/A$ is the only free parameter, one obtains $B/A = 90\pm30$. The difference compared with the fit without the additional denominator is only marginal and the two different fits basically coincide, i.e. if the second fit were shown in Figure 7.11, it would be indistinguishable from the Fermi liquid fit which is already shown there.

Thus the observed frequency dependence of the low-temperature scattering rate, though apparently quadratic, disagrees quantitatively with Fermi liquid theory by three orders of magnitude and thus it is hard to maintain Fermi liquid theory as a reasonable explanation for the frequency dependence of the scattering rate found in the experiment.

### 7.4.3  Multiple Drude Responses

A different explanation might arise from a completely different extension of the simple Drude model. The Drude model just assumes that all carriers contributing to charge transport are scattered after an average relaxation time $\tau$, no matter what the origin of the scattering might be. If there are different scattering mechanisms, e.g. for the Fermi liquid model discussed above electron-electron and

impurity scattering, then the scattering rates add according to Matthiessen's rule [104], leading to an effective scattering rate entering the Drude model. In contrast to this, one might also assume that there are several distinct, independent systems of charge carriers that are characterized by different scattering rates (and also different charge carrier densities and effective masses) that do not interact and therefore cannot be described by a simple Drude model using an effective scattering rate for the complete system. Instead two or more independent Drude responses add only when it comes to the actual measurement that probes all subsystems simultaneously leading to a combined signal.[5]

The possibility of such distinct electronic subsystems is justified by de Haas-van Alphen measurements [152, 164] where different effective masses as well as different scattering rates ('Dingle temperatures') were found corresponding to different orbits on the multi-sheeted Fermi surface that was determined theoretically [164, 171, 175, 176] and that was found to be in accordance with the results of the de Haas-van Alphen measurements. The Fermi surface of UPd$_2$Al$_3$ as calculated by Knöpfle *et al.* [176] is shown in Figure 7.12. Here the very different structure of the different sheets of the Fermi surface is evident. The variety of experimentally observed de Haas-van Alphen orbits as indicated in Figure 7.12 displays cyclotron effective masses from 5.7 to 65 and relaxation times from $4.3 \cdot 10^{-12}$ s to $1.2 \cdot 10^{-11}$ s, i.e. a rather non-uniform response for different parts of the Fermi surface. As already mentioned in Section 7.3.2, results from de Haas-van Alphen measurements cannot be transferred directly to transport measurements in a quantitative manner. In particular transport measurements do not probe particular orbits on the Fermi surface but the low-energy excitations of the complete Fermi surface simultaneously. However, since the Fermi surface consists of several sheets of very different structure (e.g. compare the large 'party hat' to the small 'cigar' in Figure 7.12), one can expect different parts of the

---

[5]The possibility of multiple Drude responses for a heavy-fermion compound was mentioned for UPt$_3$ by Sulewski *et al.* [118] but abandoned in favor of the pioneering introduction of a frequency-dependent scattering rate.
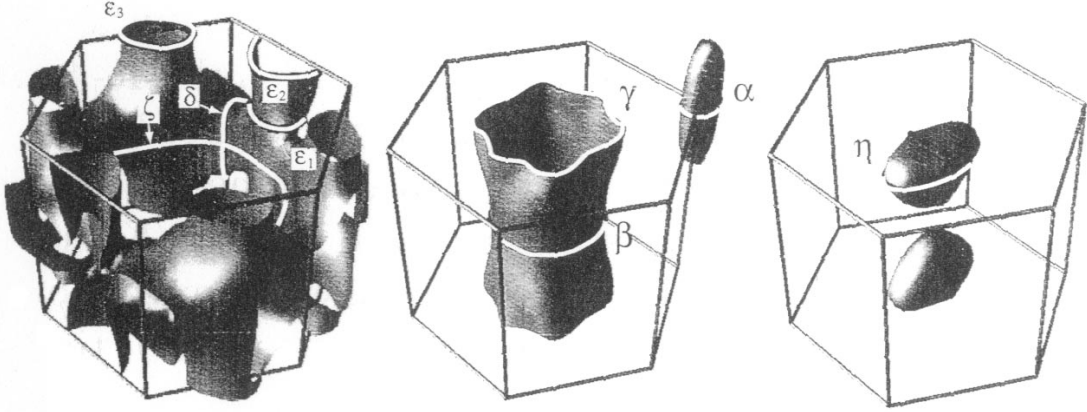
**Figure 7.12:** Multi-sheeted Fermi surface of UPd$_2$Al$_3$ as calculated by Knöpfle *et al.* [176]. The first figure shows the 'party hat', the second the 'column' and the 'cigar', and the third the 'egg'. The indicated orbits correspond to those found in de Haas-van Alphen measurements. Figure taken from [164].

Fermi surface to have very different properties in terms of effective mass and scattering rate determining the transport properties, and one can expect these parts to be distinct from each other.

If such distinct electronic subsystems exist, then the conductivity of each subsystem can be Drude-like, but the overall response will not follow the simple Drude model since the scattering rates do not combine to an effective scattering rate of the complete system. Thus the conductivity found in experiment has to be modelled as the combination $\sum \sigma_i$ of several independent Drude systems with distinct scattering rates $\Gamma_i = 1/\tau_i$ and dc conductivities $\sigma_{0,i}$ (which in turn depend on the effective masses $m_i$, charge carrier densities $n_i$, and relaxation times $\tau_i$). The easiest such case is the combination of only two subsystems and this case is discussed in Appendix C. Of particular interest is the combination of one subsystem of low scattering rate and high dc conductivity with another one of much higher scattering rate and much lower dc conductivity (e.g. one system of heavy carriers with low scattering rate and one of light carriers with high scattering rate). The overall conductivity spectrum of this system will be completely dominated by the subsystem with low scattering rate, but the resistivity spectrum corresponding to the frequency-dependent scattering rate and effective

mass (as discussed in Section 6.3.2) displays strong features that depend on both subsystems. I.e. the second subsystem that hardly influences the conductivity spectrum can lead to huge effects in the frequency-dependent scattering rate.
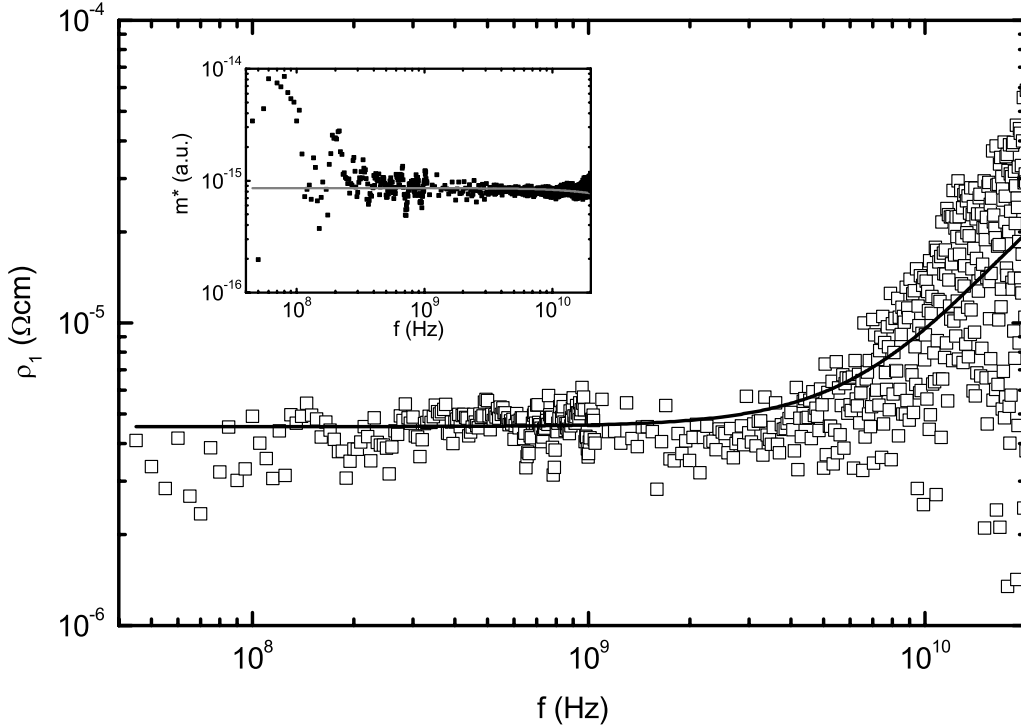


**Figure 7.13:** Real part $\rho_1$ of resistivity of the UPA233c sample at 2.5 K with a calculated curve using the combination of two independent Drude responses. The inset shows the effective mass with the same model.

An application of the model of such two independent Drude systems to the same resistivity spectrum (i.e. to the frequency-dependent scattering rate) that was already discussed in terms of Fermi liquid theory (compare Figure 7.11) is shown in Figure 7.13. Here the parameters were chosen in such a way that the conductivity spectrum is dominated by a Drude response with parameters as determined from a fit of the measured conductivity and only a much weaker second conductivity contribution with much higher scattering rate is added.[6] Obviously, this model can describe the experimental data comparably well as the quadratic

---

[6]The actual parameters are: $\sigma_{0a} = 2 \cdot 10^5 \, (\Omega\text{cm})^{-1}$, $\tau_a = 1.9 \cdot 10^{-10} \, \text{s}$, $\sigma_{0b} = 2 \cdot 10^3 \, (\Omega\text{cm})^{-1}$, and $\tau_b = 3.8 \cdot 10^{-12} \, \text{s}$.

fit of Figure 7.13. Here it should be pointed out that the calculated curve shown in Figure 7.13 is not a fit. Unfortunately the high-frequency data scatters too much to allow for a meaningful fit with two free parameters (the other two being determined from the simple Drude fit of the conductivity spectrum). Thus the current experimental results only allow for a general discussion of such a 'multiple Drude response' and not for a quantitative analysis. However, as is evident from Figure 7.13, the strong frequency dependence of the scattering rate that is orders of magnitudes stronger than predicted by Fermi liquid theory as discussed in Section 7.4.2 can easily be modelled even by the easiest case of the combination of independent subsystems, namely of only two such subsystems. In the real system the scattering rate can be expected to vary continuously throughout each of the separated sections of the Fermi surface and thus the overall scattering rate can have a yet richer frequency dependence than predicted by the easiest case of two subsystems with fixed scattering rates as was discussed here.

Thus the strong frequency dependence of the scattering rate can easily be explained by the presence of distinct electronic subsystems. Apparently this is the first time that such a mechanism is favorably discussed for electronic transport of a heavy-fermion system. This is somewhat surprising since for the superconducting state of heavy-fermion materials multiband effects have already been discussed extensively and furthermore the de Haas-van Alphen measurements gave evidence for a complex Fermi surface as was obtained theoretically. But on the other hand one has to keep in mind the experimental difficulties to study the dynamics of heavy fermions as discussed in Section 6.2.3. Broadband microwave spectroscopy as is possible with the current Corbino spectrometer is clearly the tool of choice to study such effects. A combined response of distinct subsystems might also be the reason why the frequency-dependent scattering rate of heavy-fermion UPt$_3$ as studied by Tran *et al.* [120] was inconsistent with Fermi liquid theory. Like for UPd$_2$Al$_3$, the Fermi surface UPt$_3$ is complex and multisheeted as determined theoretically [177,178,180] and experimentally by de Haas-van Alphen experiments [177,179,180], and therefore a combination of independent electronic

subsystems is as reasonable as for UPd$_2$Al$_3$. Furthermore the large difference of the prefactors of the quadratic frequency dependence of the scattering rate found for UPt$_3$ by Tran *et al.* [120] and for UPd$_2$Al$_3$ in the current study could also be easily explained since this prefactor would not represent 'universal' Fermi liquid behavior but the particular structure of the electronic subsystems that cannot be expected to coincide for UPt$_3$ and UPd$_2$Al$_3$ since the Fermi surfaces differ considerably in their details.

If the existence of different, distinct electronic subsystems is assumed, then the large quantitative discrepancy concerning the charge carrier density that was found in Section 7.3.2 can be discussed in new light. The conductivity spectra that were discussed in terms of the original Drude model in Section 7.3 only concern the quasiparticles with an extremely low scattering rate, i.e. the heavy quasiparticles that characterize the heavy-fermion state. If there are additional subsystems with higher scattering rates, they might have a considerably smaller contribution to the dc conductivity and the charge carrier density of these subsystems might be connected to the large fraction of 'missing' charge carriers that were discussed in 7.3.2. But again a factor of 30 seems to be pretty large to be explained by such an effect.

At this point where the frequency dependence of the scattering rate has been discussed extensively, one might have another look at the Drude spectra as discussed in Section 7.3. Since the scattering rate was found to be frequency dependent, one might ask why the Drude description of the conductivity spectra is so convincing. The reason for that is that the impurity scattering (as determined form the residual dc resistivity) dominates up to 5 GHz and thus the scattering rate is basically constant up to that frequency. The increase of the scattering rate at higher frequencies then causes deviations from the simple Drude behavior that can already be seen in Figures 7.5 and 7.6. Thus at frequencies above a few GHz the conductivity of UPd$_2$Al$_3$ does not perfectly follow the simple Drude model any more, but for a better description the frequency-dependent scattering rate has to be taken into account.

## 7.4.4 Frequency-Dependent Effective Mass

The previous sections only discussed the frequency-dependent scattering rate as observed in the microwave experiment. However, as was shown in Section 6.3.2, the extended Drude model does not only allow for a frequency-dependent scattering rate but also for a frequency-dependent effective mass, and the latter one can be extracted from the measured complex conductivity much the same way as the former. (Again the problem of the prefactor is avoided by studying a relative frequency dependence instead of absolute values.) However, the observed frequency dependence of the effective mass is rather weak as can be seen in the inset of Figure 7.13: within experimental resolution the effective mass is frequency independent.[7] In the framework of Fermi liquid theory this is expected [1], i.e. no further evidence against electron-electron interaction being the cause of the frequency-dependent scattering rate comes from the effective mass.

On the other hand, within the model of multiple distinct Drude subsystems the effective mass exhibits a considerable frequency dependence as shown in Appendix C. But for the parameters chosen to model the observed frequency-dependent scattering rate, the strong frequency dependence of the effective mass occurs only at slightly higher frequencies than accessible in the experiment. As shown in the inset of Figure 7.13, the calculated effective mass of the model consisting of two Drude subsystems is well within the observed data, i.e. this model is also consistent with the observed frequency-dependent effective mass. However, experimental data at higher frequency would be of great help to confirm the model of multiple independent Drude subsystems and to attach actual numbers to the parameters of the subsystems.

---

[7]The low-frequency data suggest a considerable frequency dependence, but arguably this is an experimental artefact. The effective mass is mainly determined by the imaginary part of $\sigma$, and as can be seen in Figures 7.5 and 7.6, the low-frequency results of $\sigma_2$ show strong, erratic deviations from the Drude response which are probably caused by experimental imperfections.

# 7.5   Sample Dependence

The analysis of the microwave measurements on $UPd_2Al_3$ presented up to now was based on data obtained on the highest-quality UPA233c sample. This high quality combined with the rather large thickness of 150 nm results in the particular difficulty of poor contacts. To demonstrate that the main conclusions do not depend on peculiarities of this particular sample but in fact are general properties of $UPd_2Al_3$, additional data obtained on other samples (grown by the Mainz group with the same procedure as sample UPA233c) is presented now.

## 7.5.1   Sample UPA001

In terms of quality the second best $UPd_2Al_3$ thin film sample that was available for Corbino measurements was sample UPA001. Although clearly inferior to sample UPA233c (as evident from the residual resistivity ratio of $R_{300K/2K} = 4.4$), it can still be considered a high-quality sample. The dc resistivity as deduced from the two-point measurement that was taken with the Corbino spectrometer is presented in Figure 7.14. Measurements by the group in Mainz (and included in Figure 7.14) showed that this sample becomes superconducting below 1.0 K. Unfortunately these temperatures cannot be reached with the current Corbino setup and therefore the calibration procedure could not take advantage of the superconducting state as a short. Thus bulk aluminium was used for the short calibration, and since the Corbino resistance of this sample reaches values of up to 7 $\Omega$ at the resistance maximum around 100 K, the full procedure using three standards (additionally teflon and NiCr thin film) was employed instead of the short-only procedure.

Since this sample is of lower quality and additionally because it is much thinner than the UPA233c sample (40 nm compared to 150 nm), the effective impedance of sample UPA001 of around 1.5 $\Omega$ at low temperatures compares to 0.1 $\Omega$ for the UPA233c sample. Thus for the UPA001 sample the sensitivity of the spectrometer is much higher (see Section 5.5.1), and therefore the spectra
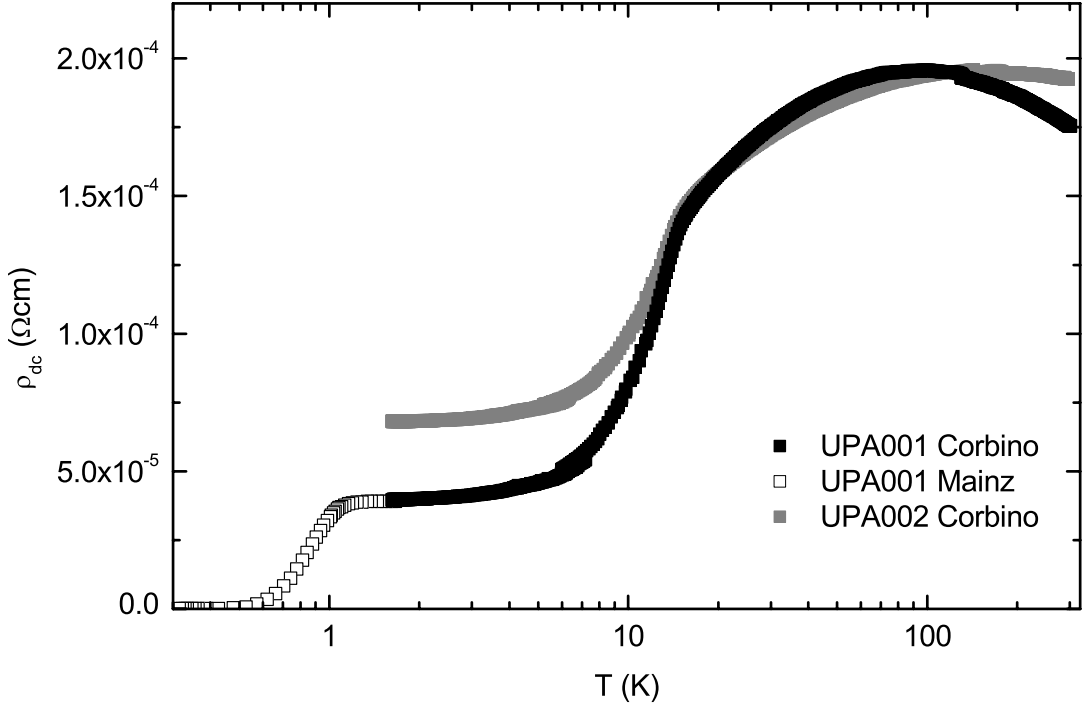
**Figure 7.14:** Temperature dependence of the dc resistivity of samples
UPA001 and UPA002 as obtained from two-point measurements
using the Corbino setup. For UPA001 additional data obtained
in Mainz, revealing the superconducting transition, is shown.

obtained on the UPA001 sample like those shown in Figure 7.15 appear much
less 'noisy' than those taken on the UPA233c sample. On the other hand the
same reason causes unwanted features in the spectra of the UPA001 sample: sub-
strate effects can clearly be seen like a resonant feature around 4 GHz (only at
high temperatures, at lower temperatures it is weakened due to the increased
conductivity of the film) and strong features above 10 GHz. But the general
features that are known from the UPA233c sample are also found in the UPA001
sample: at low frequencies the conductivity is basically independent of frequency
and follows the dc conductivity. But at low temperatures the real part of the
conductivity exhibits a clear roll-off above 4 GHz, at higher frequencies than for
the UPA233c sample. This higher scattering rate is a direct evidence of the re-
duced sample quality as already expected from the smaller residual resistivity
ratio (which is proportional to the low-temperature relaxation time). Similar to
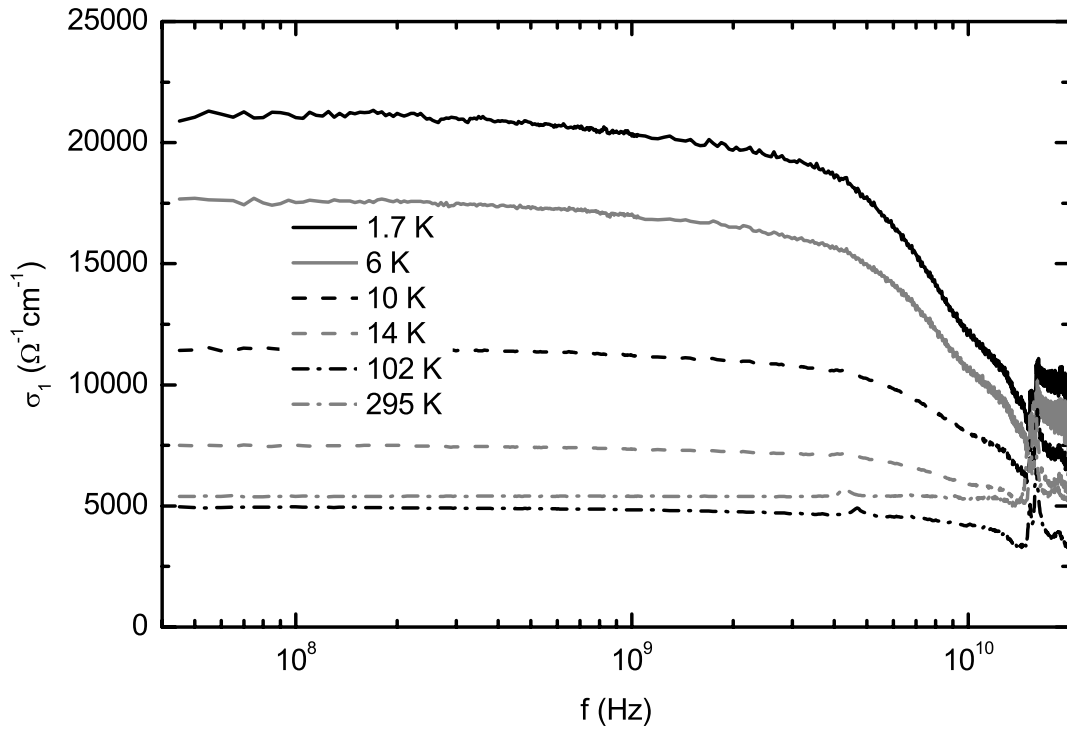
**Figure 7.15:** Conductivity spectra of the UPA001 sample at different temperatures. Resonances at high frequencies are due to the substrate.
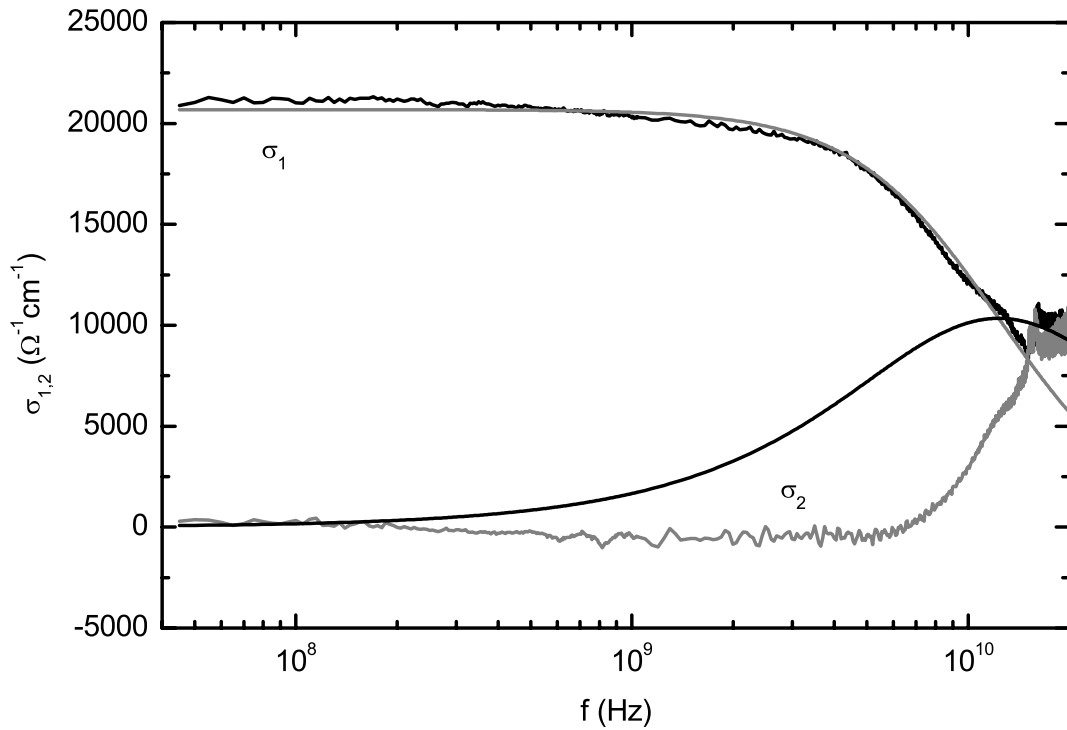


**Figure 7.16:** Complex conductivity of the UPA001 sample at 1.7 K with a Drude fit of $\sigma_1$ up to 15 GHz. The resulting spectrum for $\sigma_2$ is shown as well.

the observations on the UPA233c sample, the roll-off in $\sigma_1$ follows closely the
Drude model as can be seen in Figure 7.16 where $\sigma_1$ was fit up to 15 GHz. But
the imaginary part $\sigma_2$ does not obey the Drude prediction as would be expected
from the real part $\sigma_1$. The origin for this discrepancy is not clear, but it cannot
be ruled out completely that this is due to problems with the contact resistance
between the Corbino probe and the gold pads that were deposited onto the sam-
ple to serve as contacts. Here it should be noted that for the UPA233c sample,
using the superconducting sample as a short, this contact resistance due to the
mechanical contact at the probe is eliminated as this contact resistance arguably
does not change below 20 K. Thus for broadband microwave experiment on the
current UPA001 sample it would be of great help to reach superconductivity at
temperatures below 1 K where the superconducting sample can act as the short
standard.

## 7.5.2   Sample UPA002

The third sample to be presented, labelled UPA002, has a thickness of 40 nm
(like the UPA001 sample). The dc resistivity of this sample is included in Fig-
ure 7.14, and the reduced quality of this sample is immediately evident in the
much higher resistivity at low temperatures and correspondingly in a lower resid-
ual resistivity ratio of $R_{300K/2K} = 2.8$. Samples with such low residual resistivity
ratios do not become superconducting [154]. Figure 7.17 shows the conductiv-
ity spectra obtained on the UPA002 sample at a representative set of tempera-
tures. As already familiar from samples UPA233c and UPA001, the low-frequency
conductivity follows the dc behavior and the high-temperature spectra reveal a
frequency-independent conductivity. At low temperatures the conductivity also
shows a roll-off at high frequencies, but this effect is much weaker than for the
two previous samples: while for UPA001 the roll-off could be followed to approx-
imately half of the dc conductivity, for UPA002 only a reduction of one quarter
can be observed. This is mainly caused by the reduced sample quality and the
correspondingly poor dc and low-frequency conductivity at low temperatures, but
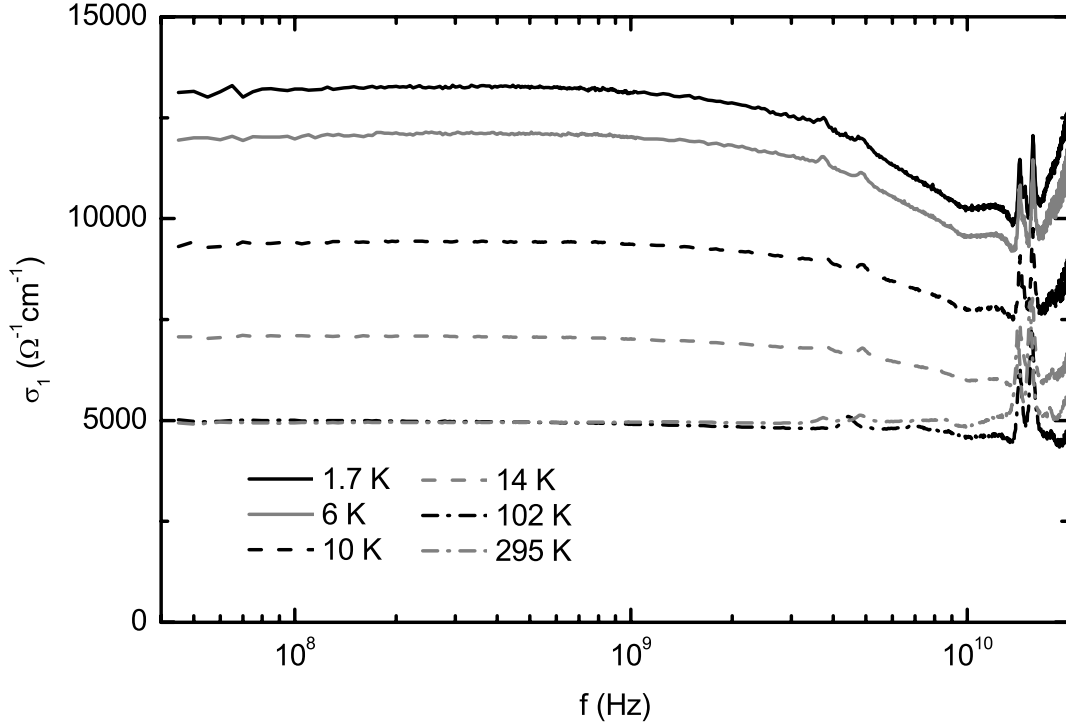
**Figure 7.17:** Conductivity spectra of the UPA002 sample at different temperatures.

additionally the spectra are strongly perturbed by substrate resonances at high frequencies similar to those seen in the UPA001 sample, effectively setting an upper frequency limit of 10 GHz for studies on this sample which again restricts the observable part of the conductivity roll-off. However, the general behavior that was observed in the higher-quality samples UPA233c and UPA001 can still be found on this sample UPA002, but it is also clear that the definite attribution of the Drude-type roll-off and the quantitative analysis relies on the higher quality of the two samples UPA233c and UPA001.

Besides the three samples presented here, additional samples with yet reduced sample quality were measured, but there no clear roll-off was observed. The conductivity was found to be frequency independent at lower frequencies whereas substrate resonances prevented clear results above a few GHz, but extrapolating from the three samples that were already discussed, no reduction of the conductivity would be expected anyway in the generally accessible frequency range of up to 20 GHz. However, these measurements confirm the strong sample dependence

of the low-frequency conductivity in UPd$_2$Al$_3$ and the requirement of high-quality samples to study the dynamics of the heavy quasiparticles.

## 7.6   Power Dependence

To ensure that the results described above were obtained in the Ohmic regime, power-dependent measurements were performed as described in Section 5.2. Neither in the spectra that were obtained at 4.2 K for power levels changed by a factor of 1000 were any signs of non-linear response found nor in a complete measurement performed with the UPA233c sample at a power level 100 times higher than usual. A spectrum obtained during this measurement is compared to that of a standard measurement (with low power level) in Figure 7.18. Clearly, the frequency dependence of the conductivity is not affected by the power level.
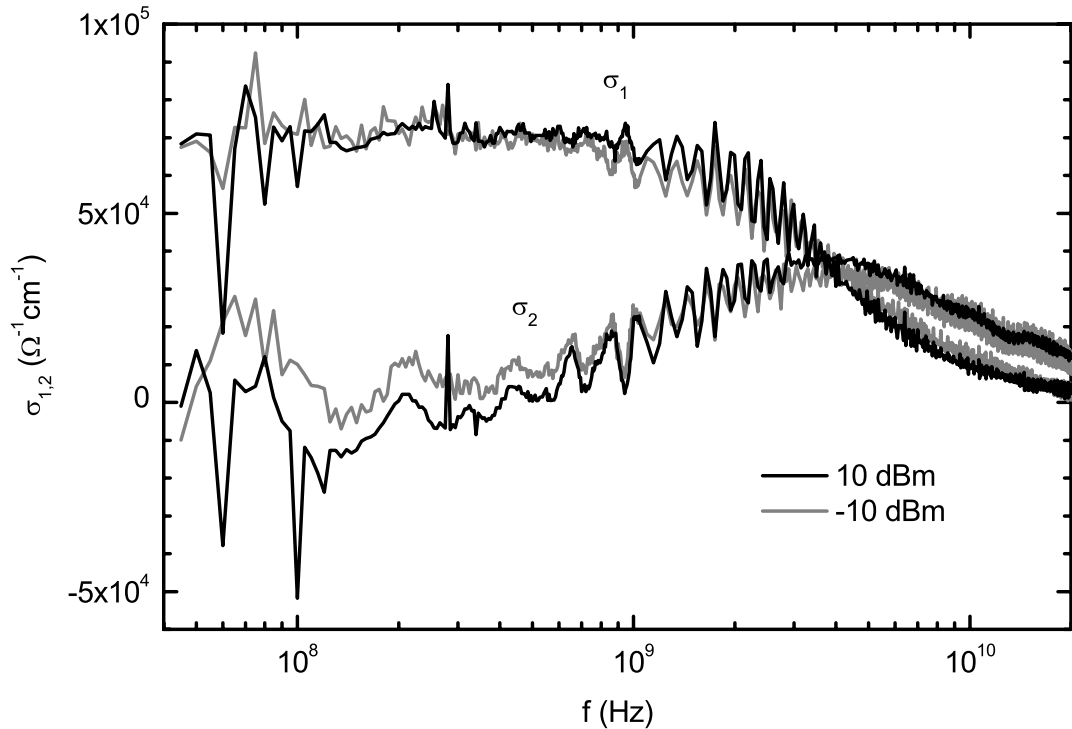
**Figure 7.18:** Conductivity spectra of the UPA233c sample at 2.3 K obtained with different power levels.

# 7.7 Future Microwave Studies on Heavy-Fermion Systems

The broadband microwave measurements on $UPd_2Al_3$ that were presented in the previous sections are the first to directly observe the complete Drude behavior of the heavy quasiparticles in a heavy-fermion compound. The characteristic frequency corresponding to the scattering rate that was found here is much lower than those previously reported as results of conventional far-infrared spectroscopic studies. Therefore the question arises whether these new results only apply to $UPd_2Al_3$ or whether also for other heavy-fermion materials much lower scattering rates are to be expected than deduced from the far-infrared experiments. Additionally, the yet unsettled problem of the quantitative discrepancy in charge carrier density as well as the possible indication of multi-band Drude conduction definitely call for confirmation in a different material.

## 7.7.1 Future Broadband Microwave Measurements on Other Heavy-Fermion Compounds

Before the Corbino measurements were started on $UPd_2Al_3$, there existed already the detailed submillimeter studies [3, 4] on this material that revealed that the Drude roll-off has to be at extremely low frequencies, below 1 cm$^{-1}$. Up to now there exist no comparable submillimeter measurements on other heavy-fermion materials simply because no comparable samples, i.e. high-quality thin films, were available. The only other compound that has been studied rather extensively in the submillimeter and microwave frequency ranges is $UPt_3$ [116, 120] where a Drude-like conductivity roll-off was inferred at much higher frequencies than the present study showed for $UPd_2Al_3$. Thus even if there were suitable samples of $UPt_3$ available, one would not expect to observe a strong frequency dependence of the conductivity with the Corbino spectrometer. However, such a study would be an important confirmation of the results by Tran *et al.* [120] since their data was obtained with several different instruments on several different samples.

The lack of suitable thin film samples is also the reason why up to this moment no measurements on other heavy-fermion materials were performed with the Corbino spectrometer. Generally the study on heavy-fermion materials concentrates on single-crystal samples and only very little attention is paid to thin films. Although there were several attempts to grow thin films of different heavy-fermion compounds (UBe$_{13}$ [181, 182], CeCu$_2$Si$_2$ [183], CeAl$_3$ [184], UPt$_3$ [185], CeCu$_6$ [186–190]), most of them were not successful when it comes to obtained sample quality compared to single crystals, in particular none of these thin films were epitaxial. The only epitaxial thin films that have been available are the UPd$_2$Al$_3$ films grown by the Mainz group and that enabled not only the present microwave experiments but also the quasioptical submillimeter studies [3, 4].

Fortunately there is hope for suitable thin film samples of a different compound, UNi$_2$Al$_3$, as the Mainz group has recently succeeded in growing thin film samples of this material [191] using the same techniques of the previous growth of UPd$_2$Al$_3$ thin films. UNi$_2$Al$_3$ is isostructural to UPd$_2$Al$_3$ and undergoes antiferromagnetic and superconducting transitions at $T_N = 4.6$ K and $T_c =1.0$ K, respectively [192]. The availability of high-quality UNi$_2$Al$_3$ thin films is particularly fortunate since the quality of UNi$_2$Al$_3$ single crystals is comparably low due to difficulties in the crystal growth [193]. This is a major reason why up to now UNi$_2$Al$_3$ has not been studied optically in as much detail as other compounds, the single optical study so far by Cao *et al.* in 1996 went down to frequencies of 30 cm$^{-1}$ and only spectra at temperatures 300 K, 100 K, and 10 K are published [194]. Merely general heavy-fermion behavior was reported there, including a narrow Drude roll-off with a scattering rate of 25.3 cm$^{-1}$. Thus broadband microwave measurements seem to be inappropriate as the frequency scale is much smaller, but one has to keep in mind that also UPd$_2$Al$_3$ was considered to have an even higher scattering rate [114] at low temperatures until the submillimeter measurements showed that this assumption was wrong. Furthermore 10 K is far above the Neel-temperature of UNi$_2$Al$_3$ , and thus any possible magnetic excitations in the antiferromagnetic state could not be observed by that study. Detailed

178

studies on $UNi_2Al_3$ thin films in the near future seem particularly opportune as such samples are grown right now, and therefore submillimeter and broadband microwave measurements should be performed on samples of the same quality, in contrast to the $UPd_2Al_3$ studies where differences in sample quality cannot be ruled out completely, see Section 7.3.3. Additionally, the thickness of the films can hopefully be adjusted to reach higher resolution for the Corbino measurements than for the UPA233c sample. Since the residual resistivity of $UNi_2Al_3$ thin films at the moment is around $2 \cdot 10^{-5}\,\Omega cm$ [191], considerably higher than for the UPA233c sample (and a factor of two higher than for single-crystalline $UNi_2Al_3$ [195]), it is hard to estimate right now whether the scattering rate might actually be accessible with the Corbino spectrometer, again demanding the combination with submillimeter measurements.

A disadvantage of $UNi_2Al_3$ compared to $UPd_2Al_3$, however, are the lower $T_N$ and $T_c$ which are harder to reach experimentally. In particular the superconducting state cannot be reached with the current Corbino spectrometer and this will not change until a $^3$He-system is established (compare Section 5.6.2). However, the studies on $UPd_2Al_3$ showed that the results of the superconducting calibration give high-resolution data and are more reliable concerning the imaginary part of the conductivity, but the calibration with an aluminium short showed qualitatively the same results, and even quantitative differences are small. Thus broadband microwave measurements on $UNi_2Al_3$ seem promising even if the superconducting state cannot be reached.

## 7.7.2   Superconducting State of $UPd_2Al_3$

Up to now the heavy-fermion state of $UPd_2Al_3$ was studied with the Corbino spectrometer, and the superconducting state only served as a calibration standard. However, superconductivity in heavy-fermion compounds in general has attracted enormous interest ever since it was first discovered in $CeCu_2Si_2$ by Steglich *et al.* in 1979 [196], with the evidence of unconventional superconductivity in $UPd_2Al_3$ by the Mainz group [146,154] being an extraordinary achievement.

Optical studies on superconductors are best known for the determination of the superconducting energy gap [1] but also for studies at comparably lower frequencies (recall the studies on high-$T_c$ superconductors in the group of Steven M. Anlage at the University of Maryland with a Corbino spectrometer [45, 46, 70]). Up to now the energy gap of UPd$_2$Al$_3$ has only been measured by the Mainz group, using tunnelling spectroscopy on thin films like those used for our studies and revealing an energy gap of 235 $\mu$eV (corresponding to 57 GHz) in the low-temperature limit [146, 153, 154]. But there the energy gap perpendicular to the films was probed whereas optical or microwave studies would probe the energy gap in the parallel direction. Since UPd$_2$Al$_3$ is an anisotropic system with respect to these two directions, a determination of the energy gap by optical means is of particular interest. However, since with the current Corbino spectrometer the base temperature of 1.63 K is only slightly below the $T_c$ of 2.0 K, significant Corbino measurements on superconducting UPd$_2$Al$_3$ will not be possible before lower temperatures can be reached.

# Chapter 8

# Conclusions and Outlook

In the present work the microwave conductivity of UPd$_2$Al$_3$, a heavy-fermion compound, was studied. At low temperatures several physical properties of heavy-fermion materials (best reputed is the specific heat) exhibit peculiar behavior that is described quantitatively by attributing a large effective mass to the charge carriers. Such a mass enhancement goes hand in hand with a slowing down of the characteristic time scale of charge transport that is the relaxation time $\tau$. To study this relaxation time, a broadband measurement of the optical conductivity is well-suited since the Drude model predicts a roll-off in the real part $\sigma_1$ and a peak in the imaginary part $\sigma_2$ of the conductivity at the scattering rate $\Gamma = 1/\tau$, two strong features to be found in the conductivity spectra. The experimental problem of this approach comes along with the slowing down: while for normal metals the characteristic frequency, the scattering rate, is found at far-infrared frequencies (a spectral range where experimental techniques and expertise are available for a long time), for heavy fermions the scattering rate is much lower, at frequencies that are much less common in solid state physics. In particular when the frequencies of interest reach the microwave range, there is no 'conventional' tool available for cryogenic spectroscopic studies. That is the reason why in the present study a new spectrometer was designed and established to allow for such experiments.

This novel spectrometer employs the Corbino geometry, i.e. the disc-shaped sample terminates a coaxial transmission line, thus reflecting the microwave signal that travels through that line. From the reflection coefficient that can be obtained phase-sensitively and as a function of frequency by use of a vector network analyzer, the complex conductivity spectra can be calculated. The realization of this concept for cryogenic measurements is difficult due to the elaborate calibration scheme that is necessary to extract the response of the sample from the measured signal which is dominated by imperfections of the different microwave elements. However, numerous tests have proven that with the present spectrometer broadband microwave measurements can be performed at temperatures down to 1.65 K, low enough to study the heavy-fermion behavior of $UPd_2Al_3$.

These experiments on $UPd_2Al_3$ now revealed that the scattering rate of the heavy quasiparticles is even lower than previously expected: while Degiorgi *et al.* determined a scattering rate of 60 $cm^{-1}$ at 6 K using far-infrared spectroscopy [114], the recent submillimeter results by Dressel *et al.* lead to estimates of 10 $cm^{-1}$ (300 GHz) at 8 K and 2 $cm^{-1}$ (60 GHz) at 2 K [3, 4],[1] whereas our microwave measurements now revealed that the actual scattering rates are yet much smaller: around 5 GHz at 2 K. The two former studies obtained incorrect values simply because their available spectral range did not reach low enough frequencies, they could not observe the characteristic Drude behavior directly but had to extrapolate.

In contrast to those investigations, the present broadband microwave experiments not only showed a roll-off in $\sigma_1$ and a corresponding peak in $\sigma_2$ but an overall frequency dependence that closely follows the prediction of the Drude model for more than two orders of magnitude in frequency. Actually these spectra not only constitute the most complete experimental observation of a Drude response in a heavy-fermion compound that was ever performed, but arguably among any metal that was ever studied spectroscopically, there is no comparably complete, direct measurement of the Drude response.

---

[1]The data shown in these articles is the non-renormalized scattering rate and has to be divided by the effective mass.

Since for the present measurements on $UPd_2Al_3$ a textbook-like Drude response was found, the attribution of the characteristic frequency of the roll-off and the peak to the scattering rate of the charge carriers is well established. This allows for a quantitative analysis of the conductivity spectra in terms of the ratio of charge carrier density and effective mass. Assuming the effective mass known from independent measurements, our studies reveal a much smaller charge carrier density than previously expected. But from an experimental point of view no independent determination of the charge carrier density is available at present, thus our study is the first to quantitatively address this question.

The observation of a rather low density of heavy quasiparticles is backed by deviations from the Drude model that could be found in the high-frequency limit of our spectra, at frequencies above the scattering rate. These can be analyzed in terms of a frequency-dependent scattering rate, and the effects found there are much stronger than can be explained in the framework of Fermi-liquid theory, the generally accepted description of the heavy quasiparticles in $UPd_2Al_3$. One possible explanation for these deviations is the combination of several conducting subsystems with distinct scattering rates as can easily be conceived by heavier and lighter quasiparticles. Then the low density of the heavy quasiparticles simply means that there is a considerable amount of other, lighter quasiparticles which do not contribute as much to the overall properties as the heavy ones.

Now that the broadband microwave studies on $UPd_2Al_3$ have revealed surprising results in terms of the extremely low scattering rate and the quantitative analysis of the charge carrier density, one should continue this path by studying related heavy-fermion materials. Unfortunately the present resolution of the Corbino spectrometer requires that heavy-fermion samples to be studied are available as thin films which are rather uncommon in the general study of these materials. We were very fortunate in obtaining the high-quality $UPd_2Al_3$ thin films grown by the group of Prof. Adrian in Mainz. Now this group has turned their attention to $UNi_2Al_3$, a related heavy-fermion systems. Thus thin films of this compound will be available in the near future, and they should be studied in the same way as the $UPd_2Al_3$ samples.

But the possible studies on correlated electron systems using the now established Corbino spectrometer go far beyond heavy-fermion thin films. A related group of materials are the Kondo insulators where the Fermi energy is not within the maximum of the density of states like in the heavy-fermion compounds, but within the adjacent hybridization gap. This directly results in a low conductivity at low temperatures and thus the reflection coefficient of these materials is much lower than for heavy-fermion compounds. Therefore with the current spectrometer measurements on bulk samples of Kondo insulators should be possible, and high-quality, single-crystalline samples of these materials are available. Furthermore there are experimental studies in the submillimeter frequency range on the exemplary Kondo insulator $SmB_6$ [197] that suggest that also for these materials at intermediate temperatures (around 15 K) a Drude-like roll-off in $\sigma_1$ with a rather low scattering rate exists whereas at lower temperatures there is a strong increase in $\sigma_1$ with increasing frequency, attributed to hopping processes. Here broadband microwave experiments can help to settle these attributions.

A rather different system of correlated electrons is the so-called Coulomb glass consisting of randomly distributed, localized electrons with Coulomb interaction. In these systems the electronic transport is dominated by hopping and the temperature- as well as the frequency-dependent conductivity depends on the correlations. The model realizations of electron glasses are highly doped silicon, and there have already been a few experimental studies in the GHz frequency range on Si:B [34], Si:As [31], and Si:P [32, 33] and in the submillimeter range on Si:P [35, 36]. But all these studies were restricted in the available frequency range, and this can limit the accessible conductivity range corresponding to the concentration of doping atoms. At the 1. Physikalisches Institut we now have the unique possibility to study the frequency-dependent conductivity of the same samples in the submillimeter as well as the microwave frequency ranges. Recently this work was started with experiments on Si:P in the submillimeter range [37], and now the frequency range of these studies can be considerably enhanced by the Corbino spectrometer. However, these studies are preferably performed at

rather low temperatures, and one has to find out experimentally whether the current setup is sufficient in this regard. Furthermore the conductivity of Si:P in these temperature and frequency ranges is rather small, i.e. a modification of the data analysis (how the conductivity is obtained from the reflection coefficient) might be necessary, but here the work by Martens *et al.* [62] might serve as a guiding line.

Even further possibilities to explore the dynamics of correlated electron systems open up if the restriction of the current spectrometer to isotropic systems can be lifted. At the present stage two-dimensional systems could be studied with respect to their in-plane properties whereas for the other direction as well as for one-dimensional systems a different probe design that is sensitive to the conductivity of only one direction is desired. But in principle such a probe, e.g. based on a microstrip, can be incorporated into the current spectrometer.

Thus a huge variety of different continuations of the current project opens up. The first step should be further studies on heavy fermions to confirm and extend the present result. But after that many different directions of research are possible and hopefully the present dissertation will serve as solid ground for these future endeavors.

# Appendix A

# Data Analysis

## A.1 Reflection Coefficient

The physical quantity that is measured by a network analyzer is the reflection coefficient $S_{11}$ which depends on the impedance $Z_L$ of the load that terminates the transmission line. The relationship between the two can be deduced as follows:

The load impedance $Z_L$ can be considered to be the termination of an ideal transmission line with characteristic impedance $Z_0$ as indicated in Figure A.1.
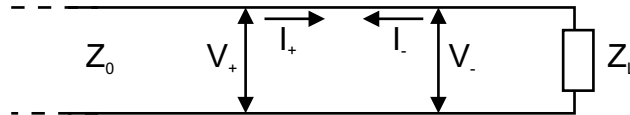


**Figure A.1:** Model of microwave reflection at the end of a transmission line.

On the transmission line two waves propagate, one towards the load (with voltage $V_+$ and current $I_+$ at the location of the load) and the other away from the load (with voltage $V_-$ and current $I_-$ at the location of the load). The load impedance is the ratio of the appropriately assigned voltage $V_L = V_+ + V_-$ and current $I_L = I_+ - I_-$:

$$Z_L = \frac{V_L}{I_L} = \frac{V_+ + V_-}{I_+ - I_-} \quad . \tag{A.1}$$

Since both waves propagate through the transmission line, their voltages and currents are related:

$$Z_0 = \frac{V_+}{I_+} = \frac{V_-}{I_-} \quad . \tag{A.2}$$

Using the definition of the reflection coefficient $S_{11} = V_-/V_+$ one obtains:

$$Z_L = \frac{V_+ + V_-}{V_+ - V_-} Z_0 = \frac{1 + S_{11}}{1 - S_{11}} Z_0 \quad . \tag{A.3}$$

This is equivalent to:

$$S_{11} = \frac{Z_L - Z_0}{Z_L + Z_0} \quad . \tag{A.4}$$

## A.2  General Error Model

As described in Chapter 4, the extraction of sample properties from the measured reflection coefficient relies on the calibration procedure. The following sections document the most important formulae that were used in the course of the current project. For clarity reasons the reflection coefficient that was denoted '$S_{11}$' in the main part of the dissertation will be marked 'S' in this section.

The basis equation for the error correction procedure is:

$$S_m = E_D + \frac{E_R S_a}{1 - E_S S_a} \quad . \tag{A.5}$$

This equation relates the measured reflection coefficient $S_m$ to the actual reflection coefficient $S_a$ of a sample. If the three error coefficients $E_R$, $E_D$, and $E_S$ are known, then the actual reflection coefficient $S_a$ can be obtained from the measured one by inverting the above equation:

$$S_a = \frac{S_m - E_D}{E_R + E_S(S_m - E_D)} \quad . \tag{A.6}$$

However, this procedure requires that the three error coefficients are known. To obtain the error coefficients, calibration measurements have to be performed.

## A.3  Three Additional Calibration Measurements

In the most general case three calibration measurements of known samples are performed and from these three measurements the three error coefficients are obtained. I.e. three reflection coefficients $S_{m,a}$, $S_{m,b}$, and $S_{m,c}$ are measured of

samples with known actual reflection coefficients $S_{a,a}$, $S_{a,b}$, and $S_{a,c}$, respectively. Then three equations

$$S_{m,j} = E_D + \frac{E_R S_{a,j}}{1 - E_S S_{a,j}} \tag{A.7}$$

can be solved for $E_D$, $E_S$, and $E_R$, and these three error coefficients can be determined as a function of the $S_{m,j}$ and $S_{a,j}$. Equations (A.7) were solved with Maple and the result was verified manually. Using a common denominator N defined as

$$
\begin{aligned}
N &= S_{m,a} S_{a,a} S_{a,c} - S_{a,a} S_{m,a} S_{a,b} - S_{a,a} S_{m,c} S_{a,c} - \\
&- S_{m,b} S_{a,b} S_{a,c} + S_{a,b} S_{m,c} S_{a,c} + S_{a,a} S_{a,b} S_{m,b} \quad,
\end{aligned} \tag{A.8}
$$

the results for the error coefficients are:

$$E_S \cdot N = S_{a,b} S_{m,c} - S_{m,c} S_{a,a} + S_{m,a} S_{a,c} - S_{m,b} S_{a,c} - S_{m,a} S_{a,b} + S_{a,a} S_{m,b} \tag{A.9}$$

$$
\begin{aligned}
E_D \cdot N &= -(-S_{a,a} S_{m,a} S_{m,b} S_{a,c} + S_{a,a} S_{m,a} S_{a,b} S_{m,c} + S_{a,a} S_{m,c} S_{m,b} S_{a,c} + \\
&+ S_{m,a} S_{a,c} S_{a,b} S_{m,b} - S_{m,a} S_{a,c} S_{a,b} S_{m,c} - S_{a,a} S_{m,c} S_{a,b} S_{m,b})
\end{aligned} \tag{A.10}
$$

$$
\begin{aligned}
E_R \cdot N^2 &= S_{a,a}^2 S_{m,a}^2 S_{m,b} S_{a,b} - S_{m,c} S_{m,b}^2 S_{a,b}^2 S_{a,a} - S_{m,c} S_{m,a}^2 S_{a,a}^2 S_{a,b} - \\
&- S_{a,a}^2 S_{m,a} S_{m,b}^2 S_{a,b} - S_{m,a}^2 S_{a,b}^2 S_{m,b} S_{a,a} + S_{m,a} S_{a,b}^2 S_{m,b}^2 S_{a,a} - \\
&- S_{a,a}^2 S_{m,c}^2 S_{a,b} S_{m,b} + S_{a,a}^2 S_{m,c} S_{a,b} S_{m,b}^2 - S_{m,c} S_{a,c}^2 S_{m,b}^2 S_{a,b} - \\
&- S_{m,c}^2 S_{a,c}^2 S_{m,a} S_{a,b} - S_{m,c}^2 S_{a,c}^2 S_{m,b} S_{a,a} + S_{m,c}^2 S_{a,c}^2 S_{m,b} S_{a,b} - \\
&- S_{m,c} S_{a,c}^2 S_{m,a}^2 S_{a,a} + S_{m,c}^2 S_{a,c}^2 S_{m,a} S_{a,a} - S_{a,a}^2 S_{m,a}^2 S_{m,b} S_{a,c} - \\
&- S_{m,a} S_{a,c} S_{a,b}^2 S_{m,b}^2 - S_{m,b} S_{a,b}^2 S_{a,c} S_{m,c}^2 - S_{m,a} S_{a,a}^2 S_{a,c} S_{m,c}^2 + \\
&+ S_{m,c} S_{m,b}^2 S_{a,b}^2 S_{m,c} + S_{m,c} S_{m,a}^2 S_{a,a}^2 S_{a,c} - S_{m,a}^2 S_{a,c} S_{a,b}^2 S_{m,c} + \\
&+ S_{a,a} S_{m,a}^2 S_{m,b} S_{a,c}^2 - S_{a,a} S_{m,a} S_{m,b}^2 S_{a,c}^2 + S_{a,a}^2 S_{m,a} S_{m,b}^2 S_{a,c} - \\
&- S_{a,a} S_{m,a} S_{a,b}^2 S_{m,c}^2 + S_{a,a}^2 S_{m,a} S_{a,b} S_{m,c}^2 + S_{a,a} S_{m,a}^2 S_{a,b}^2 S_{m,c} + \\
&+ S_{a,a}^2 S_{m,c}^2 S_{m,b} S_{a,c} + S_{a,a} S_{m,c} S_{m,b}^2 S_{a,c}^2 - S_{a,a}^2 S_{m,c} S_{m,b}^2 S_{a,c} - \\
&- S_{m,a}^2 S_{a,c}^2 S_{a,b} S_{m,b} + S_{m,a} S_{a,c}^2 S_{a,b} S_{m,b}^2 + S_{m,a}^2 S_{a,c} S_{a,b}^2 S_{m,b} + \\
&+ S_{m,a} S_{a,c} S_{a,b}^2 S_{m,c}^2 + S_{m,a}^2 S_{a,c}^2 S_{a,b} S_{m,c} + S_{a,a} S_{m,c}^2 S_{a,b}^2 S_{m,b} \quad. 
\end{aligned} \tag{A.11}
$$

## A.4   One Additional Calibration Measurement

If only one low-temperature calibration measurement is performed, one has to assume that the general temperature dependence of the three error coefficients can be satisfactorily replaced by letting just one error coefficient, $E_R$, be temperature dependent. This procedure can convert the data obtained by the network analyzer (NWA) using the room temperature calibration directly, without the need to recalculate the raw data measured by the NWA.

The NWA uses the error coefficients $E_D$, $E_S$, and $E_{R,NWA}$ (obtained by conventional room-temperature calibration) to determine the NWA-calibrated reflection coefficient $S_{NWA}$ from the measured raw reflection coefficient $S_m$:

$$S_{NWA} = \frac{S_m - E_D}{E_{R,NWA} + E_S(S_m - E_D)} \quad . \tag{A.12}$$

But at low temperature the actual reflection tracking $E_{R,a}$ differs from the room temperature reflection tracking $E_{R,NWA}$ and thus the measured $S_m$ is determined as follows (with $S_a$ being the actual reflection coefficient of the sample):

$$S_m = E_D + \frac{E_{R,a}S_a}{1 - E_S S_a} \quad . \tag{A.13}$$

Combining equations (A.12) and (A.13) one obtains:

$$S_{NWA} = \frac{E_{R,a}S_a}{E_{R,NWA} + S_a E_S(E_{R,a} - E_{R,NWA})} \quad . \tag{A.14}$$

To determine the low-temperature reflection tracking $E_{R,a}$, one performs an additional low-temperature measurement with a known standard with actual reflection coefficient $S_a^{stand}$, whereas the NWA obtains $S_{NWA}^{stand}$ (including room-temperature calibration), i.e. equation (A.14) now reads

$$S_{NWA}^{stand} = \frac{E_{R,a}S_a^{stand}}{E_{R,NWA} + S_a^{stand}E_S(E_{R,a} - E_{R,NWA})} \quad . \tag{A.15}$$

From such a measurement the low-temperature $E_{R,a}$ can be obtained:

$$E_{R,a} = E_{R,NWA}\frac{E_S - \frac{1}{S_a^{stand}}}{E_S - \frac{1}{S_{NWA}^{stand}}} \quad . \tag{A.16}$$

In the current project a short was used as low-temperature standard with actual reflection coefficient $S_a^{\text{short}} = -1$. Thus equation (A.16) becomes

$$E_{R,a} = E_{R,NWA} \frac{E_S + 1}{E_S - \frac{1}{S_{NWA}^{\text{short}}}} \quad . \tag{A.17}$$

If the actual reflection tracking is obtained like this, then the actual reflection coefficient $S_{11,a}$ of an arbitrary sample can be obtained from (A.14):

$$S_a = \frac{S_{NWA} E_{R,NWA}}{E_{R,a} + S_{NWA} E_S (E_{R,NWA} - E_{R,a})} \quad . \tag{A.18}$$

# Appendix B

# Performing Corbino Measurements

Many details of the Corbino spectrometer are mentioned in the main body of this dissertation. Some supplementary details of our experimental procedure and the course of typical measurements are additionally documented in the following sections.

## B.1   Preparing Samples for Corbino Measurements

To reduce the contact resistance between Corbino probe and sample, usually contact pads of a good metal (typically gold, 100 nm thick) are deposited onto the samples. The contact pads correspond to the Corbino probe, i.e. the (flat) surface of the sample is covered completely by the metal except for the ring of the Corbino disc. This geometry rules out the use of a conventional mask during the evaporation because the ring that acts as a mask has to be fixed somehow, and it is hard to avoid that the fastener prevents some part of the outer contact area to be covered by the metal. The Virginia group has solved this problem using photolithography [5, 63], but we have followed the procedure established by the Maryland group [70]: a solid shadow mask is used that is manufactured of a ferromagnetic material (we have used iron, 100 $\mu$m thick) and held in fixed

position on the sample by permanent magnets located on the back side of the sample holder that is used for the deposition.

To ensure that the Corbino contacts of the sample match the Corbino probe, the sample has to be aligned properly on the cylindrical sample holder that is used for the microwave measurements. Therefore the sample is fixed on the sample holder by a little amount of cryogenic vacuum grease [198] and then moved to the appropriate position (with the center contact in the axis of the sample holder cylinder) by a special alignment jig.

## B.2 Poor Contacts

The data analysis presented in Section 5.4 assumes that the sample is probed only in the area that is part of the Corbino disc defined by the inner and outer radii ($a_1$ and $a_2$, respectively) which is the area that is between the Corbino contacts that are usually deposited on the sample to accurately define this particular geometry corresponding to the dimensions of the adapter used as the Corbino probe. Close inspection of the samples after the measurements showed that this is not the case in reality: the scratches that can often be seen show that the strongest contact of the outer conductor is not at the radius $a_2$ but at a considerably larger one. Furthermore the scratches on the inner contact pad are usually very small, i.e. the effective contact area is probably much smaller than that corresponding to the inner radius $a_1$. Although these effects were not desired, they usually do not affect the final results of the measurements because this modified geometry of the Corbino adapter only means that a larger area of the contact pads is part of the current path and therefore contributes to the effective combined impedance of sample and contact. However, the contacts are not accounted for in the data analysis relying on the impedance of the contacts being small compared to that of the sample. Usually this assumption still holds even in the case of the real Corbino probe contact areas because the conductivity of the contact material (usually gold) is much higher than that of the sample, and therefore the larger

geometry of the sample still complies with the assumption that the contacts can
be neglected.

In the current study this assumption was violated only for one sample, unfor-
tunately this particular $UPd_2Al_3$ sample is the highest-quality sample UPA233c
and most of the data presented in Chapter 7 was taken on it. Therefore for this
special case the influence of the contacts had to be kept in mind, and the data
were also analyzed in a way to extract the intrinsic properties of the sample by
taking the contribution of the contacts into account.

## B.2.1 Experimental Evidence

The importance of the contribution of the contacts for measurements on the
UPA233c sample was recognized because the low-temperature low-frequency and
dc conductivity obtained with the Corbino spectrometer differs significantly from
independent four-point dc resistivity measurements (using the van der Pauw-
geometry) that were performed on the same sample. This effect can be seen in
Figure B.1 where the conductivity obtained by the van der Pauw-type measure-
ment is compared to the data obtained from the two-point measurement of $R_{dc}$ in
the Corbino spectrometer using 400 nm thick gold contacts (the offset of $R_{dc}$ that
has to be subtracted was deduced from the superconducting state of the sample
below 2 K): while at high temperatures the two curves basically coincide, there
are strong deviations at low temperatures when the conductivity of $UPd_2Al_3$ in-
creases dramatically. In particular the conductivity deduced from the Corbino
data consistently underestimates the four-point data.

An explanation for this effect based on too poor performance (i.e. too high
resistance) of the gold contacts and described in Section B.2.2 was then backed
experimentally by applying zinc contacts (plus additional gold ones on top) which
become superconducting below $\approx 3.5$ K: below this temperature the conductiv-
ity obtained from Corbino data matches those from the four-point-measurements
whereas above this temperature the mismatch known from gold contacts is found
again. Unfortunately below $T_c$ of the zinc contacts the microwave spectra of
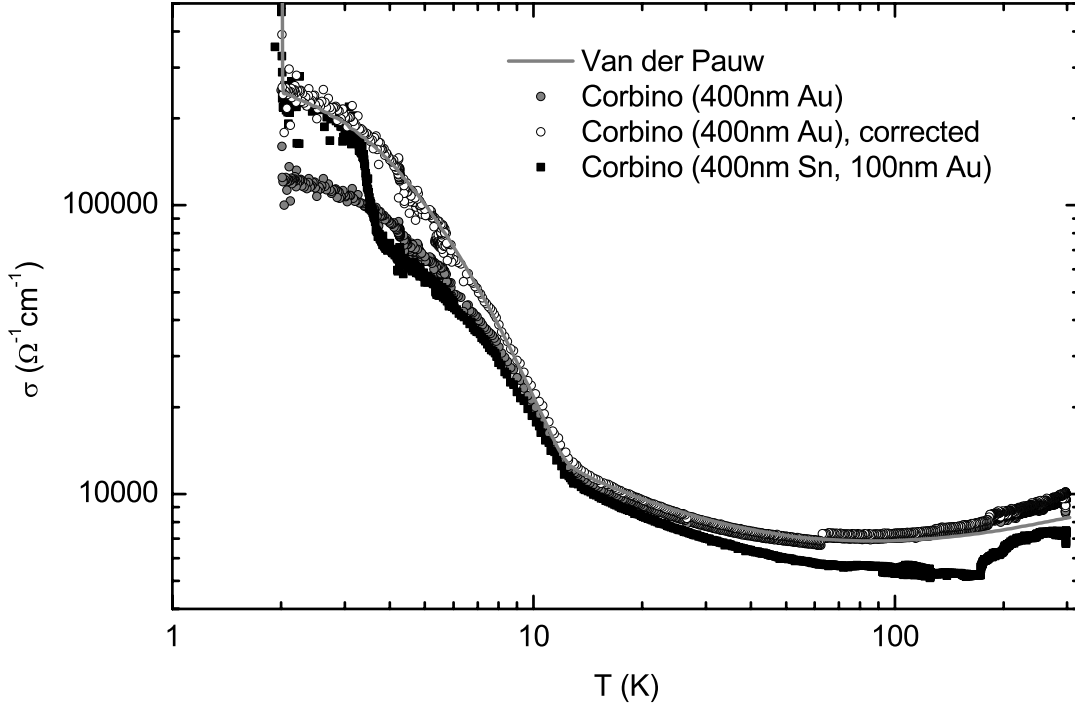
**Figure B.1:** dc conductivity of UPA233c sample as obtained by four-point van der Pauw-measurements and $R_{dc}$ measurements during two cooldowns of the Corbino spectrometer (with different contacts, one curve additionally after correction of contact contribution).

this sample did not improve compared to gold contacts (i.e. the superconducting state of the contacts at microwave frequencies was not as desired, a general problem already mentioned in Section 4.4.1), and also other contacts that were tried did not improve the outcome of the microwave experiments. (Recalling the impedance-dependent sensitivity of the spectrometer discussed in Section 5.5.1, one might doubt whether better contacts would actually lead to improved microwave spectra.) Thus the effect of the contacts could only be taken into account mathematically.

## B.2.2   Theoretical Modelling

The model used to explain this effect is as follows: the gold contacts are applied on top of the $UPd_2Al_3$ thin film sample, and since the currents are not injected right at the edges of the Corbino disc, the current flows some distance within the

196

contacts, parallel to the sample. In this case some fraction of the current will also flow within the $UPd_2Al_3$ sample below the contacts, i.e. in the area of the contacts where the current flows, the contacts and the sample will act like two resistors, $R_{cont,Au}$ and $R_{cont,UPA}$, in parallel. The total resistance of the combination of sample and contacts is obtained if the resistance $R_{Corb,UPA}$ of the Corbino disc (which is the resistance we usually consider when the contacts are neglected) is added in series as shown in Figure B.2. Since $R_{cont,UPA}$ and $R_{Corb,UPA}$ are the
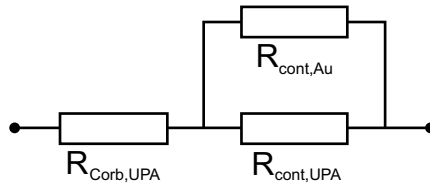


**Figure B.2:** Diagram of resistor model to describe the effect of poor contacts in Corbino geometry.

resistances of different sections of the same film, they differ only by a geometrical factor $G = R_{cont,UPA}/R_{Corb,UPA}$ which could be determined from measurements on the UPA233c sample without contacts to be in the range 4 to 5 (a surprisingly large value that is assigned to the small contact area of the center pin as the major reason).[1] Defining a resistance $R_{Corb,Au} = 1/G \, R_{cont,Au}$ (i.e. $R_{Corb,Au}$ would be the resistance of the corresponding gold contact in Corbino geometry), the total resistance $R_{comb}$ (which is measured with the Corbino experiment) of the

---

[1]Uncontacted measurements on the UPA233c sample can only be analyzed by using the superconducting state below 2 K for the offset determination of the dc resistance for the measured two-point resistance as well as for the calibration procedure (acting as short standard) on the network analyzer data. For low-frequency network analyzer data (below 1 GHz) the superconducting state can be used as a short up to rather high temperatures, and thus for these frequencies temperature-dependent conductivity data can be obtained as well as from the two-point dc data. In both cases the temperature dependence below 100 K corresponds to that from the independent four-point data not only qualitatively, but the resistance ratios that can be obtained at characteristic temperatures also coincide. This means that the conductivity obtained from the Corbino and four-point measurements only differ by the geometrical factor $(G + 1)$ that can now be obtained from the ratio of the conductivity values of the two measurements.

above resistor network

$$R_{comb} = R_{Corb,UPA} + \frac{1}{1/R_{cont,Au} + 1/R_{cont,UPA}} \tag{B.1}$$

can be solved to obtain the resistance of the Corbino disc alone:

$$
\begin{aligned}
R_{Corb,UPA} &= \frac{R_{comb} - (G+1)R_{Corb,Au}}{2} + \\
&+ \sqrt{\left(\frac{R_{comb} - (G+1)R_{Corb,Au}}{2}\right)^2 + R_{comb}R_{Corb,Au}} \quad .
\end{aligned} \tag{B.2}
$$

From this resistance the conductivity of the $UPd_2Al_3$ thin film can be calculated assuming the usual dimensions of the Corbino disc, and by adjusting the only free parameter $R_{Corb,Au}$ (to the reasonable value of 10 m$\Omega$) the corrected curve presented in Figure B.2 is obtained in good agreement with the four-point data.

Equation (B.2) can now also be used to remove the contact contribution from the microwave spectra,[2] but one has to keep in mind that the resistance $R_{Corb,Au}$ of the contacts was only determined for dc or low frequencies and it is not known whether $R_{Corb,Au}$ is frequency dependent at higher frequencies and in particular whether it becomes a complex quantity.

## B.3   Operating Sequence

The following steps constitute the course of the standardized low-temperature microwave measurements:

- attach the samples to the probes
- measure room-temperature spectra, check for good contact (including $R_{dc}$)
- start recording of temperature and $R_{dc}$ versus time
- attach stainless steel cylinder (contact gas volume) and close cryostat
- insert helium transfer line (with closed valve)
- evacuate cryostat and contact gas volume

---

[2]Then complex quantities enter Equation B.2, and one has to keep track of the sign of the square root. The unphysical solution reveals itself by a negative real part of the impedance.

- fill cryostat and contact gas volume with helium gas, connect cryostat to helium recovery

- evacuate and flush again contact gas volume several times, finally setting the pressure to 0.2-0.3 mbar

- fill in liquid nitrogen

- wait until the temperature has decreased considerably, typically to 150 K

- evacuate and flush the contact gas volume again several times, finally setting the pressure to $\approx 0.2$ mbar

- transfer liquid helium

- wait until the temperature has decreased and stabilized below 10 K

- increase contact gas (pressure to about 90 mbar) as well as liquid helium and nitrogen (levels slightly above standardized values), and maintain the three quantities at these values

- start rotary pump (valve closed)

- perform power-dependent measurements, if desired

- wait until temperature settles below 4.25 K

- remove helium transfer line

- when contact gas pressure and liquid helium and nitrogen levels are at standardized values, close the helium recovery and start to pump on the helium bath by carefully opening the bypass valve

- watch the temperature drop and open the bypass valve further

- with fully open bypass and the temperature decreasing below 1.9 K open major butterfly valve

- temperature should level around 1.63 K

- stop recording of temperature and $R_{dc}$ and start main measurement program (with appropriate settings concerning the list of temperatures to be approached, temperature stability requirements etc.)

- automated measurements are performed with temperature increasing according to setpoint list

- wait until the temperature has increased enough (currently about one hour

APPENDIX B. PERFORMING CORBINO MEASUREMENTS

until the spectra at setpoint 5 K have been measured), then close valves and shut pump off

- wait until the pressure in the helium bath has slightly surpassed atmospheric pressure (currently about one hour, around setpoint 14 K), then open helium recovery

- let computer program continue the automated measurements

- wait until automated measurements finish at 300 K (currently approximately 16:30 hours after opening the helium recovery), long after the liquid helium and nitrogen have evaporated completely

- close helium recovery, pump helium gas out of the cryostat and the contact gas volume

- vent the cryostat

- remove cryostat from insert, cover cryostat with lid (keep in mind that, depending on the time that has elapsed since the measurement finished, the stainless steel cylinder can be rather cold again, check temperature sensors)

- wait until temperature of the insert is close to room temperature

- vent contact gas volume and remove stainless steel cylinder

- remove samples and proceed with next measurement

The complete procedure can be performed within less than 24 hours, i.e. standard low-temperature measurements can be performed one per day.

# Appendix C

# Multiple Drude Responses

In Section 7.4.1 a possible explanation of the frequency-dependent scattering rate of $UPd_2Al_3$ was given in terms of an electronic system consisting of several distinct subsystems with each of them following the Drude model but with different relaxation times and effective masses. The main features of such a 'multiple Drude response' should be discussed here for the simplest case of only two distinct systems although the multi-sheeted Fermi surface of $UPd_2Al_3$ at once hints at more than two subsystems.

## C.1   General Formulae

We assume that we have two distinct subsystems with conductivities $\sigma_a$ and $\sigma_b$, with scattering rates $\tau_a$ and $\tau_b$, and with dc conductivities $\sigma_{0a}$ and $\sigma_{0b}$, respectively:

$$\sigma_a(\omega) = \sigma_{0a} \; \frac{1}{1 - i\omega\tau_a} \quad , \quad \sigma_b(\omega) = \sigma_{0b} \; \frac{1}{1 - i\omega\tau_b} \quad . \tag{C.1}$$

The total conductivity of the system is the combination of the conductivities of the two subsystems:

$$\sigma_{total} = \sigma_a + \sigma_b \quad . \tag{C.2}$$

As described in Section 7.4.1, we are particularly interested in the frequency dependence of the 'effective' scattering rate of the total system in terms of the extended Drude model as discussed in Section 6.3.2. To avoid the problem of the

charge carrier density, we again study the real part $\rho_1$ of the complex resistivity instead of the scattering rate which differs just by a frequency-independent constant. Thus we have to separate real and imaginary parts of the frequency-dependent resistivity:

$$\rho_{total} = 1/\sigma_{total} = \frac{(1 - i\omega\tau_a)(1 - i\omega\tau_b)}{\sigma_{0a}(1 - i\omega\tau_b) + \sigma_{0b}(1 - i\omega\tau_a)} \quad . \tag{C.3}$$

Some algebra then leads to $\rho_{total} = \rho_{1,total} + i\rho_{2,total}$ where:

$$\rho_{1,total} = \frac{(\sigma_{0a} + \sigma_{0b}) + \omega^2(\sigma_{0a}\tau_b^2 + \sigma_{0b}\tau_a^2)}{(\sigma_{0a} + \sigma_{0b})^2 + \omega^2(\sigma_{0a}\tau_b + \sigma_{0b}\tau_a)^2} \quad , \tag{C.4}$$

$$\rho_{2,total} = \frac{-\omega(\sigma_{0a}\tau_a + \sigma_{0b}\tau_b + \omega^2\tau_a\tau_b(\sigma_{0a}\tau_b + \sigma_{0b}\tau_a))}{(\sigma_{0a} + \sigma_{0b})^2 + \omega^2(\sigma_{0a}\tau_b + \sigma_{0b}\tau_a)^2} \quad . \tag{C.5}$$

Now we discuss the frequency dependence of the real part $\rho_{1,total}$. At low frequencies $\omega \ll 1/\tau_a, 1/\tau_b$, it is frequency independent:

$$\rho_{1,total} = \frac{1}{\sigma_{0a} + \sigma_{0b}} \quad \text{for} \quad \omega \ll 1/\tau_{\mathrm{a}}, 1/\tau_{\mathrm{b}}, \tag{C.6}$$

a result that is directly evident from Equation (C.2). At high frequencies $\omega \gg 1/\tau_a, 1/\tau_b$, the real part $\rho_{1,total}$ is also frequency independent:

$$\rho_{1,total} = \frac{\sigma_{0a}\tau_b^2 + \sigma_{0b}\tau_a^2}{(\sigma_{0a}\tau_b + \sigma_{0b}\tau_a)^2} \quad \text{for} \quad \omega \gg 1/\tau_{\mathrm{a}}, 1/\tau_{\mathrm{b}}. \tag{C.7}$$

In the intermediate frequency range, there is a transition of $\rho_{1,total}$ between these two values, and the details of this transition depend on the particular values of the parameters $\tau_a$, $\tau_b$, $\sigma_{0a}$, and $\sigma_{0b}$. This can lead to frequency ranges where $\rho_{1,total}$ depends quadratically on frequency, the same power dependence as predicted for the scattering rate of a Fermi liquid and discussed in Section 6.4.

## C.2   Example

In Section 7.4.3 it was shown that the combination of two distinct Drude systems can lead to a frequency-dependent scattering rate of the complete system consistent with the data obtained on the UPA233c sample. The parameters chosen there are: $\sigma_{0a} = 2 \cdot 10^5 \, (\Omega\text{cm})^{-1}$, $\tau_a = 1.9 \cdot 10^{-10}\,\text{s}$, $\sigma_{0b} = 2 \cdot 10^3 \, (\Omega\text{cm})^{-1}$, and
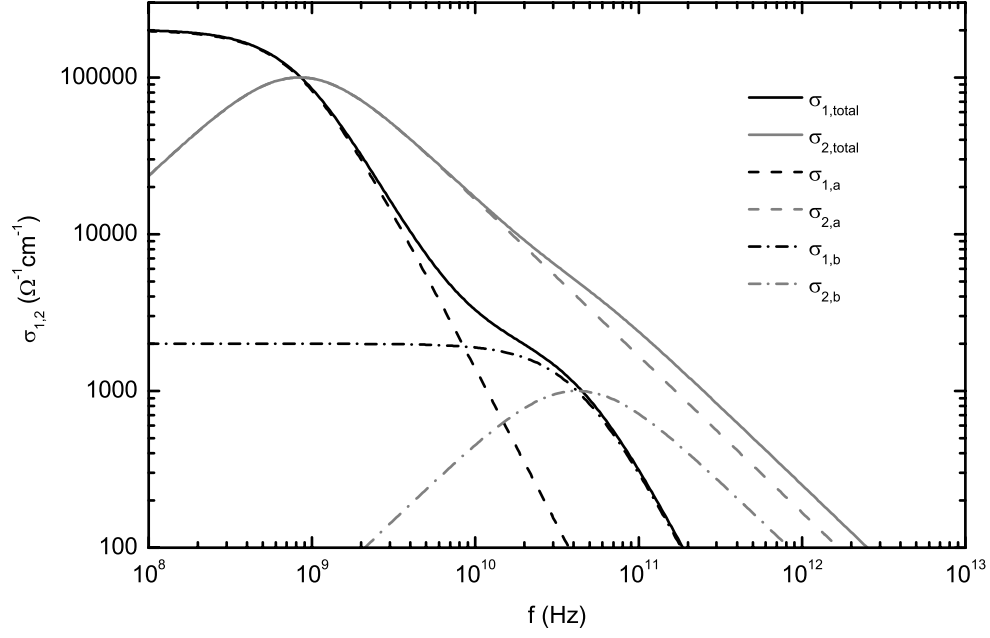
**Figure C.1:** Calculated conductivity of two Drude responses as well as their combination.
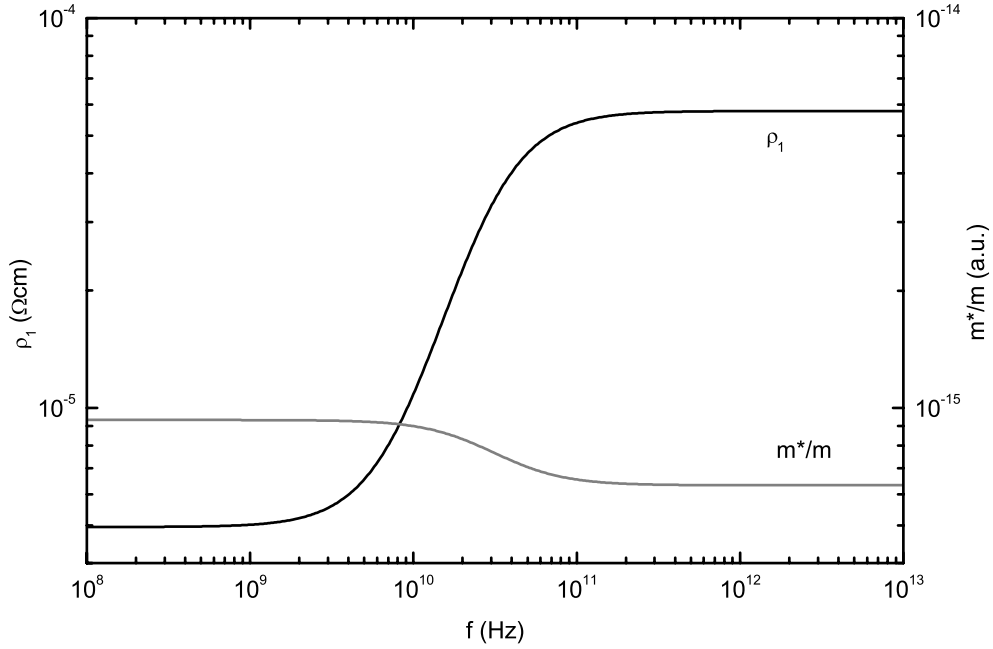


**Figure C.2:** Calculated real part $\rho_1$ of resistivity and effective mass of the combination of two Drude responses.

$\tau_a = 3.8 \cdot 10^{-12}$ s, respectively. The resulting frequency dependences for $\sigma_a$, $\sigma_b$, and $\sigma_{total} = \sigma_a + \sigma_b$ are shown in Figure C.1. Obviously, the contribution of $\sigma_b$ only has a small effect on the total conductivity (keep in mind the logarithmic scales). The corresponding frequency-dependent scattering rate and effective mass on the other hand clearly exhibit the influence of the second subsystem as is shown in Figure C.2. There the real part $\rho_{1,total}$ of the resistivity (which is proportional to the scattering rate $\Gamma$) is plotted as well as the quantity $-\omega\rho_{2,total}$, which is proportional to the effective mass (and which is denoted as such in the figure). The frequency ranges of constant scattering rate and effective mass can clearly be found at low as well as at high frequencies, with a considerable frequency dependence in the intermediate region.

# Bibliography

[1] Martin Dressel and George Grüner, *Electrodynamics of Solids: Optical Properties of Electrons in Matter* (Cambridge University Press, Cambridge, 2002).

[2] A. J. Millis and P. A. Lee, Phys. Rev. B **35**, 3394 (1987).

[3] M. Dressel, N. Kasper, K. Petukhov, B. Gorshunov, G. Grüner, M. Huth, and H. Adrian, Phys. Rev. Lett. **88**, 186404 (2002).

[4] M. Dressel, N. Kasper, K. Petukhov, D. N. Peligrad, B. Gorshunov, M. Jourdan, M. Huth, and H. Adrian, Phys. Rev. B **66**, 035110 (2002).

[5] M. L. Stutzman, Mark Lee, and R. F. Bradley, Rev. Sci. Instrum. **71**, 4596 (2000).

[6] Hans Kuzmany, *Solid-State Spectroscopy* (Springer-Verlag, Berlin, 1998).

[7] For a review of the pairing symmetry of high-$T_c$ superconductors see: C. C. Tsuei and J. R. Kirtley, Rev. Mod. Phys. **72**, 969 (2000).

[8] For an introduction see e.g.: F. Kremer and A. Schönhals, *Broadband Dielectric Measurement Techniques ($10^{-6}$ Hz to $10^{12}$ Hz)*, in *Broadband dielectric spectroscopy*, edited by F. Kremer and A. Schönhals (Springer-Verlag, Berlin, 2003).

[9] Gennadi Kozlov and Alexander Volkov, *Coherent Source Submillimeter Wave Spectroscopy*, in *Millimeter and Submillimeter Wave Spectroscopy of Solids*, edited by G. Grüner; Topics in Applied Physics, Vol. 74 (Springer-Verlag, Berlin, 1998).

[10] Claus Dahl, Philippe Goy, and Jörg P. Kotthaus, *Magneto-Optical Millimeter-Wave Spectroscopy*, in *Millimeter and Submillimeter Wave Spec-*

*troscopy of Solids*, edited by G. Grüner; Topics in Applied Physics, Vol. 74 (Springer-Verlag, Berlin, 1998).

[11] J. A. Reedijk, H. C. F. Martens, B. J. G. Smits, and H. B. Brom, Rev. Sci. Instrum. **71**, 478 (2000).

[12] Martin C. Nuss and Joseph Orenstein, *Terahertz Time-Domain Spectroscopy*, in *Millimeter and Submillimeter Wave Spectroscopy of Solids*, edited by G. Grüner; Topics in Applied Physics, Vol. 74 (Springer-Verlag, Berlin, 1998).

[13] For an introduction on conductivity measurements using cavities: Olivier Klein, Steve Donovan, Martin Dressel, and George Grüner, International Journal of Infrared and Millimeter Waves **14**, 2423 (1993); Steve Donovan, Olivier Klein, Martin Dressel, Kàroly Holczer, and George Grüner, International Journal of Infrared and Millimeter Waves **14**, 2459 (1993); Martin Dressel, Olivier Klein, Steve Donovan, and George Grüner, International Journal of Infrared and Millimeter Waves **14**, 2489 (1993).

[14] S. Sridhar and W. L. Kennedy, Rev. Sci. Instrum. **59**, 531 (1988).

[15] R. C. Taber, Rev. Sci. Instrum. **61**, 2200 (1990).

[16] Vladimir V. Talanov, Lucia V. Mercaldo, Steven M. Anlage, and John H. Claassen, Rev. Sci. Instrum. **71**, 2136 (2000).

[17] W. N. Hardy and L. A. Whitehead, Rev. Sci. Instrum. **52**, 213 (1981).

[18] D. A. Bonn, D. C. Morgan, and W. N. Hardy, Rev. Sci. Instrum. **62**, 1819 (1991).

[19] Monty Mola, Stephen Hill, Philippe Goy, and Michel Gross, Rev. Sci. Instrum. **71**, 186 (2000).

[20] A. Hosseini, R. Harris, Saeid Kamal, P. Dosanjh, J. Preston, Ruixing Liang, W. N. Hardy, and D. A. Bonn, Phys. Rev. B **60**, 1349 (1999).

[21] Steven M. Anlage, Hsuan Sze, Howard J. Snortland, Shuichi Tahara, Brian Langley, Chang-Beom Eom, M. R. Beasley, and Robert Taber, Appl. Phys. Lett. **54**, 2710 (1989).

[22] B. W. Langley, S. M. Anlage, R. F. W. Pease, and M. R. Beasley, Rev. Sci. Instrum. **62** 1801, (1991).

[23] Steven M. Anlage, Brian W. Langley, Guy Deutscher, Jürgen Halbritter, and M. R. Beasley, Phys. Rev. B **44** 9764, (1991).

[24] David M. Pozar, *Microwave Engineering* (John Wiley & Sons, New York, 1998).

[25] A. Andreone, A. Cassinese, C. Cantoni, A. Di Chiara, F. Miletto Granozio, M. Salluzzo, and R. Vaglio, Nuovo Cimento D **16**, 1909 (1994).

[26] D. E. Oates, A. C. Anderson, and P. M. Mankiewich, J. Supercond. **3**, 251 (1990).

[27] Nathan Belk, D. E. Oates, D. A. Feld, G. Dresselhaus, and M. S. Dresselhaus, Phys. Rev. B **53**, 3459 (1996).

[28] M. S. DiIorio, Alfredo C. Anderson, and B.-Y. Tsaur, Phys. Rev. B. **38**, 7019 (1988).

[29] David Grissom and William H. Hartwig, J. Appl. Phys. **37**, 4784 (1966).

[30] R. J. Deri, Rev. Sci. Instrum. **57**, 82 (1986).

[31] R. J. Deri and T. G. Castner, Phys. Rev. Lett. **57**, 134 (1986).

[32] M. Migliuolo and T. G. Castner, Solid State Commun. **67**, 863 (1988).

[33] M. Migliuolo and T. G. Castner, Phys. Rev. B **38**, 11593 (1988).

[34] Mark Lee and M. L. Stutzmann, Phys. Rev. Lett. **87**, 056402 (2001).

[35] E. Helgren, N. P. Armitage, and G. Grüner, Phys. Rev. Lett. **89**, 246601 (2002).

[36] E. Helgren, N. P. Armitage, and G. Grüner, Phys. Rev. B **69**, 014201 (2004).

[37] Marco Hering, *Optische Untersuchungen der dynamischen Leitfähigkeit im Variable Range Hopping Regime des Elektronenglases Si:P*, Diplomarbeit, Universität Karlsruhe (TH), Karlsruhe, 2004.

[38] Robert Diehl, David M. Wheatley, and T. G. Castner, Rev. Sci. Instrum. **67**, 3904 (1996).

[39] K. J. Song and T. G. Castner, Rev. Sci. Instrum. **72**, 1760 (2001).

[40] Georges Roussy, Jean-Marie Thiebaut, Francis Ename-Obiang, and Eric Marchal, Meas. Sci. Technol. **12**, 542 (2001).

[41] *User's Guide, HP 8360 B-Series Swept Signal Generator (Including Options 001, 002, 004, 006, and 008)*, Hewlett-Packard Company, Santa Rosa, 1999.

[42] F. Hohls, U. Zeitler, and R.J. Haug, Phys. Rev. Lett. **86**, 5124 (2001).

[43] F. Hohls, U. Zeitler, R.J. Haug, R. Meisels, K. Dybko, and F. Kuchar Phys. Rev. Lett. **89**, 276801 (2002).

[44] J. C. Booth, Dong Ho Wu, and Steven M. Anlage, Rev. Sci. Instrum. **65**, 2082 (1994).

[45] Dong Ho Wu, J. C. Booth, and Steven M. Anlage, Phys. Rev. Lett. **75**, 525 (1995).

[46] James C. Booth, Dong Ho Wu, S. B. Qadri, E. F. Skelton, M. S. Osofsky, Alberto Piqué, and Steven M. Anlage, Phys. Rev. Lett. **77**, 4438 (1996).

[47] Andrew Schwartz, Marc Scheffler, and Steven M. Anlage, Phys. Rev. B **61**, R870 (2000).

[48] Andrew Schwartz, Marc Scheffler, and Steven M. Anlage, cond-mat/0010172 (2000).

[49] Marc Scheffler, *Broadband Microwave Surface Impedance Measurements on $La_{0.8}Sr_{0.2}MnO_3$*, Master of Science Thesis, University of Maryland, College Park, 1998.

[50] G. Goglio, S. Pignard, A. Radulescu, L. Piraux, I. Huynen, D. Vanhoenacker, and A. Vander Vorst, Appl. Phys. Lett. **75**, 1769 (1999).

[51] L. W. Engel, D. Shahar, Ç. Kurdak, and D. C. Tsui, Phys. Rev. Lett. **71**, 2638 (1993).

[52] C.-C. Li, L. W. Engel, D. Shahar, D. C. Tsui, and M. Shayegan, Phys. Rev. Lett. **79**, 1353 (1997).

[53] C.-C. Li, J. Yoon, L. W. Engel, D. Shahar, D. C. Tsui, and M. Shayegan, Phys. Rev. B **61**, 10905 (2000).

[54] P. D. Ye, L. W. Engel, D. C. Tsui, J. A. Simmons, J. R. Wendt, G. A. Vawter, and J. L. Reno, Phys. Rev. B **65**, 121305 (2002).

[55] R. M. Lewis, P. D. Ye, L. W. Engel, D. C. Tsui, L. N. Pfeiffer, and K. W. West, Phys. Rev. Lett. **89**, 136804 (2002).

[56] Yong Chen, R. M. Lewis, L. W. Engel, D. C. Tsui, P. D. Ye, L. N. Pfeiffer, and K. W. West, Phys. Rev. Lett. **91**, 016801 (2003).

[57] Ophelia K. C. Tsui, N. P. Ong, Y. Matsuda, Y. F. Yan, and J. B. Peterson, Phys. Rev. Lett. **73**, 724 (1994).

[58] Y. Matsuda, N. P. Ong, Y. F. Yan, J. M. Harris, and J. B. Peterson, Phys. Rev. B **49**, 4380 (1994).

[59] M. B. Gaifullin, Yuji Matsuda, N. Chikumoto, J. Shimoyama, K. Kishio, and R. Yoshizaki, Phys. Rev. Lett. **83**, 3928 (1999).

[60] P. J. Turner, D. M. Broun, Saeid Kamal, M. E. Hayden, J. S. Bobowski, R. Harris, D. C. Morgan, J. S. Preston, D. A. Bonn, and W. N. Hardy, Rev. Sci. Instrum. **75**, 124 (2004).

[61] P. J. Turner, R. Harris, Saeid Kamal, M. E. Hayden, D. M. Broun, D. C. Morgan, A. Hosseini, P. Dosanjh, G. K. Mullins, J. S. Preston, Ruixing Liang, D. A. Bonn, and W. N. Hardy, Phys. Rev. Lett. **90**, 237005 (2003).

[62] H. C. F. Martens, J. A. Reedijk, and H. B. Brom, Rev. Sci. Instrum. **71**, 473 (2000).

[63] Marcy Lynn Stutzman, *Coulomb Correlation Effects in Barely Insulating Si:B*, Dissertation, University of Virginia, 2000.

[64] J. David Kokales, Patrick Fournier, Lucia V. Mercaldo, Vladimir V. Talanov, Richard L. Greene, and Steven M. Anlage, Phys. Rev. Lett. **85**, 3696 (2000).

[65] D. A. Bonn, P. Dosanjh, R. Liang, and W. N. Hardy, Phys. Rev. Lett. **68**, 2390 (1992).

[66] W. N. Hardy, D. A. Bonn, D. C. Morgan, Ruixing Liang, and Kuan Zhang, Phys. Rev. Lett. **70**, 3999 (1993).

[67] D. A. Bonn, Ruixing Liang, T. M. Riseman, D. J. Baar, D. C. Morgan, Kuan Zhang, P. Dosanjh, T. L. Duty, A. MacFarlane, G. D. Morris, J. H. Brewer, W. N. Hardy, C. Kallin, and A. J. Berlinsky, Phys. Rev. B **47**, 11314 (1993).

[68] D. A. Bonn, S. Kamal, Kuan Zhang, Ruixing Liang, D. J. Baar, E. Klein, and W. N. Hardy, Phys. Rev. B **50**, 4051 (1994).

[69] O. M. Corbino, Nuovo Cimento **1**, 397 (1911).

[70] James Clay Booth, *Novel Measurements of the Frequency Dependent Microwave Surface Impedance of Cuprate Thin Film Superconductors*, Dissertation, University of Maryland, College Park, 1996.

[71] Stephan Mair, *Entwicklung eines optischen Nahfeld-Spektrometers im Terahertz-Bereich*, Dissertation, Universität Stuttgart, Stuttgart, 2003.

[72] S. Mair, B. Gompf, and M. Dressel, Appl. Phys. Lett. **84**, 1219 (2004).

[73] Andrew Schwartz, private communication.

[74] R. Böhmer, M. Maglione, P. Lunkenheimer, and A. Loidl, J. Appl. Phys. **65**, 901 (1989).

[75] *Semi-Rigid Coaxial Cable*, catalogue including specifications, Micro-Coax, Pottstown, 1998.

[76] *Type UT85-LL-TP*, by Micro-Coax.

[77] *Type UT85-SS*, by Micro-Coax.

[78] *Types 8501-7985-02, 8501-7885-02, and 8502-7885-02*, by M/A-COM, Inc.

[79] *Types V101M and V101F*, by Anritsu.

[80] *Type 08 S 121-K00 S3*, by Rosenberger Hochfrequentechnik.

[81] *Type 8001-HFHM-02*, by Spectrum Elektrotechnik GmbH.

[82] *Type 8582-0000-02*, by M/A-COM, Inc.

[83] *Type HP 11900C*, by Hewlett-Packard GmbH, now Agilent.

[84] *Model 2000 Multimeter*, by Keithley Instrumentes, Inc.

[85] *Model CX-1050-AA*, by LakeShore Cryotronics, Inc.

[86] *Nichrome Heater Wire NC-32*, by LakeShore Cryotronics, Inc.

[87] See e.g. *User's Manual, Model 340 Temperature Controller*, Lake Shore Cryotronics, Inc., Westerville, 1999.

[88] For an introduction on network analysis and calibration procedures see e.g.: *Taschenbuch der Hochfrequenztechnik*, edited by K. Lange and K.-H. Löcherer (Springer-Verlag, Berlin, 1992).

[89] *2.4 mm Calibration Kit HP 85056A*, by Hewlett-Packard GmbH, now Agilent.

[90] *Dünnschichttechnologie*, edited by Hartmut Frey and Gerhard Kienel (VDI-Verlag, Düsseldorf, 1987).

[91] Deposition system Veeco VES 770.

[92] Product number 042368 by Alfa Aesar.

[93] G. Nocerino and K. E. Singer, Thin Solid Films **57**, 343 (1979).

[94] Joachim Lang, *Phononendetektion mit supraleitenden Tunnelkontakten geringer Schichtdicke in hohen Magnetfeldern*, Dissertation, Universität Stuttgart, Stuttgart, 1995.
Here aluminium films on silicon were studied while we used sapphire as a substrate, but our experiments are in daccord with those of Lang.

[95] Werner Buckel, *Supraleitung*, 5. Auflage (VCH, Weinheim, 1994).

[96] H. Sixl, J. Gromer, and H. C. Wolf, Z. Naturforsch. **29 a**, 319 (1974).

[97] For brief introductions to the field of heavy fermions see [98, 99], longer ones [100–102] can be found in the *Handbook on the Physics and Chemistry of Rare Earths*.

[98] Z. Fisk, D. W. Hess, C. J. Pethick, D. Pines, J. L. Smith, J. D. Thompson, and J. O. Willis, Science **239**, 33 (1988).

[99] Z. Fisk, J. L. Sarrao, J. L. Smith, and J. D. Thompson, Proc. Natl. Acad. Sci. USA **92**, 6663 (1995).

[100] Norbert Grewe and Frank Steglich, in *Handbook on the Physics and Chemistry of Rare Earths*, edited by K.A. Gschneidner, Jr. and L. Eyring, Vol. 14 (Elsevier, Amsterdam, 1991), p. 343.

[101] S.H. Liu, in *Handbook on the Physics and Chemistry of Rare Earths*, edited by K.A. Gschneidner, Jr., L. Eyring, G.H. Lander, and G.R. Choppin, Vol. 17 (Elsevier, Amsterdam, 1993), p. 87.

[102] P. Wachter, in *Handbook on the Physics and Chemistry of Rare Earths*, edited by K.A. Gschneidner, Jr., L. Eyring, G.H. Lander, and G.R. Choppin, Vol. 19 (Elsevier, Amsterdam, 1994), p. 177.

[103] P. Drude, Phys. Z. **1**, 161 (1900).

[104] Neil W. Ashcroft and N. David Mermin, *Solid State Physics* (Saunders College Publishing, Fort Worth, 1976).

[105] Martin van Exter and D. Grischkowsky, Appl. Phys. Lett. **56**, 1694 (1990).

[106] Tae-In Jeon and D. Grischkowsky, Phys. Rev. Lett. **78**, 1106 (1997).

[107] S. J. Allen, Jr., D. C. Tsui, and F. DeRosa, Phys. Rev. Lett. **35**, 1359 (1975).

[108] D.C. Tsui, S.J. Allen, Jr., R.A. Logan, A. Kamgar, and S.N. Coppersmith, Surf. Sci. **73**, 419 (1978).

[109] P. J. Burke, I. B. Spielman, J. P. Eisenstein, L. N. Pfeiffer, and K. W. West, Appl. Phys. Lett. **76**, 745 (2000).

[110] L. Degiorgi, Rev. Mod. Phys. **71**, 687 (1999).

[111] A. J. Schofield, Contemp. Phys. **40**, 95 (1999).

[112] G. R. Stewart, Rev. Mod. Phys. **73**, 797 (2001).

[113] P. Coleman, C. Pépin, Qimiao Si, and R. Ramazashvili, J. Phys.: Condens. Matter **13**, R723 (2001).

[114] L. Degiorgi, St. Thieme, H.R. Ott, M. Dressel, G. Grüner, Y. Dalichaouch, M.B. Maple, Z. Fisk, C. Geibel, and F. Steglich, Z. Phys. B **102**, 367 (1997).

[115] L. Degiorgi, F.B.B. Anders, and G. Grüner, Eur. Phys. J. B **19**, 167 (2001).

[116] S. Donovan, A. Schwartz, and G. Grüner, Phys. Rev. Lett. **79**, 1401 (1997).

[117] W. P. Beyermann, G. Grüner, Y. Dalicheouch, and M. B. Maple, Phys. Rev. B **37**, 10353 (1988).

[118] P. E. Sulewski, A. J. Sievers, M. B. Maple, M. S. Torikachvili, J. L. Smith, and Z. Fisk, Phys. Rev. B **38**, 5338 (1988).

[119] A. M. Awasthi, W. P. Beyermann, J. P. Carini, and G. Grüner, Phys. Rev. B **39**, 2377 (1989).

[120] P. Tran, S. Donovan, and G. Grüner, Phys. Rev. B **65**, 205102 (2002).

[121] W. P. Beyermann, G. Grüner, Y. Dalichaouch, and M. B. Maple, Phys. Rev. Lett **60**, 216 (1988).

[122] B. C. Webb, A. J. Sievers, and T. Mihalisin, Phys. Rev. Lett. **57**, 1951 (1986).

[123] A. M. Awasthi, L. Degiorgi, G. Grüner, Y. Dalichaouch, and M. B. Maple, Phys. Rev. B **48**, 10692 (1993).

[124] S. V. Dordevic, D. N. Basov, N. R. Dilley, E. D. Bauer, and M. B. Maple, Phys. Rev. Lett. **86**, 684 (2001).

[125] E. J. Singley, D. N. Basov, E. D. Bauer, and M. B. Maple, Phys. Rev. B **65**, 161101(R) (2002).

[126] A. A. Brown Holden, G. M. Wardlaw, M. Reedyk, and J. L. Smith, Phys. Rev. Lett. **91**, 136401 (2003).

[127] J. W. Allen and J. C. Mikkelsen, Phys. Rev. B **15**, 2952 (1977).

[128] G. A. Thomas, J. Orenstein, D. H. Rapkine, M. Capizzi, A. J. Millis, R. N. Bhatt, L. F. Schneemeyer, and J. V. Waszczak, Phys. Rev. Lett. **61**, 1313 (1988).

[129] A. V. Puchkov, D. N. Basov, and T. Timusk, J. Phys.: Condens. Matter **8**, 10049 (1996).

[130] J. R. Simpson, H. D. Drew, V. N. Smolyaninova, R. L. Greene, M. C. Robson, Amlan Biswas, and M. Rajeswari, Phys. Rev. B **60**, R16263 (1999).

[131] A. Schwartz, M. Dressel, G. Grüner, V. Vescoli, L. Degiorgi, and T. Giamarchi, Phys. Rev. B **58**, 1261 (1998).

[132] John S. Toll, Phys. Rev. **104**, 1760 (1956).

[133] J. S. Helman, W. Baltensperger, Phys. Rev. B **17**, 2427 (1978).

[134] L. D. Landau, Sov. Phys. JETP **3**, 920 (1957).

[135] David Pines and Philippe Nozières, *The Theory of Quantum Liquids. Volume I: Normal Fermi Liquids* (Benjamin, New York, 1966).

[136] Gordon Baym and Christiopher Pethick, *Landau Fermi-Liquid Theory: Concepts and Applications* (John Wiley and Sons, New York, 1991).

[137] H. v. Löhneysen, Phys. Bl. **51**, 941 (1995).

[138] Dieter Vollhardt and Peter Wölfle, *The Superfluid Phases of Helium 3* (Taylor & Francis, London, 1990).

[139] Pierre Morel and Philippe Nozières, Phys. Rev. **126**, 1909 (1962).

[140] A. A. Abrikosov, L. P. Gor'kov, and I. Ye. Dzyaloshinskii, *Quantum Field Theoretical Methods in Statistical Physics* (Pergamon Press, Oxford, 1965).

[141] G. M. Éliashberg, Sov. Phys. JETP **15**, 1151 (1962).

[142] R. N. Gurzhi, Sov. Phys. JETP **8**, 673 (1959).

[143] R. T. Beach and R. W. Christy, Phys. Rev. B **16**, 5277 (1977).

[144] G. R. Parkins, W. E. Lawrence, and R. W. Christy, Phys. Rev. B **23**, 6408 (1981).

[145] C. Geibel, C. Schank, S. Thies, H. Kitazawa, C.D. Bredl, A. Böhm, M. Rau, A. Grauel, R. Caspary, R. Helfrich, U. Ahlheim, G. Weber, and F. Steglich, Z. Phys. B **84**, 1 (1991).

[146] M. Jourdan, M. Huth, and H. Adrian, Nature **398**, 47 (1999).

[147] N. K. Sato, N. Aso, K. Miyake, R. Shiina, P. Thalmeier, G. Varelogiannis, C. Geibel, F. Steglich, P. Fulde, and T. Komatsubara, Nature **410**, 340 (2001).

[148] F. Steglich, N.K. Sato, N. Aso, P. Gegenwart, J. Custers, K. Neumaier, H. Wilhelm, C. Geibel, and O. Trovarelli, Physica B **329-333**, 441 (2003).

[149] Masahiko Hiroi, Masafumi Sera, Norio Kobayashi, Yoshinori Haga, Etsuji Yamamoto, and Yoshichika Ōnuki, J. Phys. Soc. Jpn. **66**, 1595 (1997).

[150] Y. Dalichaouch, M. C. de Andrade, and M. B. Maple, Phys. Rev. B **46**, 8671 (1992).

[151] M. Dressel, B.P. Gorshunov, A.V. Pronin, A.A. Mukhin, F. Mayr, A. Seeger, P. Lunkenheimer, A. Loidl, M. Jourdan, M. Huth, and H. Adrian, Physica B **244**, 125 (1998).

[152] Yoshinori Haga, Yoshihiko Inada, Kenji Sakurai, Yoshihumi Tokiwa, Etsuji Yamamoto, Tetsuo Honma, and Yoshichika Ōnuki, J. Phys. Soc. Jpn. **68**, 342 (1999).

[153] M. Jourdan, M. Huth, S. Mouloud, and H. Adrian, Physica C **282-287**, 1883 (1997).

[154] Martin Jourdan, *Tunneling Spectroscopy on the heavy-fermion superconductor $UPd_2Al_3$*, Dissertation, Johannes Gutenberg-Universität Mainz, Mainz, 1999.

[155] M. Huth, A. Kaldowski, J. Hessert, Th. Steinborn, and H. Adrian, Solid State Commun. **87**, 1133 (1993).

[156] Yoshinori Haga, Etsuji Yamamoto, Yoshihiko Inada, Dai Aoki, Kenichi Tenya, Masataka Ikeda, Toshiro Sakakibara, and Yoshichika Ōnuki, J. Phys. Soc. Jpn. **65**, 3646 (1996).

[157] M. Huth, A. Kaldowski, J. Hessert, C. Heske, and H. Adrian, Physica B **199&200**, 116 (1994).

[158] M. Huth, J. Hessert, M. Jourdan, A. Kaldowski, and H. Adrian, Phys. Rev. B **50**, 1309 (1994).

[159] K. Bakker, A. de Visser, L.T. Tai, A.A. Menovsky, and J.J.M. Franse, Solid State Commun. **86**, 497 (1993).

[160] R. Caspary, P. Hellmann, M. Keller, G. Sparn, C. Wassilew, R. Köhler, C. Geibel, C. Schank, F. Steglich, and N. E. Phillips, Phys. Rev. Lett. **71**, 2146 (1993).

[161] For an introduction to de Haas-van Alphen experiments see: D. Shoenberg, *Magnetic oscillations in metals* (Cambridge University Press, Cambridge, 1984).

[162] Y. Inada, H. Aono, A. Ishiguro, J. Kimura, N. Sato, A. Sawada, and T. Komatsubara, Physica B **199 & 200**, 119 (1994).

[163] Y. Inada, A. Ishiguro, J. Kimura, N. Sato, A. Sawada, T. Komatsubara, and H. Yamagami, Physica B **206 & 207**, 33 (1995).

[164] Yoshihiko Inada, Hiroshi Yamagami, Yoshinori Haga, Kenji Sakurai, Yoshi-humi Tokiwa, Tetsuo Honma, Etsuji Yamamoto, Yoshichika Ōnuki, and Takashi Yanagisawa, J. Phys. Soc. Jpn. **68**, 3643 (1999).

[165] Y. Inada, and Y. Ōnuki, Low Temp. Phys. **25**, 573 (1999).

[166] R. G. Chambers, *Electrons in Metals and Semiconductors* (Chapman and Hall, London, 1990).

[167] Yoshichika Ōnuki and Akira Hasegawa, in *Handbook on the Physics and Chemistry of Rare Earths*, edited by K.A. Gschneidner, Jr. and L. Eyring, Vol. 20 (Elsevier, Amsterdam, 1995), p. 1.

[168] R. B. Dingle, Proc. R. Soc. London, Ser. A **211**, 517 (1952).

[169] R. Feyerherm, A. Amato, F. N. Gygax, A. Schenck, C. Geibel, F. Steglich, N. Sato, and T. Komatsubara, Phys. Rev. Lett. **73**, 1849 (1994).

[170] G. Zwicknagl and P. Fulde, J. Phys.: Condens. Matter **15**, S1911 (2003).

[171] G. Zwicknagl, A. Yaresko, and P. Fulde, Phys. Rev. B **68**, 052508 (2003).

[172] Konrad Kopitzki, *Einführung in die Festkörperphysik* (B. G. Teubner, Stuttgart, 1993).

[173] U. Rauchschwalbe, W. Lieke, C. D. Bredl, F. Steglich, J. Aarts, K. M. Martini, and A. C. Mota, Phys. Rev. Lett. **49**, 1448 (1982).

[174] T. P. Orlando, E. J. McNiff, Jr., S. Foner, and M. R. Beasley, Phys. Rev. B **19**, 4545 (1979).

[175] L.M. Sandratskii, J. Kübler, P. Zahn, and I. Mertig, Phys. Rev. B **50**, 15834 (1994).

[176] K. Knöpfle, A. Mavromaras, L. M. Sandratskii, and J. Kübler, J. Phys.: Condens. Matter **8**, 901 (1996).

[177] N. Kimura, T. Tani, H. Aoki, T. Komatsubara, S. Uji, D. Aoki, Y. Inada, Y. Ōnuki, Y. Haga, E. Yamamoto, and H. Harima, Physica B **281 & 282**, 710 (2000).

[178] G. Zwicknagl, A. N. Yaresko, and P. Fulde, Phys. Rev. B **65**, 081103(R) (2002).

[179] L. Taillefer and G. G. Lonzarich, Phys. Rev. Lett. **60**, 1570 (1988).

[180] Noriaki Kimura, Takemi Komatsubara, Dai Aoki, Yoshichika Ōnuki, Yoshi-nori Haga, Etsuji Yamamoto, Haruyoshi Aoki, and Hisatomo Harima, J. Phys. Soc. Jpn. **67**, 2185 (1998).

[181] J.H. Quateman and P.M. Tedrow, Physica B **135**, 154 (1985).

[182] P. M. Tedrow and J. H. Quateman, Phys. Rev. B **34**, 4595 (1986).

[183] G. Holter and H. Adrian, Solid State Commun. **58**, 45 (1986).

[184] G. M. Roesler, Jr. and P. M. Tedrow, Phys. Rev. B **45**, 12893 (1992).

[185] M. Huth, S. Reber, C. Heske, P. Schicketanz, J. Hessert, P. Gegenwart, and H. Adrian, J. Phys.: Condens. Matter **8**, 8777 (1996).

[186] D. Groten, G.J.C. van Baarle, R.W.A. Hendrikx, J. Aarts, G.J. Nieuwen-huys, and J.A. Mydosh, Physica B **259-261**, 30 (1999).

[187] D. Groten, J. Aarts, G.J.C. van Baarle, R.W.A. Hendrikx, G.J. Nieuwen-huys, and J.A. Mydosh, Physica B **281&282**, 53 (2000).

[188] D. Groten, G. J. C. van Baarle, J. Aarts, G. J. Nieuwenhuys, and J. A. Mydosh, Phys. Rev. B **64**, 144425 (2001).

[189] A. Otop, S. Süllow, M.B.S. Hesselberth, and J. Aarts, Acta Phys. Pol. B **34**, 1169 (2003).

[190] A. Otop, G. R. Boogaard, R. W. A. Hendrikx, M. B. S. Hesselberth, C. Ciuhu, A. Lodder, and J. Aarts, Europhys. Lett. **64**, 91 (2003).

[191] M. Jourdan, A. Zakharov, M. Foerster, and H. Adrian, cond-mat/0403634 (2004).

[192] C. Geibel, S. Thies, D. Kaczorowski, A. Mehner, A. Grauel, B. Seidel, U. Ahlheim, R. Helfrich, K. Petersen, C.D. Bredl, and F. Steglich, Z. Phys. B **83**, 305 (1991).

[193] C. Geibel, A. Böhm, R. Caspary, K. Gloos, A. Grauel, P. Hellmann, R. Modler, C. Schank, G. Weber, and F. Steglich, Physica B **186-188**, 188 (1993).

[194] N. Cao, J. D. Garrett, T. Timusk, H. L. Liu, and D. B. Tanner, Phys. Rev. B **53**, 2601 (1996).

[195] Noriaki Sato, Nobuhiko Koga, and Takemi Komatsubara, J. Phys. Soc. Jpn. **65**, 1555 (1996).

[196] F. Steglich, J. Aarts, C. D. Bredl, W. Lieke, D. Meschede, W. Franz, and H. Schäfer, Phys. Rev. Lett. **43**, 1892 (1979).

[197] B. Gorshunov, N. Sluchanko, A. Volkov, M. Dressel, G. Knebel, A. Loidl, and S. Kunii , Phys. Rev. B **59**, 1808 (1999).

[198] *N Grease*, by Apiezon Products, M&I Materials Ltd.

# Acknowledgements

ACKNOWLEDGEMENTS

Furthermore I would like to thank all members of the 1. Physikalisches Institut for help in one way or another, many stimulating discussions, and a very pleasant atmosphere. Here special thanks go to Marco Hering for his help with a Maple calculation.

Among the colleagues of the 1. Physikalisches Institut, I particularly thank Stephan Mair and Peter Weber not only for the time at the institute but also for countless hours in Stuttgart-West.

Also I would like to thank Eva Sittig for comments concerning the layout of this thesis and Michael Dumm for proofreading it.

Finally I thank my family, friends, and all other people who supported me during my studies that finally led to this dissertation.

# Curriculum Vitae

Born August 17th, 1973 in Hildesheim

**Education:**
1980 - 1984: Didrik-Pining-Schule Hildesheim

1984 - 1986: Orientierungsstufe Ost Hildesheim

1986 - 1993: Scharnhorstgymnasium Hildesheim

May 1993: Abitur (high school graduation)

**Military Service:**
July 1993 - June 1994: Draftee

**Studies:**
October 1994 - July 1997: Student of physics and mathematics,
Technische Universität Braunschweig

September 1996: Prediploma in physics

August 1997 - December 1998: Graduate student of physics,
University of Maryland, College Park

December 1998: Master of Science, thesis: 'Broadband Microwave Surface
Impedance Measurements on $La_{0.8}Sr_{0.2}MnO_3$', advisor Steven M. Anlage

Since June 1999: PhD student at 1. Physikalisches Institut, Universität Stuttgart

**Internships:**
1994, 1995: SQUID section, Forschungsgesellschaft für Informationstechnik,
Bad Salzdetfurth

1997: Superconductivity section, Siemens AG research division, Erlangen

**Honors:**
1994: National champion of 'Jugend forscht' (German science fair competition)

1995 - 1999: Grantee of Studienstiftung des deutschen Volkes
(German National Scholarship Foundation)

1997 - 1998: Fulbright-Grantee